Search for $\tau \to \ell\ell\ell$ and $\tau \to \ell hh$ at Belle experiment

Yosuke Yusa

Department of Physics, Faculty of Science,

Tohoku University

February 2005

Abstract

In the Standard Model (SM), lepton-number-violating (LNV) and lepton-flavor-violating (LFV) decays of charged leptons are forbidden or highly suppressed. However, many extensions of the SM expect the LNV or LFV decays with the branching fractions of observable scale. Some of those models predict LFV decays of charged τ leptons enhanced to a level accessible at present B-factories. Observation of LNV or LFV would provide evidence for new physics beyond the SM. In this thesis, we report on a search for twenty LFV τ decay modes: $\tau^- \to e^-e^+e^-$, $\tau^- \to e^-\mu^+\mu^-$, $\tau^- \to e^+\mu^-\mu^-$, $\tau^- \to \mu^-e^+e^-$, $\tau^- \to \mu^+e^-e^-$, $\tau^- \to \mu^-\mu^+\mu^-$, $\tau^- \to e^-\pi^+\pi^-$, $\tau^- \to e^+\pi^-\pi^-$, $\tau^- \to \mu^-\pi^+\pi^-$, $\tau^- \to \mu^+\pi^-\pi^-$, $\tau^- \to e^-\pi^+K^-$, $\tau^- \to e^-\pi^-K^+$, $\tau^- \to e^+\pi^-K^-$, $\tau^- \to e^-K^+K^-$, $\tau^- \to e^+K^-K^-$, $\tau^- \to \mu^-\pi^+K^-$, $\tau^- \to \mu^-\pi^-K^+$, $\tau^- \to \mu^+\pi^-K^-$, $\tau^- \to \mu^-K^+K^-$ and $\tau^- \to \mu^+K^-K^-$. Charge conjugate decay modes are implied throughout this thesis. We present here a new search based on a data sample of 158 fb^{-1} corresponding to 144 million τ-pairs collected with the Belle detector at the KEKB asymmetric energy e^+e^- collider operating at a center-of-mass energy $\sqrt{s}$ of 10.6 GeV. Because the number of observed signals is compatible with that expected from the background, we set 90% confidence level upper limits on the branching fractions in the range $(1.9 - 16.6) \times 10^{-7}$ for various decay modes.

Acknowledgment

First, I would like to express my apprecation to my supervisor Prof. A. Yamaguchi for his supervising and educationing for high energy physics.
I am deeply grateful to Prof. H. Yamamoto. He gave me much useful advice for my study. I apprreciate Dr. T. Nagamine for introducing me the basics of analysis and setting up computing environments of our laboratory. Without the supprot of the Tohoku Belle group staff, I can not finish this analysis.
I would like to express my thanks to Prof. M. Yamaguchi of Particle Thorety group of Tohoku unuiversity for having discussion and giving me advice for theory part of the thesis.
I also appriciate the all members of Belle collaboration and KEKB operation team.
I am thankful for members of Tau and Two-photon group which I belongs to. Among them, I would like to express special appreciation to Prof. T. Ohshima, Prof. H. Hayashii, Prof. S. I. Eidelman and Dr. K. Inami for suggestions and advice not only at group meeting but also at many times of discussions. I am also thankful for Prof. I. Adachi and Prof. J-P. Perroud who are internal referees of the journal paper of this analysis.
I would like to thank the members of N-laboratory of Nagoya university since τ data is mainly located in their computer system and I used it many times. With their kind support, I smoothly worked on their system.
My appreciation also goes to the KLM and muon ID group members who supported me and worked together for task on detector maintenance.
I am thankful to the members of Reserch Center for Neutrino Science, Tohoku KamLAND group. They gave me chance to know another experimental topics.
I also stayed at Tsukuba hall at KEK not a short time. I wish to thank all colleagues whom I shared a life in both place.
Finally, I would like to thank my family for their support.

Contents

List of Figures

List of Tables

Chapter 1

Introduction

In the SM, lepton decays which violates a lepton number or lepton flavor are forbidden or highly suppressed even if the effect of neutrino mixing is taken into account [1]. However, LFV is expected in many extensions of the SM such as right-handed neutrinos [2, 3], SUSY models with Higgs mediation [4], multi-Higgs bosons [5], extra Z' gauge bosons [6] and R-parity violating interactions [7]. Some of those models predict LNV or LFV decays of charged τ leptons enhanced to a level accessible at present B-factory experiment and observation of LFV would provide the evidence of new physics beyond the SM. In this thesis, we have searched for six LNV or LFV τ decay modes into three charged leptons:

$$\begin{gathered}\tau^- \to e^-e^+e^-,\ \tau^- \to e^-\mu^+\mu^-,\ \tau^- \to e^+\mu^-\mu^-,\\ \tau^- \to \mu^-e^+e^-,\ \tau^- \to \mu^+e^-e^- \text{ and } \tau^- \to \mu^-\mu^+\mu^-\end{gathered} \tag{1.1}$$

with 87.1 fb^{-1} of data and fourteen LNV or LFV τ decay modes into one charged lepton and two charged psudescholar particles:

$$\begin{gathered}\tau^- \to e^-\pi^+\pi^-,\ \tau^- \to e^+\pi^-\pi^-,\\ \tau^- \to \mu^-\pi^+\pi^-,\ \tau^- \to \mu^+\pi^-\pi^-,\\ \tau^- \to e^-\pi^+K^-,\ \tau^- \to e^-\pi^-K^+,\ \tau^- \to e^+\pi^-K^-,\\ \tau^- \to e^-K^+K^-,\ \tau^- \to e^+K^-K^-,\\ \tau^- \to \mu^-\pi^+K^-,\ \tau^- \to \mu^-\pi^-K^+,\ \tau^- \to \mu^+\pi^-K^-,\\ \tau^- \to \mu^-K^+K^- \text{ and } \tau^- \to \mu^+K^-K^-\end{gathered} \tag{1.2}$$

with 158 fb^{-1} of experimental data. For these decay modes, charge conjugate modes are implied throughout this thesis. Upper limits on the branching fractions for these decays on the order of 10^{-6} at 90% confidence level. We present here a new search based on a data sample collected with the Belle detector [8] at the KEKB asymmetric energy e^+e^- collider [9] operating at a center-of-mass energy $\sqrt{s}$ near 10.6 GeV.
In Chapter 2, we illustrate theoretical evaluations of LNV or LFV branching ratios in both case of Standard Model with neutrino mixing and expanded Standard Model with the elements of new physics such as SUSY seesaw mechanism. After examining the physics motivation of this analysis, we describe the experimental apparatus

involving KEKB accelerator, Belle detector and software system in Chapter 3. The event reconstruction and selection criteria is mentioned in front part of Chapter 4. In last part of the chapter, the result of experimental data analysis is shown. In Chapter 5, summary of the analysis, interpretation of obtained result and future prospect of this analysis are described.

Chapter 2

Lepton Flavor Violation

In this chapter, we introduce the origin of LFV and LNV processes and demonstrate the calculation of decay rates of those processes in the scheme of established Standard Model and that of extension with new physics contributions. Finally, we specify the motivation of this search, in other words, the advantage of search for LFV or LNV processes using the modes of Eq. (1.1) and (1.2).

2.1 Lepton Flavor Violation with Neutrino Mixing

In quark sector of the scheme of the Standard Model, flavor changing neutral currents (FCNC) process occurs owing to the quark mixing. Transition between the second and third generation $b \to s$ happens through the W boson exchanging penguins that is shown with a Feynman diagram of Figure 2.1. They are observed as the decays of B meson, for example $B \to K^*\gamma$ and $B \to K\ell\ell$ [10, 11]. As shown in Figure 2.2, we can write the transition diagram for lepton sector as same as quark sector. In the Standard Model with zero mass neutrino, this process is forbidden because lepton mixing does not occur due to the neutrino mass degeneracy. However, several neutrino experiments have observed the evidence of non-zero neutrino mass and they possess different masses between different generations [12, 13, 14, 15]. In case we introduce the neutrinos which have non-zero masses and their mixing between different generations, LFV process is permitted. We describe a weak eigenstate ν_ℓ, (ℓ is e, μ, τ) as a superposition of mass eigenstate ν_i ($i = 1, 2, 3$), each with different masses m_{ν_i},

$$\nu_\ell = \sum_{i=1}^{N} U_{\ell i}\nu_i \tag{2.1}$$

where U_{li} is a unitary mixing matrices. To simplify the calculation of decay rate, we consider the flavor mixing process only between the second and third generation; the mixing matrix is then characterized with a single parameter of mixing angle θ. The decay rate of the τ-μ transition is then evaluated in the extended Weinberg-Salam

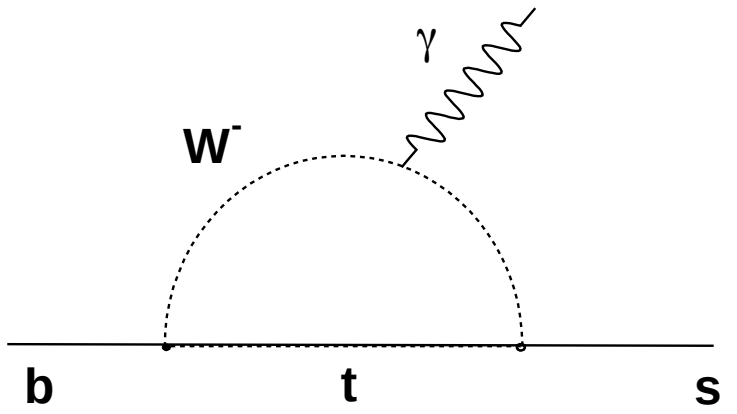

Figure 2.1: Feynman diagram of $b \to s$ flavor changing neutral current process.

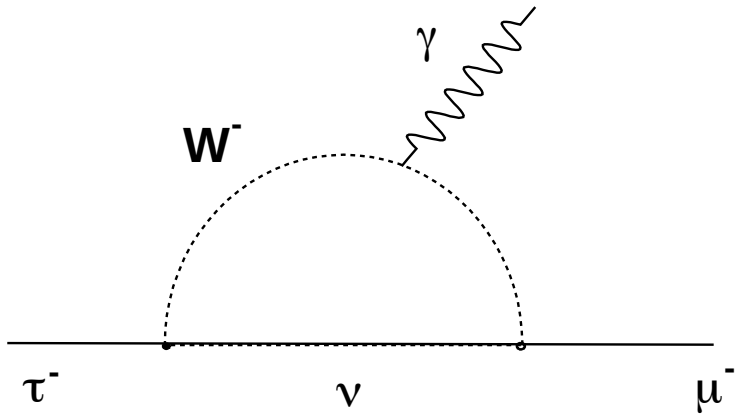

Figure 2.2: Feynman diagram of $\tau \to \mu$ process through neutrino mixing.

model [16] with left-handed currents with Dirac neutrino,

$$\Gamma(\tau \to \mu\gamma) = \frac{1}{16}\frac{G_F^2 m_\tau^5}{128\pi^3}\frac{\alpha_w}{\pi}\left(\frac{m_2^2 - m_3^2}{M_W^2}\right)^2 \sin^2\theta\cos^2\theta, \tag{2.2}$$

where G_F is Fermi coupling constant, m_τ is invariant mass of τ, α_w is weak fine-structure constant and M_W is mass of $W^\pm$ gauge boson. m_2 and m_3 is mass of the eigenstate ν_2 and ν_3, respectively. The branching ratio with respect to the τ decay is, therefore,

$$\begin{aligned}\mathcal{B}(\tau \to \mu\gamma) &= 1.3 \times 10^5 \frac{\alpha_w}{\pi}\left(\frac{m_2^2 - m_3^2}{M_W^2}\right)^2 \sin^2\theta\cos^2\theta \\ &= 7 \times 10^{-42}(\Delta m^2)^2 \sin^2\theta\cos^2\theta. \end{aligned}\tag{2.3}$$

where $\Delta m^2 = |m_2^2 - m_3^2|$ in the unit of $(\mathrm{eV})^2$. Thus, the branching fraction of decay which includes the τ-μ transition through neutrino mixing is unobservably small even if Δm^2 is in the $(\mathrm{MeV})^2$ range and $\theta = \pi/4$.

2.2 Lepton Flavor Violation in Models beyond the Standard Model

We extend the SM including the concept of a particle which is identical to its antiparticle propounded by Majorana. We refer to such a particle as a Majorana particle. We examine the Standard Model introducing a number n_L of left-handed neutrinos ν_L and an additional set of a number n_R right-handed neutrinos. The neutrino mass term can be written as

$$-\mathcal{L}_Y^\nu = \frac{1}{2}\left(\bar{\nu_L}, \bar{\nu_R^C}\right) M^\nu \begin{pmatrix} \nu_L^C \\ \nu_R \end{pmatrix} + h.c., \tag{2.4}$$

containing an $(n_L + n_R) \times (n_L + n_R)$-dimensional matrix M. This matrix can always be diagonalized by means of a congruent transformation involving a unitary matrix U,

$$\begin{aligned} M^\nu &= \begin{pmatrix} 0 & m_D \\ m_D^T & m_M \end{pmatrix}, \\ UM^\nu U^T &= \hat{M}^\nu. \end{aligned}\tag{2.5}$$

The resulting $(n_L + n_R)$ mass eigenstates n_i are Majorana neutrinos, related to the interaction eigenstates ν_a with the matrix U

$$\begin{aligned} \begin{pmatrix} \nu_L \\ \nu_R^C \end{pmatrix}_a &= \sum_{i=1}^{n_L+n_R} U_{ia}^* n_{Li}, \\ \begin{pmatrix} \nu_L^C \\ \nu_R \end{pmatrix}_a &= \sum_{i=1}^{n_L+n_R} U_{ia} n_{Ri}. \end{aligned}\tag{2.6}$$

The first n_L eigenstates are the light neutrinos which is the partners of the charged leptons (*i.e.*, $n_L = 3$), while the other n_R eigenstates are heavy Majorana neutrinos. The interaction of the Majorana neutrinos n_i and charged leptons l_i with the gauge bosons, $W^{\pm}$ and Z^0, and the Goldstein bosons, $G^{\pm}$ and G^0 in the Feynman-'t Hooft gauge), are correspondingly obtained from the following Lagrangian.

$$\mathcal{L}^W_{int} = -\frac{g_w}{\sqrt{2}} W^{-\mu} \sum_{i=1}^{n_L} \sum_{j=1}^{n_L+n_R} B_{l_i,j} \bar{l_i} \gamma_\mu P_L n_j + h.c., \tag{2.7}$$

$$\mathcal{L}^Z_{int} = -\frac{g_w}{4c_w} Z^\mu \sum_{i,j=1}^{n_L+n_R} n_i \bar{\gamma}_\mu \left[iImC_{ij} - \gamma_5 ReC_{ij} \right] n_j, \tag{2.8}$$

and

$$\mathcal{L}^{G^{\mp}}_{int} = -\frac{g_w}{\sqrt{2}M_W} G^- \sum_{i=1}^{n_L} \sum_{j=1}^{n_L+n_R} B_{l_i,j} \bar{l_i} \left[m_{l_i} P_L - m_j P_R \right] n_j + h.c., \tag{2.9}$$

$$\mathcal{L}^{G^0}_{int} = -\frac{ig_w}{4M_W} G^0 \sum_{i,j=1}^{n_L+n_R} \bar{n}_i \left[\gamma_5 (m_i + m_j) ReC_{ij} + i(m_j - m_i) ImC_{ij} \right] n_j, \tag{2.10}$$

where g_w is the weak coupling constant, $c_w^2 = 1 - s_w^2 = M_W^2/M_Z^2$, P_L and P_R is the chiral projection operators, $P_{L,R} = \dfrac{1 \pm \gamma_5}{2}$ and m_i denotes the neutrino masses. B and C are $n_L \times (n_L + n_R)$- and $(n_L + n_R) \times (n_L + n_R)$-dimensional matrices, respectively, defined as

$$B_{l_i j} = \sum_{k=1}^{n_L} V^l_{l_i k} U^{\nu *}_{kj} \tag{2.11}$$

and

$$C_{ij} = \sum_{k=1}^{n_L} U^{\nu}_{ki} U^{\nu *}_{kj} \tag{2.12}$$

where V^l is the Cabbibo-Kobayashi-Masukawa (CKM) matrix [17] for the lepton sector. The ratio between the Dirac mass and Majorana mass characterizes the strength of the heavy-to-right neutrino mixings,

$$(s_L^{\nu_l})^2 \equiv \sum_h |U_{hl}|^2 \left(\sim \frac{|m_D|^2}{|m_M|^2} \right), \tag{2.13}$$

as well as the size of the light neutrino masses,

$$m_{\nu_{light}} \sim \frac{m_D^2}{m_M}. \tag{2.14}$$

In this model, low experimental bounds on $m_{\nu_{light}}$ impose severe constraints on the $|m_M| \gg |m_D|$ hierarchy required, and consequently also on the heavy-to-light

neutrino mixings. We refer to this model as "Model I."
We introduce another scenario which predicts the light neutrinos are strictly massless and serves an extension of the Standard Model. In this model (called "Model II"), left-handed neutral singlets S_{L_i}, and additionally the right-handed neutrinos ν_{R_i} are introduced. Furthermore, two fact that the interaction which break the lepton number is absent from the model, and the number of the right-handed neutrinos n_R equals the number of the singlet fields S_{L_i}, is assumed. After electroweak symmetry breaking, the neutrino mass terms are described as,

$$-\mathcal{L}_Y^\nu = \frac{1}{2}(\nu_L^0, \nu_R^{0C}, \bar{S_L})\mathcal{M}^\nu \begin{pmatrix} \nu_L^{0C} \\ \nu_R^0 \\ S_L^C \end{pmatrix} + h.c., \tag{2.15}$$

where the $\mathcal{M}^\nu$ is the $(n_L + 2n_R) \times (n_L + 2n_R)$ neutrino mass matrix

$$\mathcal{M}^\nu = \begin{pmatrix} 0 & m_D & 0 \\ m_D^T & 0 & m_M^T \\ 0 & m_M & 0 \end{pmatrix}. \tag{2.16}$$

In case of $n_L = n_R$, this model predicts, for each of the n_L generations, a massless Weyl neutrino and two degenerate neutral Majorana neutrinos. Consequently, the restriction of Eq. (2.14) of Model I does not apply here. Therefore, it is not the smallness of the light neutrino masses but the present experimental lower bounds on $(s_L^{\nu_l})^2$ which impose a certain level of hierarchy of $|m_D| < |m_M|$ between the Dirac and Majorana mass sector. Although this model predicts the massless neutrinos in the light sector, non-zero masses for the light neutrinos can be generated with introduction of small perturbation in the lower right block of the neutrino-mass matrix $\mathcal{M}^\nu$, i.e., small Majorana mass terms for the neutral singlets S_{L_i}, without much effect on the mixings of heavy-to-light fields.
Within Model I and II, the amplitude of $\ell \to 3\ell'$ receives contribution from $\gamma-$penguins, $Z-$penguins and $W(G)$-exchange box diagrams shown in Figure 2.3,

$$\mathcal{M}_{total} = \mathcal{M}_\gamma + \mathcal{M}_Z + \mathcal{M}_{box}, \tag{2.17}$$

$$\mathcal{M}_\gamma = -i\frac{\alpha_w^2 s_w^2}{2M_W^2}\bar{u}_{l'}\gamma^\mu v_{l'}\bar{u}_{l'}\left[F_\gamma^{ll'}\left(\gamma_\mu - \frac{q_\mu \not{q}}{q^2}\right)P_L - G_\gamma^{ll'} i\sigma_{\mu\nu}\frac{q^\nu}{q^2}(m_{l'}P_L + m_l P_R)\right]u_l, \tag{2.18}$$

$$\mathcal{M}_Z = -i\frac{\alpha_w^2}{8M_W^2}\bar{u}_{l'}\gamma^\mu P_L u_l \bar{u}_{l'}\gamma^\mu\left[(2-4s_w^2)P_L - 4s_w^2 P_R\right]v_{l'}F_Z^{ll'}, \tag{2.19}$$

$$\mathcal{M}_{box} = -i\frac{\alpha_w^2}{4M_W^2}\bar{u}_{l'}\gamma^\mu P_L u_l \bar{u}_{l'}\gamma^\mu P_L v_{l'}F_{box}^{ll'}, \tag{2.20}$$

where $q = p_1 + p_2$ for the decay $\ell(p) \to \ell'(p')\ell_1(p_1)\ell_2(p_2)$. In the above expressions, $G_\gamma^{ll'}, F_\gamma^{ll'}, F_Z^{ll'}$ and $F_{box}^{ll'}$ are combinations of mixing matrix elements and some special

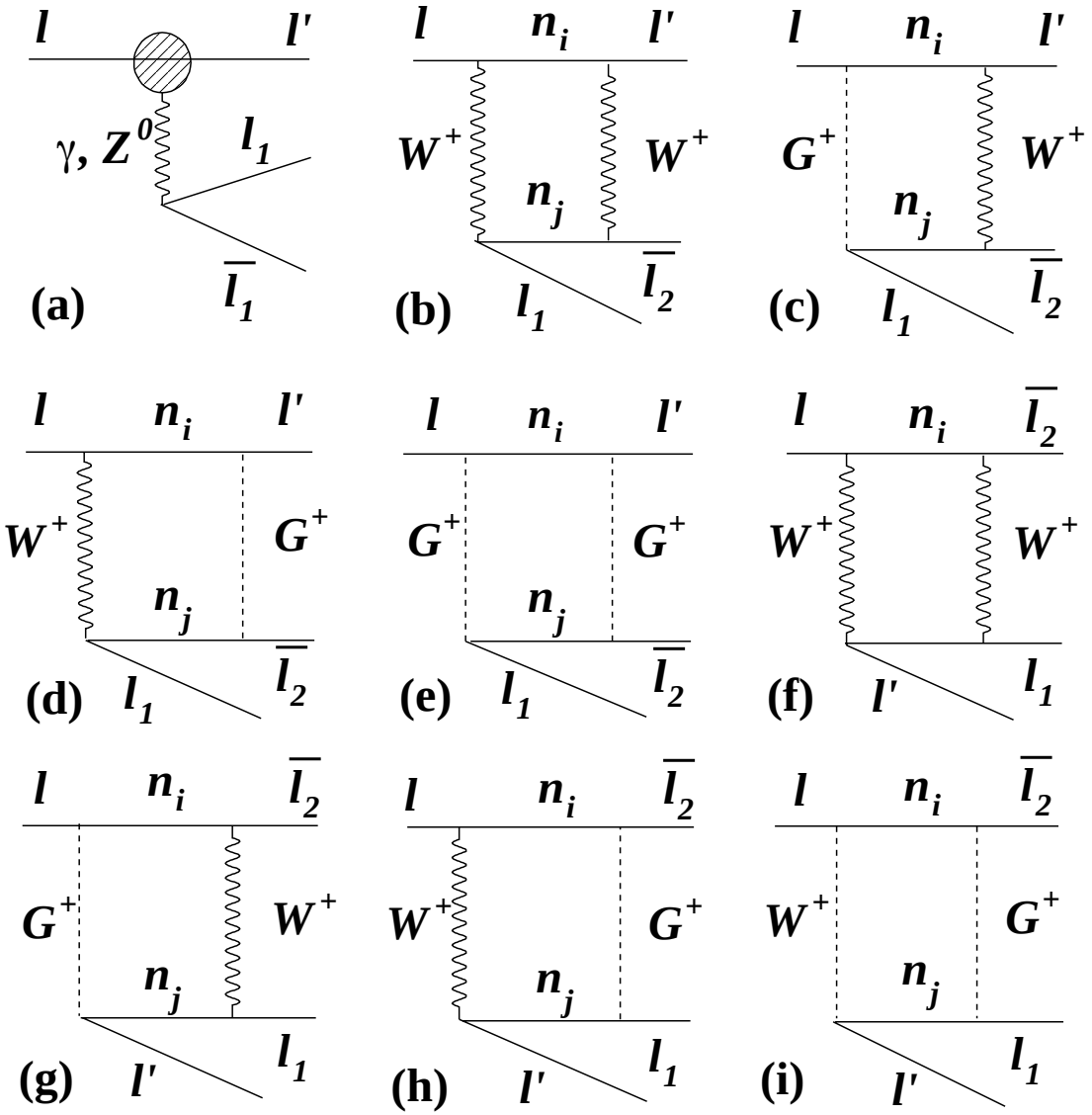

Figure 2.3: Feynman diagram of γ-, Z-penguins (a) and $W(G)$-exchange box (b–i) in the model with right-handed Majorana neutrino.

functions that appear in the loop diagrams of the corresponding processes.

$$G_\gamma^{ll'} = \sum_{i=1}^{n_L+\tilde{n}_R} B_{li}^* B_{l'i} G_\gamma(\lambda_i), \tag{2.21}$$

$$F_\gamma^{ll'} = \sum_{i=1}^{n_L+\tilde{n}_R} B_{li}^* B_{l'i} F_\gamma(\lambda_i), \tag{2.22}$$

$$F_Z^{ll'} = \sum_{i=1}^{n_L+\tilde{n}_R} B_{li}^* B_{l'j} \left[\delta_{ij} F_Z(\lambda_i) + C_{ij} H_Z(\lambda_i,\lambda_j) + C_{ij}^* G_Z(\lambda_i,\lambda_j)\right], \tag{2.23}$$

$$F_{box}^{ll'} = \sum_{i=1}^{n_L+\tilde{n}_R} \left[2B_{l'i}B_{l'j}B_{li}^*B_{l'j}^* F_{box}(\lambda_i,\lambda_j) + B_{l'i}B_{li}B_{lj}^*B_{l'j}^* G_{box}(\lambda_i,\lambda_j)\right], \tag{2.24}$$

where the loop functions of $G_\gamma(x),\ldots,F_{box}(x,y)$ are expressed as

$$F_\gamma(x) = \frac{7x^3-x^2-12x}{12(1-x)^3} - \frac{x^4-10x^3+12x^2}{6(1-x)^4}\ln x, \tag{2.25}$$

$$G_\gamma(x) = \frac{2x^3+5x^2-x}{4(1-x)^3} - \frac{3x^3}{2(1-x)^4}\ln x, \tag{2.26}$$

$$F_Z(x) = -\frac{5x}{2(1-x)^3} - \frac{5x^2}{2(1-x)^2}\ln x, \tag{2.27}$$

$$G_Z(x,y) = -\frac{1}{2(x-y)}\left[\frac{x^2(1-y)}{1-x}\ln x - \frac{y^2(1-x)}{1-y}\ln y\right], \tag{2.28}$$

$$H_Z(x,y) = \frac{\sqrt{xy}}{4(x-y)}\left[\frac{x^2-4x}{1-x}\ln x - \frac{y^2-4y}{1-y}\ln y\right], \tag{2.29}$$

$$\begin{aligned} F_{box}(x,y) = {} & \left(\frac{4+xy}{4(x-y)}\right)\left(\frac{1}{1-x} + \frac{x^2\ln x}{(1-x)^2} - \frac{1}{1-y} - \frac{y^2\ln y}{(1-y)^2}\right) \\ & -\frac{2xy}{x-y}\left(\frac{1}{1-x} + \frac{x\ln x}{(1-x)^2} - \frac{1}{1-y} - \frac{y\ln y}{(1-y)^2}\right), \end{aligned} \tag{2.30}$$

$$\begin{aligned} G_{box}(x,y) = {} & -\frac{\sqrt{xy}(4+xy)}{x-y}\left(\frac{1}{1-x} + \frac{x\ln x}{(1-x)^2} - \frac{1}{1-y} - \frac{y\ln y}{(1-y)^2}\right) \\ & +\frac{2\sqrt{xy}}{x-y}\left(\frac{1}{1-x} + \frac{x^2\ln x}{(1-x)^2} - \frac{1}{1-y} - \frac{y^2\ln y}{(1-y)^2}\right). \end{aligned} \tag{2.31}$$

The calculations for these functions are the square of the masses of the Majorana neutrinos inside the loop, in units of $W^\pm$ boson mass M_W.

$$\lambda_i = m_i^2/M_W^2. \tag{2.32}$$

Eqs. (2.21)−(2.24) involve a summation over all Majorana neutrinos, $\tilde{n}_R$ being the number of heavy ones which equals n_R in Model I and $2n_R$ in Model II. From the amplitude of Eq. (2.18)−(2.20), the decay rates are obtained.

$$\begin{aligned} \Gamma(\ell\to 3\ell') = {} & \Gamma(\ell\to e\bar{\nu}_e\nu_\ell)\cdot\Big\{2|g_4|^2 + |g_6|^2 + 8Re(eA_R(2g_4^* + g_6^*)) \\ & +(1+m_{l'}^2/m_l^2)(32\log(m_l^2/3m_{l'}^2) - 104/3)|eA_R|^2\Big\} \times \Big\{1+\mathcal{O}(m_{l'}^2/m_l^2)\Big\}, \end{aligned} \tag{2.33}$$

where g_4, g_6 and A_R are the coefficients of the operators in the effective Lagrangian related to the processes given by:

$$g_4 = \frac{\alpha_w}{8\pi}\{2s_w^2 F_\gamma^{ll'} + (1-2s_w^2)F_Z^{ll'} + F_{box}^{ll'}\},$$
$$g_6 = \frac{\alpha_w}{8\pi}\{2s_w^2 F_\gamma^{ll'} + (-2s_w^2)F_Z^{ll'}\},$$
$$eA_R = \frac{\alpha}{8\pi}G_\gamma^{ll'}, \tag{2.34}$$

where α is electromagnetic fine structure constant.
To extract the possible branching fraction of LFV decays, we have to set several parameters in the above equations such as masses and mixings of light and heavy neutrinos. We decide them with the result of the recent experiments listed in the latest Particle Data Group review (PDG) [18]: Tritium β-decay provides the bounds on the electron neutrino mass, $m_{\nu_e} < 3$ GeV. The Solar neutrino deficit can be interpreted either by matter enhanced neutrino oscillations if $\Delta m^2_{sol} \sim 1\times 10^{-5}$ eV^2 with small or large mixing, or due to vacuum oscillations if $\Delta m^2_{sol} \sim 10^{-10}$ eV^2 with maximal mixing. Atmospheric neutrino experiments show evidence for $\Delta m^2_{atm} \sim 2.2\times 10^{-3}$ eV^2 with maximal mixing. We assume that $\Delta m^2_{sol} = |m^2_{\nu_\mu} - m^2_{\nu_e}|$ and $\Delta m^2_{atm} = |m^2_{\nu_\tau} - m^2_{\nu_\mu}|$, Since $\Delta m^2_{sol} \ll \Delta m^2_{atm}$, $|m^2_{\nu_\tau} - m^2_{\nu_e}| = \Delta m^2_{atm}$ as well. Since $\Delta m^2_{atm} \gg 3^2$ eV^2, the 3 eV upper limit applies to all three light neutrino masses:

$$m_{\nu_e} < 3 \text{ eV},\ m_{\nu_\mu} < 3 \text{ eV and } m_{\nu_\tau} < 3 \text{ eV}. \tag{2.35}$$

Experimental evidence indicates that ν_τ-ν_e mixing is nearly zero [19]. In Ref. [19], the possible patterns of Majorana neutrino mass matrix are investigated. The result is compatible with the results above and the non-observation of neutrinoless double β-decay [20]. In the models we are considering, a number of low-energy experiments set upper limits on possible non-Standard-Model couplings, which are characterized in [21], as

$$(s_L^{\nu_l})^2 \equiv \sum_h |B_{lh}|^2, \tag{2.36}$$

where h indicates heavy neutrinos. Analysis for models in which the additional neutrinos are $SU(2)_L$-singlets [22] gives the bound

$$(s_L^{\nu_e})^2 < 0.005,\ (s_L^{\nu_\mu})^2 < 0.002, (s_L^{\nu_\tau})^2 < 0.010. \tag{2.37}$$

There is also a theoretical constraint, a perturbative unitarity condition (PUB) [23], which states that perturbation theory to one loop is applicable only in case of the decay width Γ_{n_h} of a heavy Majorana neutrino is small compared to its mass M_{n_h},

$$\Gamma_{n_h} < M_{n_h}/2. \tag{2.38}$$

At the limit of large masses $M_{n_h} \gg M_W, M_Z, M_H$, where M_W, M_Z and M_H are the masses of W, Z gauge and Higgs bosons, respectively, the PUB constitutes an upper

limit for heavy neutrino masses [24, 25]

$$M_{n_h}^2 \sum_{l=1}^{n_L} |B_{lh}|^2 < \frac{2}{\alpha_w} M_W^2, \quad h = 1, \ldots, \tilde{n}_R. \tag{2.39}$$

In addition, there is a lower bound

$$M_{n_h} > 100 \text{ GeV}, \tag{2.40}$$

arising from the non-observation of heavy neutrinos in the direct search experiments. In Eq. (2.37), the bound on the $(s_L^{\nu_\mu})^2$ is tighter than those on $(s_L^{\nu_e})^2$ and $(s_L^{\nu_\tau})^2$, LFV μ decays are suppressed more restrictive than τ decays.
In the case of Model I, we have two light lepton generation (ν_ℓ, ℓ^-) and (ν_τ, τ^-), where ℓ represents for either e or μ. In the considered case there are two independent physical phases $(\delta_i, i = 1, 2)$, so that we can take the Dirac and Majorana submatrices in Eq. (2.5) to be of the form of

$$m_D = \begin{pmatrix} a & be^{i\delta_1} \\ ce^{i\delta_2} & d \end{pmatrix}, \quad m_M = \begin{pmatrix} M_1 & 0 \\ 0 & M_2 \end{pmatrix}, \tag{2.41}$$

where a, b, c and d are the real numbers. We take the convention $M_2 \geq M_1$. The matrix M^ν can be diagonalized via the congruent transformation of Eq. (2.5) — in numerical calculations we use the diagonalization approach as described in [26]. The transformation matrix U can be presented as a product of a seesaw transformation block matrix U_s and a light-sector mixing matrix $V^\dagger$:

$$U = V^\dagger U_s. \tag{2.42}$$

The seesaw transformation produces an effective light neutrino mass matrix $m_{\nu_{light}} \sim m_D m_M^{-1} m_D^T$ in case of $m_D \ll m_M$:

$$m_{\nu_{light}} = \begin{bmatrix} \left(\frac{a^2}{M_1} + \frac{b^2}{M_2} e^{2i\delta_1}\right) & \left(\frac{ac}{M_1} e^{i\delta_2} + \frac{bd}{M_2} e^{i\delta_1}\right) \\ \left(\frac{ac}{M_1} e^{i\delta_2} + \frac{bd}{M_2} e^{i\delta_1}\right) & \left(\frac{c^2}{M_1} e^{2i\delta_2} + \frac{d^2}{M_2}\right) \end{bmatrix} \times \left(1 + \mathcal{O}(m_D^2 m_M^{-2})\right), \tag{2.43}$$

and order of the LFV mixings is approximately same as $m_D m_M^{-1}$. The light sector mixing matrix $V^\dagger$, which is the upper left part of U, is approximately unitary and of the form:

$$V^\dagger \approx \begin{pmatrix} \cos\theta & \sin\theta \exp(-i\epsilon) \\ -\sin\theta \exp(i\epsilon) & \cos\theta \end{pmatrix}, \tag{2.44}$$

where $\theta = 0$ and $\pi/4$ correspond to zero and maximal mixing, respectively, and where ϵ is a CP phase, in general a function of δ_1 and δ_2. According to the result of atmospheric neutrino experiments, we take maximal mixing $\theta = \pi/4$. If we demand that this maximal mixing is obtained independently of the values M_1 and M_2 of

the heavy Majorana sector, the following simple relations in light Dirac sector are implied:

$$a^2 = c^2, \quad b^2 = d^2 \tag{2.45}$$

$$\text{and} \quad \delta_1 = \delta_2 \equiv \delta. \tag{2.46}$$

The value of δ can be restricted to lie in the range $-\pi/2 < \delta < \pi/2$. The eigenmasses of the two light neutrinos are thus

$$m_{\nu_1,\nu_2} = \left| \left[\left(\frac{a^2}{M_1}\right)^2 + \left(\frac{b^2}{M_2}\right)^2 + 2\frac{a^2 b^2}{M_1 M_2}\cos(2\delta) \right]^{1/2} \pm \left(\frac{ac}{M_1} + \frac{bd}{M_2}\right) \right|. \tag{2.47}$$

The heavy-to-light mixing parameters are

$$(s_L^{\nu_\mu})^2 = (s_L^{\nu_\tau})^2 = \frac{a^2}{M_1^2} + \frac{b^2}{M_2^2} \equiv s_L^2, \tag{2.48}$$

and the CP-violating parameter ϵ is

$$\tan\epsilon = \tan\delta \times \frac{(a^2/M_1) - (b^2/M_2)}{(a^2/M_1) + (b^2/M_2)}. \tag{2.49}$$

The conditions of Eq. (2.45) mean two possible case: (i) $a = \pm c$ and $b = \pm d$ or (ii) $a = \pm c$ and $b = \mp d$.
(i) Case $a = \pm c$ and $b = \pm d$: $m_{\nu_\tau} \geq (a^2/M_1 + b^2/M_2)$, in consequence $s_L^2 \leq m_{\nu_\tau}/M_1 < 3$ eV$/M_1 \leq 3 \times 10^{-11}$. Since the branching ratio $\mathcal{B}(\tau \to 3\mu)$ is approximately proportional to $(s_L^{\nu_\mu})^2 (s_L^{\nu_\tau})^2 \equiv s_L^4$, it follows that $\mathcal{B}(\tau \to 3\mu)$ is below 10^{-24}.
(ii) Case $a = \pm c$ and $b = \mp d$: $m_{\nu_\tau} \geq 2|a^2/M_1 - b^2/M_2|$, with the equality being reached only when $\delta = \pi/2$. In the latter case, $m_{\nu_\mu} = 0$, and $m_{\nu_\tau} = 2|a^2/M_1 - b^2/M_2| = (\Delta m^2_{atm})^{1/2} \approx 0.047$ eV. This case ($\delta = \pi/2$) thus avoids the suppression of $s_L^2 = (a^2/M_1 + b^2/M_2)$ while keeping a^2/M_1 extremely close to b^2/M_2. The value of s_L^2 can be saturated to $(s_L^2)_{\max} = 0.002$ (the limit in Eq. 2.37) with the following parameters in the Dirac matrix m_D:

$$a = c = M_1 (s_L)_{\max}/\sqrt{1 + M_1/M_2}, \quad b = -d = a(1 \pm \eta)\sqrt{M_2/M_1},$$
$$\eta = \sqrt{\Delta m^2_{atm}} \left(1 + \frac{M_1}{M_2}\right) \frac{1}{4 M_1 (s_L^2)_{\max}} \approx 1.17 \times 10^{-13} \times \frac{1}{(s_L^2)_{\max}} \left(1 + \frac{M_1}{M_2}\right), \tag{2.50}$$

and where, as mentioned, $\delta = \pi/2$. The branching ratio $\mathcal{B}(\tau \to 3\mu)$ is again practically proportional (s_L^4) and approach their maximum in the case of Eq. (2.50). This condition gives the largest branching ratios in Model I, $\mathcal{B}(\tau \to 3\mu) \leq 10^{-10}$. The branching ratio as a function of M_2 are shown in Figure 2.4 for two different ratios of $M_1/M_2 = 0.1$ and $M_1/M_2 = 0.5$, respectively, accounting also for the PUB conditions. In case δ is moved away from $\pi/2$, the allowed branching fraction drops sharply, mainly due to the upper limits on $m_{\nu_\mu}, m_{\nu_\tau}$, i.e., a situation similar to case

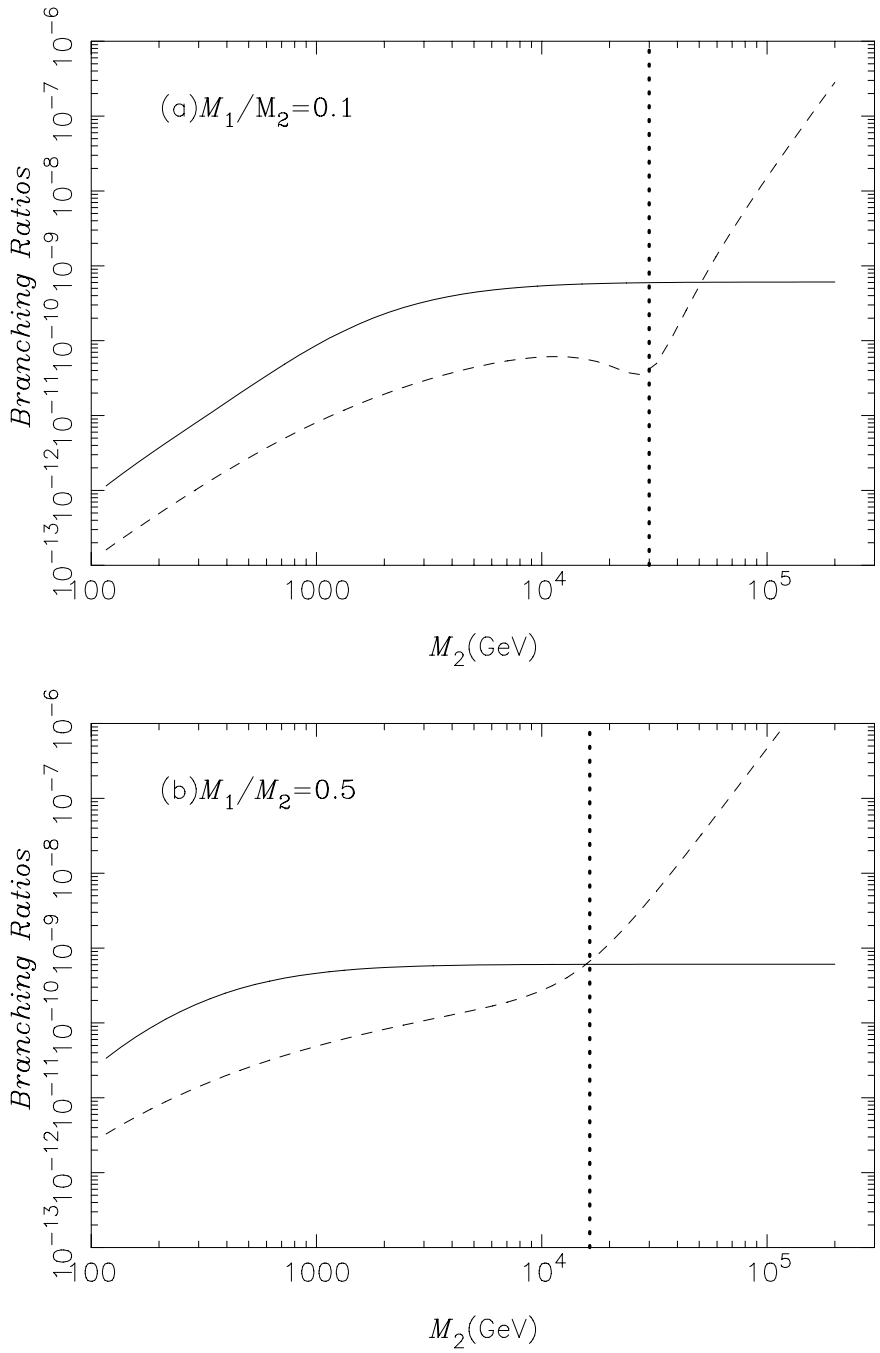

Figure 2.4: Maximal branching ratios for $\tau \to 3\mu$ (dashed lines) as function of M_2 in Model I, for a fixed ratio $M_1/M_2 = 0.1$ (a) and 0.5 (b). M_1 and M_2 are restricted to be above 100 GeV and below the perturbative unitarity bounds of Eq. 2.39, indicated by the vertical line. The Dirac mass parameters are taken in the form Eq. (2.50) and $\delta_1 = \delta_2 = \pi/2$ which give maximal branching ratio at any given M_1 and M_2. The branching fraction for $\tau \to \mu\gamma$ is also shown with a solid line.

(i) sets in. Accordingly, we do not consider other situations in Model I. In case $\tau \to e$, i.e. the process $\tau \to 3e$, the neutrino oscillation experiments indicates that the mixing is almost zero [19]: $\theta \approx 0$ in Eq. (2.44). When we assume that the zero mixing condition is fulfilled independently of the heavy Majorana sector, we obtain the relations $ac = 0$ and $bd = 0$. In cases $a = b = 0$, $(s_L^{\nu_e})^2 = 0$ and similarly, $c = d = 0$ for $(s_L^{\nu_\tau})^2 = 0$. Therefore, the branching ratio is suppressed extremely. In case $a = d = 0$ or $b = c = 0$, $(s_L^{\nu_e})^2(s_L^{\nu_\tau})^2 < m_\nu/M_1 < 3$ eV/100 GeV $= 3 \times 10^{-11}$, i.e., as in case (i), we obtain extremely suppressed branching ratios.
In the two-generation case of $n_L = 2, \tilde{n}_R = 4$ for LFV τ decays which is introduced as Model II, the submatrices m_D and m_M can be taken in the form of

$$m_D = \begin{pmatrix} a & be^{i\xi} \\ ce^{i\xi} & d \end{pmatrix}, \quad m_M = \begin{pmatrix} M_1 & 0 \\ 0 & M_2 \end{pmatrix}. \tag{2.51}$$

In the scheme of this model, there is one CP-violation phase ξ. Since the (n_L) light neutrinos are massless, the LFV τ decay rates neither be affected from the experimental light neutrino mass bounds nor the solar and atmospheric neutrino experiments and their requirements of the maximal (ν_μ-ν_τ, ν_e-ν_μ) or minimal (ν_e-ν_τ) mixing. The rates however is affected from the PUB restrictions, as well as from the mixing parameter bounds in Eq. (2.37). Therefore the rates are proportional to the terms of $(s_L^{\nu_\tau})^2(s_L^{\nu_\mu})^2$ or $(s_L^{\nu_\tau})^2(s_L^{\nu_e})^2$. The rate of $\tau \to \mu$ process is suppressed in comparison to $\tau \to e$ rate because the upper limit for $(s_L^{\nu_\mu})^2$ is smaller than $(s_L^{\nu_e})^2$. Therefore, we argue $\tau \to 3e$ LFV rate below. With a method similar to that demonstrated in the Model I case, we first find the Dirac parameters such that the branching ratios of LFV process gets maximum in case of changing the Majorana masses M_1 and M_2. The amplitude squared $|A|^2$ for the $l \to 3l'$ LFV process is, calculated from Eqs. (2.18−2.20) and (2.21−2.24). In the leading order in $m_D m_M^{-1}$, and there is no CP violation, in other word, in case of matrix U is real, $|A|^2$ is proportional to $\left| \sum_{h=n_L+1}^{n_L+\tilde{n_R}} U_{h2} U_{h1}^* \right|^2$ with some approximation. This proportionality can be supplemented with the Schwartz inequality

$$|A|^2 \propto \left| \sum_h U_{h2} U_{h1}^* \right|^2 \leq \sum_h |U_{h2}|^2 \sum_{h'} |U_{h'1}|^2 \equiv (s_L^{\nu_2})^2 (s_L^{\nu_1})^2. \tag{2.52}$$

The equality is achieved only the case of a set of following proportionality is satisfied

$$\left. \frac{U_{h2}}{U_{h1}} \right|_{h=n_L+1} = \left. \frac{U_{h2}}{U_{h1}} \right|_{h=n_L+2} = \cdots = \left. \frac{U_{h2}}{U_{h1}} \right|_{h=n_L+\tilde{n_R}}. \tag{2.53}$$

For four Dirac parameters a, b, c and d, this requirement gives the relation such as

$$ad = bc, \tag{2.54}$$

and the upper limits of Eq. (2.37) give other conditions. This still allows us the freedom of fixing one of the four Dirac parameters without affecting the rates. We can

, for example, require the symmetry of the m_D matrix: $b = c$. All of the conditions above are considered, the approximately "optimized " choice of m_D parameters are

$$a = \frac{M_2}{\sqrt{(M_2/M_1)^2 + (s_{2m}/s_{1m})^2}} \frac{s_{1m}}{\sqrt{1 - s_{1m}^2 - s_{2m}^2}},$$
$$b = c = a(s_{2m}/s_{1m}), \quad d = a(s_{2m}/s_{1m})^2, \tag{2.55}$$

where $s_{1m}^2 = (s_L^{\nu_e})^2 = 0.005$ and $s_{2m}^2 = (s_L^{\nu_\tau})^2 = 0.010$, taking the numerical values of $(s_L^{\nu_e})^2$ and $(s_L^{\nu_\tau})^2$ to be the upper limits. The branching ratio of $\mathcal{B}(\tau \to 3e)$ as a function of M_2, for two fixed ratios $M_1/M_2 = 0.1$ and 0.5, and for the CP phase $\xi = 0$ are shown in Figure 2.5. From these plots, the LFV branching ratio in case of Model II is expected to be $\mathcal{B}(\tau \to 3e) \leq 10^{-9}$. This bound get smaller slowly when the parameters of Dirac sector (a, b, c, d; ξ) are moved away from the "optimal" ones. As mentioned above, the maximal branching fraction in the process of $\tau \to \mu$ in this model is suppressed due to the additional factor of $(s_L^{\nu_\mu})^2/(s_L^{\nu_e})^2 = 0.002/0.005 = 0.4$.

Evaluation for another τ LFV decay modes is demonstrated in [27] with the model introduced above and the assumption of degeneracy of heavy neutrino masses ($m_{N1} = m_{N2} = m_N$). The diagrams of ℓ-q box, Higgs and W^+W^- shown in 2.6 are considered for $\tau \to \ell P_1 P_2$ modes, where P denotes the pseudoscalar mesons. The quoted theoretical prediction for branching fraction of LFV τ decays are summarized in Table 2.1. The branching ratios of lepton number violation decays $\tau^- \to \ell'^+ P_1^- P_2^-$ are excluded from the table because they are extremely smaller than 10^{-26}. In the branching ratios on the table, x and y are the parameter combinations of matrix elements $B_{l_i,j}$, heavy neutrino masses, $\lambda_N = m_N/M_W^2$ and upper limit values for $s_L^{\nu_l}$. All of the combinations are always smaller than one. With measurements of the branching fraction of LFV processes, we determine or give constraint for these values. As shown in Figure 2.4 and 2.5, $\tau \to \mu\gamma$ and $\tau \to e\gamma$ have better sensitivity than $\tau \to 3\mu$ and $\tau \to 3e$ for presence of new physics model introduced in previous section in most part of the parameter space. In following part, we introduce another model in which the search for $\tau \to \ell\ell\ell$ process is good probe of the new physics search.

We demonstrate a new way in which the LFV on the slepton mass matrices. The slepton can be communicated with the light charged leptons through exchange of Higgs bosons H_u and H_d, where H_u couples only to u-type quarks and H_d couples only to d-type quarks. This provides the possibility of new and flavor violation in the lepton sector. We demonstrate that the decay $\tau \to 3\mu$ is a particularly sensitive probe of LFV at large $\tan\beta$, where $\tan\beta$ is defined as a ratio of vacuum expectations, $\langle H_u \rangle \langle H_d \rangle$. The Lagrangian for the flavor violation among the slepton is

$$-\mathcal{L} = \bar{E}_R Y_E L_L H_d + \bar{\nu}_R Y_\nu L_L + \frac{1}{2} \nu_R^\top M_R \nu_R \tag{2.56}$$

where E_R, L_L and ν_R represent 3×1 matrices in flavor space of right-handed charged leptons, left-handed lepton doublets and right-handed neutrino, and Y_E, Y_ν and M_R are 3×3 matrices in flavor space; for example, $E_R = (e_R, \mu_R \tau_R)^\top$. This Lagrangian

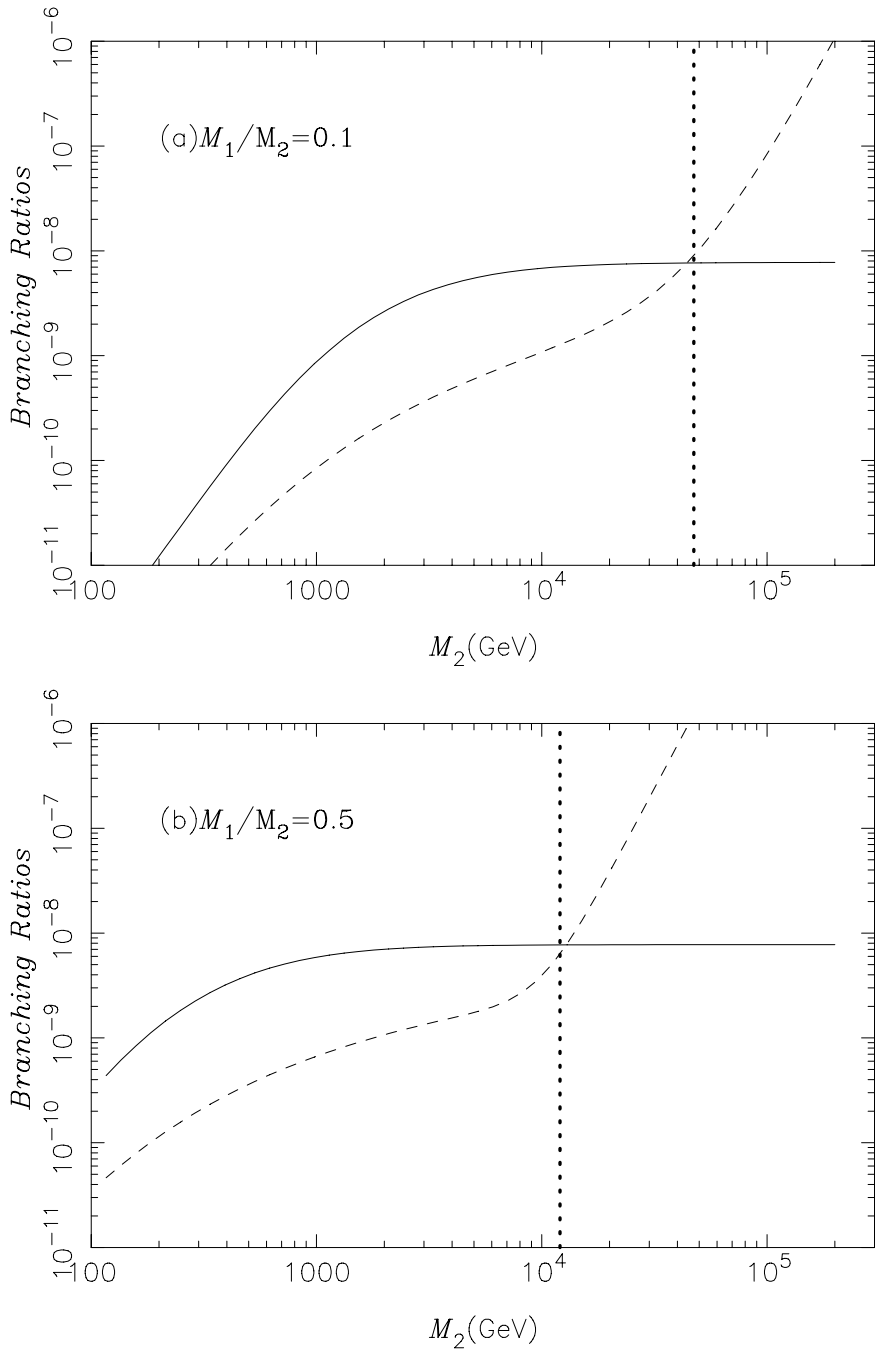

Figure 2.5: Maximal branching ratios for $\tau \to 3e$ (dashed lines) as function of M_2 in Model II, for a fixed ratio $M_1/M_2 = 0.1$ (a) and 0.5 (b). M_1 and M_2 are restricted to be above 100 GeV and below the perturbative unitarity bounds of Eq. 2.39, indicated by the vertical line. The Dirac mass parameters are taken in the form Eq. (2.55) which give approximately maximal branching ratio. The branching fraction for $\tau \to e\gamma$ is also shown with a solid line.

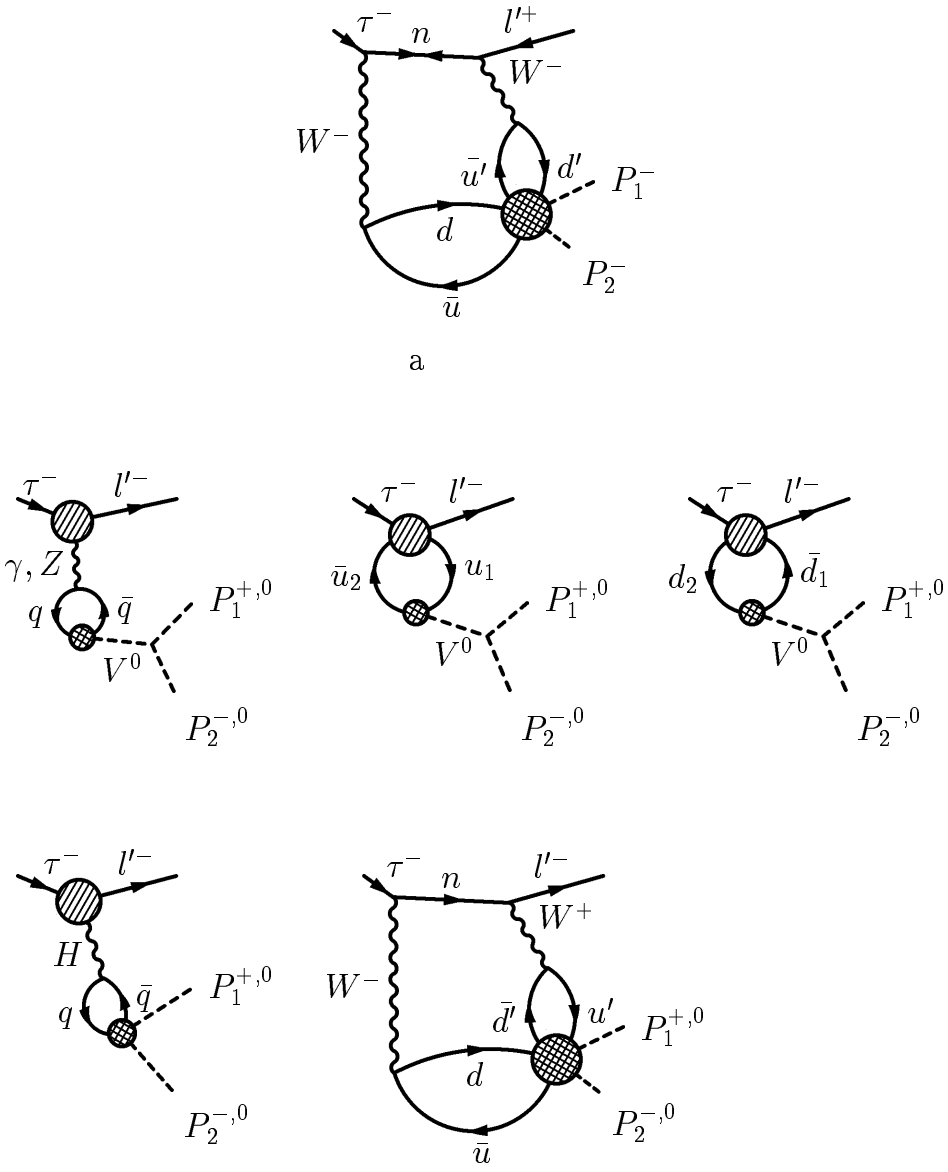

Figure 2.6: Feynman diagrams pertinent to the lepton number violation decay $\tau^- \to \ell'^+ P_1^- P_2^-$ (a) and the lepton flavor violation decays $\tau^- \to \ell'^- P_1 P_2$ (b). The hatched blobs represent sets of lowest order diagrams contributing to three-point and four-point functions which violates the lepton flavor. The double hatched blobs represent interaction through which the final state pseudoscalar mesons are formed.

Table 2.1: Theoretical prediction for branching fraction of LFV τ decays, where x and y are combinations of matrix elements $B_{l_i,j}$, heavy neutrino masses, $\lambda_N = m_N^2/M_W^2$ and upper limit values for $s_L^{\nu_l}$. All of the combinations are always smaller than one.

Mode	Evaluated branching fractions
$\tau^- \to e^- e^+ e^-$	$2.69 \times 10^{-6} y_{\tau e}^2$
$\tau^- \to e^- \mu^+ \mu^-$	$1.44 \times 10^{-6} y_{\tau e}^2$
$\tau^- \to e^+ \mu^- \mu^-$	$1.32 \times 10^{-9} y_{\tau\mu\mu e}^2$
$\tau^- \to \mu^- e^- e^+$	$3.71 \times 10^{-7} y_{\tau\mu}^2$
$\tau^- \to \mu^+ e^- e^-$	$6.67 \times 10^{-9} y_{\tau e e\mu}^2$
$\tau^- \to \mu^- \mu^+ \mu^-$	$4.48 \times 10^{-7} y_{\tau\mu}^2$
$\tau^- \to e^- \pi^+ \pi^-$	$2.67 \times 10^{-6} y_{\tau e}^2$
$\tau^- \to \mu^- \pi^+ \pi^-$	$5.19 \times 10^{-7} y_{\tau\mu}^2$
$\tau^- \to e^- \pi^+ K^-$	$3.29 \times 10^{-15} x_{\tau e}^2$
$\tau^- \to e^- \pi^- K^+$	$3.29 \times 10^{-15} x_{\tau e}^2$
$\tau^- \to e^- K^+ K^-$	$1.07 \times 10^{-6} y_{\tau e}^2$
$\tau^- \to \mu^- \pi^+ K^-$	$6.37 \times 10^{-16} x_{\tau\mu}^2$
$\tau^- \to \mu^- \pi^- K^+$	$6.37 \times 10^{-16} x_{\tau\mu}^2$
$\tau^- \to \mu^- K^+ K^-$	$2.07 \times 10^{-7} y_{\tau\mu}^2$

clearly violates both family and total lepton number due to the presence of the ν_R Majorana mass term. We can choose to work in a basis in which both Y_E and M_R have been diagonalized, but Y_ν remains an arbitrary, complex matrix.
Within the Standard Model, $O(1)$ flavor violation in the neutrinos does not translate into appreciable flavor violation in the charged lepton sector due to $1/M_R$ suppressions. This is, however different in slepton sector. The SUSY breaking slepton masses are unprotected due to chiral symmetries and are therefore sensitive to physics at all mass scales between $m_{\tilde{L}}$ and the scale of M, at which SUSY breaking is communicated to the visible sector, assuming $M > M_R$. This can be seen by examining the renormalization group equation for $m_{\tilde{L}}^2$ at scale above M_R:

$$\frac{d}{d\log Q}(m_{\tilde{L}}^2)_{ij} = \left(\frac{d}{d\log Q}(m_{\tilde{L}}^2)_{ij}\right)_{MSSM}$$
$$+\frac{1}{16\pi^2}\left[m_{\tilde{L}}^2 Y_\nu^\dagger Y_\nu + Y_\nu^\dagger Y_\nu m_{\tilde{L}}^2 + 2(Y_\nu^\dagger m_{\tilde{\nu u}_R}^2 Y_\nu + m_{H_u}^2 Y_\nu^\dagger Y_\nu + A_\nu^\dagger A_\nu)\right]_{ij} \qquad (2.57)$$

where the first term represents the L-conserving term present in the usual minimal supersymmetric Standard Model (MSSM) at scales below M_R. Because Y_ν is off-dimensional, it generates flavor-mixing in the slepton mass matrix. This equation is solved approximately for the flavor mixing piece:

$$(\Delta m_{\tilde{L}}^2)_{ij} \simeq -\frac{\log(M/M_R)}{16\pi^2}\Big(6m_0^2(Y_\nu^\dagger Y_\nu)_{ij} + 2(A_\nu^\dagger A_\nu)_{ij}\Big) \qquad (2.58)$$

where m_0 is a common scalar mass evaluated at the scale $Q = M$, and $i \neq j$. In the assumption that the A-terms are proportional to Yukawa matrices, thus,

$$(\Delta m^2_{\tilde{L}})_{ij} \simeq \xi (Y^\dagger_\nu Y_\nu)_{ij} \tag{2.59}$$

where

$$\xi = -\frac{\log(M/M_R)}{16\pi^2}(6 + 2a^2)m_0^2. \tag{2.60}$$

and a is constant of order 1. In the simplest SUSY breaking scenarios, gravity plays the role of messenger and mass is the Plank mass ($\sim 10^{19}$ GeV), so that the logarithm in Eq. (2.60) equals approximately 10. To provides an excellent fit to existing neutrino data, the form for m_ν is considered to be

$$m_\nu \propto \begin{pmatrix} \epsilon & \epsilon & \epsilon \\ \epsilon & 1 & 1 \\ \epsilon & 1 & 1 \end{pmatrix} \tag{2.61}$$

where ϵ is a small parameter that is similar to approximately 0.1. In case of assumption that M_R is an identity matrix, $Y^\dagger_\nu Y_\nu$ also have the form of Eq. (2.61). Another possibility is provided from grand unified theory (GUT) models with lopsided mass matrices for charged leptons; such models have $(Y_E)_{32} \simeq (Y_E)_{33}$ and lead to a light neutrino mass matrix as in Eq. (2.61) with $(Y_\nu)_{32} \simeq (Y_\nu)_{33} \simeq y_t$, where y_t is the top Yukawa coupling. In either case, the $Y^\dagger_\nu Y_\nu$ has a flavor violation of amplitude order of 1 in the ν_τ-ν_μ sector in case of $M_R \simeq 10^{14}$ GeV.

The MSSM is not protected against the possibility of FCNC with neutral Higgs bosons mediation. Though the MSSM is a two-Higgs doublet model at tree level, no symmetry protect the structure. In particular, the presence of a non-zero μ-term which coupled with SUSY breaking, is enough to induce non-holomorphic Yukawa interactions for the quarks and leptons. The two leading diagrams considered as a source for non-holomorphic quark coupling which are not present in the lepton sector since they involving gluinos and top squark inside the loops [28, 29]. There are additional diagrams which are present in the lepton sector [30] involving loops of sleptons and charginos or neutralinos. Those diagrams are shown in Figure 2.7. The effective Lagrangian for the couplings of the charged leptons to the neutral Higgs fields are written as:

$$-\mathcal{L} = \bar{E}_R Y_E R_L H^0_d + \bar{E}_R Y_E (\epsilon_1 + \epsilon_2 Y^\dagger_\nu Y_\nu) E_L H^{0*}_u + h.c. \tag{2.62}$$

The first term is the standard Yukawa coupling, while the second term arises from the non-holomorphic loop corrections. The contribution for the constant ϵ_2 shown as the diagram of Figure 2.7 contains a single interaction of $\Delta m^2_{\tilde{L}}$ which introduces LFV into the process. This is approximated with inserting a single $\Delta m^2_{\tilde{L}}$ mass insertion onto each of the internal $\tilde{E}_L$ lines. The higgsinos and gauginos are treated approximately as mass eigenstates in following calculations. For diagram (a), the contribution to ϵ_2 is

$$\epsilon_{2a} \simeq \frac{\alpha'}{4\pi}\xi\mu M_1 f_2(M_1^2, m^2_{\tilde{\ell}_L}, m^2_{\tilde{\tau}_L}, m^2_{\tilde{\ell}_R}), \tag{2.63}$$

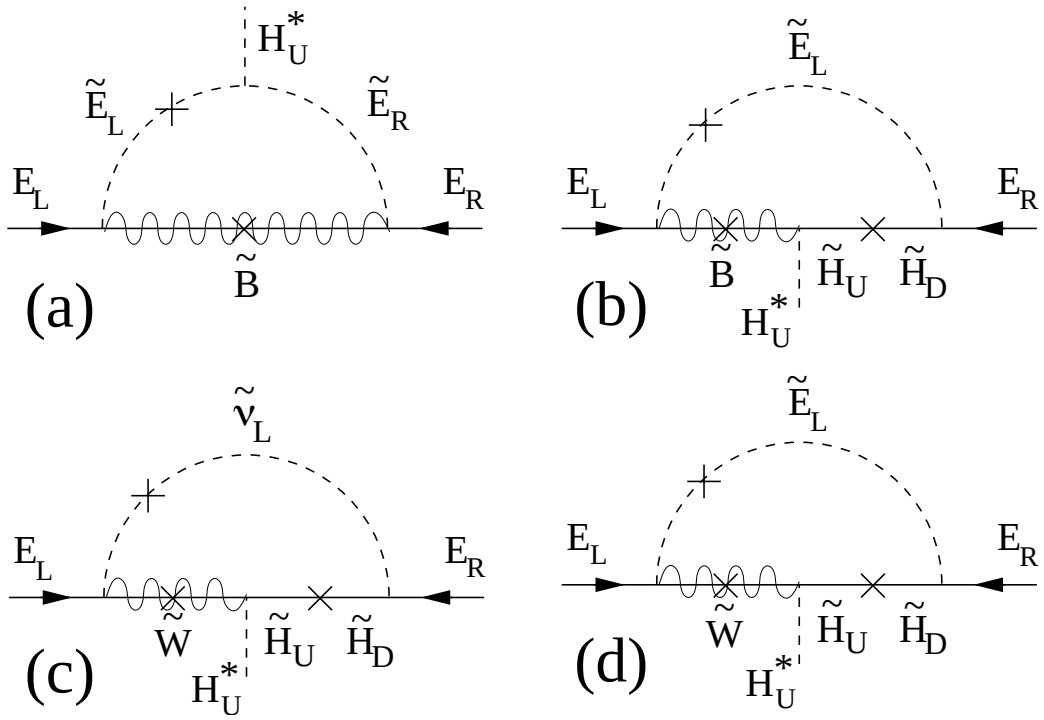

Figure 2.7: Diagrams that contribute to ϵ_2. The crosses on the internal slepton lines represent LFV mass insertions due to loops of ν_R.

where $\tilde{\ell}$ represents for $\tilde{\mu}$ or $\tilde{e}$. The diagram (b) provides a contribution given by

$$\epsilon_{2b} \simeq \frac{\alpha'}{8\pi}\xi\mu M_1 f_2(\mu^2, m^2_{\tilde{\ell}_L}, m^2_{\tilde{\tau}_L}, M_1^2). \tag{2.64}$$

The diagram (c) yields

$$\epsilon_{2c} \simeq \frac{\alpha_2}{4\pi}\xi\mu M_2 f_2(\mu^2, m^2_{\tilde{\nu}_\ell}, m^2_{\tilde{\nu}_\tau}, M_2^2) \tag{2.65}$$

and the contribution of (d) is

$$\epsilon_{2d} \simeq \frac{\alpha_2}{8\pi}\xi\mu M_2 f_2(\mu^2, m^2_{\tilde{\ell}_L}, m^2_{\tilde{\tau}_L}, M_2^2), \tag{2.66}$$

where M_1 and M_2 are the $U(1)$ and $SU(2)$ gaugino masses, respectively, and the function f_2 is defined such that

$$-f_2(a,b,c,d) \equiv \frac{a\log a}{(a-b)(a-c)(a-d)} + \frac{b\log b}{(b-a)(b-c)(b-d)} + \frac{c\log c}{(c-b)(c-a)(c-d)} + \frac{d\log d}{(d-b)(d-c)(d-a)}. \tag{2.67}$$

From the Lagrangian, the charged lepton masses cannot be diagonalized in the same basis as their Higgs couplings. Therefore, neutral Higgs bosons mediate with the

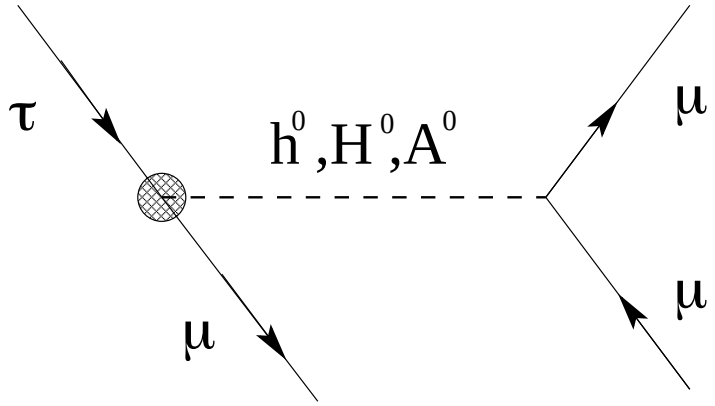

Figure 2.8: The Feynman diagram of $\tau \to 3\mu$ with contribution of MSSM Higgs bosons, h^0, H^0 and A^0. The shaded interaction vertex is the new vertex derived in Eq. (2.70).

rates proportional to ϵ_2^2 in LFV processes. The diagrams which contribute to ϵ_1 are similar to Figure 2.7, however the slepton mass is not inserted.

$$\epsilon_1 = \frac{\alpha'}{8\pi}\mu M_1 \left[2f_1(M_1^2, m_{\tilde{\ell}_L}^2, m_{\tilde{\ell}_R}^2) - f_1(M_1^2, \mu^2, m_{\tilde{\ell}_L}^2) + 2f_1(M_1^2, \mu^2, m_{\tilde{\ell}_R}^2)\right] + \frac{\alpha_2}{8\pi}\mu M_2 \left[f_1(\mu^2, m_{\tilde{\ell}_L}^2, M_2^2) + 2f_1(\mu^2, m_{\tilde{\nu}}^2, M_2^2)\right], \tag{2.68}$$

where

$$-f_1(a,b,c) \equiv \frac{ab\log(a/b) + bc\log(b/c) + ca\log(c/a)}{(a-b)(b-c)(c-a)}. \tag{2.69}$$

These terms do not induce LFV but generate a mass shift for the charged leptons appeared as a second-order effect.
The term $\tau_R\mu_L$ in the effective Lagrangian Eq. (2.62) of is extracted using algebra described in [31]

$$\mathcal{L} \simeq (2G_F^2)^{1/4}\frac{m_\tau \kappa_{32}}{\cos^2\beta}(\bar{\tau}_R\mu_L)\left[\cos(\beta-\alpha)h^0 - \sin(\beta-\alpha)H^0 - iA^0\right] + h.c., \tag{2.70}$$

where

$$\kappa_{ij} = -\frac{\epsilon_2}{\left[1 + \left(\epsilon_1 + \epsilon_2(Y_\nu^\dagger Y_\nu)_{33}\right)\tan\beta\right]^2}(Y_\nu^\dagger Y_\nu)_{ij}. \tag{2.71}$$

The Lagrangian for $(\bar{\tau}_R e_L)$-Higgs can be derived from this expressions replacing the term κ_{32} with κ_{31}. From these interactions, the decay $\tau \to 3\mu$ can be occurred via exchange of MSSM Higgs bosons, h^0, H^0 and A^0 as in the diagram of Figure 2.8. The branching fraction of the process is calculated as

$$\mathcal{B}(\tau \to 3\mu) = \frac{G_F^2 m_\mu^2 m_\tau^7 \tau_\tau}{768\pi^3 m_A^4}\kappa_{32}^2 \tan^6\beta, \tag{2.72}$$

where τ_τ is the τ lifetime and m_μ, m_τ and m_A are the masses of μ, τ and MSSM Higgs bosons, respectively. In case of

$$\mu = M_1 = M_2 = m_{\tilde{\ell}} = m_{\tilde{\nu}}, \quad M_R = 10^{14} \text{ GeV} \text{ and } (Y_\nu^\dagger Y_\nu)_{32} = 1, \tag{2.73}$$

$\epsilon \simeq 4 \times 10^{-4}$ and

$$\mathcal{B}(\tau \to 3\mu) \simeq (1 \times 10^{-7}) \times \left(\frac{\tan\beta}{60}\right)^6 \times \left(\frac{100 \text{ GeV}}{m_A}\right)^4. \tag{2.74}$$

Another parameter space is considered that

$$\mu \gg M_1 = M_2 \simeq m_{\tilde{\ell}}. \tag{2.75}$$

As a result, the bino contribution is enhanced with a factor μ/M_1; for $M_1 \simeq 100$ GeV and $\mu \simeq 1000$ GeV. Thus, $\epsilon \simeq 8 \times 10^{-4}$, resulting in a branching fraction 4 times larger than that stated above.

As mentioned, in the LFV processes, slepton generate large amplitude in the coupling of the lepton to Higgs bosons. The sleptonic flavor violation can induce LFV in certain magnetic moment transitions such as $\tau \to \mu\gamma$, so it is useful to compare this to the $\tau \to 3\mu$ decay. The effective operator for $\tau \to 3\mu$ is dimension-6 such as $(1/m_A^2)\bar{\tau}\mu\bar{\mu}\mu$. The $\tau \to \mu\gamma$ operator is formally dimension-5, but chiral symmetry requires an m_τ insertion, so that the operator is actually dimension-6 such as $(m_\tau/M_{SUSY}^2)\bar{\tau}\sigma^{\mu\nu}\mu F_{\mu\nu}$ where M_{SUSY} represents the heaviest mass scale to enter the slepton-gaugino loops. In case of that sleptons and gauginos are light and A^0 is heavy, $\tau \to \mu\gamma$ would tend to dominate. In the opposite limit and with large $\tan\beta$, $\tau \to 3\mu$ dominate. Because of different coupling behavior, it is impossible to correlate the two decays without choosing a specific model. Therefore, the comparison between the results of search for $\tau \to \mu\gamma$ [32] and $\tau \to 3\mu$ can provide insight into the fundamental SUSY breaking parameters in this model. The presence of the $\tau \to \mu\gamma$ operator also leads to $\tau \to 3\mu$ if the photon goes off-shell. However, for the operator the relation between the two branching fractions is, approximately saying, model independent as described in [33]. Therefore, in case of no Higgs mediation,

$$\frac{\mathcal{B}(\tau \to 3\mu)}{\mathcal{B}(\tau \to \mu\gamma)} \simeq 0.003. \tag{2.76}$$

Thus, if the ratio between the branching ratios of these decays is much larger than above threshold, that clearly indicates the evidence that $\tau \to 3\mu$ decay occurs with new process in which Higgs mediation is a leading contender.

Another option would be the inverted mass hierarchy in which element of (1,2) and (1,3) in Yukawa matrix $Y_\nu^\dagger Y_\nu$ would be the order 1 and the remainder order ϵ. Such matrix can lead to observable $\tau \to e\mu\mu$ process, although the constraints from $\tau \to \mu\gamma$ are strong:

$$M_{SUSY} \simeq 100 \text{ GeV and } (Y_\nu^\dagger Y_\nu)_{21} < 10^{-2}. \tag{2.77}$$

But in the limit of large two parameters of M_{SUSY} and $\tan\beta$, this bound is weakened and $\tau \to e\mu\mu$ process becomes dominant.

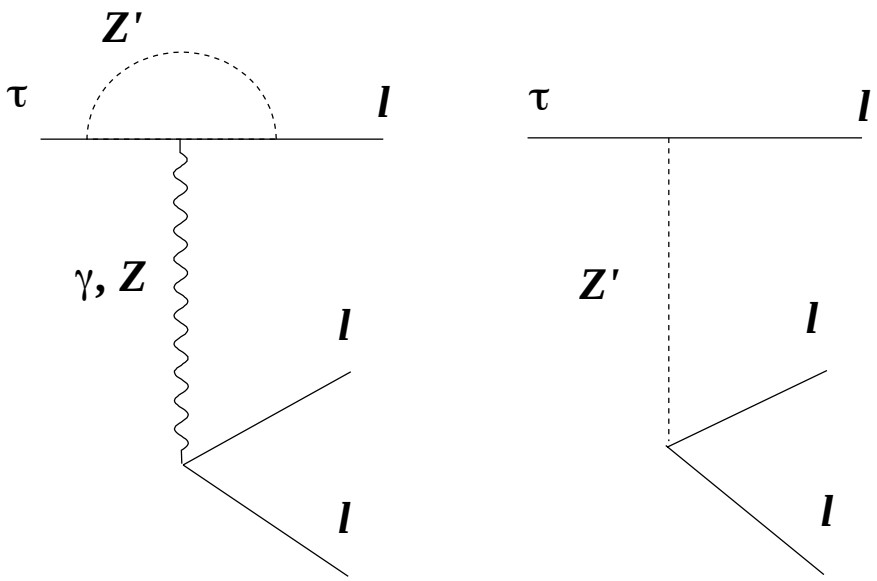

Figure 2.9: Feynman diagrams for decays of $\tau \to \ell\ell\ell$ induced by non-universal gauge bosons Z' exchange.

As with the Higgs bosons, non-universal gauge bosons Z' contributes the LFV processes as shown in the diagram of Figure 2.9 [6]. Z' is predicted in strong top dynamical models, such as the topcolor-assisted technicolor (TC2) models [34] and flavor-universal TC2 models [35]. The flavor-diagonal couplings of Z' to leptons can be written as:

$$\mathcal{L}^{FD}_{Z'} = -\frac{1}{2}\cot\theta' Z'_\mu(\bar{\tau}_L\gamma^\mu\tau_L + 2\bar{\tau}_R\gamma^\mu\tau_R)$$
$$- -\frac{1}{2}\cot\theta' Z'_\mu(\bar{\mu_L}\gamma^\mu\mu_L + 2\bar{\mu_R}\gamma^\mu\mu_R + \bar{e_L}\gamma^\mu e_L + 2\bar{e_R}\gamma^\mu e_R), \tag{2.78}$$

where g_1 is the ordinary hypercharge gauge coupling constant, θ' is the mixing angle with $\tan\theta' = \frac{g_1}{\sqrt{4\pi k_1}}$. To obtain the top quark condensation and not form a $b\bar{b}$ condensation, there must be the condition of $\tan\theta' \ll 1$. Flavor changing couplings of Z' to leptons can be written as:

$$\mathcal{L}^{FC}_{Z'} = -\frac{1}{2}g_1 Z'_\mu[k_{\tau\mu}(\bar{\tau}_L\gamma^\mu\mu_L + 2\bar{\tau}_R\gamma^\mu\mu_R)+$$
$$k_{\tau e}(\bar{\tau}_L\gamma^\mu e_L + 2\bar{\tau}_R\gamma^\mu e_R) + k_{\mu e}\tan^2\theta(\bar{\mu}_L\gamma^\mu e_L + 2\bar{\mu}_R\gamma^\mu e_R)], \tag{2.79}$$

where k_{ij} are the flavor mixing factors and $k_{\tau\mu} = k_{\tau e} = k_{\mu e} = \lambda$ is taken in the following estimation, where λ is the Wolfenstein parameter and equal 0.22 [36]. The

partial widths of $\tau \to \ell\ell\ell$ decay is written as

$$\begin{aligned}\Gamma(\tau \to 3\mu) = \Gamma(\tau \to 3e) = \Gamma(\tau \to ee\mu) = \Gamma(\tau \to \mu\mu e) \\ = \frac{25\alpha^3}{384\pi k_1 \cos^6\theta_W} \frac{m_\tau^5}{M_Z^4} k^2,\end{aligned} \tag{2.80}$$

where θ_W is the Weinberg angle and M_Z is the mass of the non-universal gauge bosons Z' [37]. Because the contributions of the off-shell γ- and Z-penguin are much smaller than those of the Z'-exchange at tree level, The contributions of penguin diagrams are ignored for the calculation of the decay rate above. The widths of $\tau \to \ell\ell\ell$ decays are common to all four LFV decay modes because Z' only treat the fermions in the third generation differently from those in the first and second generations. Thus the branching ratio is derived as

$$\mathcal{B}(\tau \to \ell\ell\ell) = \mathcal{B}(\tau \to e\nu_e\nu_\tau) \cdot \frac{25\pi^2\alpha k^2}{2G_F^2 k_1 \cos^6\theta_W M_Z^4} \tag{2.81}$$

In [6], the branching ratio of $\tau \to \ell\gamma$ decays are also calculated for similar physics model. These processes are generated with the on-shell photon penguin diagrams and the branching fraction is

$$\mathcal{B}(\tau \to \ell\gamma) = \mathcal{B}(\tau \to e\nu_e\nu_\tau) \cdot \frac{\pi\alpha^2 k^2 k_1}{6G_F^2 \cos^2\theta_W M_Z^4} \tag{2.82}$$

In Fugure 2.10 and 2.11, branching ratios $\mathcal{B}(\tau \to \ell\ell\ell)$ and $\mathcal{B}(\tau \to \ell\gamma)$ as function of M_Z for three values of mixing parameters k_1 are plotted, respectively. In these plots, $\mathcal{B}(\tau \to \ell\gamma)$ increase in case k_1 increasing, while $\mathcal{B}(\tau \to \ell\ell\ell)$ decrease in case k_1 increasing. However, $\mathcal{B}(\tau \to \ell\gamma)$ does not exceed $\mathcal{B}(\tau \to \ell\ell\ell)$ although we change M_Z. Therefore in this model, searching for $\tau \to \ell\ell\ell$ decays are more sensitive on the contribution of new physics than $\tau \to \mu\gamma$ and any other τ LFV decays search.

2.3 Experimental Upper Limits

The LFV process has not been observed in any of phenomena of charged leptons yet. Most of the model beyond the Standard Model predicts the branching fraction of LFV τ decays are larger than LFV μ decays because the coupling between τ and new particle introduced in the new models is stronger than that of muon because mass of τ is much heavier than μ. However obtaining the τ sample is more difficult than μ. The first search for τ LFV decays carried out in the MARK II experiment with 17 pb^{-1} of data at center-of-mass (CMS) energy $\sqrt{s} = 3.8 - 6.8$ GeV. They set upper limits for branching ratio of $\tau \to \ell\ell\ell$ decays in the range of $(3.3 - 4.9) \times 10^{-4}$ with 90% confidence level (CL) [38]. In the CLEO experiment, LFV process of $\tau \to \ell\ell\ell$ and $\tau \to \ell hh$ have been searched using the integrated luminosity of 4.79 fb^{-1} of data at the CMS energy of $\Upsilon(4S)$ on resonance region and sets upper limits in the range of $\mathcal{B}(\tau \to \ell\ell\ell) < (1.5 - 2.9) \times 10^{-6}$ and $\mathcal{B}(\tau \to \ell hh) < (1.9 - 15) \times 10^{-6}$ with 90% CL [39]. Recently, high luminosity B-factory experiment, BELLE and

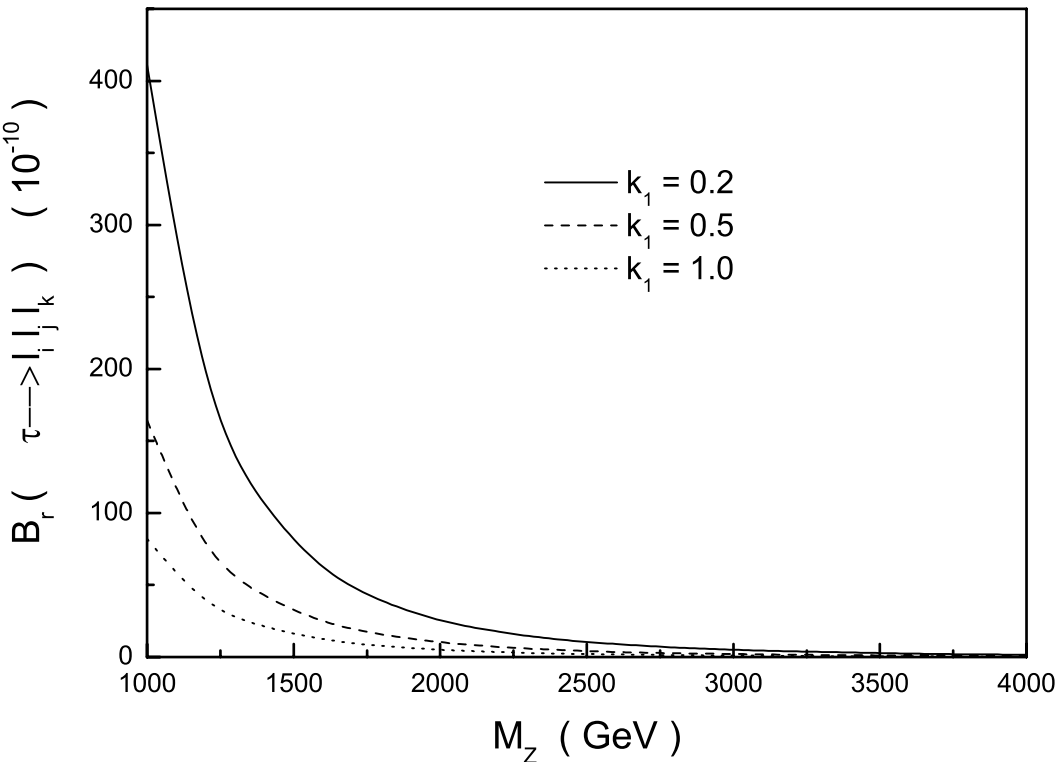

Figure 2.10: Feynman diagrams for decays of $\tau \to \ell\ell\ell$ induced by non-universal gauge bosons Z' exchange.

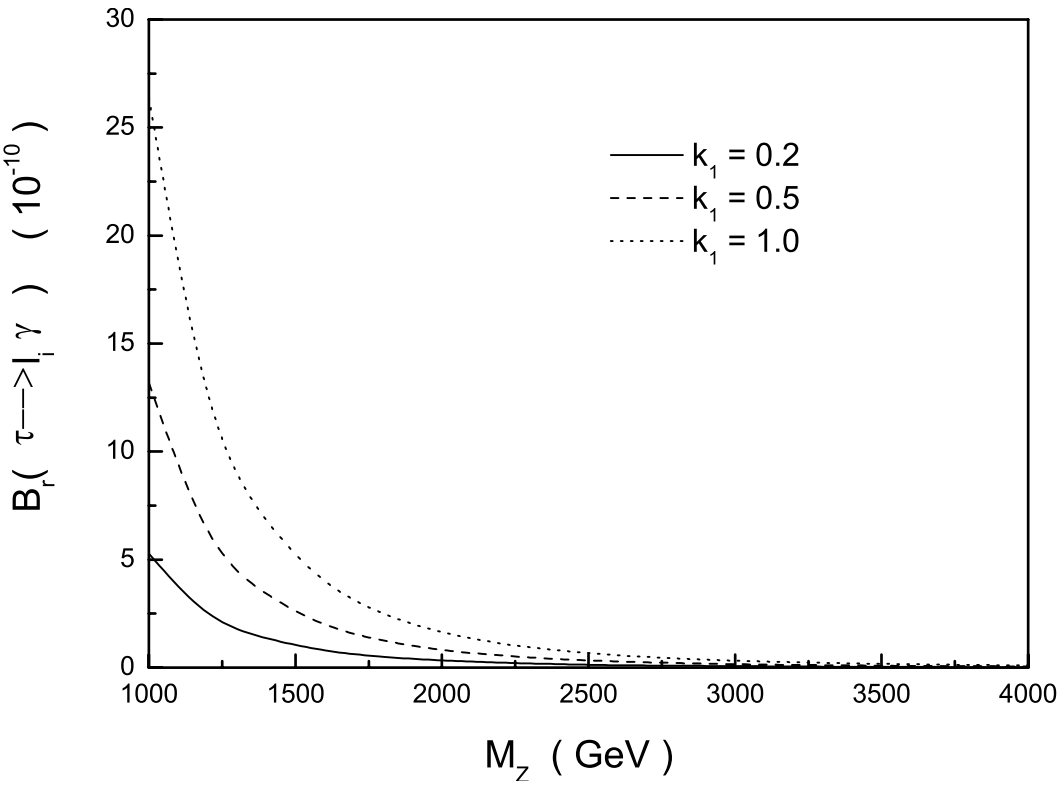

Figure 2.11: Feynman diagrams for decays of $\tau \to \ell\gamma$ induced by non-universal gauge bosons Z' exchange.

Table 2.2: Upper limits of branching ratios 90% confidence level set in other experiments.

Mode	MARKII 82	CLEO 98	BABAR 04
$\tau^- \to e^- e^+ e^-$	4.0×10^{-4}	2.9×10^{-6}	2.0×10^{-7}
$\tau^- \to e^- \mu^+ \mu^-$	3.3×10^{-4}	1.8×10^{-6}	1.3×10^{-7}
$\tau^- \to e^+ \mu^- \mu^-$	—	1.5×10^{-6}	3.3×10^{-7}
$\tau^- \to \mu^- e^+ e^-$	4.4×10^{-4}	1.7×10^{-6}	1.1×10^{-7}
$\tau^- \to \mu^+ e^- e^-$	—	1.5×10^{-6}	2.7×10^{-7}
$\tau^- \to \mu^- \mu^+ \mu^-$	4.9×10^{-4}	1.9×10^{-6}	1.9×10^{-7}
$\tau^- \to e^- \pi^+ \pi^-$	—	2.2×10^{-6}	1.2×10^{-7}
$\tau^- \to e^+ \pi^- \pi^-$	—	1.9×10^{-6}	2.7×10^{-7}
$\tau^- \to \mu^- \pi^+ \pi^-$	—	8.2×10^{-6}	2.9×10^{-7}
$\tau^- \to \mu^+ \pi^- \pi^-$	—	3.4×10^{-6}	0.7×10^{-7}
$\tau^- \to e^- \pi^+ K^-$	—	6.4×10^{-6}	3.2×10^{-7}
$\tau^- \to e^- \pi^- K^+$	—	3.8×10^{-6}	1.7×10^{-7}
$\tau^- \to e^+ \pi^- K^-$	—	2.1×10^{-6}	1.8×10^{-7}
$\tau^- \to e^- K^- K^+$	—	6.0×10^{-6}	1.4×10^{-7}
$\tau^- \to e^+ K^- K^-$	—	3.8×10^{-6}	1.5×10^{-7}
$\tau^- \to \mu^- \pi^+ K^-$	—	7.5×10^{-6}	2.6×10^{-7}
$\tau^- \to \mu^- \pi^- K^+$	—	7.4×10^{-6}	3.2×10^{-7}
$\tau^- \to \mu^+ \pi^- K^-$	—	7.0×10^{-6}	2.2×10^{-7}
$\tau^- \to \mu^- K^- K^+$	—	15×10^{-6}	2.5×10^{-7}
$\tau^- \to \mu^+ K^- K^-$	—	6.0×10^{-6}	4.8×10^{-7}

BABAR, start operation and the B-factory accelerator provide enormous amount of τ sample. The BABAR collaboration reported the upper limits of the range of $\mathcal{B}(\tau \to \ell\ell\ell) < (1.1 - 3.3) \times 10^{-7}$ obtained from a 91.5 fb^{-1} data sample [40] and $\mathcal{B}(\tau \to \ell hh) < (0.7 - 4.8) \times 10^{-7}$ obtained from a 221.4 fb^{-1} data sample with 90% CL [41]. These upper limits are summarized in Table 2.2.

Chapter 3

Experimental apparatus

The measurements of CP violation of B meson decay was a main subject of BELLE experiment. The KEKB accelerator and Belle detector were optimized to satisfy the requirements for physics analysis such as precious vertex measurement, charged particle track reconstruction, photon reconstruction and particle identification. Currently, we have accumulated a large amount of CP violation event sample and have been investigated about those physics themes. We are now also focusing the study of rare decay of B, D mesons and τ lepton. The design of experimental devices is also useful for these studies. In this chapter, we give the description of the KEKB accelerator, the Belle detector and software system that we used for this study.

3.1 KEKB accelerator

KEKB accelerator, located in Tsukuba, Japan is a high luminosity 8.0 GeV electron and 3.5 GeV positron collider. It is operated at CMS energy $\sqrt{s}$ near 10.58 GeV that is equal to the invariant mass of $\Upsilon(4S)$ that mainly decays into $B\bar{B}$ pairs. In this CMS energy region, τ-pairs are created in QED processes that is illustrated with tree type Feynman diagram in Figure 3.1 with the cross section of 0.91 nb. The designed luminosity of the accelerator is 10^{34} cm^{-2}s^{-1} and 100 fb^{-1} of data will be integrated by each year. This number corresponds to 90 million τ-pair events. Figure 3.2 shows the illustration of KEKB accelerator. Electron and positron beams are accelerated by use of linear accelerator (Linac) and injected into two main ring at Fuji area. The KEKB accelerator has two separate rings for electron and positron beams. The positron beam circulates with an energy of 3.5 GeV in low energy ring (LER) anti-clockwise, and the electron beam circulates with an energy of 8.0 GeV in high energy ring (HER) clockwise. Both of these rings are approximately 3 km long circumference and installed in existent tunnel which was used for TRISTAN accelerator. The RF cavities which provide an energy to the beams are installed at Nikko and Oho area for HER and at Fuji area for LER. These rings are crossing at Tsukuba and Fuji experimental hall and the beams are made collide at the interaction point in the Tsukuba experimental hall, where the Belle detector is located. The designed and achieved record of the KEKB parameters are listed in Table 3.1. Figure 3.3 shows two kinds of luminosity plots: luminosity

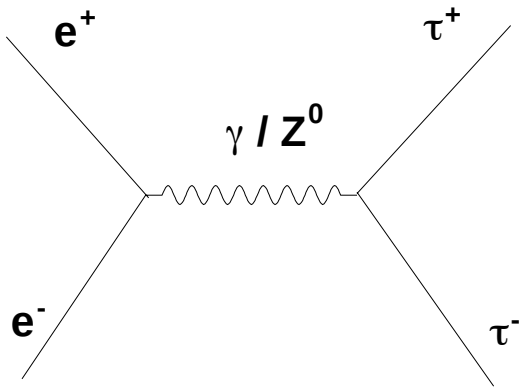

Figure 3.1: Feynman diagram of $e^+e^- \to \tau^+\tau^-$ process.

integrated in each day and total accumulated luminosity. The commissioning of the KEKB accelerator started in December, 1998. The first beam collision was observed in February, 1999 without the detector at beam interaction region. The Belle detector was installed in May, 1999. In May, 2003, peak luminosity exceeds design value (10^{34} cm^{-2}s^{-1}). The KEKB performance is the best in the world: peak luminosity has reached 1.392×10^{34} cm^{-2}s^{-1}, daily delivered luminosity exceeds 1 fb^{-1}, and total integrated luminosity is recorded 308.7 fb^{-1} until the end of October, 2004.

3.2 Belle detector

The Belle detector is installed at the interaction region of e^+e^- beams in Tsukuba experimental hall. Figure 3.4 show the overview of the Belle detector. Because the beam energy is asymmetric and particles tend to fly to the direction of electron beam in laboratory system, the detector is also configured to be asymmetric. We define the direction of electron beam as forward and other as backward direction and the acceptance of the detector is larger in forward. The detector is configured with superconducting solenoid which provides 1.5 T magnetic field and iron structure surrounding the beams.

The Belle detector makes precise measurements of decay vertex, momentum, energies and particle identifications for charged and neutral particles. The detector components dedicated for this analysis are a silicon vertex detector (SVD) [42], a central drift chamber (CDC) [43], an array of 1188 aerogel Čerenkov counter (ACC) [44], 128 time-of-flight scintillation counters (TOF) [45], and an electromagnetic calorimeter containing 8736 CsI(Tl) crystals (ECL) [46], all located inside the su-

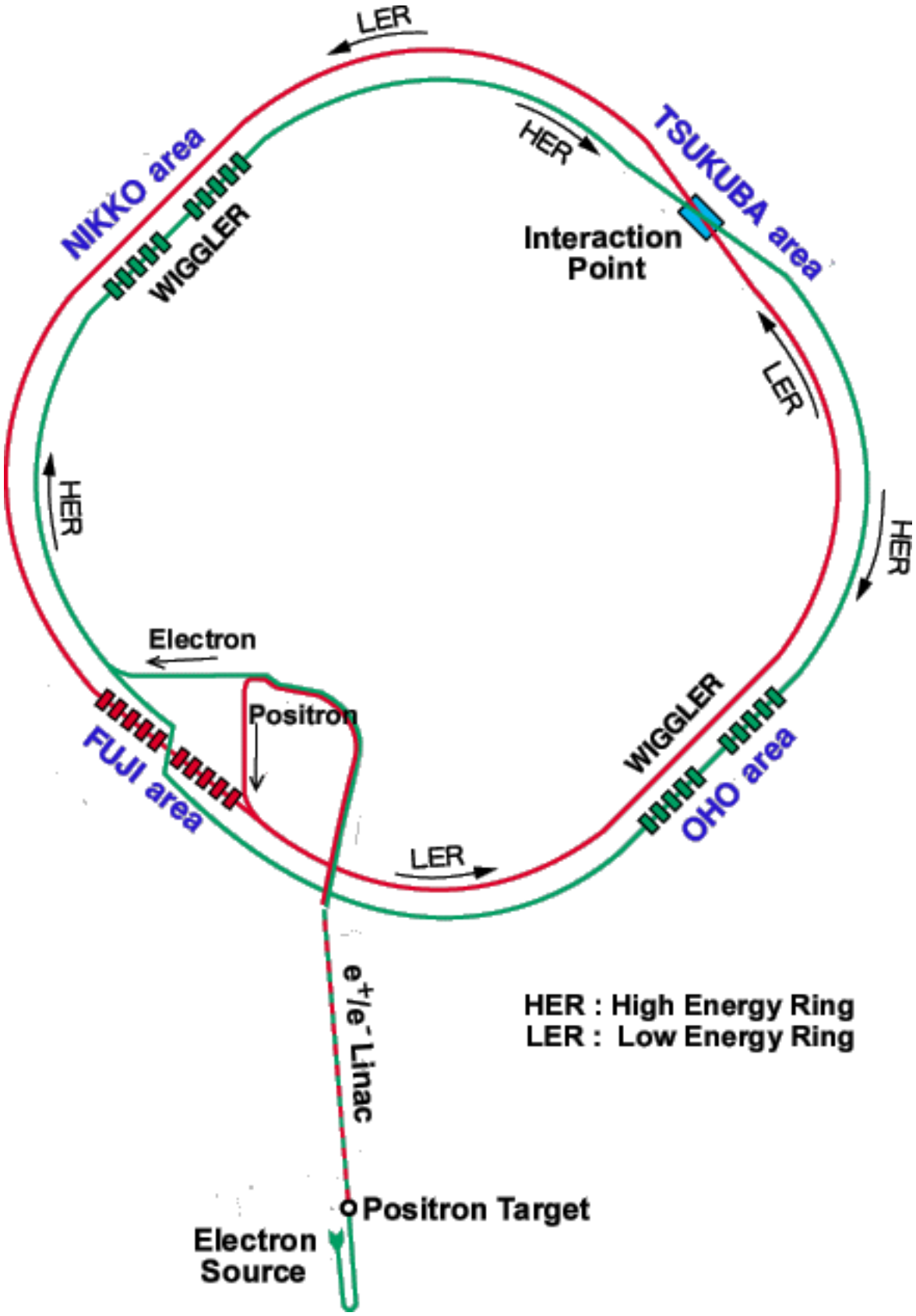

Figure 3.2: Configuration of the KEKB storage ring.

Table 3.1: Parameters of KEKB (number in the brackets are design value. †: without wiggles, ‡: with wiggles)

Parameters	LER	HER	Units
Particles	e^+	e^-	
Energy (E)	3.5	8.0	GeV
circumstance (C)	3016.26		m
Luminosity (L)	13.92×10^{33} (10×10^{33})		$\mathrm{cm}^{-2}\mathrm{s}^{-1}$
Crossing angle (θ_x)	+11		mrad
Tune shifts (ξ_x/ξ_y)	0.039/0.052		
Beta function at IP (β_x^*/β_y^*)	0.33/0.01		m
Beam current (I)	1.6 (2.6)	1.2 (1.1)	A
Natural bunch length (σ_z)	0.4		cm
Energy spread (σ_E/E)	7.1×10^{-4}	6.7×10^{-4}	
Bunch spacing (s_B)	0.59		m
Particles/bunch	3.3×10^{10}	1.4×10^{10}	
Emittance (ϵ_x/ϵ_y)	1.8×10^{-8}/ 3.6×10^{-10}		m
Synchrotron tune (ν_s)	0.01 - 0.02		
Betatron tune (ν_x/ν_y)	45.52/45.08	47.52/43.08	
Momentum compaction factor (α_p)	$1 \times 10^{-4} - 2 \times 10^{-4}$		
Energy loss/turn (U_0)	$0.81^{\dagger}/1.5^{\ddagger}$	4.8	MeV
RF voltage (V_c)	$5 - 10$	$10 - 20$	MV
RF frequency (f_{RF})	508.887		MHz
Harmonic number (h)	5120		
Longitudinal dumping time (τ_ϵ)	$43^{\dagger}/23^{\ddagger}$	23	ms
Total beam power (P_b)	$2.7^{\dagger}/4.5^{\ddagger}$	4.0	MW
Radiation power (P_{SR})	$2.1^{\dagger}/4.0^{\ddagger}$	3.8	MW
HOW power (P_{HOM})	0.57	0.15	MW
Bending radius (ρ)	16.3	104.5	m
Length of bending magnet (L_b)	0.915	5.86	m

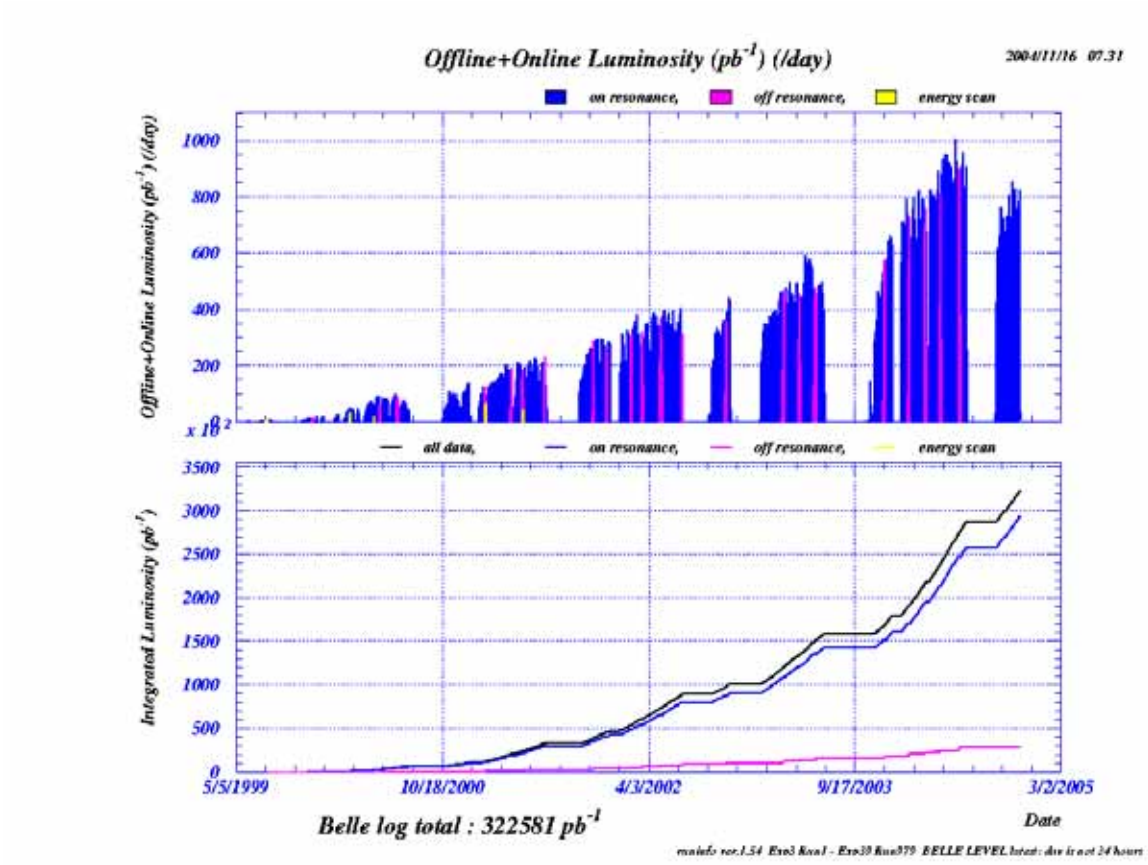

Figure 3.3: Luminosity plots. Top histogram shows integrated luminosity for each day and bottom line shows the accumulated luminosity from start of experiment.

perconducting solenoid that generates a magnetic field. An iron return yoke outside the solenoid is segmented into 14 layers alternating 4.7-cm-thick iron plates with a system of resistive plate counters. This set of counters is used for identification of muons and detection of K_L^0 mesons (KLM) [47]. An extreme forward calorimeter (EFC) [48] containing 160 BGO($Bi_4Ge_3O_12$) crystals in each endcap is placed surrounding the beam line. Detailed descriptions of the detector components are given in the following subsections. Note that the coordinate system used in this dissertation is defined as:

x: horizontal, positive direction is outward from the KEKB ring,

y: vertical, positive direction is upward,

z: opposite direction of the positron beam,

r: $\sqrt{x^2 + y^2}$,

θ: polar angle measured from $+z$ direction, and

ϕ: azimuthal angle surrounding the z-axis.

The coordinate system is illustrated in Figure 3.5.

3.2.1 Beam Pipe

Beam pipe that is located near the region of interaction point consists of two cylinders with different radii, the inner one is $r = 20.0$ mm and the outer is 23.0 mm. Each cylinder has 0.5 mm thickness. The cylinders are made of beryllium to reduce the multiple scattering of particles at the beam pipe wall. The space between two cylinders is filled with chiller-helium gas.

3.2.2 Silicon Vertex Detector(SVD)

The SVD is a silicon semiconductor detector. Silicon semiconductor detector is a p-n junction diodes operated at reverse bias. This forms a sensitive region depleted of mobile charge and sets up an electric field that sweeps charge liberated through radiation to the electro nodes. The SVD measures charged track hit points with approximately 10 μm of position resolution. The tracking is performed using the SVD and the CDC measurements. The scheme of the track reconstruction is described in following CDC section. As shown in Figure 3.6, the SVD comprises three cylindrical detection layers. Each layer consists of 8, 10 and 14 ladders from the inner to the outer layer. The ladder is composed of two, three or four 300-μm-thick double-sided silicon strip detectors (DSSD). Each DSSD has orthogonal strips in each sides and provides two orthogonal measurements along ϕ- and z-directions. The SVD occupies the region from 20.5 mm to 75 mm in radius, and from -150 mm to 220 mm in z direction, the acceptance in polar angle is $20° < \theta < 150°$. The DSSD strip pitch for the p-side (n-side) is 25 (42) μm and the readout pitch is 50 (84) μm. The total number of readout channel is 81,920. The resolution of impact parameter, the distance between a position at the closest approach to one point and

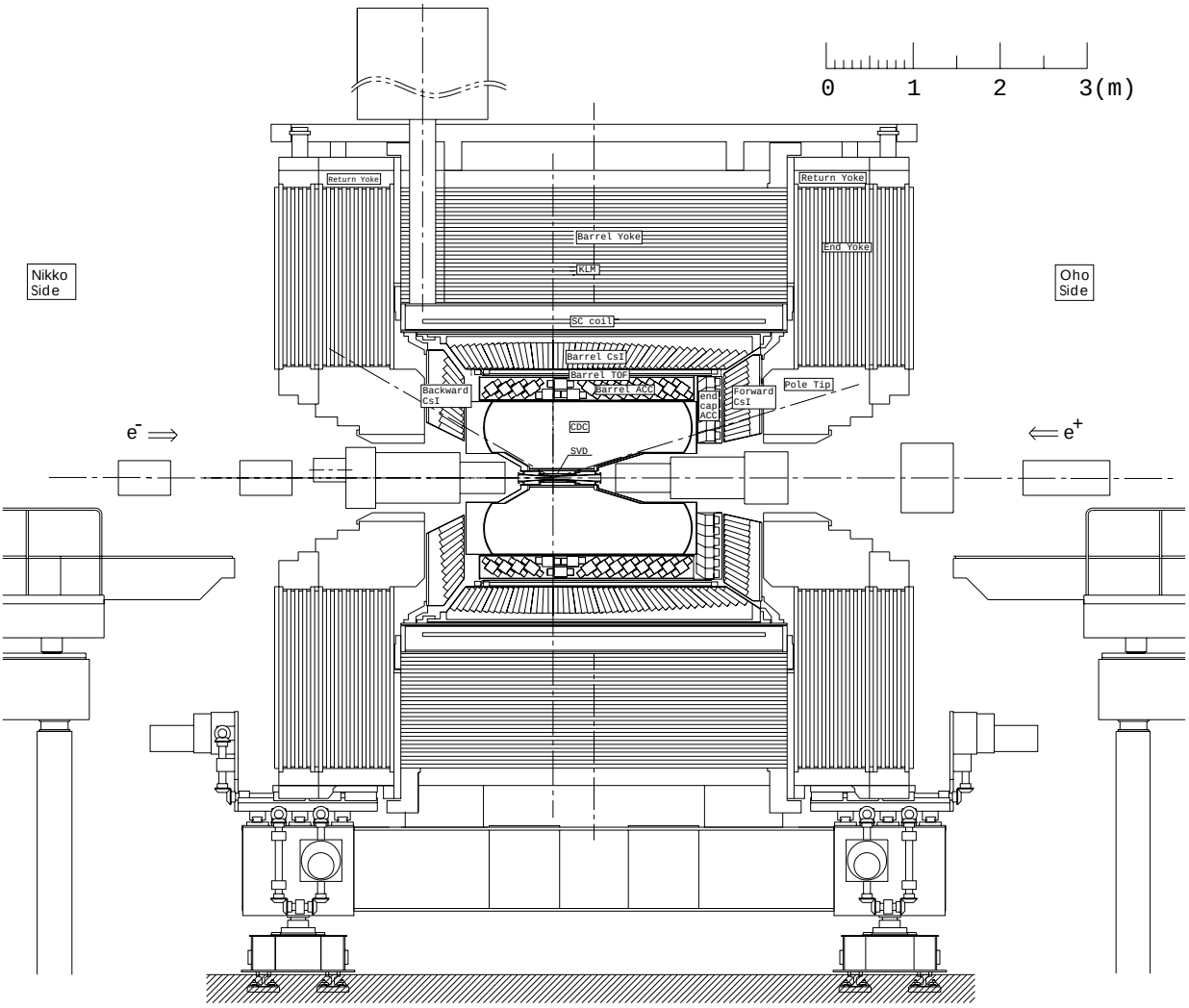

Figure 3.4: Sideview of Belle detector.

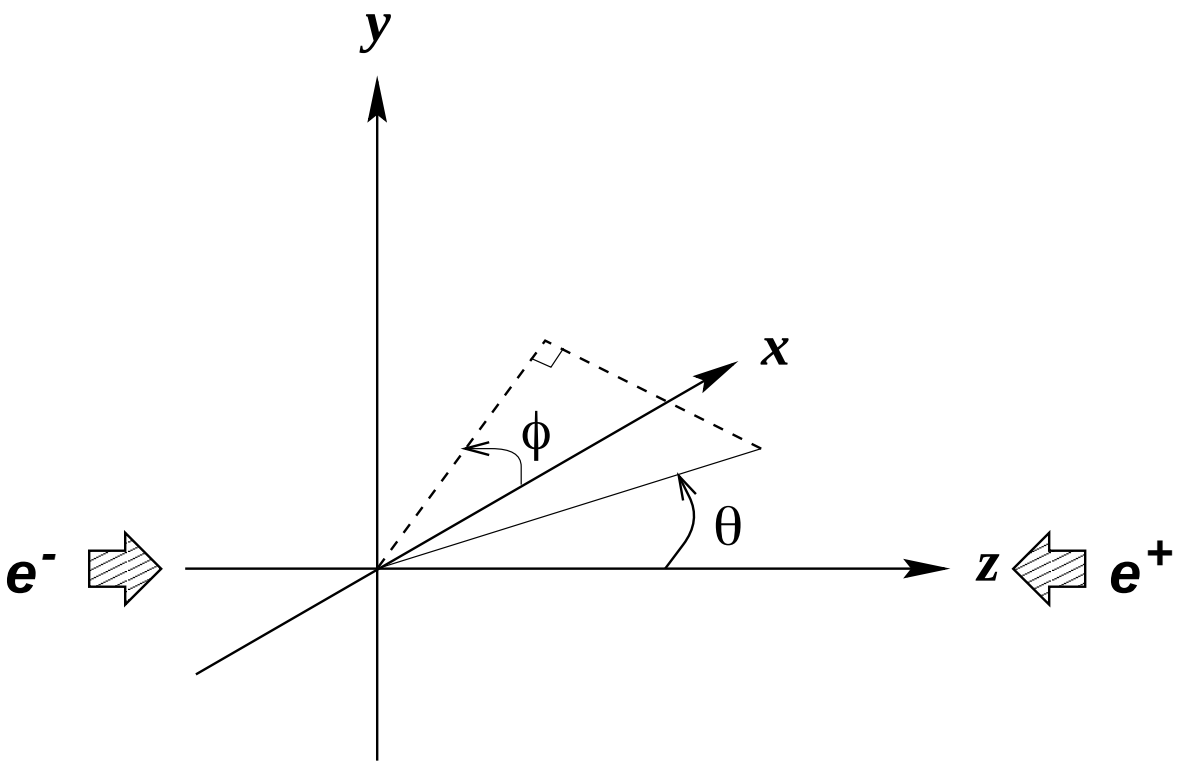

Figure 3.5: Definition of Belle coordinate system.

the point, at the interaction point position is $(19 + 50/p\beta\sin^{3/2}\theta)$ μm in r-ϕ and $(36 + 42/p\beta\sin^{5/2}\theta)$ μm in z direction, where p is a momentum of charged track.

3.2.3 Central Drift Chamber (CDC)

The role of the CDC is to measure the track positions, momentum and specific ionization dE/dx of charged particles. The information regarding the dE/dx is used for the electron identification and K/π separation combined with the information from other particle identification detector components, ACC and TOF. In addition, another indispensable role of the CDC is to provide an on-line hardware trigger called "Level 1 trigger". The CDC provides a trigger for charged particles which come from near the IP. The CDC is a small-cell drift chamber containing 50 anode layers (32 axial and 18 stereo wire layers) and 3 cathode strip layers. The anode layers are grouped into 11 super-layers (6 axial and 5 stereo super-layers). Combining axial and stereo hits, it becomes to be possible to reconstruct 3-dimensional track. The cathode layers are located at the inner most part of the CDC, which measure the z-position of charged tracks. The number of readout channels is 8400 for anodes and 1792 for cathode in total. The configuration of CDC is shown in Figure 3.8. The CDC covers the region of 77 mm to 880 mm in radius and 17° to 150° in polar angle. A 50% helium-50% ethane gas mixture is used in the chamber to reduce the multiple

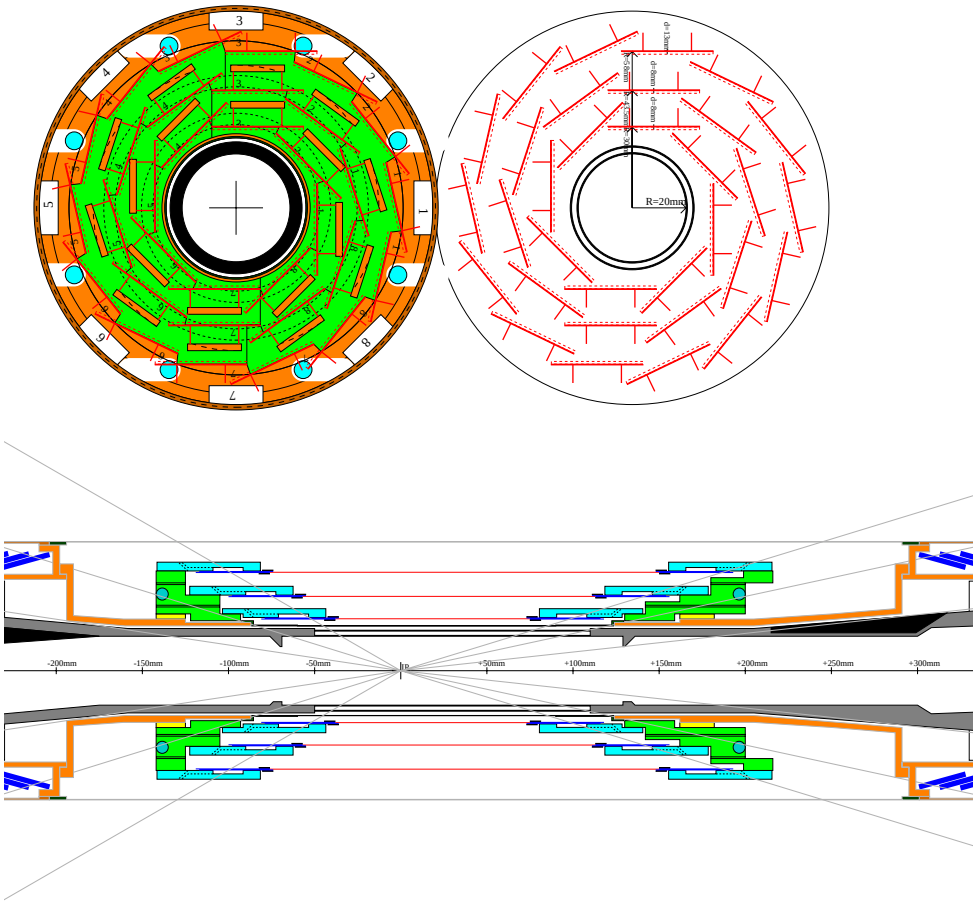

Figure 3.6: Silicon vertex detector.

Coulomb scattering of charged particles in order to minimize the contribution to the momentum resolution. The spacial resolutions is estimated to be 130 μm in r-ϕ plane and less than 2 mm in z-direction, which leads the transverse momentum resolution σ_{p_t}/p_t of $(0.20p_t \oplus 0.29)\%$ where p_t is the transverse momentum of charged particle in unit of GeV/c. Figure 3.7 shows the plot of dE/dx vs. momentum of track p for experimental data with expected line from theory. The dE/dx resolution is 7.8% for minimum ionizing pion samples in K^0_S decay and 6.0% for electron in Bhabha and muon samples in μ-pair events.

The charged particle reconstruction is initiated with finding of track-segment-hit-patterns in the CDC. The track projected onto the r-ϕ plane is searched for by use of the axial wires. Next, the hits of the stereo wires are combined to determine z-position of the track. The parameters of the found track are fitted using the Kalman filtering technique [49] which takes an account of the effects of the multiple Coulomb scattering and non-uniformity of the magnetic field in the CDC in the determination of the track parameters. Finally, the reconstructed charged particle trajectory is extrapolated toward the SVD and connected to the SVD hits to improve the resolution of the track parameters. The track momenta is calibrated for which the reconstructed invariant masses of J/ψ and D^0 mesons become consistent with the world averages listed in the latest PDG [18]. We first reconstruct J/ψ mass from $J/\psi \to \mu^+\mu^-$ decay and D^0 mass from $D^0 \to K^-\pi^+$ decay and the means of reconstructed mass distributions are compared to the world averages. The track momentum is tuned with scaling. The calibrations are made corresponding to each change of the detector configuration. The major source of a fluctuation in the calibration constant comes from the fluctuation of a solenoid magnet current after long shutdown. The amount of the correction is of order 10^{-3}. The estimated errors of track positions and momenta are also scaled with calibration. We also calibrate tracking parameters by use of a cosmic ray which penetrates the center part of the detector. We deal with the path of the cosmic ray particle as two individual tracks which originate from beam interaction point. In ideal case, track parameters of the "two" tracks should be same, while the differences between the parameters of two tracks follow Gaussian distribution due to the limit of the detector resolution. The scaling constants are introduced for which the standard division of the distribution should be equivalent to the error of the track parameters estimated using the Kalman filtering. Typical amounts of the corrections with the scaling constants are in the range from 10% to 15%.

3.2.4 Aerogel Čerenkov Counter (ACC)

The ACC is an array of threshold Čerenkov counters which is made of silica aerogel. When particle passes through matter, the Čerenkov light is emitted in the situation that

$$m < p \times \sqrt{n^2 - 1}, \tag{3.1}$$

where m, p and n are particle mass, momentum, and refractive index of the matter, respectively. We can separate the two kind of particles that have different masses

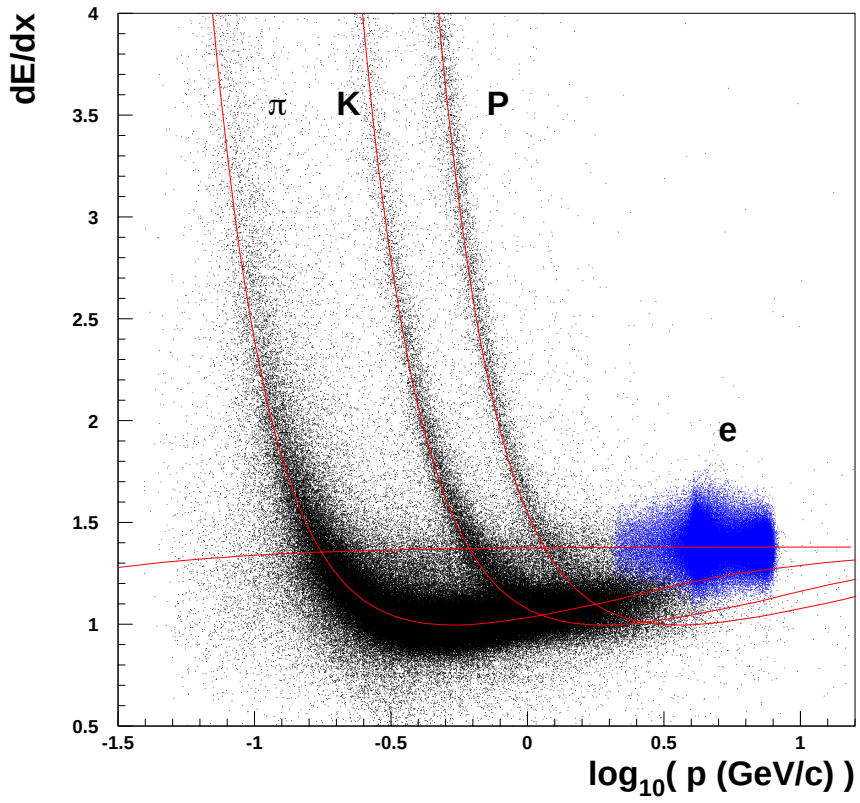

Figure 3.7: Measured dE/dx using CDC as a function of particle momentum p. Curves represent the expected energy losses for each particles.

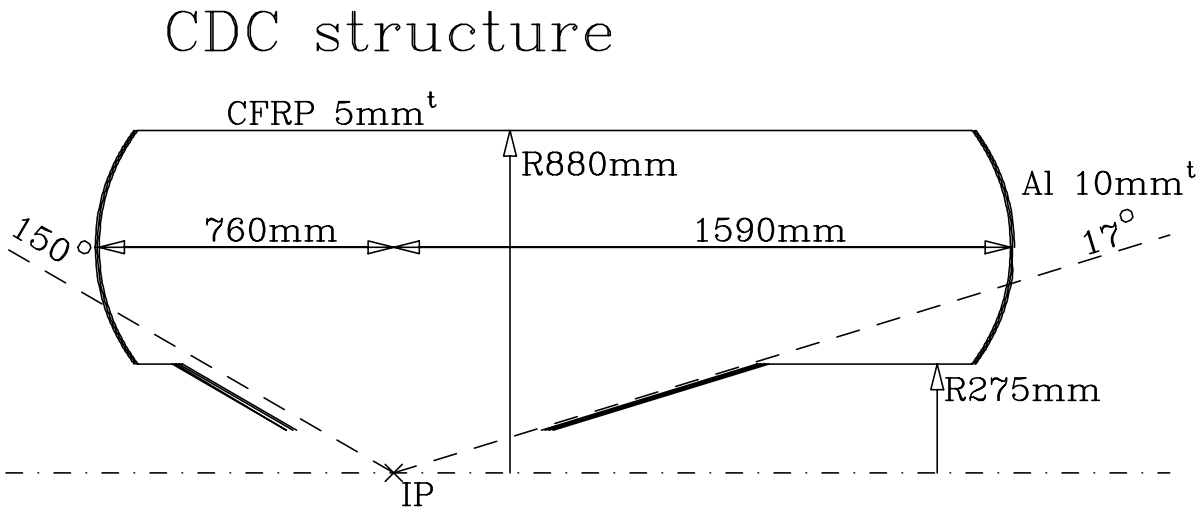

Figure 3.8: Configuration of the Belle Central drift chamber.

when we make the measurement of the emission of Čerenkov light in the mater of which refractive index is selected to satisfy (3.1) for lighter particle and not for heavier one. This is a basic concept for the particle identification using the threshold Čerenkov counter. To meet the significant kaon and pion separation performance in the momentum range of a few GeV/c, the counters are required to have refractive index between those of liquid and solid. The silica aerogel satisfies this requirement. The silica aerogel is a porous colloidal form of $(SiO_2)_n$ with more than 95% porosity. It has low density because of the structure, and consequently it has low refractive index. The density and the consequent refractive index is determined corresponding to its chemical production procedure. The ACC consists of two part; barrel, the polar angle region of $34.2^\circ < \theta < 120.7^\circ$, and endcap, $17.0^\circ < \theta < 34.2^\circ$ and $120.7^\circ < \theta < 150.0^\circ$. Figure 3.9 shows the configuration of barrel ACC. The barrel part consists of 960 aerogel counters that are segmented into 16 divisions in z and 60 in ϕ. A single ACC module consists of a block of silica aerogel contained in a 0.2 mm-thick aluminum box. The aerogel refractive index varies with the poler angle (n = 1.01, 1.013, 1.015, 1.020 and 1.028) and has been optimized to obtain good K/π separation for broad kinematic range of particles from asymmetric e^+e^- collision. The Čerencov light from each barrel counter is detected with one or two fine-mesh photo-multipliers (FM-PMT) which can work in the 1.5 T magnetic field. The number of readout channels for the barrel ACC is 1560 in total. The endcap ACC consists of 228 counters with n = 1.03 as shown in Figure 3.10. The counters are mounted in five concentric rings with different radii. Each ring contains 36, 36, 48, 48 and 60 counters from inner to outer. Each endcap counter has one FM-PMT for readout and therefore the number of readout channels is 228.

3.2.5 Trigger/Time of Flight counter (TSC/TOF)

The TOF is used to distinguish charged kaons from charged pions which has low momentum. The trigger scintillation counter (TSC) together with the TOF generates the primary timing signal for the trigger system called "Level 1 trigger" to generate gate signals for ADCs and stop signals for TDCs. The counter measure the elapsed time between a collision at the interaction point and the time when the particle hits the TOF counter. The relation between the measured flight time T and a particle mass m is represented as

$$m = p \times \sqrt{\frac{T^2}{L^2} - 1}, \tag{3.2}$$

where L is flight path length and p is momentum of particle. We obtain p and L from the tracking information, therefore determination of T gives us the information regarding the particle species. For example, the time of flight at p = 1.2 GeV/c is 4.3 nsec for kaon and 4.0 nsec for pion, respectively. The designed time resolution of TOF is 100 psec, for this reason, kaon and pion is expected to be separated with the capability in three times of standard division. The configuration of TOF/TSC module is shown in Figure 3.11. Two trapezoid-shape 4 cm-thick TOF scintillators and one 0.5 cm-thick plate TSC scintillator form one module. The scintillators are

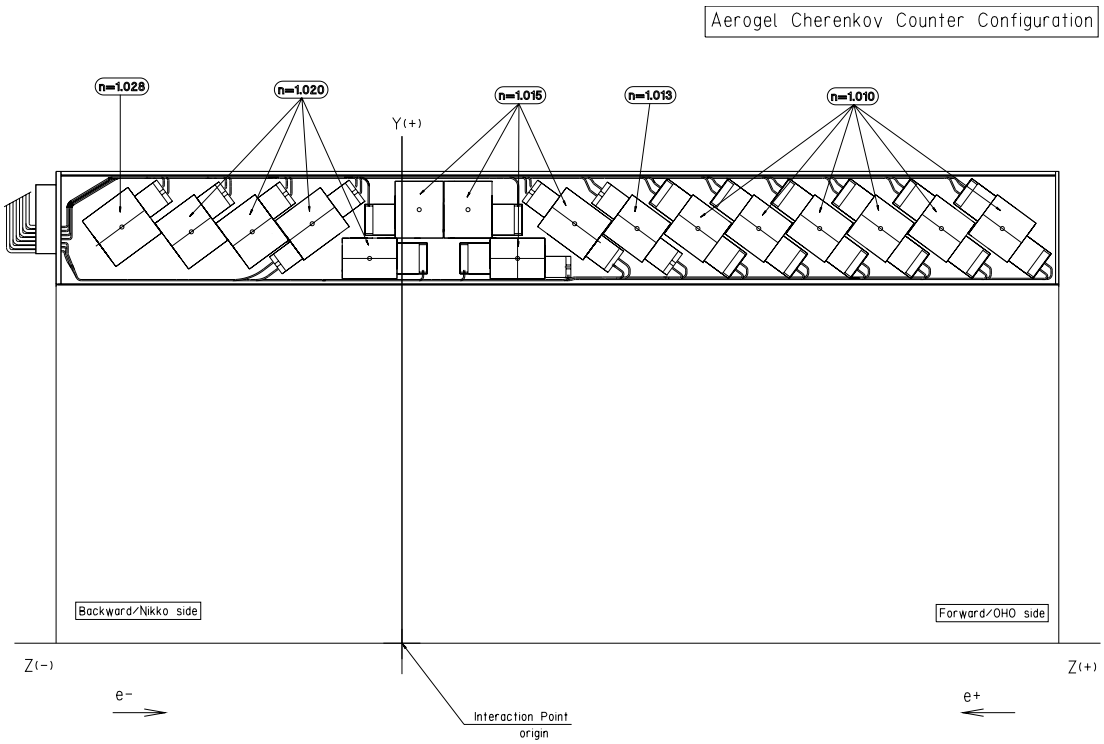

Figure 3.9: Barrel aerogel Čerencov counter.

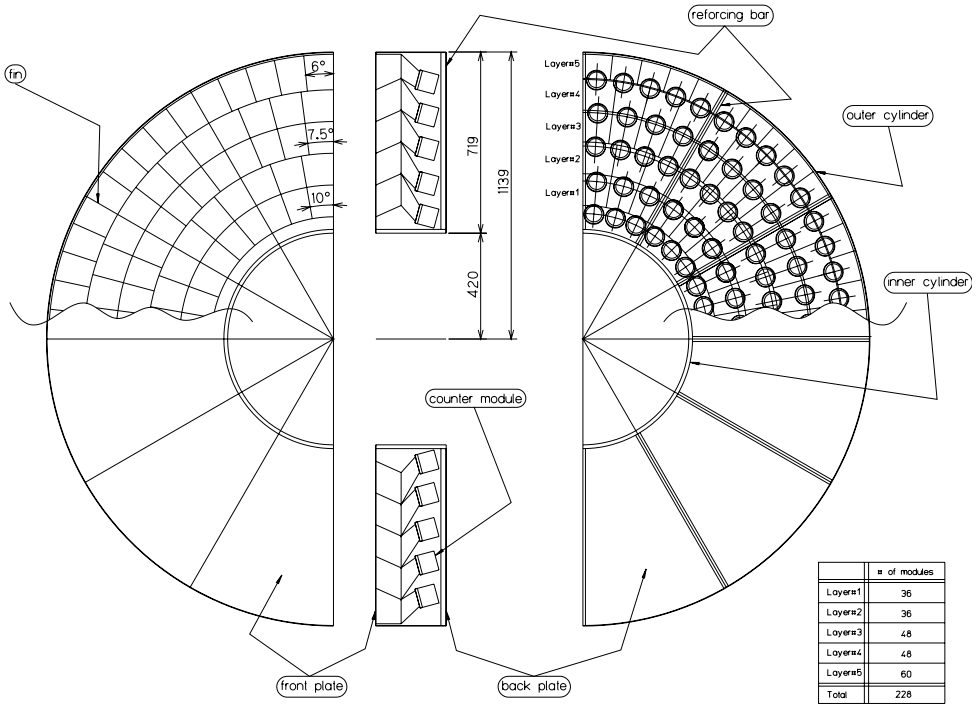

Figure 3.10: Endcap aerogel Čerencov counter.

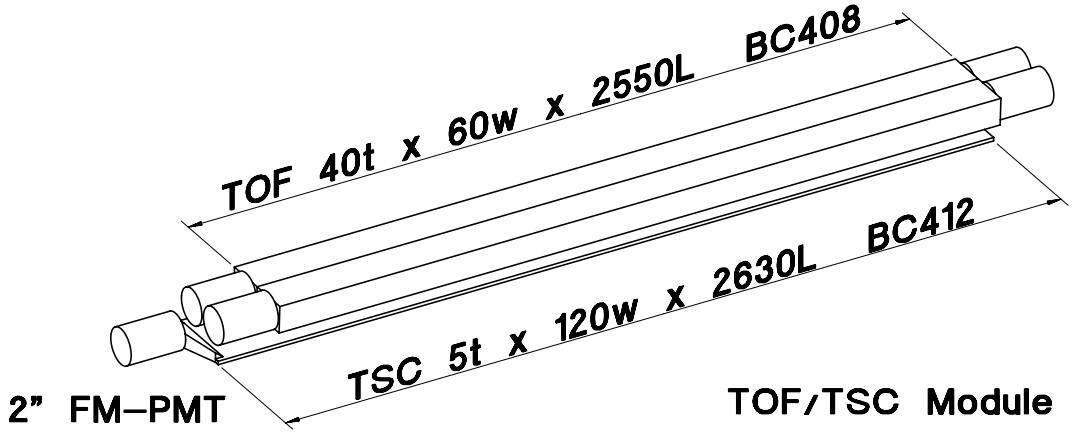

Figure 3.11: Time of flight and trigger scintillator counters.

wrapped with 45 μm thick polyvinyl film for light tightness and surface protection. 64 modules are placed at 1.2 m from IP and cover the polar angle range of $34° < \theta < 120°$. The information of TOF is obtained using FM-PMTs at both ends of scintillators, and TSC is read out using a FM-PMT at the backward end. The total number of readout channels of TOF is 320. Figure 3.12 shows the time resolution of forward and backward PMTs of TOF, separately, and for the weighted average as functions of hit position. Figure 3.13 shows the mass distribution measured using TOF. We clearly distinguish peak of kaon from that of pion in the distribution.

3.2.6 Electromagnetic Calorimeter (ECL)

The ECL measures the energy deposit of particles by means of detecting the scintillation light from electromagnetic shower which charged and neutral particles generate in the CsI(Tl) crystals. Photons deposit most of their energy in the crystals, therefore we can measure the energy of the photons. Electrons deposit most of the energy, while muons and hadrons deposit small fraction of their energy. Therefore one can identify the electron and measure the energy. The ECL provides various triggers and also provides the secondary timing signal for the L1 trigger. Figure 3.14 shows the configuration of the ECL. The ECL consists of 8736 thallium doped CsI crystals counters. CsI(Tl) crystal have various nice features such as a large photon yield, weak hygroscopicity, mechanical stability and moderate price. The barrel part ECL is installed at radii of 125 cm from IP and covers the polar angle region of $32.2° < \theta < 128.7°$. The forward and backward endcap ECL is placed at $z = 196$ cm and -102 cm and covers polar angle of $12.01° < \theta < 31.36°$ and $131.5° < \theta < 155.0°$ respectively. The 6624, 1152 and 960 crystals with two 2cm $\times$ 1 cm photo diodes for read out are filled in barrel, endcap forward and endcap backward modules respectively. The position resolution $\sigma_{\rm position}$ is measured and it

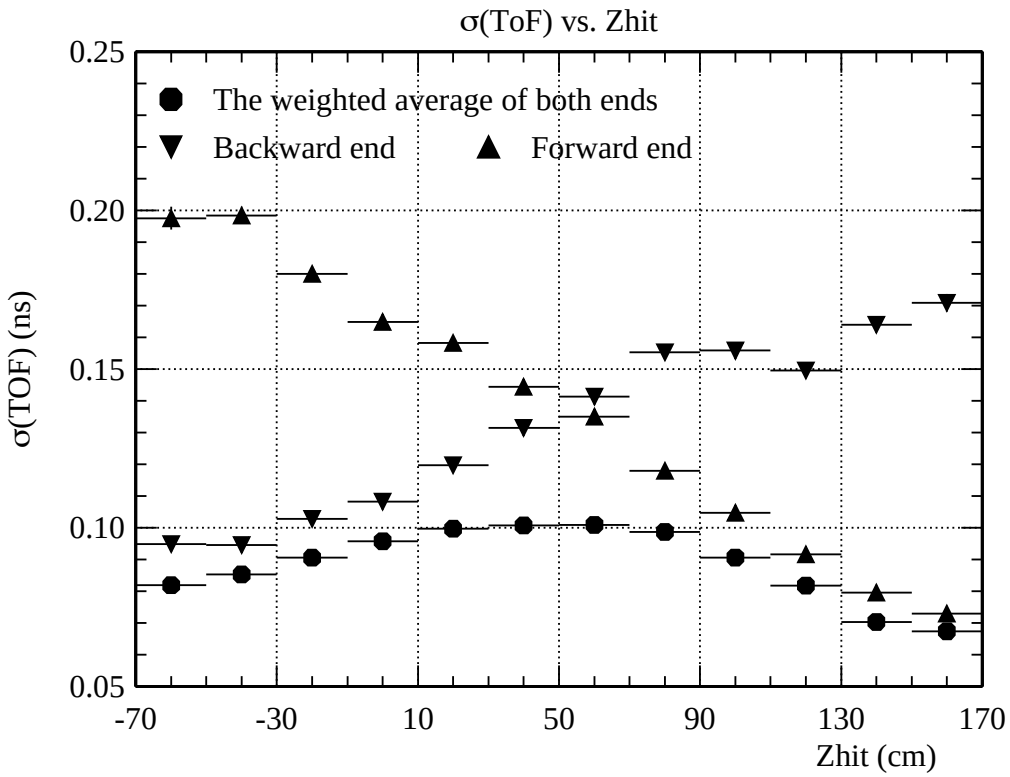

Figure 3.12: Time resolution of TOF counters.

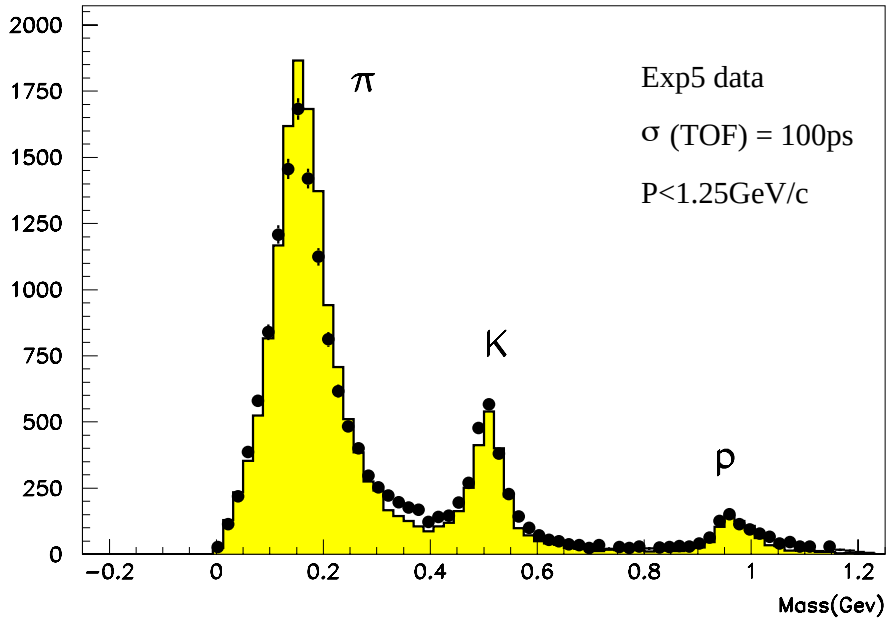

Figure 3.13: Mass distribution from TOF measurement. Plots are made for particles which have momenta below 1.2 GeV /c. The points show the distribution for hadronic events in experimental data and histogram is Monte Carlo (MC) prediction assuming the TOF time resolution of 100 psec in detector simulation.

depends on the photon energy E as

$$\sigma_{\text{position}} = \left(0.27 + \frac{3.4}{\sqrt{E}} + \frac{1.8}{\sqrt[4]{E}}\right) \text{mm}, \tag{3.3}$$

where E is in GeV. The energy resolution measured through a photon beam test for the threshold energy of 0.5 MeV and with the 5×5 crystal matrix is obtained as

$$\frac{\sigma_E}{E} = \left(1.34 \oplus \frac{0.066}{E} \oplus \frac{0.81}{\sqrt[4]{E}}\right) \%, \tag{3.4}$$

with the unit of E is GeV. With these performance, we can reconstruct $\pi^0 \to \gamma\gamma$ decay with invariant mass resolution of 4.8 MeV/c^2 and $\eta \to \gamma\gamma$ decay with the resolution of 12 MeV/c^2.
At the beginning of the photon reconstruction, ECL clustering performed as following. The crystal which has the highest energy deposit than any neighboring crystal is searched for. Total energies into 3×3 crystal matrices $E9$ and 5×5 crystal matrices $E25$ in the neighborhood of the crystal which has the highest energy deposit are calculated. In this calculation, the crystals taken into account should have energy deposit at least 500 keV. To be identified as a photon cluster, the crystal surface of the cluster should not be associated to charged particle trajectory extrapolated from tracking system. In case that such a cluster has total energy deposit greater than 500 MeV, we treated it photon. In the case that the cluster energy is smaller than 500 MeV but larger than 20 MeV, $E9/E25 > 0.75$ is required for the photon identification. In the case that the energy deposit is smaller than 20 MeV, the cluster is considered as junk cluster and we do not use them in this analysis.

3.2.7 Magnetic Field

A charged particle in a magnetic field runs through helical path of which radius proportional to the momentum. To measure particle momentum in the CDC, Belle detector has a magnetic field $B = 1.5$ T parallel to the beam pipe. To provide the magnetic field, a superconducting coil which consists of a single layer of a niobium-titanium-copper alloy embedded in a high purity aluminum stabilizer. It is wound encircling the inner surface of an aluminum support cylinder with 3.4 m in diameter and 4.4 m in length. Indirect cooling is provided by using liquid helium circulating through a tube on the inner surface of the cylinder. The return path of the magnetic flux is provided from the iron end yoke. The iron end yoke also works as an absorber material for the KLM and a support for all of the detector components.

3.2.8 K_L/μ detector (KLM)

The KLM detector is designed to identify the K_L^0 mesons and muons over a broad momentum range beyond 600 MeV/c. The KLM consists of alternating layers of glass resistive plate counter (RPC) and 4.7 cm-thick iron plates. RPC is a gaseous detector with parallel resistive electrodes. The gap between the electrodes is filled

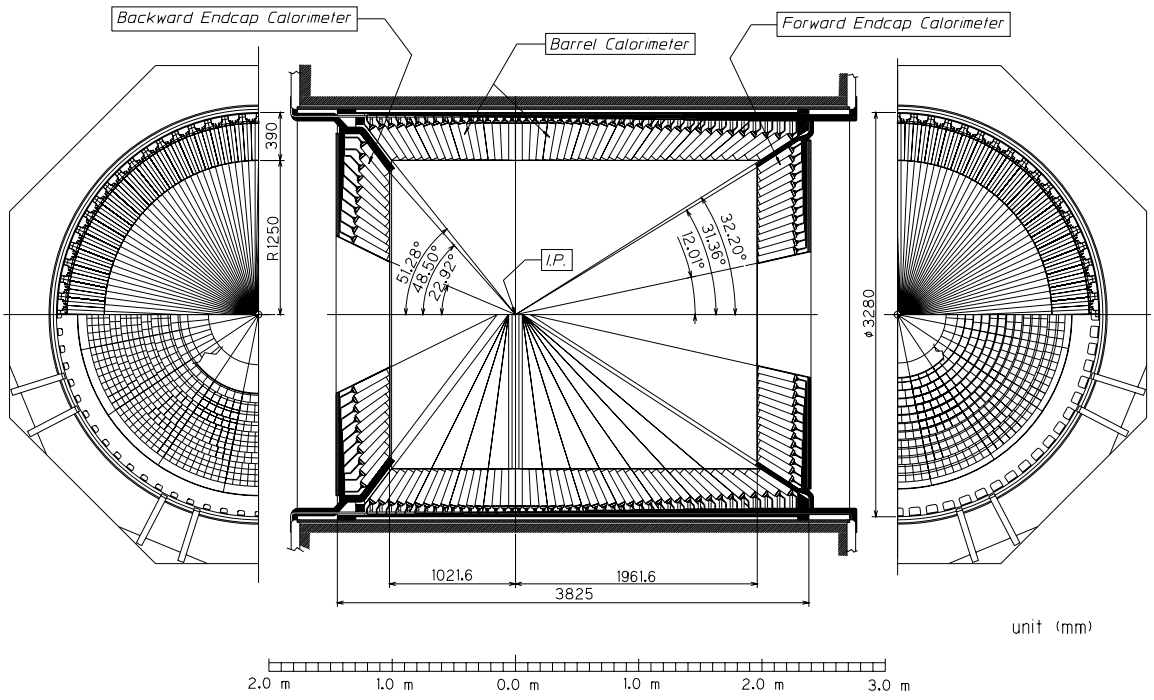

Figure 3.14: Electromagnetic calorimeter

up with the gas mixture of 30% argon, 8% butane and 62% freon HFC134a. Figure 3.15 shows the mechanism of charged particle detection by use of the RPC. When we apply the high voltage between the electrodes, current concentrates at the surface because gas gap conduct no charge. When charged particle passes through the gas gap, argon and butane are ionized and ion pairs are generated along the particle path. The number of these ion pairs, called as "initial ion pairs", are proportional to the probability of interaction between gas molecules and charged particle. Therefore the distribution of initial ion pairs follows a Poisson distribution. The electron and positron pairs are accelerated due to the electric field in the gas gap and move to the anode and cathode, respectively. The group of ions is multiplied itself through the interaction with gas molecules during the traveling and electric avalanche happens. After reaching each electrodes, ions are discharged and we can detect coming charged particle. This process is occurred in small region approximately at the position that the charged particle is passed due to following facts, (i) Large current does not flow because the resistivity at the electrodes is very high. Therefore, voltage drop happens only where the ion streamer happens. As a result, electric field weaken and streamer does not grow. (ii) Because butane absorb the ultraviolet light which is generated in the process of the re-coupling of argon ion, avalanche is limited only at once. (iii) The size of the streamer is limited along the horizontal direction because freon absorb the electron in the streamer. We can treat the RPC as a set of small discharge cell [50]. Each discharge cell has a structure of small spark counter whose equivalent circuit is shown in Figure 3.16. Capacitor C and C_g and register R and

R_g corresponds to the electrodes and gas gap, respectively. In case that the gas is not ionized (Figure 3.16 a), $R_g \sim \infty$ and voltage is applied between the electrodes of C_g. When charged particle passes, discharge happens and electric current I passes through inside of the gas gap (Figure 3.16 b)). During this state, the discharge cell can not detect the newly coming particle. The dead time τ is calculated as

$$\tau = R(C + C_g) = \rho\epsilon_0 \left(\epsilon_\tau + \frac{2d}{g}\right), \tag{3.5}$$

where ρ is resistivity of electrodes for each volume, ϵ_τ is dielectric constant, d is a thickness of electrodes and g is distance of gas gap. This formula indicates that increase of the resistivity of electrode surface lead the dead time longer. The area of each discharged cell S is also calculated:

$$S = \frac{Qg}{\epsilon_0 V}, \tag{3.6}$$

where Q is current of streamer and V is difference of the electric potentials between the electrodes. Therefore, the inefficiency for charged particles at injection rate of r (Hz/cm^2) are

$$r\tau S = \frac{rQ\rho}{V}(g\epsilon_\tau + 2d). \tag{3.7}$$

To reduce the inefficiency against high injection rate, we have two ideas: suppress the dead time using the small ρ materials for electrodes or suppress the streamer current increasing the ρ and limit the dead area to be small. The suitable resistivity for RPC is $10^{10} - 10^{12}$ Ω·cm^2. To satisfy the requirement, we use float glass for electrodes. The readout of the signal is done with the pad or strip located on the outside of RPC. Discharge in the RPC induces current on the readout pad. The signal pulse is observed on both side of RPC therefore we can determine two-dimensional position of the hit point of particle with the readout strips along different direction on each side of the RPC. Figure 3.17 shows the structure of an RPC module for endcap part of the KLM. We combine two RPC modules to form a KLM module called "super-layer" as shown in 3.18. The RPC modules are shifted the position for associating super-layer, so that the dead region due to the spacers and edge of RPC modules are covered. The typical efficiency for a cosmic ray muon using a single RPC is 90% and the efficiency increase to approximately 99% in case that we use super-layer. Another advantage of the super-layer is amplification of signal pulse. Because we supply high voltage same direction to each RPC as shown in Figure 3.19, induced current in readout strips is also enhanced. Figure 3.20 and 3.21 shows the configuration of the barrel and endcap KLM respectively. The KLM consists of an octagonal barrel part and two endcap part that are divided into quadrant super-layer modules. The barrel modules are rectangular in shape and vary in size from 220 $\times$ 151 to 220 $\times$ 267 cm^2. The endcap modules are fan-shaped, and the inner radius is 130.5 cm, outer radius is 331 cm. The KLM covers the polar angle range of $25° < \theta < 145°$. The number of readout channels of KLM is 21856 in

barrel and 16128 in endcap. From the cosmic ray measurement, we estimate the angular resolution of hit point from the IP is better than 10 mrad and the time resolution of KLM system is several nsec. The K_L mesons interact with iron and give a small hadron showers. It is observed as isolated cluster of hits on KLM, so that we can identify the K_L meson and get the directional information. Muon is identified through its interaction with multiple KLM layers. Muon loses energy only due to ionization and penetrates most of KLM layers. On the other hand, hadrons interact strongly with the iron and penetrate only a few KLM layers. In this way we can separate muon from hadrons. The detail of muon identification method is described in next chapter.

3.2.9 Extreme Forward Calorimeter (EFC)

The EFC measures the energy of the photons and electrons at the extreme forward and backward direction out of the ECL acceptance. The EFC covers the polar angler range from 6.4° to 11.5° in the forward direction and from 163.3° to 171.2° in the backward direction. We use BGO ($Bi_4Ge_3O_{12}$) crystals because the EFC is exposed in high irradiation (approximately 5 MRad/year) of photons from the synchrotron radiation photon and the spent electrons from beam. The BGO crystal provides good resolution for electron and photon energy E,

$$\sigma_E/E = (0.3 - 1.0)\%/\sqrt{E(\mathrm{GeV})}. \tag{3.8}$$

In order to provide better position resolution, both forward and backward EFC consist of BGO crystals segmented into five regions in the polar angle and 32 regions in the azimuth angle. Typical cross section of a crystal is approximately 2×2 cm^2 with $12X_0$ for forward and 10.5 X_0 in backward, where X_0 is the radiation length. EFC is installed attached to the front faces of the cryostats of the compensation solenoid magnets of the KEKB storage ring, surrounding the beam pipe as shown in the Figure 3.22.

3.2.10 Trigger and Data Acquisition (DAQ) system

The Belle triggering and filtering system consists of three levels: hardware trigger called "Level-1 trigger", on-line software trigger "Level-3 trigger" and off-line software trigger"Level-4 trigger".
In order to record the data of the physics events of our interest, we have to provide the common stop signal for TDC's and the gate signal for ADC's. The Level-1 trigger collect the signal from sub-detectors as shown in Figure 3.23 and make a trigger signal on the basis of them, thus timing of the trigger signal is determined with the TSC signal. The trigger system consists of several parts which corresponds to sub-detectors, and categorized into two types: one is a track trigger and the other is an energy trigger. The CDC provides r-ϕ and r-z track trigger signals. The TOF trigger system provides an event timing signal and information about the hit multiplicity and event topology. The ECL generates trigger signals with the total energy deposit and the cluster counting. Two-photon events and Bhabha events are tagged

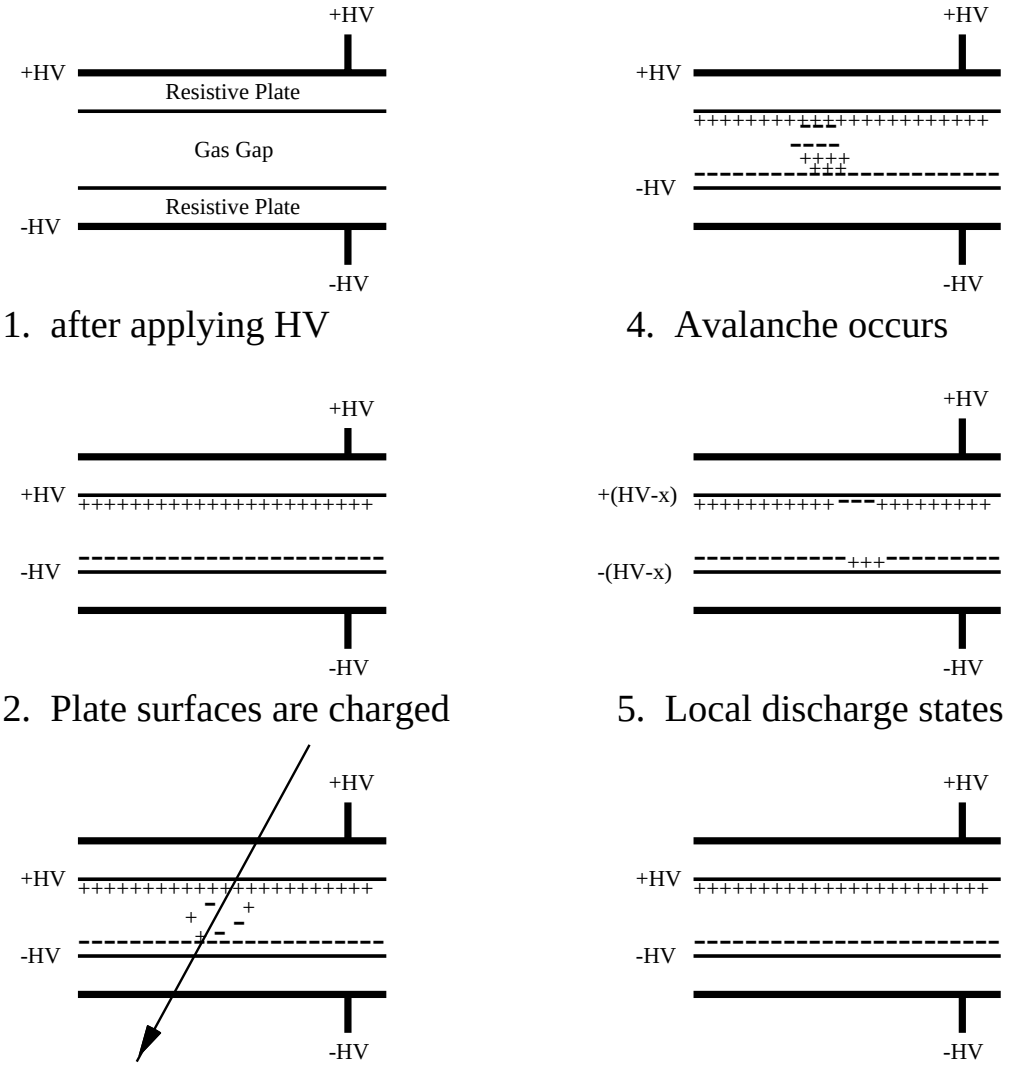

Figure 3.15: Mechanism of charged particle detection in RPC.

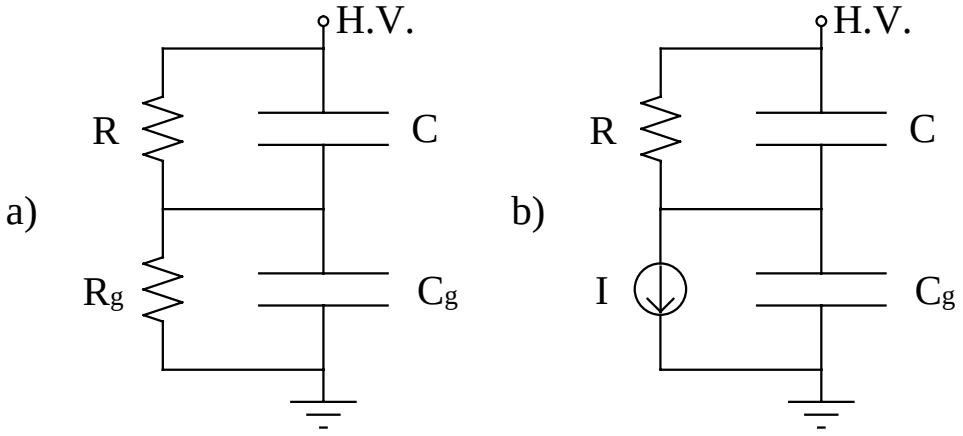

Figure 3.16: The equivalent circuit of discharge cell. a) shows the state of 1 and b) shows the state of 4 in Figure 3.15.

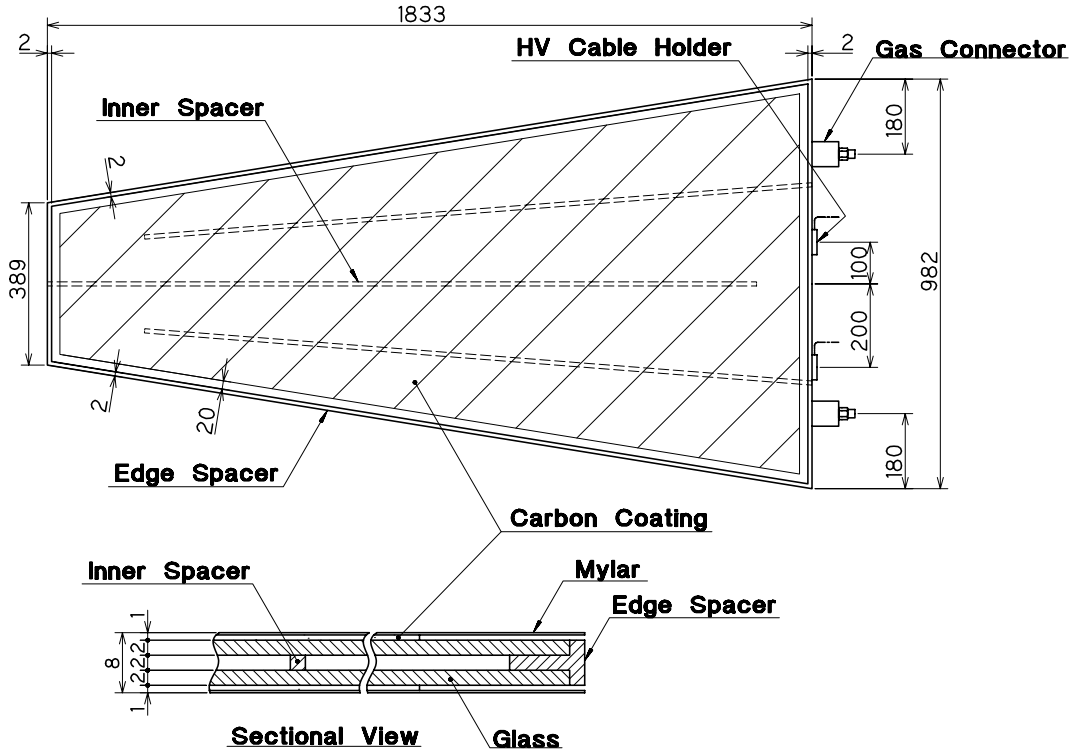

Figure 3.17: Structure of endcap RPC.

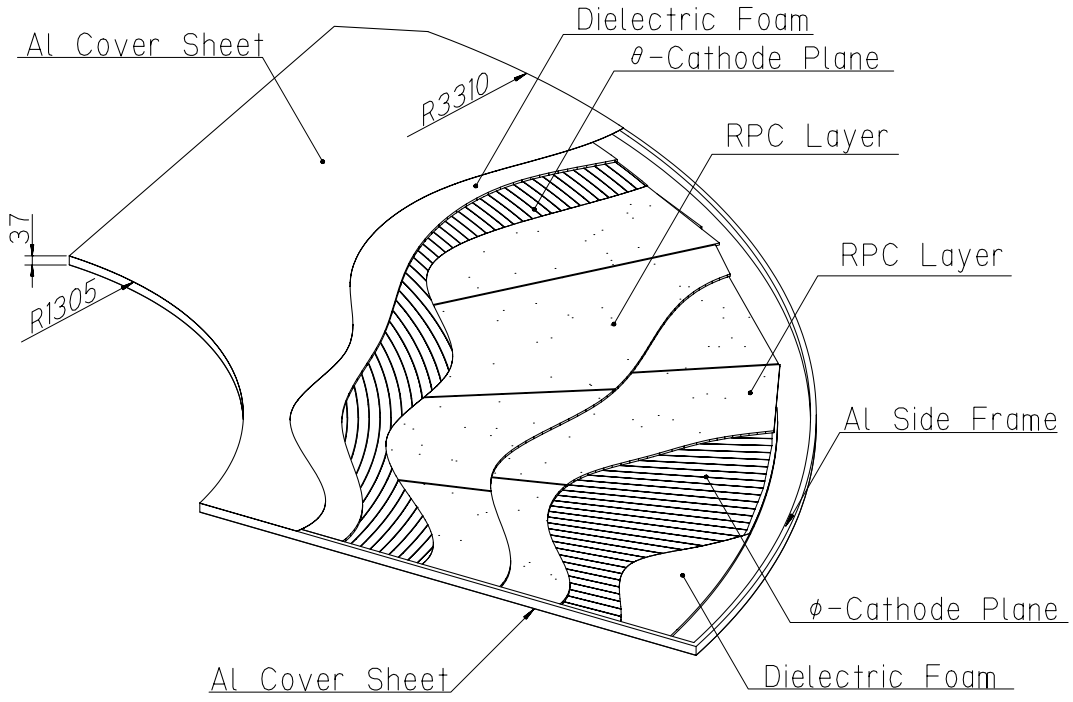

Figure 3.18: Structure of endcap super layer.

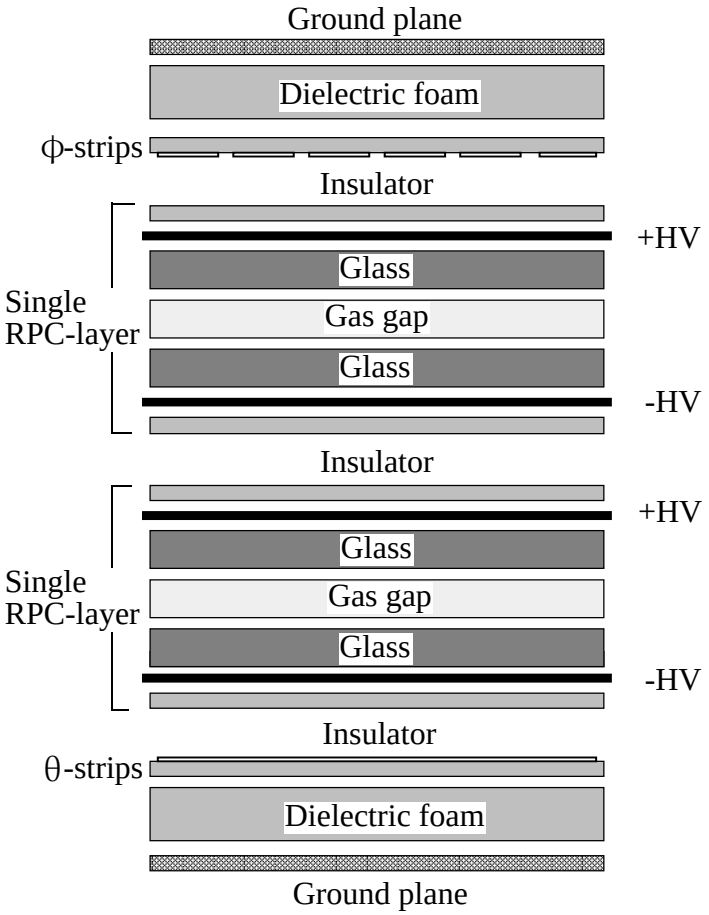

Figure 3.19: Cross section of a KLM super layer.

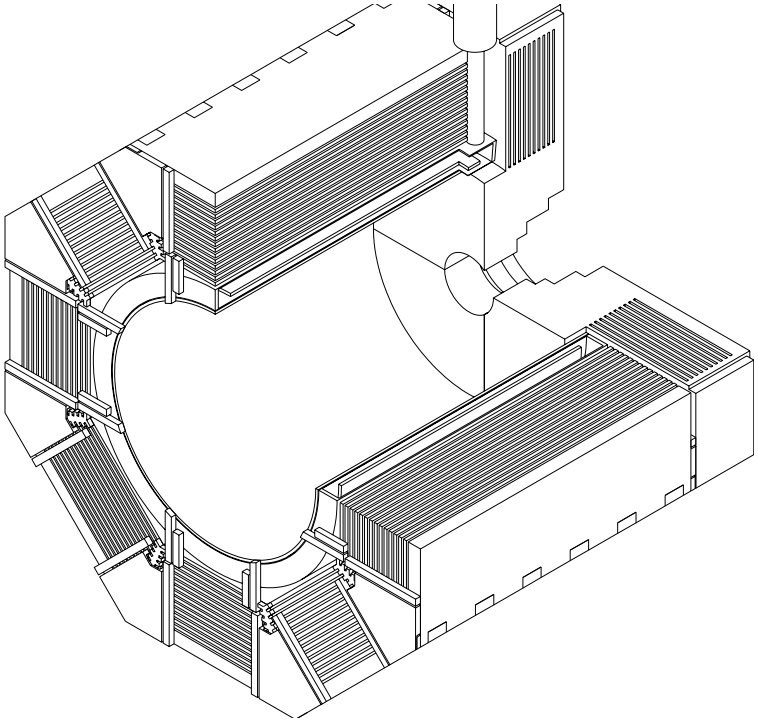

Figure 3.20: Schematic view of barrel KLM.

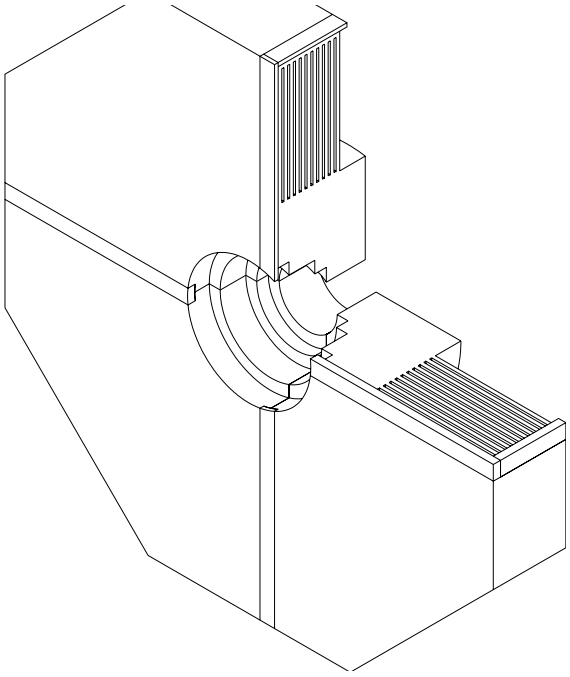

Figure 3.21: Schematic view of endcap KLM.

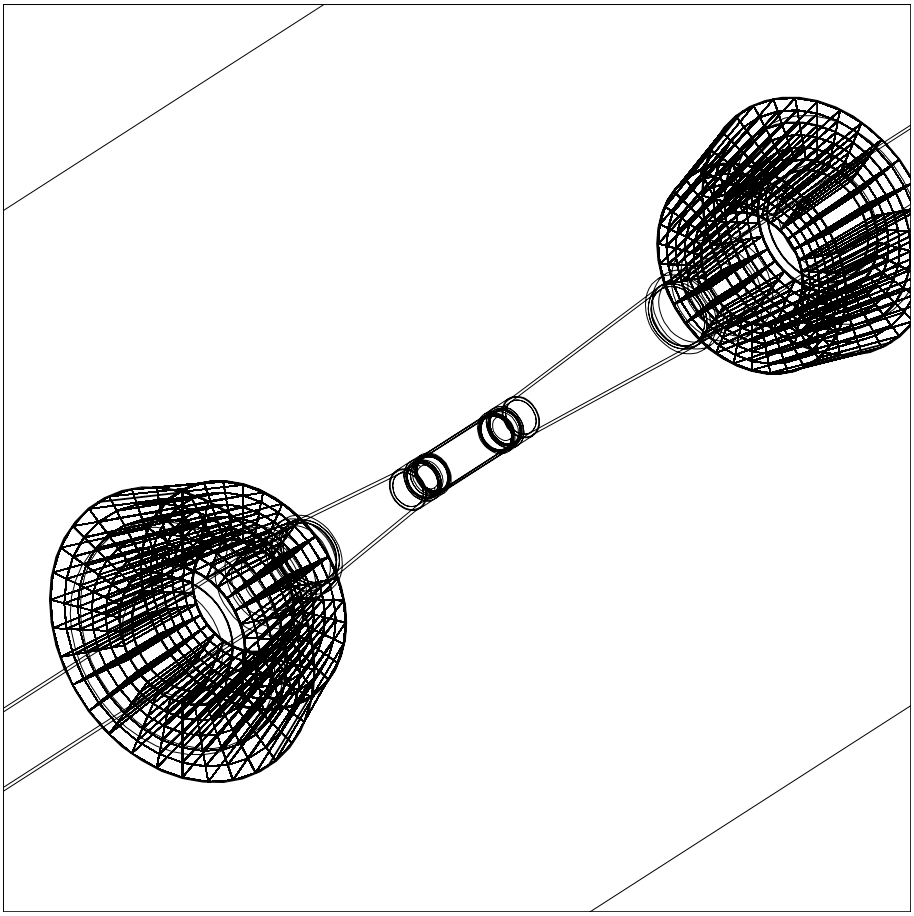

Figure 3.22: The configuration of Extreme forward calorimeter.

using the ECL trigger. The KLM trigger gives us additional information about the events which contains muon. The Global Design Logic (GDL) combines the trigger signals from each sub-detector and makes a final decision to initiate a data acquisition using whole Belle detector within 2.2 μsec from a beam crossing and provide the common stop signals of TDCs and gate signals of ADCs back to each sub-detectors. Since the background rates are sensitive to the accelerator condition, it is difficult to establish reliable estimation. Therefore, the trigger conditions should be flexible enough in order that background rates are kept within tolerant level for DAQ system, while the efficiency of physics events is kept high. The trigger condition installed in the GDL is designed to be programmable to realize the flexibility. The typical trigger rate of current experiment is 400 Hz with that the DAQ dead time is 4-5% at the peak luminosity of 10^{34} cm^{-2}s^{-1}.
Figure 3.24 shows a schematic view of the Belle DAQ system. The designed performance of the system is the dead time less than 10% at 500 Hz trigger rate. To satisfy this condition, the output signal from sub-detectors should be digitized within 200 μsec. The readout subsystem at sub-detectors and also from the trigger systems run in parallel. We adopt a charge-to-time (Q-to-T) conversion front-end electronics for DAQ, except for the KLM and SVD. KLM provides the time-multiplexed information. All sub-detectors except for the SVD use FASTBUS TDC readout system which is controlled with the aid of VME. The data signals from the SVD are sent to flash ADC's (FADC) and the data are stored in a memory module. The data from each subsystem are combined into a single event record using the event builder which converts the "detector-by-detector" parallel data streams to "event-by-event" stream. The data from event builder output is transfered to the on-line computer farm consisted of 120 processors for the fast event reconstruction at up to 15 MBytes/sec event data stream.
The on-line computer farm forms the event data structure and filters them with Level-3 software trigger, which consist of ultra fast track finder that can handle at 500Hz of event rate. Approximately 60% of events are selected using the Level-3 trigger based on the z-vertex position of tracks from ultra fast track finder together with the Level-1 trigger information. After passing the computer farm, the events are stored into the mass storage system and eventually stored into the tapes for off-line use.
The recorded events are processed at off-line computing farm and filtered precisely using the Level-4 trigger. The basic logic of Level-4 trigger is based on the production vertex information regarding charged tracks and the total energy deposit information from the ECL. The Level-4 trigger consists of following three components: the fast track finder, the fast cluster finder and the event filtering routine. The fast track finder finds charged tracks and reconstruct the vertex position. The fast cluster finder finds the energy shower of clusters and reconstructs their energies. The event filtering routine select the events using the information from the fast track finder, the fast cluster finder and the Level-1 hardware trigger. The Level-4 trigger reduce the data size to smaller than 30% against the Level-1 triggered events, while keeping the efficiency for τ-pair, μ-pair and hadronic events above 97%, within the small computing time.

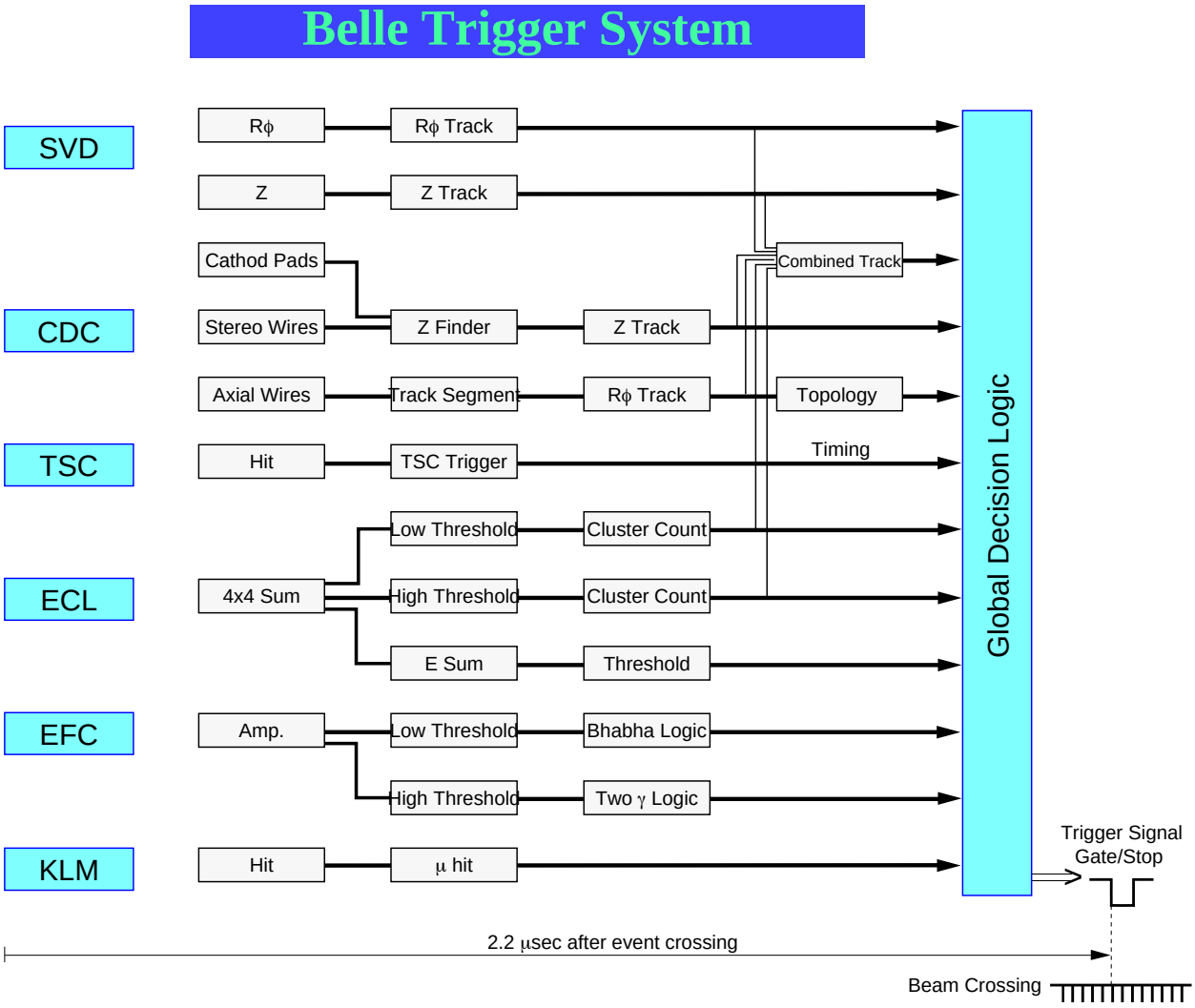

Figure 3.23: Logic diagram of Belle trigger system

The events which pass through the Level-4 trigger are send to the full Data Summary Tape (DST) production chain. Tracks, photons and information about particle identifications are reconstructed using the digitalized signals from sub-detectors and converted to summary table. At the end of the DST production chain, each event is classified into categories of physics process including τ-pair events, hadronic events, QED processes. In this analysis, we use the events that are classified as τ-pair event. Detail of the event classification is mentioned in first section of next chapter.

3.3 Software

We give an overview of the structure of the analysis environment and the description of Monte Carlo (MC) simulation program optimized to the Belle experiment. To manage data and get the results, we use many kind of program modules for analysis,

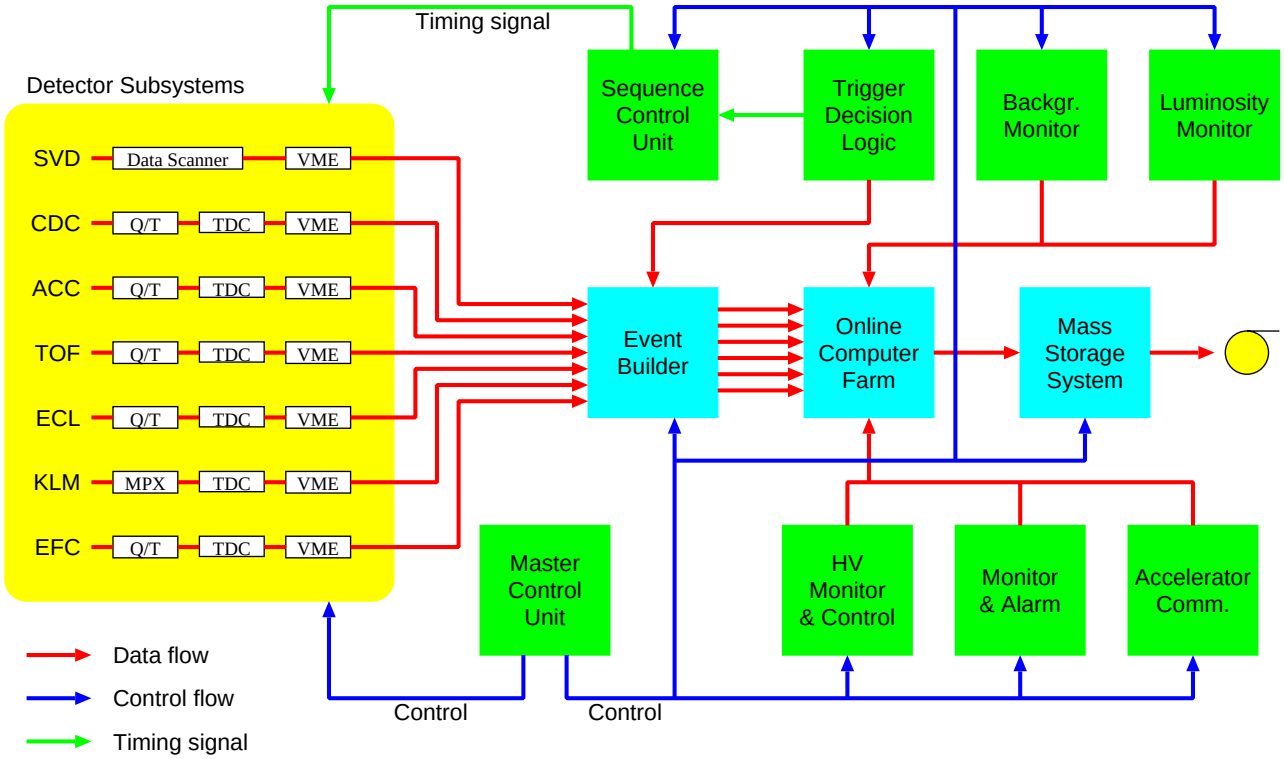

Figure 3.24: Logic diagram of Belle Data Acquisition system

simulation and DST production. They are executed on a framework software called "BASF" which stands for the "Belle AnalysiS Framework"[51]. In this framework, the branching output path for the HBOOK [52] is equipped.

3.3.1 Monte Carlo simulator

For Monte Carlo event generation, we use several kind of physics process simulation programs called "generators". For τ-pair event generation, KORALB [53] event generator is used. The KORALB was developed for the τ-pair production process at low energy, $\sqrt{s} < 30$ GeV. The initial state photon radiation in the process is reproduced using the KKMC generator [54]. We use CLEO QQ [55] event generator for background hadronic events ($B\bar{B}$ and $q\bar{q}$ for continuum). The QQ was developed for study of B mesons in the $\Upsilon(4S)$ resonance. Both of generators are developed in the analysis of CLEO experiment and designed for a symmetric collider, they have been adjusted to the Belle experiment. Also for the background events, we use aafhb generator [56] for the two photon process. The aafhb is the modified aafh [57] generator for the BELLE experiment. The aafh calculates the four-fermion production from photon collision in e^+e^- reaction. The decay table that is control the decay of generated particle is described using the values on the PDG, also it can be modified to define the interactions and the final products. We generate $\tau \to$ LFV events (we define them as "signal events") with KORALB generator and a modified

decay table with an assumption of uniform angular distribution of LFV τ decay in the rest system of τ. The treatment of the case of another decay angular distribution is described below. For detector response simulation, we have two kinds of detector simulators. One is the fast simulator and another is the full detector simulator. The fast simulator, called "FSIM", does not need much computing power, but can not simulate detailed environment, for example the detector resolution. Thanks to the great advantage of computer environment in recent years, we can simulate enormous number of interaction between particles and detector within short time. Therefore we use full detector simulator which is based on GEANT3 [58] called "GSIM" in this analysis. The MC data generated using GSIM is processed through same reconstruction tools, as in the real data analysis.

Chapter 4

Analysis

In the collision process of electron and positron at an energy of 10.6 GeV, many kind of events are generated as well as τ-pair event as listed in Table 4.1. To observe signal events, we should get rid of those background events requiring selection criteria for topological and kinematical variables. Considering the cross sections in Table 4.1 and integrated luminosity of experimental data, we aim that the number of background events should be suppressed to the factor in the range in $10^{-10} - 10^{-8}$ after applying all selections. In this chapter, the selection criteria and its optimization is described. The optimization is carried out using signal and background MC.

4.1 τ-pair event classification

After the DST production, we classify the event for each physics analysis. Generic decay of τ emits at least one neutrino and it is missed because there is no device which observe the neutrinos at Belle detector. τ-pair events are required that the observed energy is much smaller than total beam energy. Hadronic events are reduced after this requirements. Bhabha and two-photon processes have huge number of cross sections as listed in table 4.1. While we veto using the trigger and scale down the number for these processes in data taking, size of the experimental data is still enormously large. We have to require selection criteria that veto for these processes. Generally, Bhabha event has two high energy electron tracks which travels back to back in the CM system of e^+e^-. Therefore it will be rejected with the condition for maximum opening angle between two tracks in event not to be approximately 180°. Tracks in two-photon process has small transverse momentum in laboratory system so that background contribution from this process is reduced using selections for transverse components of momentum and polar angle of tracks. Selection criteria are summarized as following list.

i) $2 \leq$ Number of charged tracks ≤ 8,

ii) $|$ charge sum in an event$| \leq 2$,

iii) Sum of $P^{\mathrm{CM}} < 10$ GeV/c,

Table 4.1: Signal and background MC samples used in this analysis.

process	Cross section (nb)	Number of processed MC (million events)
LFV $\tau^+\tau^-$ decay	—	0.1 for each mode
generic $\tau^+\tau^-$ decay	0.91	86
Υ (4S)	1.05	159
$q\bar{q}$ continuum		
uds	2.05	339
$c\bar{c}$	1.10	217
(Radiative) Bhabha	123.5	500
(Radiative) mu-pair	1.01	14
two-photon		
$eeee$	40.9	490
$ee\mu\mu$	18.9	226
$eeuu$	11.7	140
$eess$	0.23	2.8
$eecc$	0.03	0.4

iv) Sum of $E(ECL) < 10$ GeV,

v) $p_t > 0.5$ GeV/c for all charged tracks,

vi) Event vertex point is within 0.5cm transversely and 3 cm along the beam direction from zero-point,

vii) $E_{rec} > 3$ GeV or $p_t > 1.0$ GeV/c for all charged tracks,

viii) $E_{tot} < 9$ GeV or $\theta_{max} < 175$ degree,

ix) $N_{barrel} \geq 2$ or $E^{\rm CM}(ECL)_{trk} < 5.3$ GeV

where p_t, P and E denotes magnitude of transverse components of momentum, magnitude of momentum and energy of particles, respectively. The valuables with superscript "CM"are measured in CM system of e^+e^- and others are in laboratory frame. In this selection, we require the charged track should have $p_t > 0.1$ GeV/c and closest approach between charged track and interaction point within ± 1 cm transversely and ± 5 cm along the beam. The ECL cluster and photon should have $E > 0.1$ GeV. E_{rec} is sum of $P^{\rm CM}$ of charged tracks and $E^{\rm CM}$ of photons. $P^{\rm CM}_{miss}$ is momentum of missing particle boosted to e^+e^- CM system assuming massless particle. E_{tot} is $E_{rec} + P^{\rm CM}_{miss}$. N_{barrel} is number of track within the polar angle of $30 < \theta < 130$ degree. $E^{\rm CM}(ECL)_{trk}$ is sum of E^{CM} of ECL clusters — sum of $E^{\rm CM}$ of photons. θ_{max} is maximum opening angle among all combination of the track pairs. Selections i), ii) and vi) are to reject events which comes from several processes including bremsstrahlung of a charged particle and beam gas interaction. Selections iii) and iv) are similar because there is missing momentum due to the neutrino

Table 4.2: Reduction rate for each selection steps.

cut	$\tau^- \to e^-e^+e^-$	generic τ-pair	uds	Bhabha	two-photon $eeuu$
i)	0.971	0.840	0.823	0.994	0.245
ii)	0.909	0.813	0.798	0.994	0.244
iii)	0.899	0.812	0.797	0.203	0.244
iv)	0.880	0.811	0.785	0.072	0.243
v)	0.864	0.780	0.741	0.072	0.039
vi)	0.833	0.755	0.719	0.066	0.035
vii)	0.809	0.706	0.706	0.066	0.007
viii)	0.758	0.693	0.665	0.066	0.007
ix)	0.744	0.690	0.664	0.057	0.007

emission in τ-pair event. Selections v) and vii) reject the two-photon and selections viii) and ix) reduce Bhabha background. Figure 4.2 – 4.9 show the distributions of variables used in the event classification for generic τ-pair, signal $\tau^- \to e^-e^+e^-$, $q\bar{q}$ continuum events where q is light quarks u, d and s (uds continuum), Bhabha and two-photon $eeuu$ MC samples. As shown in each distribution, the selection criteria reject a large fraction of Bhabha and two-photon events, while keeping main ratio of τ-pair events. Step-by-step reduction rates for each process are summarized in Table 4.2.

4.2 Event topology

We search for $\tau^+\tau^-$ events in which one τ decays into three charged particle final states (3-prong). For other τ in the event, we accept the decay modes into one charged and arbitrary number of neutral particles (1-prong) to suppress the background and collect signal event efficiently. The branching fraction of the decay of τ into "1-prong" is (85.35±0.07)% [18]. The topological signiture of signal event is illustrated in Figure 4.10. We thus require for the responsible signal events to have four charged tracks with zero net charge and arbitrary number of photons. Each charged track must have transverse momentum $p_t > 0.1$ GeV/c and be within the detector acceptance: polar angle range $25° < \theta < 140°$. Figure 4.11 and 4.12 show the p_t and θ distributions of $\tau^- \to e^-e^+e^-$, Bhabha and two-photon MC samples, respectively. For each charged track, the distance of closest approach to the interaction point is required to be within ±1 cm transversely (dr) and ±3 cm along the beam (dz). Figure 4.13 shows the dr and dz distributions of all tracks in $\tau^- \to e^-e^+e^-$ MC after τ-pair event classification. These conditions eliminate the tracks which mainly come from non-e^+e^- collision processes and failure of track reconstruction. For the event selection, we use only reconstructed photon with an energy $E_\gamma > 0.1$ GeV and neutral ECL clusters must be separated at least 30 cm from a projection point of any charged track in the ECL. Figure 4.14 shows the E_γ

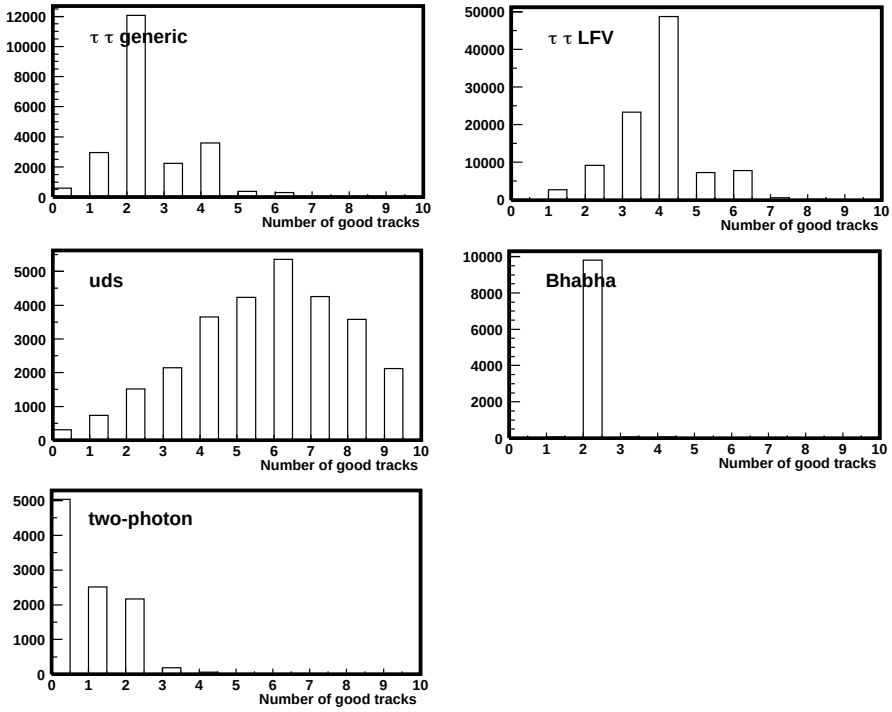

Figure 4.1: Number of "good tracks" in an event.

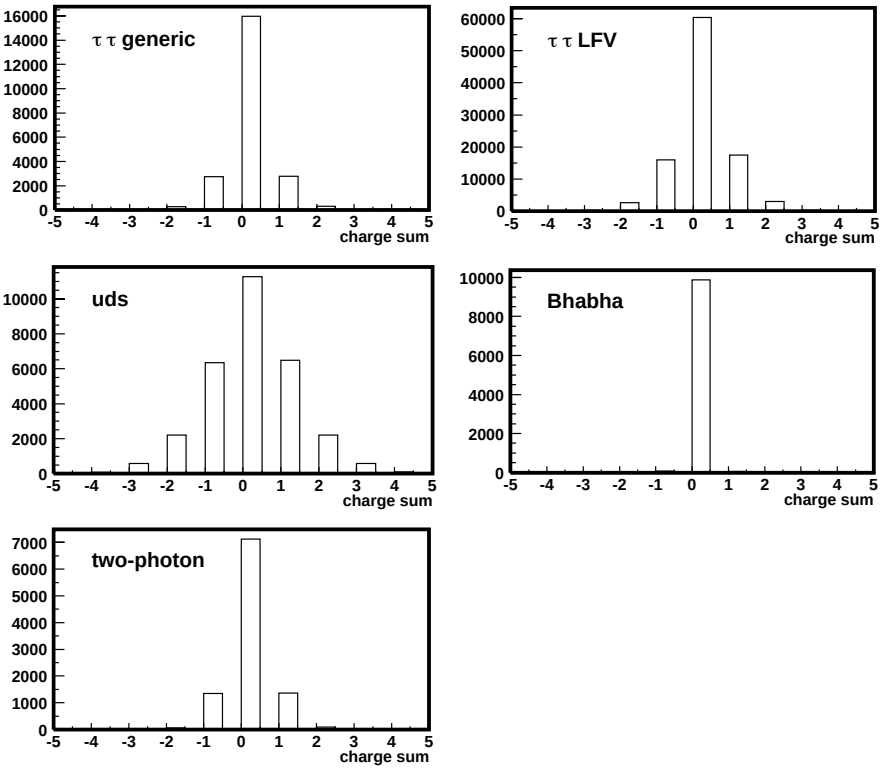

Figure 4.2: Total charge in an event.

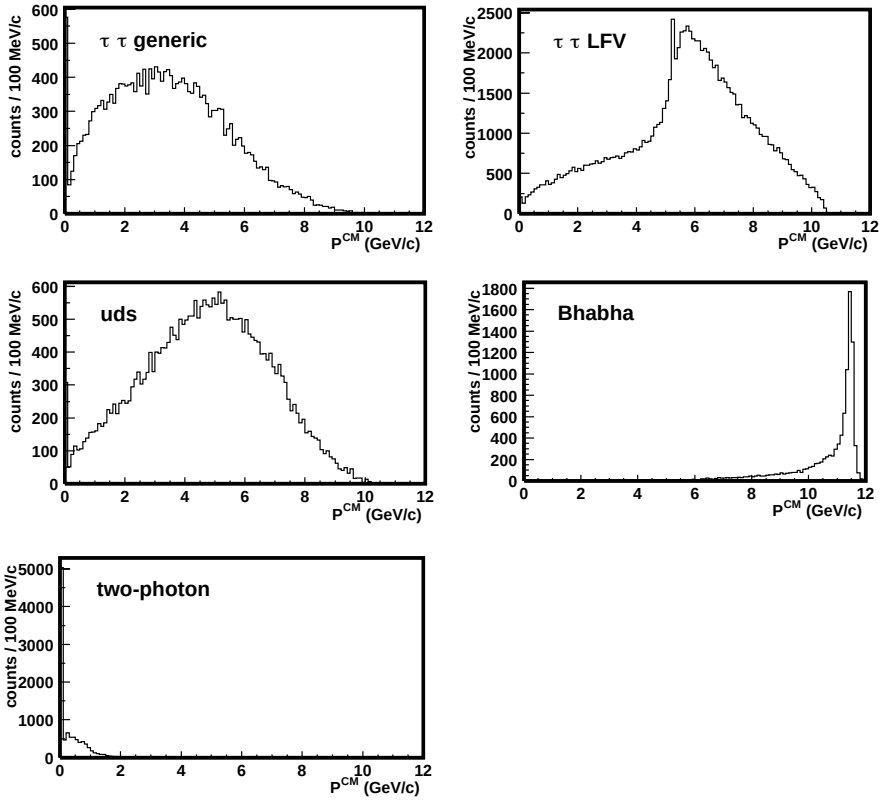

Figure 4.3: Sum of P^{CM}.

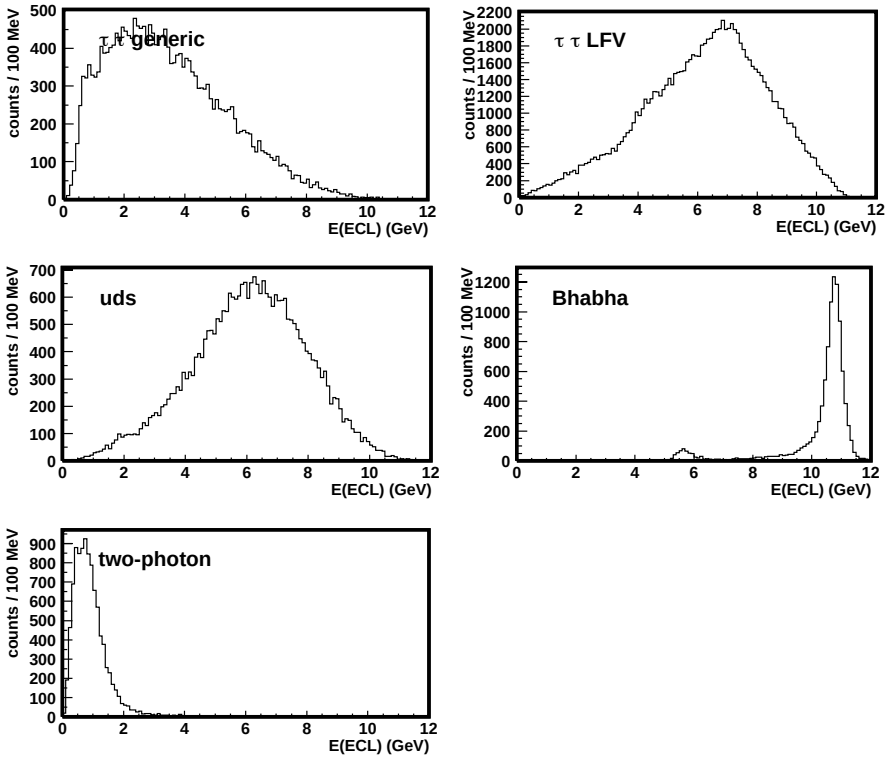

Figure 4.4: Sum of $E(ECL)$.

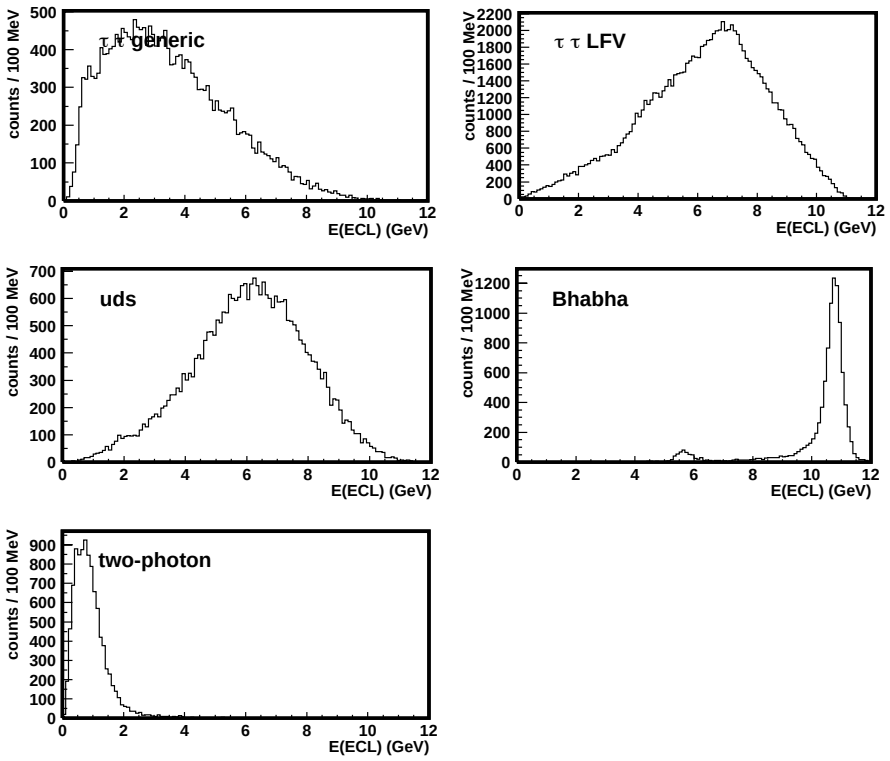

Figure 4.5: Maximum p_t among all tracks in an event.

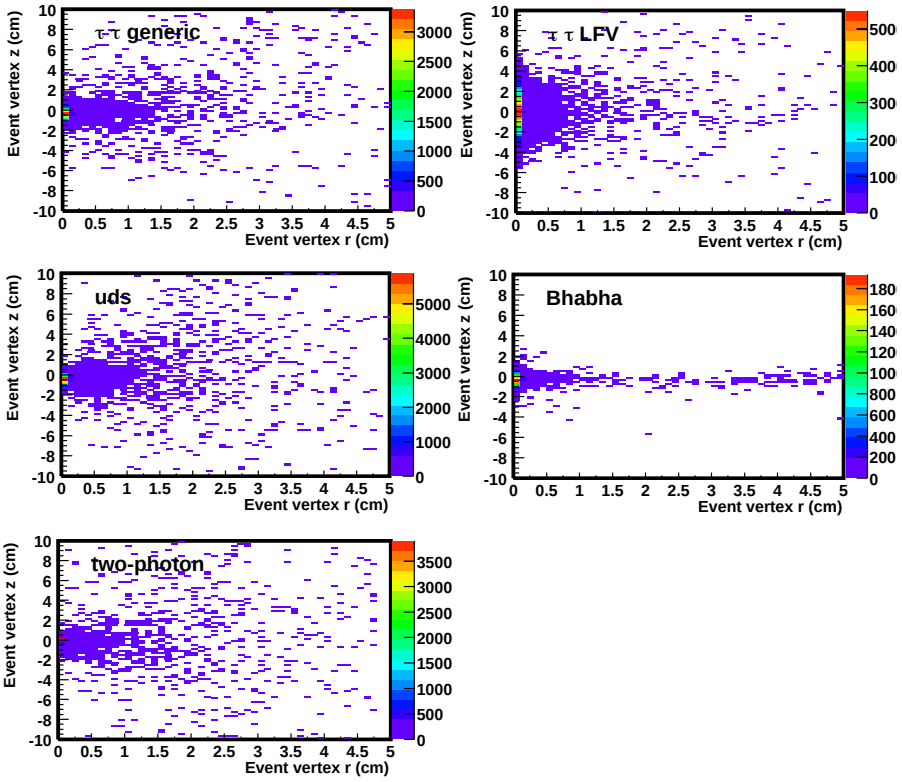

Figure 4.6: Position of vertex point of event.

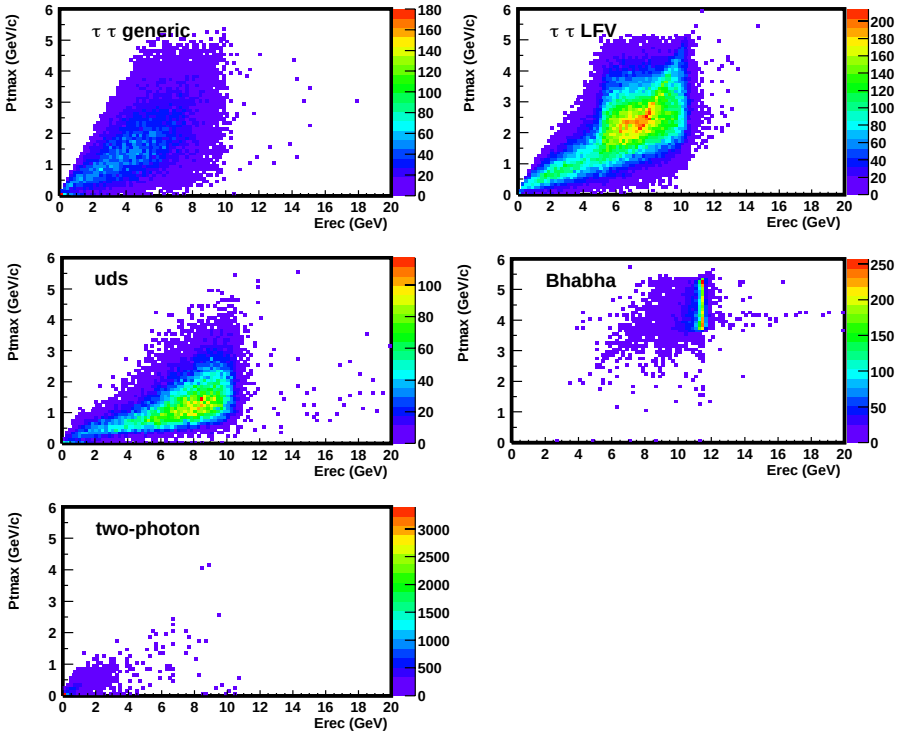

Figure 4.7: Maximum p_t among all tracks in an event vs. E_{rec}.

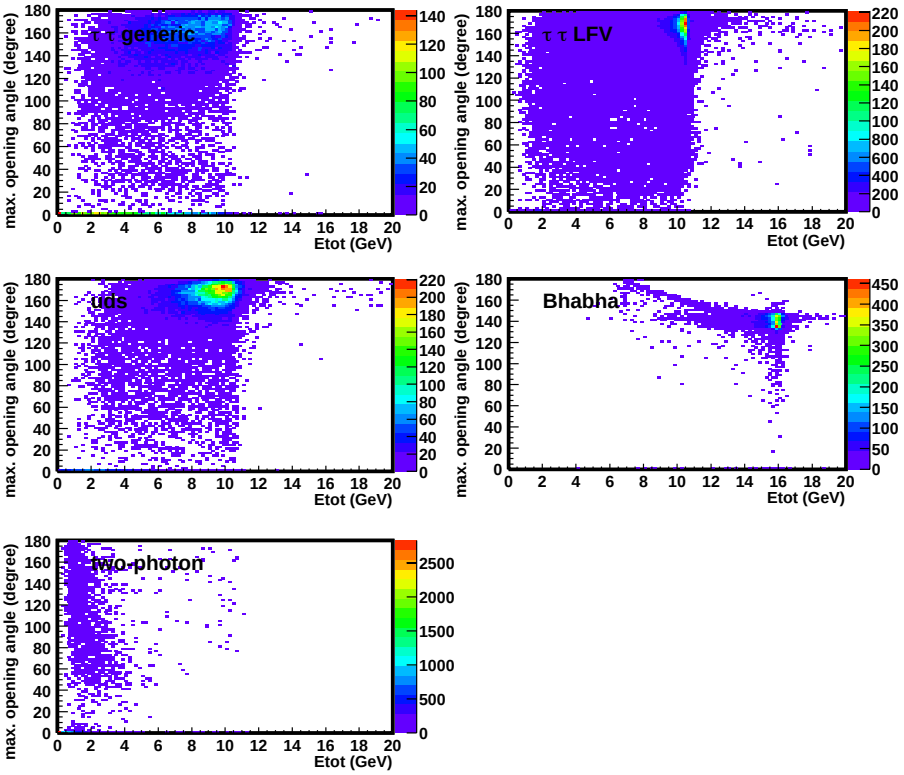

Figure 4.8: Maximum opening angle vs. E_{tot}.

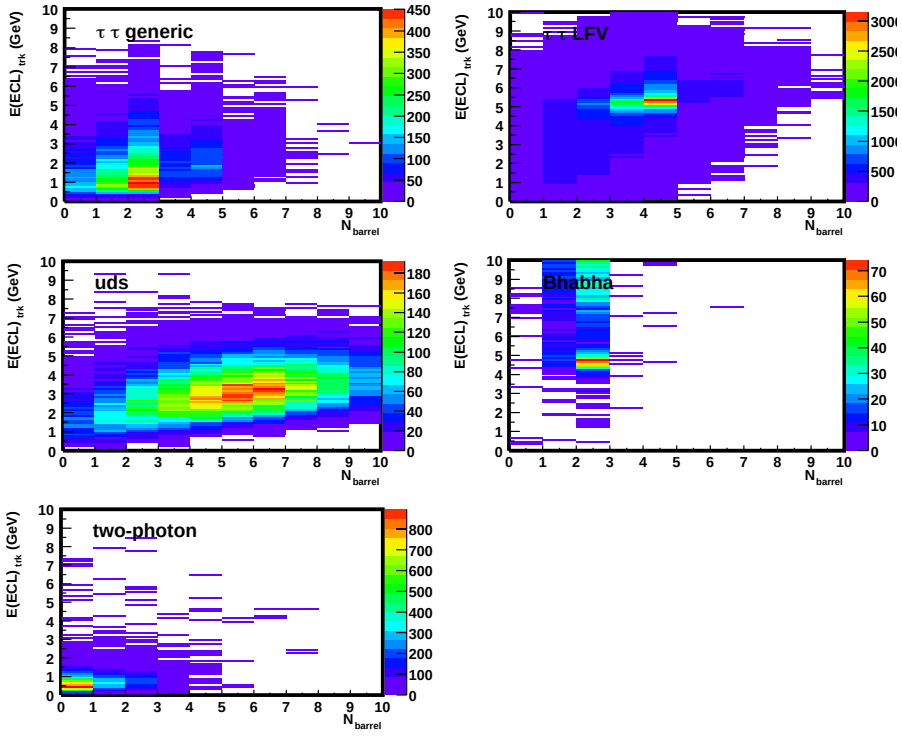

Figure 4.9: $E(ECL)_{trk}$ vs. N_{barrel}.

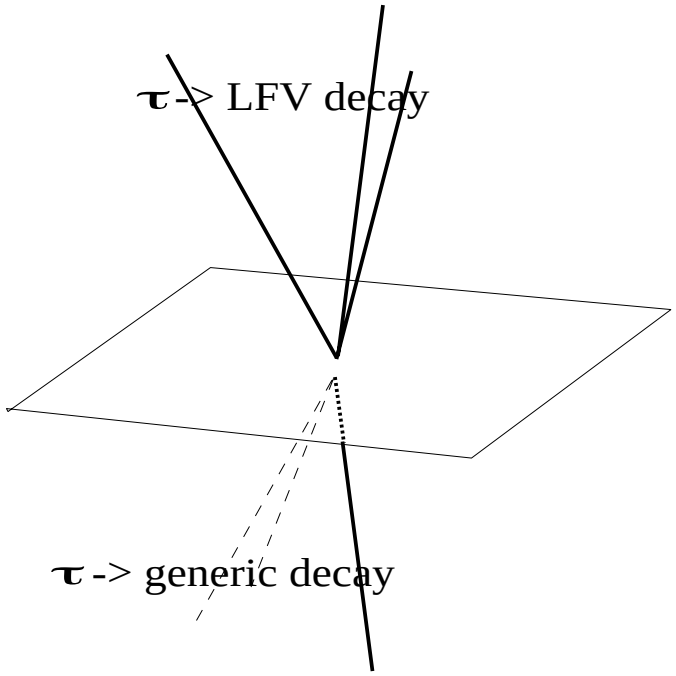

Figure 4.10: The event topology of signal event.

Table 4.3: Event topology of 4-charged event in signal MC

topology	rate (%)
0-prong vs. 4-prong	1.7
1-prong vs. 3-prong	91.7
2-prong vs. 2-prong	6.6

distribution of ECL clusters in $\tau^- \to e^-e^+e^-$ MC events. In upper plot, open histogram is distribution of all reconstructed photon and dark histogram is that come from τ decay. The bin-by-bin ratio of former histogram to latter one is shown in bottom plot and we can see that low energy reconstructed photons contains many background photons that are irrelevant to the physics process. The main part of them are considered to come from bremsstrahlung of charged particles interacting with the detector material and ECL noise. These photons are suppressed using energy threshold described above.
The tracks and photons in an event are divided into two hemispheres in the e^+e^- CMS with the plane perpendicular to the thrust axis calculated from the momenta of all charged tracks and photons in the event. Signal events have a 1-prong vs. 3-prong topology, i.e., three charged tracks are required in one hemisphere and one charged track in the other. We define the former hemisphere as the signal side and the latter as the tag side. Event topology of $\tau^- \to e^-e^+e^-$ MC events which contain 4-charged track is summarized in Table 4.3. As expected, a large fraction of signal events have "1-prong vs. 3-prong topology".
The distributions of number of photon on the signal side, n_γ, are shown in Figure 4.15 for both of signal and background samples. It should be less than or equal to 2 to allow for photons from initial state radiation and photon radiation from electrons. This selection reduces large fraction of hadronic processes and generic τ-pair event because they contains π^0 in signal hemisphere.

4.3 Particle identification

After selecting the event using the topological signature, we identify the particle of three charged tracks in signal hemisphere. In general, observed charged tracks from the interactions are ones of electrons, muons, pions and kaons, and we search for final states of three leptons and one lepton and two pseudoscalar mesons. The identification of the particle is provided through calculation of probability or likelihood ratio from the information of sub-detectors. In this part, detail of each particle identification method and the performance is described.

4.3.1 Electron

The most significant signature of electron is an energy deposit in the ECL through electromagnetic shower associated with a charged track. Since the radiation length of electron in CsI crystal is short, most of electron energy is lost in the ECL through an

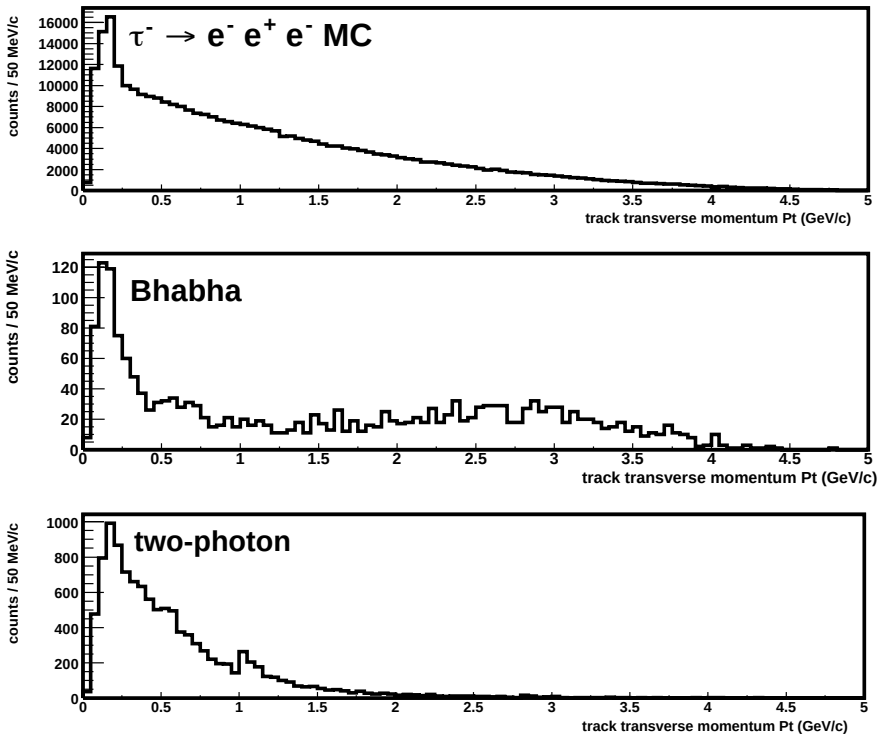

Figure 4.11: Transverse momentum Pt distribution of all tracks for $\tau^- \to e^-e^+e^-$ (top), Bhabha (middle) and two-photon $eeuu$ (bottom) MC samples.

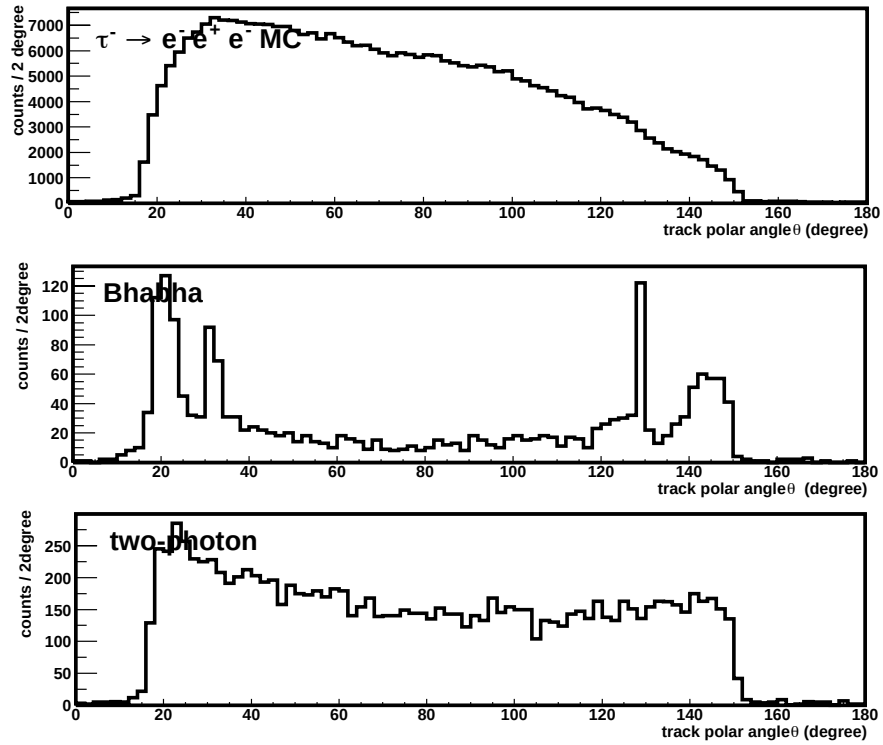

Figure 4.12: Polar angle θ distribution of all tracks for $\tau^- \to e^-e^+e^-$ (top), Bhabha (middle) and two-photon $eeuu$ (bottom) MC samples.

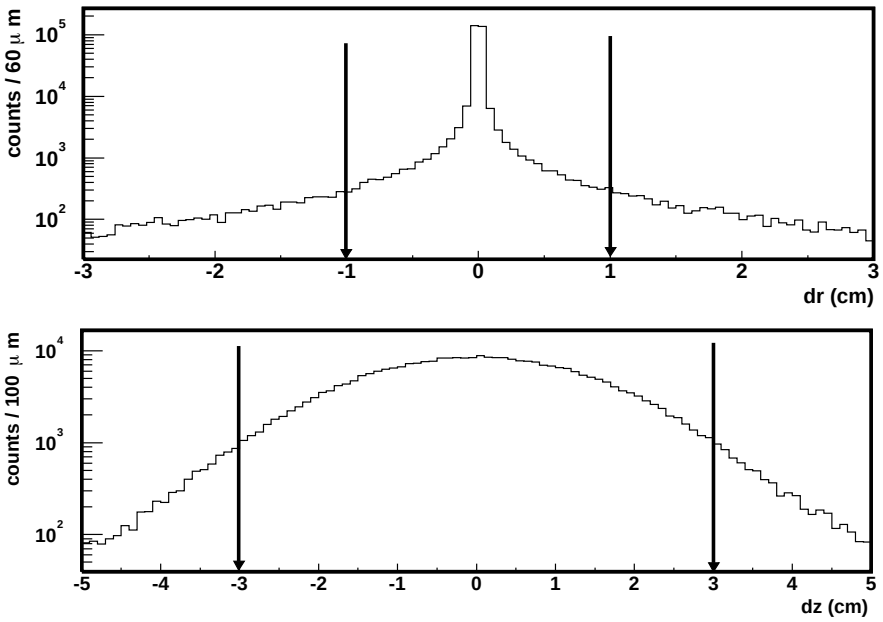

Figure 4.13: Impact parameters distributions for $\tau^- \to e^-e^+e^-$ MC. Arrows indicate signal region.

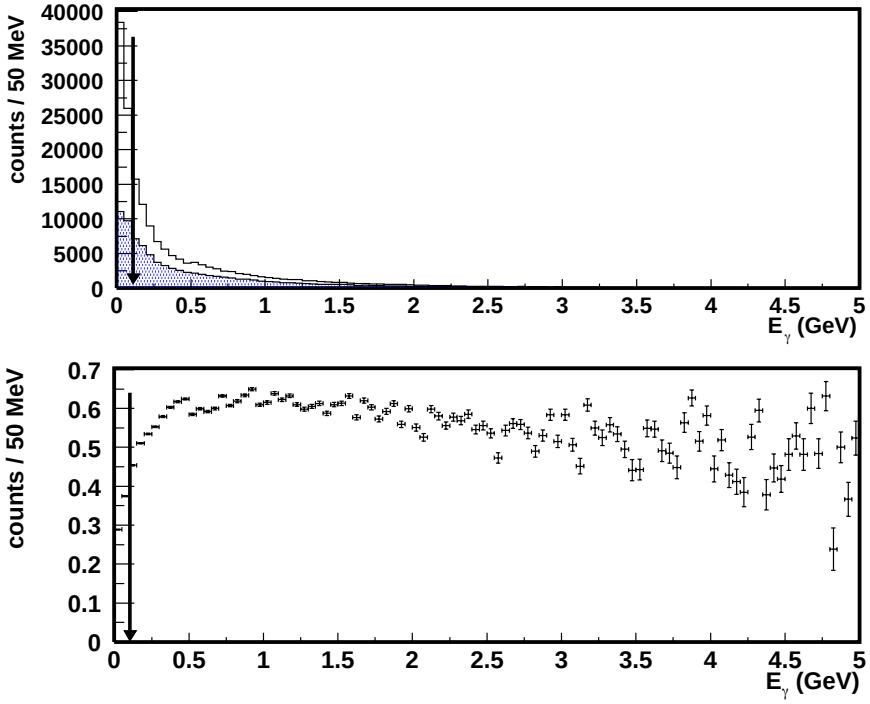

Figure 4.14: Top histograms show photon energy distributions for $\tau^- \to e^-e^+e^-$ MC. Open histogram shows all photon distribution and samples from τ decay is shown by dark histogram. Bottom plot shows ratio of photons from τ decay in all sample in each energy region.

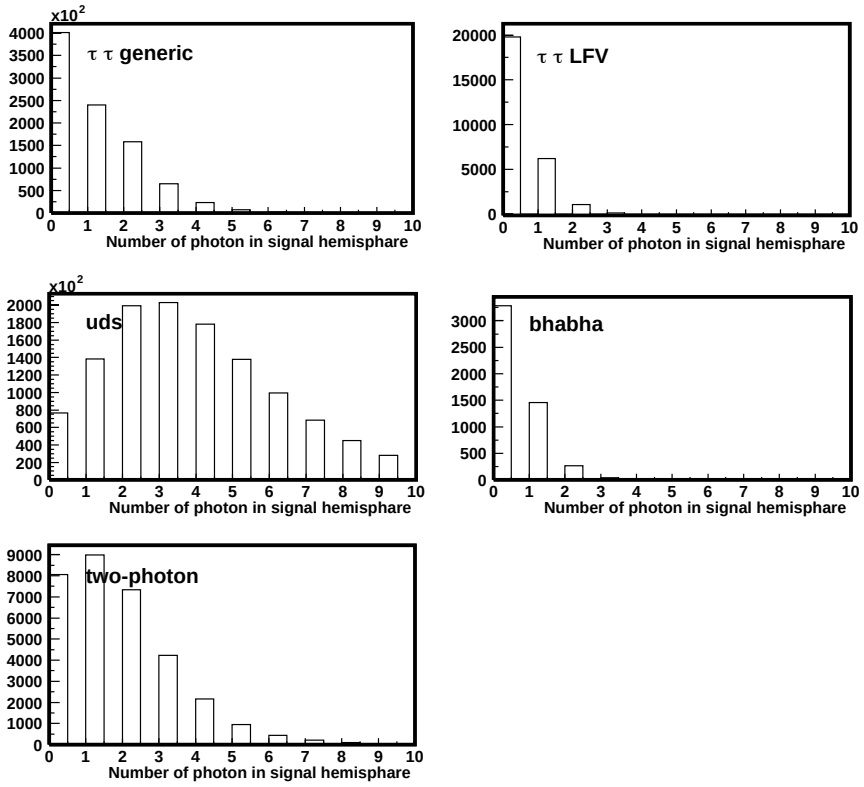

Figure 4.15: Number of photons in signal hemisphere.

electromagnetic shower, ratio of the cluster energy in the ECL to the track momentum measured with the CDC, E/p, forms a peak near 1, while that for hadrons and muons do not since the interaction length of hadron is longer than the crystal length. In addition, the lateral spread of the electromagnetic shower and hadronic shower are different because radiation length of electron is shorter than interaction length of hadron. To evaluate shower shape quantitatively, we use the quantity $E9/E25$, which is defined as the ratio of energy summed in a 3×3 array of crystals surrounding the crystal at the center of the shower to that of a sum of a 5×5 array of crystals centered on the same crystal. The amount of ionization created from a particle as it travels through a gas filled volume exhibits a well-known β dependence known as Bethe-Bloch equation. Because electron mass is much smaller than hadrons and muon, the dE/dx measured in the CDC is noteworthy signature for electron. Figure 4.16−4.18 show measured these quantities for electron and pion samples in MC. We calculate the likelihood for quantity using probability density functions (PDFs) prepared beforehand. The electron likelihood L_e and the non-electron likelihood $L_{\tilde{e}}$ are separately calculated for each discriminant. The likelihoods are combined and electron likelihood ratio function ($\mathcal{L}_{eid}$) is calculated. [59].

$$\mathcal{L}_{eid} \equiv \frac{\Pi_{i=1}^{n} L_e(i)}{\Pi_{i=1}^{n} L_e(i) + \Pi_{i=1}^{n} L_{\tilde{e}}(i)}, \tag{4.1}$$

where i runs over the quantities. For electrons, we require $\mathcal{L}_{eid} > 0.1$ and the laboratory momentum to be greater than 0.3 GeV/c. The threshold of electron track momentum is set because the performance of electron identification is much worth than higher momentum region due to the structure of detector. Efficiency of electron identification is defined as the ratio of the number of tracks identified as an electron to the number of reconstructed electron tracks. The efficiency for QED and hadronic environment are estimated using the electron samples in the radiative Bhabha events and $J/\psi \to e^+e^-$ inclusive events. Because the momentum of electron from J/ψ decay is limited in a some region, we estimate MC electron identification efficiency in hadronic environment using electron tracks which is embedded into hadronic data events. In addition, fake rate to other particles is another important parameter in particle identification. We define the fake rate as ratio of number of non-electron tracks identified as electron to number of reconstructed non-electron tracks. We use inclusive $K_S^0 \to \pi^+\pi^-$ decay to obtain charged pion samples to measure the fake rate of electron to pion. Figure 4.19 and 4.20 show distribution of efficiency and fake rate as a function of track momentum and polar angle in laboratory system, respectively. The average the efficiency is 90% and fake rate of electron to pion is 0.2%. In order to compensate for the energy loss from bremsstrahlung in the detector material, the momentum of an electron is recalculated adding the momentum of radiated photon clusters for case that an ECL cluster with energy less than 1.0 GeV is detected within a cone angle of 10° centered at the flight direction of the electron track.

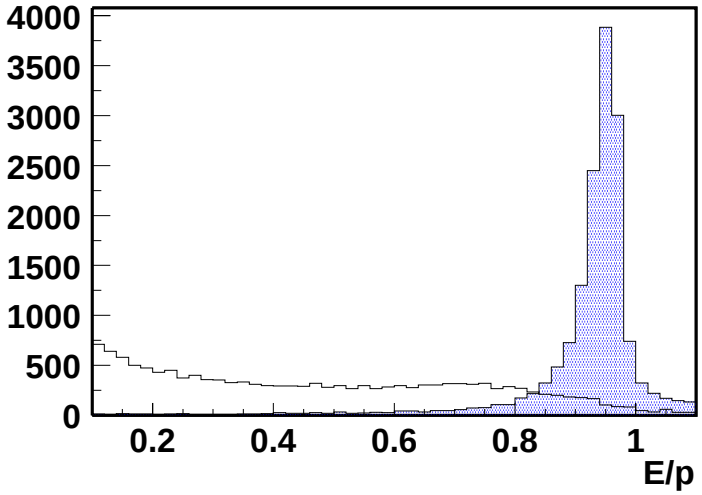

Figure 4.16: E/p distribution of MC.

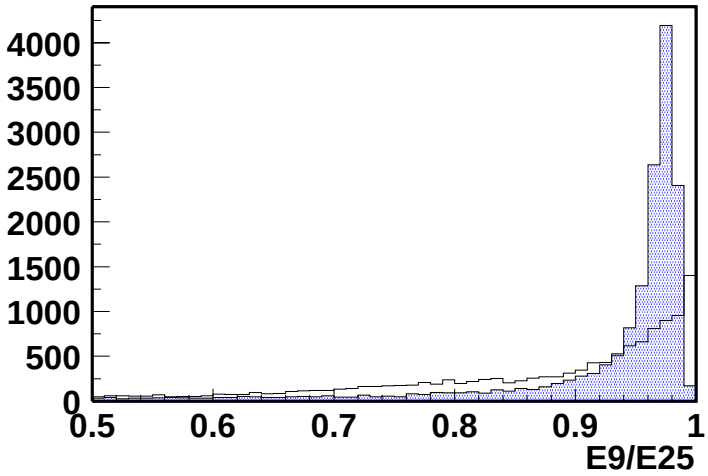

Figure 4.17: $E9/E25$ distribution of MC.

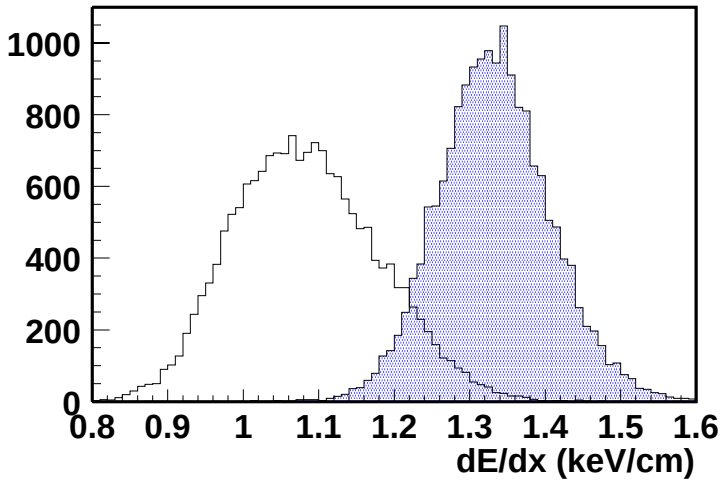

Figure 4.18: dE/dx distribution of MC.

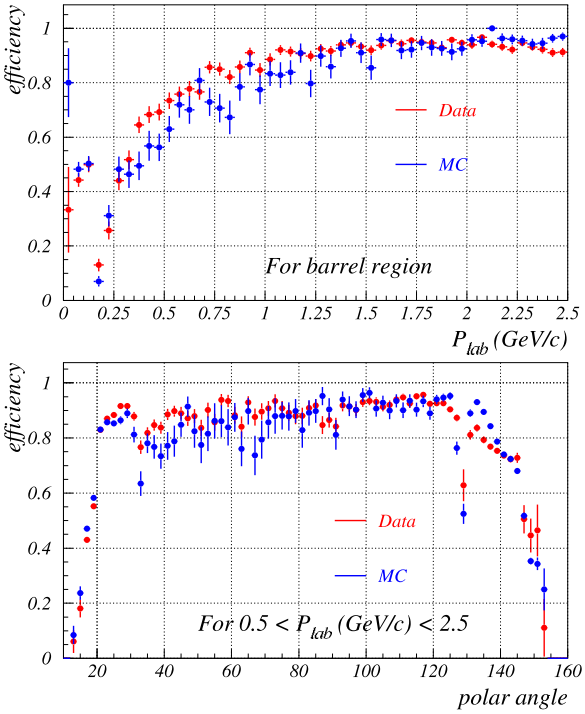

Figure 4.19: Electron efficiency as a function of track momentum and polar angle.

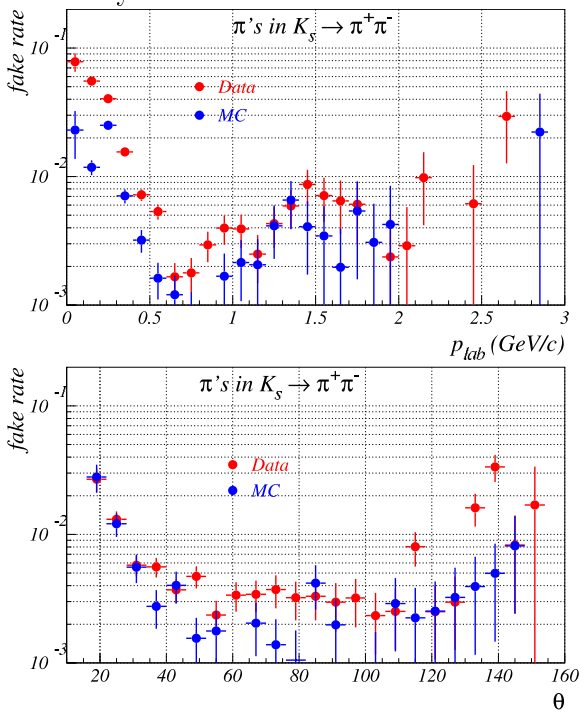

Figure 4.20: Fake rate of electron to pion as a function of track momentum and polar angle.

4.3.2 Muon

Because there is no strong interaction between muon and detector materials, muon is further penetrating than hadrons. The charged tracks are extrapolated as long as hit on KLM is found to be close to it. We count number of penetrated RPC layers R_{meas} along the extrapolated track trajectory. The number of crossing RPC layers R_{comp} is also computed from the track information assuming the muon interaction. Because muon penetrates through the larger amount of matters than hadrons, the difference of measured and computed number of penetration layers $\Delta R \equiv R_{meas} - R_{comp}$ becomes smaller. In addition, muon is less scattered from the detector materials during traveling in the KLM. Therefore the hit positions on the RPC layers do not deviate from geometrical expectation, while the deviation becomes large in case of pion. We represent the deviation as reduced χ^2, which is the goodness of fit of the transverse deviations of all hits associated with the track [60]. Figure 4.21 and 4.22 shows ΔR and χ^2/N (N is the number of track hit points in KLM) distributions for muon and pion sample picked up in MC data. The muon identification is performed computing likelihood ratio function $\mathcal{L}_{muid}$ as same as electron.

$$\mathcal{L}_{muid} \equiv \frac{\Pi_{i=1}^{n} L_m u(i)}{\Pi_{i=1}^{n} L_m u(i) + \Pi_{i=1}^{n} L_{\tilde{m}u}(i)}, \tag{4.2}$$

where i runs over ΔR and χ^2. To identify the muons, $\mathcal{L}_{muid}$ is required to be larger than 0.1 and the momentum should be larger than 0.6 GeV/c. This momentum threshold is set because muon tracks do not reach the KLM below this momentum. Efficiency and fake rates are calculated using same formula as the case of electron identification. Muon identification efficiency is measured using muon samples from two-photon $e^+e^- \to e^+e^-\mu^+\mu^-$ events and $J/\psi \to \mu^+\mu^-$ inclusive events. We also measure fake rate for pion using samples from $K^0_S \to \pi^+\pi^-$ decay. Figure 4.23 shows the muon identification efficiency and fake rate as a function of the track momentum in laboratory system. Efficiency is approximately 90% and fake rate for pion is approximately 2% in avarage of whole momentum range and polar angle region.

4.3.3 Kaon and Pion separation

Kaon and pion from LFV τ decay have various momentum. K/π separation must be applicable over a broad range of momenta. However, no single sub-detector can provide identification capability in the broad momentum region. Therefore, we combine information from three detectors which have different sensitive region on momentum and polar angle to separate kaon from pion: dE/dx measurement by use of the CDC, the TOF measurement and the Čerenkov light emission detection using the ACC. The momentum coverages of each sub-detector is illustrated in Figure 4.24. Because kaon is heavier than pion, the dE/dx measured in the CDC can separate these particles as described in electron identification section. Figure 4.25 and 4.26 shows dE/dx distribution for kaon and pion which are in the momentum region of $p < 1.0$ GeV/c and $p > 2.5$ GeV/c, respectively.

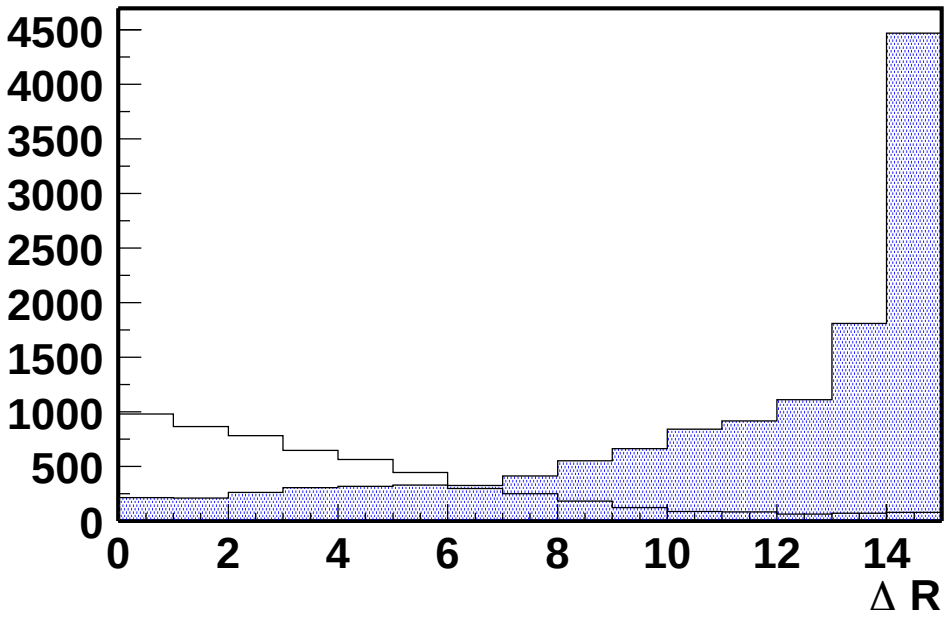

Figure 4.21: ΔR distributions for muon (shaded histogram) and pion (open histogram).

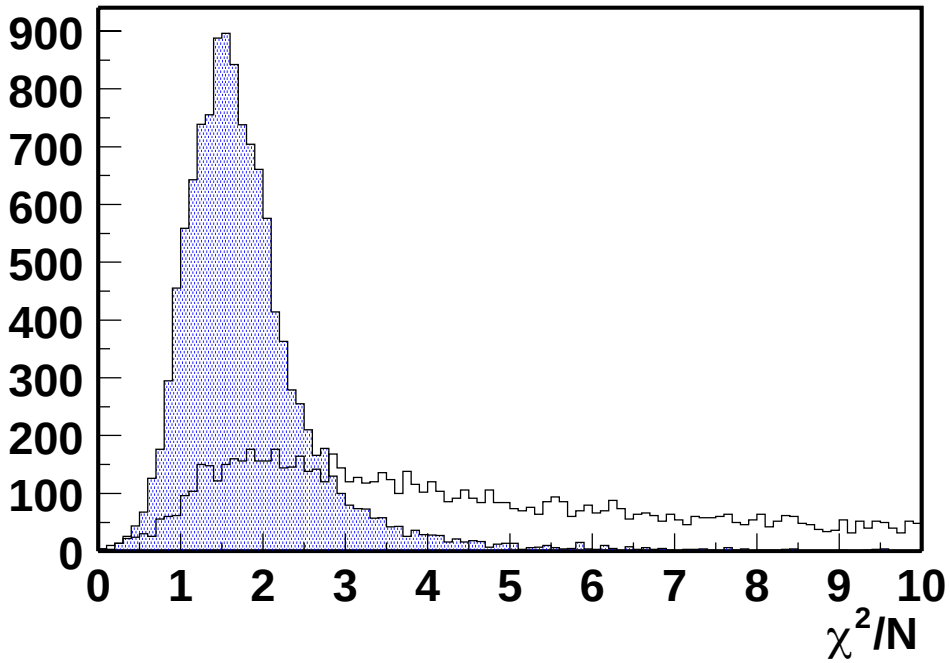

Figure 4.22: χ^2/ (Number of hit points) distributions for muon (shaded histogram) and pion (open histogram).

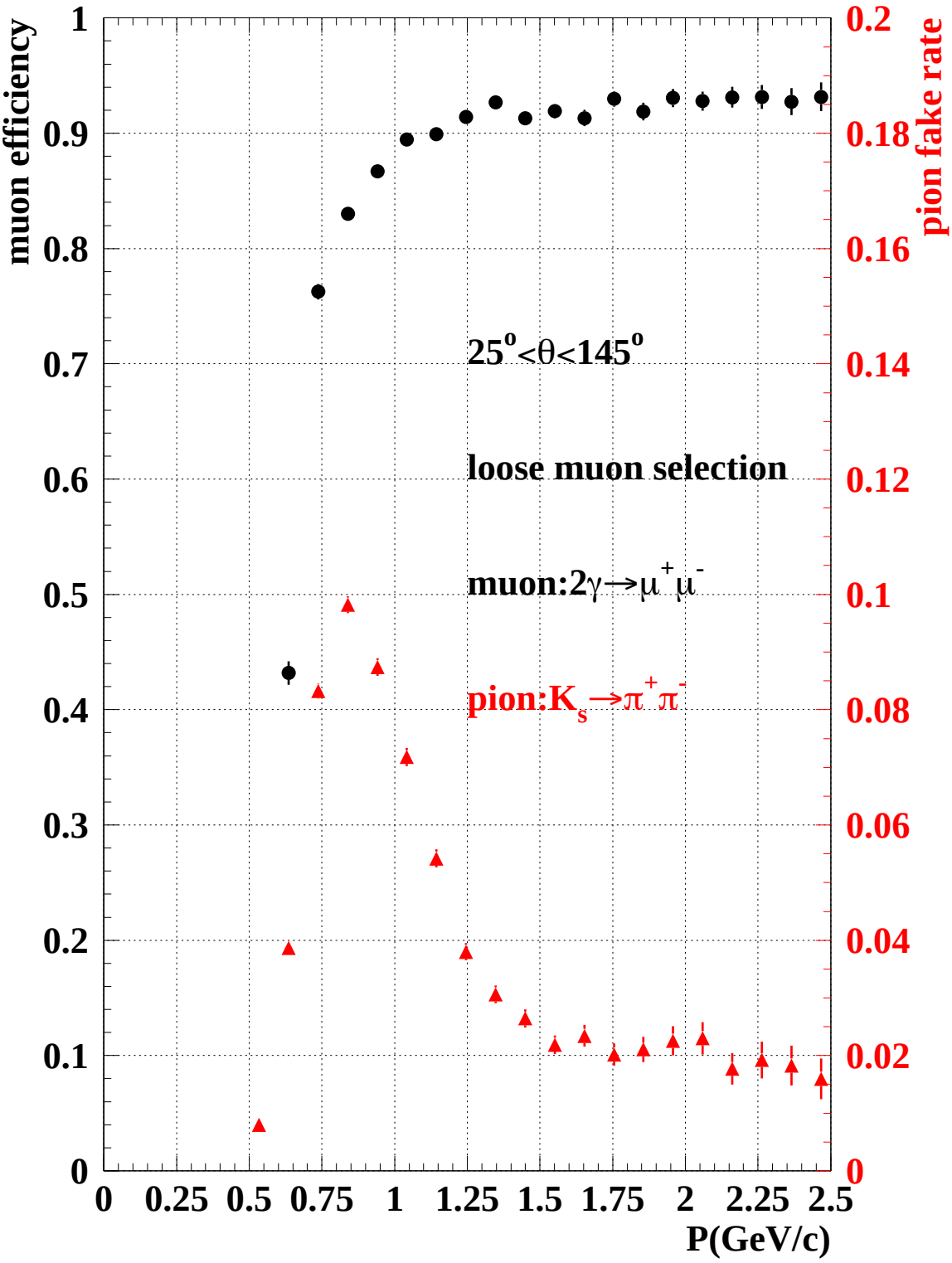

Figure 4.23: Muon efficiency and fake rate as a function of track momentum.

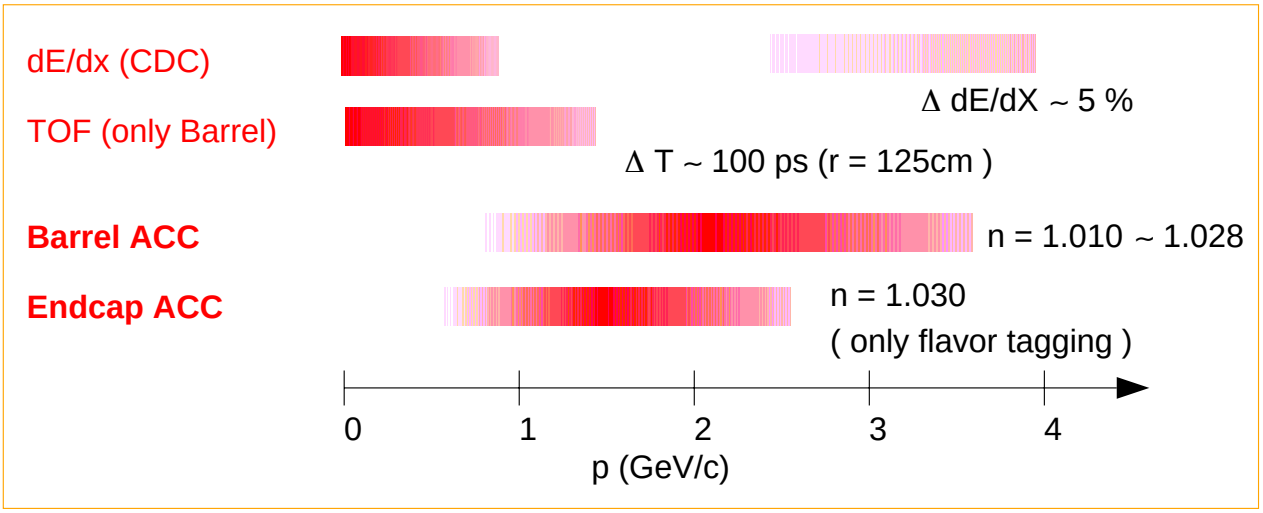

Figure 4.24: Momentum coverage for K/π separation of each sub-detectors.

A two-dimensional vector which contains the observed times in two ends of the counter is obtained from TOF measurement and computed from flight length and particle momentum assuming the mass. The TOF likelihood is calculated from difference between observed and computed times divided by the error. The error is evaluated summing up the contributions due to the uncorrelated uncertainty in the digitized times in the two photo-tube and correlated uncertainty due to the calculated time-of-flight from the tracking results. Figure 4.27 shows the difference between observed and computed time of flight using TOF.
In contrast to the dE/dx and TOF measurement, the ACC gives us an on-off threshold type information. We count the number of photoelectrons N_{pe} associate with the path length of charged track in ACC extrapolated from CDC. Figure 4.28 shows the N_{pe} distributions in each refractive index region. For particles beyond the threshold, spectrum can be interpreted as a distribution of photoelectrons at the photo-cathode following the Poisson distribution smeared with multiplicative amplification through fine-mesh dynodes. For particles below the threshold, N_{pe} is expected to be zero. However, in case of actual experiment, the ACC fires with a few N_{pe} for those particles. The main source of the accidental noise are scintillation light from reflector, Čerencov due to high energy δ-ray and electrical and thermal noise from the front-end electronics and dark current of the FM-PMTs. To consider these components, the measured N_{pe} is translated into probability for assumed kind of particle at the measured momentum. We construct PDF table from the MC simulation.
The likelihoods from the sub-detectors are combined using the same formula as the electron for muon identification.

$$\mathcal{L}_{K/\pi} \equiv \frac{\Pi_{i=1}^{n} L_K(i)}{\Pi_{i=1}^{n} L_K(i) + \Pi_{i=1}^{n} L_\pi(i)}, \tag{4.3}$$

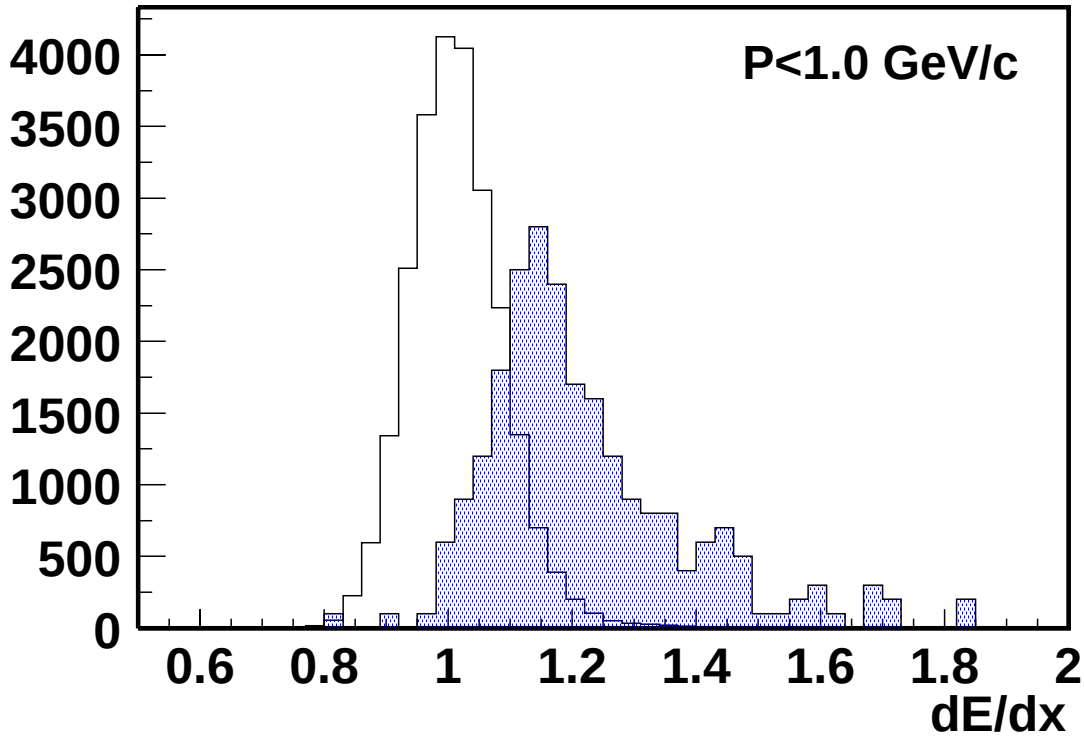

Figure 4.25: dE/dx distribution of MC. Momentum of particles are limited in $P <$ 1.0 GeV/c region. Shaded histogram is for kaon and open histogram for pion.

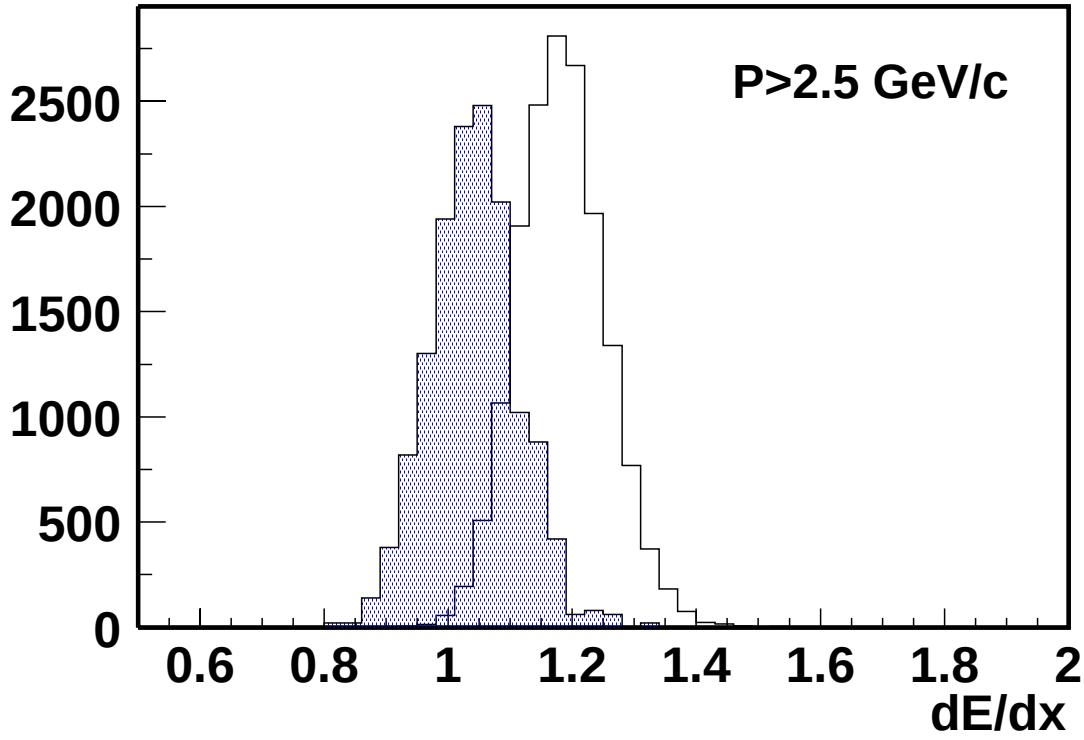

Figure 4.26: dE/dx distribution of MC. Momentum of particles are limited in $P >$ 2.5 GeV/c region. Shaded histogram is for kaon and open histogram for pion.

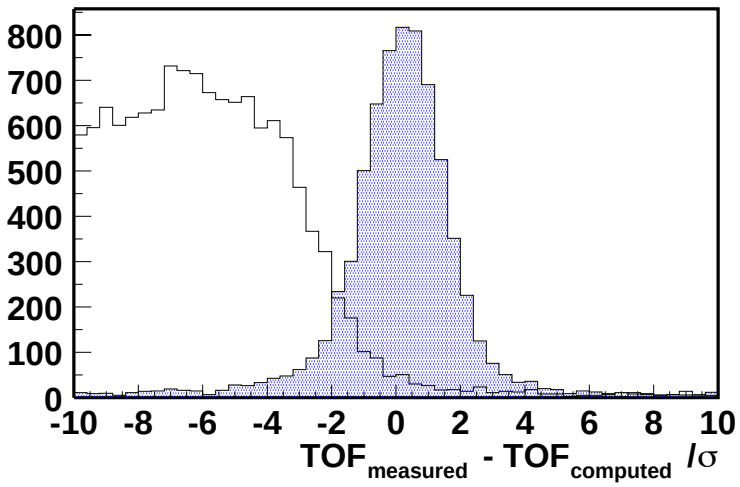

Figure 4.27: Difference between measured and computed time of flight for kaon (shaded histogram) and pion (open histogram) in MC sample. We assume a particle species as kaon. The distribution is normalized with measured error.

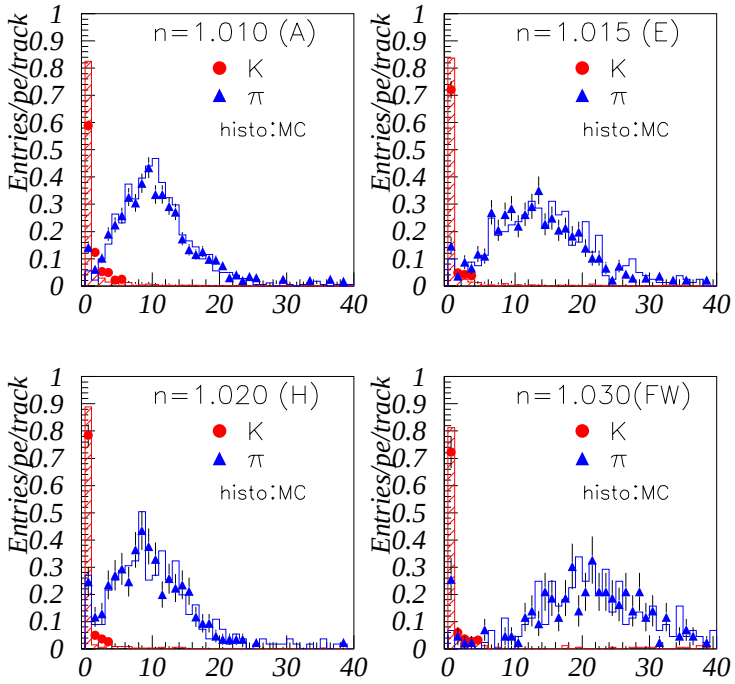

Figure 4.28: N_{pe} distributions for each refractive index region, 1.010 (upper left), 1.015 (upper right), 1.020 (lower left) and 1.030 (lower right). Data for Kaon tracks are shown as circles and pion tracks as triangles, MC expectation is shown by histograms.

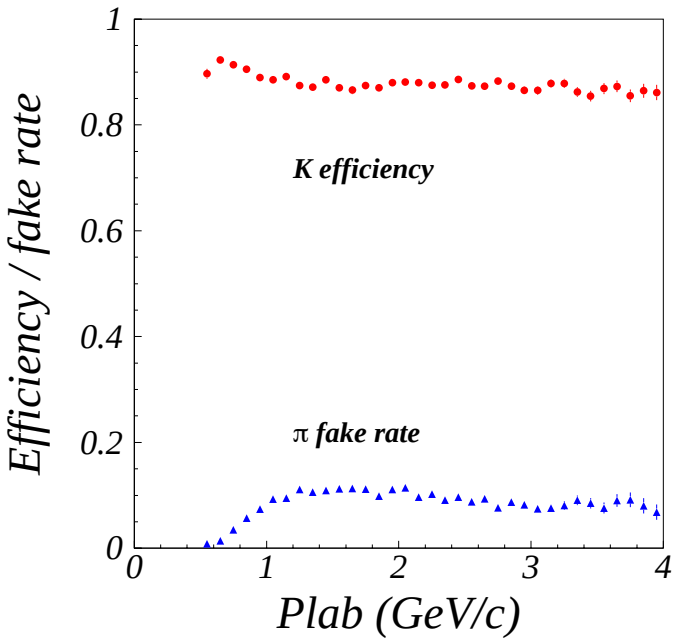

Figure 4.29: Efficiency and fake rate of likelihood as a function of particle momentum for K/π separation. Dots shows efficiency and triangles shows fake rate.

where $L_K(i)$ and $L_\pi(i)$ are the likelihood for kaon and pion, respectively, i runs over each one of dE/dx, TOF and ACC measurements. We require the $\mathcal{L}_{K/\pi}$ should be larger than 0.6 to separate kaon from pion. Performance of K/π separation is evaluated using particles from a decay chain: $D^{*\pm}(2007) \to D^0\pi^\pm$, $D^0 \to K\pi$, where the pion from $D^{*\pm}(2007)$ has small magnitude of momentum because the mass difference between $D^{*\pm}(2007)$ and $(D^0\pi^\pm)$ system is small, so that we can tag this decay chain with detection of such a slow pion and obtain kaon and pion sample which have various momentum from D^0 decay with high purity. Since the charge sign of the slow pion gives us the information of the spices of D^0 daughters. Figure 4.29 shows the efficiency and fake rate plots of the K/π separation system as a function of the track momentum in laboratory system p_{lab}. In average, efficiency is 90% for barrel part and 85% for endcap part. Overall fake rate is 8% for barrel part and 5% for endcap part.

4.4 Background suppression

One important source of background remaining after requiring the event topology and lepton identification on the signal side is radiative Bhabha events with a converted photon. Figure 4.30 shows the typical Feynman diagram of this process. This

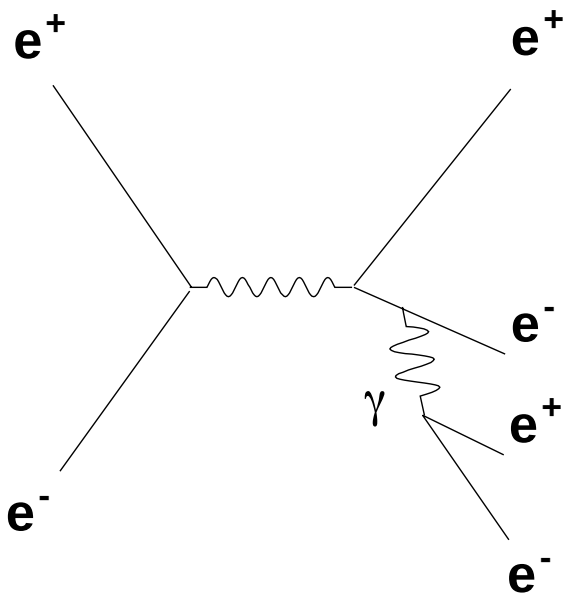

Figure 4.30: Typical Feynman diagram of radiative Bhabha process with converted photon.

background is reduced using the τ-pair event classification viii) and ix) as described previous part, but some of the events survive because the statistics of Bhabha event is enormously large. To suppress the contribution from this process to be negligible level, we require the condition for vetoing $\gamma \to e^+e^-$ process. We calculate invariant mass for all combination of two charged tracks in an event assuming the mass of the tracks to be electron,

$$M_{ee} = \sqrt{\left(\sqrt{M_e^2 + |\vec{p_i}|^2} + \sqrt{M_e^2 + |\vec{p_j}|^2}\right)^2 - |\vec{p_i} + \vec{p_j}|^2} \tag{4.4}$$

where $\vec{p_i}$ and $\vec{p_j}$ are 3-vector momentum of each track and M_e is an electron mass. We require the minimum of M_{ee} in an event should be greater than 0.2 GeV/c^2. Combination of this and τ-pair classification criteria removes Bhabha event by the factor of 10^{-7} as shown in Table

4.4.1 Bhabha and two-photon background suppression for $\tau \to \ell\ell\ell$ modes

The remaining background after removing the event which contains photon conversions mainly comes from two-photon processes, τ-pair events with generic decays into three charged hadrons, $e^+e^- \to q\bar{q}$ continuum and $B\bar{B}$ events. Those processes appeared as a background for this analysis, due to failure of lepton identification on

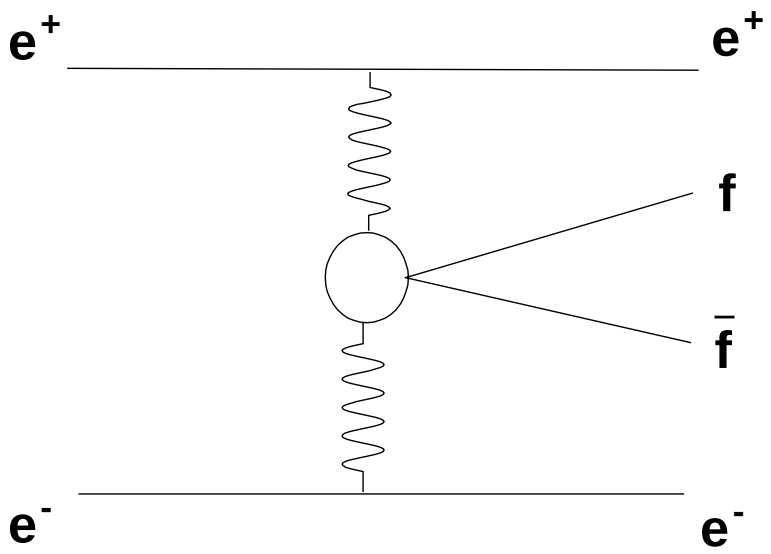

Figure 4.31: Feynman diagrams of two-photon process. f and $\bar{f}$ represent for one of the fermion and its anti-particle, respectively.

the signal side. Figure 4.31 shows the Feynman diagram of two-photon process. Because each track coming from two-photon process has small transverse momentum, we require tighter condition on transverse momentum: transverse component of the sum of momentum vectors for the four charged tracks in the CMS $p^*_{\rm T}$ to be larger than 0.4 GeV/c. In signal τ-pair events, there is a missing momentum due to neutrino emission from τ on the tag side. In Bhabha and two-photon processes, tracks tends to travel along the beam pipe. Because no detector is placed near the beam pipe, the particles that fly nearby the beam pipe are missed. To distinguish this two kinds of "missing particles", we require that the direction of missing momentum should be in the detector acceptance. We calculate the missing momentum subtracting the momentum of all charged tracks and photons from the beam momentum. The polar angle of the missing momentum in the laboratory frame $\theta_{\rm miss}$, must be in the range between 25° and 140°. In the τ LFV event, the missing momentum due to neutrinos from the τ on the tag side tends to lie in the tag side if it is a signal events, while neutrinos are emitted in both sides for generic τ-pair event. The opening angle between the 1-prong track and missing momentum in the CMS, $\theta^*_{\rm 1p-miss}$, is required to be less than 90°. Because the tag side τ decays with neutral particle(s) emission, the momentum of the 1-prong track is much smaller than the τ momentum. The momentum of the 1-prong tag side track, $p^*_{\rm 1p}$, must be less than 3 GeV/c. Figure 4.32-4.35 show the distribution of variables used in this selection step for a part of experimental data and signal MC. Background MC distributions which are

normalized to experimental data using integrated luminosity is also plotted to show which background is contributed for. As shown in these plots, most of the Bhabha and μ-pair backgrounds are rejected and a large fraction of two-photon background is suppressed after this selection. After all these requirements, the background is reduced by a factor of order 10^4, keeping an efficiency for the signal to 10%. The numerical change of each MC sample and experimental data for each selection step is summarized in Table 4.5 and 4.6.

4.4.2 Continuum background suppression for $\tau \to \ell hh$ modes

For these modes, the risk to take in $q\bar{q}$ continuum process as a signal is larger than $\tau \to \ell\ell\ell$ modes because we require that two hadrons are in the signal side. We suppress $q\bar{q}$ process with limiting the decay modes of the tag side, leptonic decays $\tau \to \ell\nu_\ell\nu_\tau$ and 1-prong pionic decay, $\tau \to \pi\nu_\tau$. To collect leptonic decay modes, we require that the $\mathcal{L}_e$ and $\mathcal{L}_\mu$ for the tag side track should be larger than 0.9 and number of photon in the tag side is less than equal to 1 to veto large number of π^0 in background. For pionic decay modes, we require that the $\mathcal{L}_e$, $\mathcal{L}_\mu$ and $\mathcal{L}_{K/\pi}$ should be smaller than 0.1, respectively. The number of photon in the tag side is limited using the same condition as leptonic decay modes.
In $q\bar{q}$ continuum process, quark-pair is created at beam interaction point and form mesons at the same point. On the other hand in τ-pair events, τ leptons fly significant direction and decay into other particles because τ lepton has lifetime. We measure flight length between beam interaction points and signal side τ vertex points to distinguish $q\bar{q}$ continuum process from τ-pair events. The position of beam interaction point depends on beam condition so that they are not significantly differ among nearby the events. We find the beam interaction point from hadronic events which happen close time of the τ-pair event. The signal side τ vertex point is found from computing the closest point of three charged tracks in the signal side.
$q\bar{q}$ continuum events is distinguishable from τ-pair events by use of the shape variables because τ-pair events have narrower jet-like shape than $q\bar{q}$ continuum events. For the shape variable selection, we use the normalized second Fox-Wolfram moment $R2$ [61]. The n-th order Fox-Wolfram moment H_n and the $R2$ is defined

$$\begin{aligned} H_n &= \Sigma_{i,j}|p_i||p_j|P_n(cos\theta_{ij}), \\ R2 &= H_2/H_0, \end{aligned} \tag{4.5}$$

where i and j runs over for all combination of charged tracks in event. P_n is the n-th order Legendre polynomial, p_i and p_j is the momentum of particles and θ_{ij} is opening angle between particle i and j. Figure 4.36 and 4.37 show the flight length vs. $R2$ distribution for τ-pair and uds continuum events, respectively. We make 2-dimensional PDF in this plane and compute likelihood for continuum veto to each event. The likelihood distribution for LFV τ decay signal and uds continuum events is shown in Figure 4.38. We can reduce 60% of $q\bar{q}$ continuum saving 90% of signal events after requiring this selection criteria. After requiring all selection criteria described in this part, background from $q\bar{q}$ continuum process is reduced by the factor of 10^{-5}.

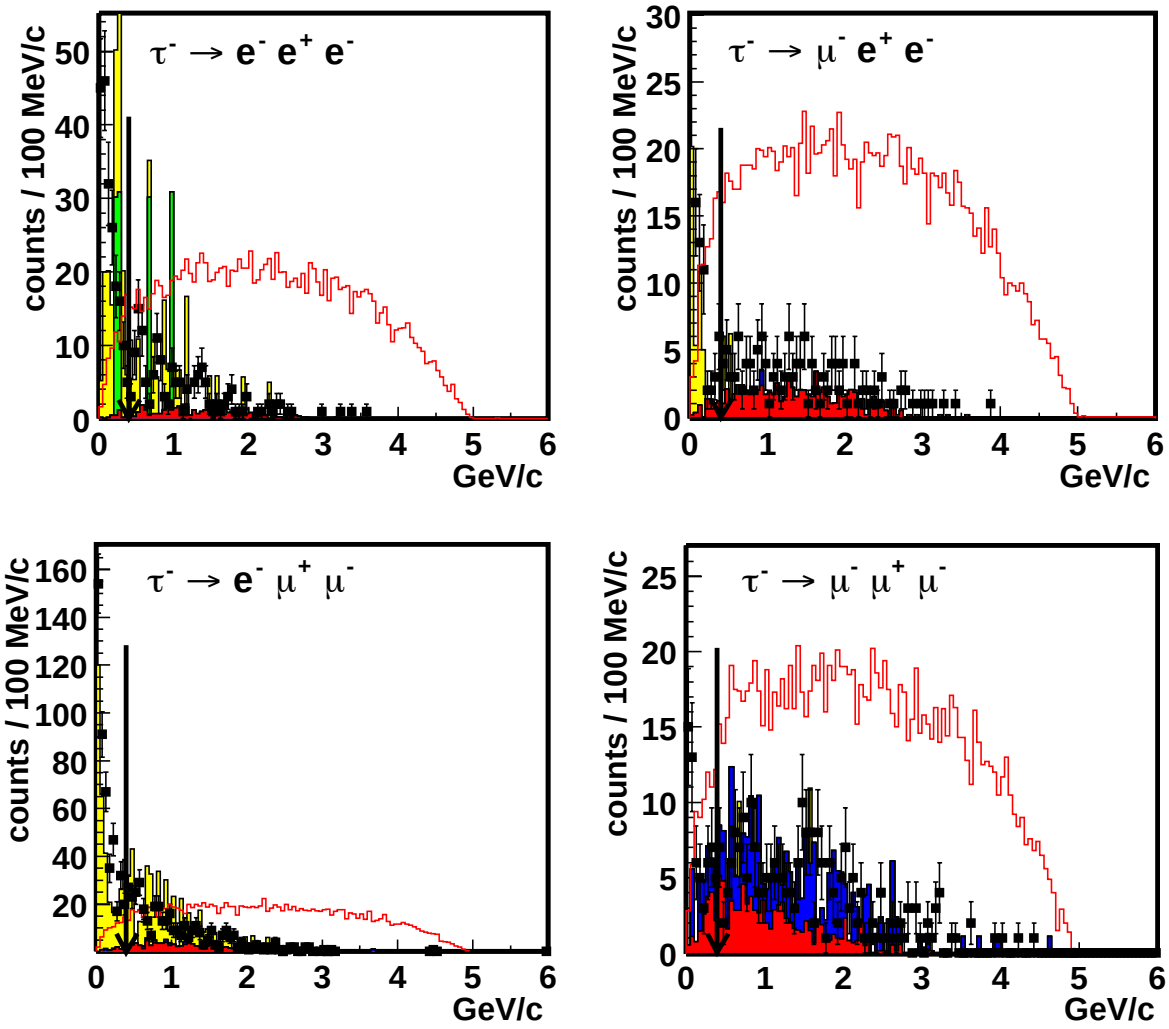

Figure 4.32: $p^*_{\rm T}$ distributions for $\tau^- \to e^-e^+e^-$ (top left), $\tau^- \to e^-e^+\mu^-$ (top right) $\tau^- \to e^-\mu^+\mu^-$ (bottom left) and $\tau^- \to \mu^-\mu^+\mu^-$ (bottom right) after lepton identification for 100k signal MC (open histogram), experimental data (dots) and MC (filled histogram), respectively. The color of MC histogram represent for its kind of the events: red is hadronic, blue is τ-pair, green is Bhabha and yellow is two-photon events and the number of each of MC is normalized with integrated luminosity of experimental data.

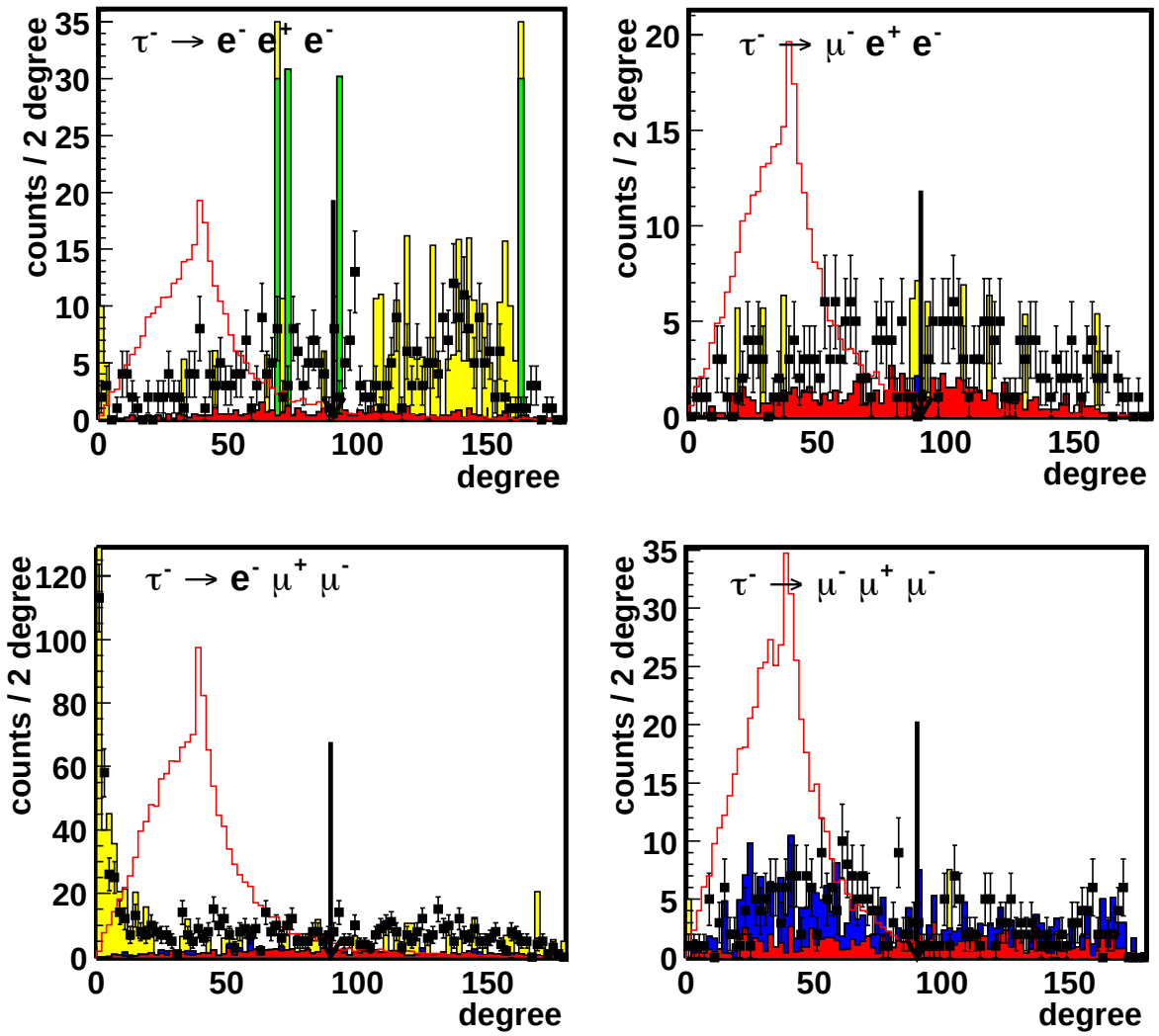

Figure 4.33: $\theta^*_{\mathrm{1p-miss}}$ distributions for $\tau^- \to e^-e^+e^-$ (top left), $\tau^- \to e^-e^+\mu^-$ (top right) $\tau^- \to e^-\mu^+\mu^-$ (bottom left) and $\tau^- \to \mu^-\mu^+\mu^-$ (bottom right) after lepton identification for 100k signal MC (open histogram), experimental data (dots) and MC (filled histogram), respectively. The color of MC histogram represent for its kind of the events: red is hadronic, blue is τ-pair, green is Bhabha and yellow is two-photon events and the number of each of MC is normalized with integrated luminosity of experimental data.

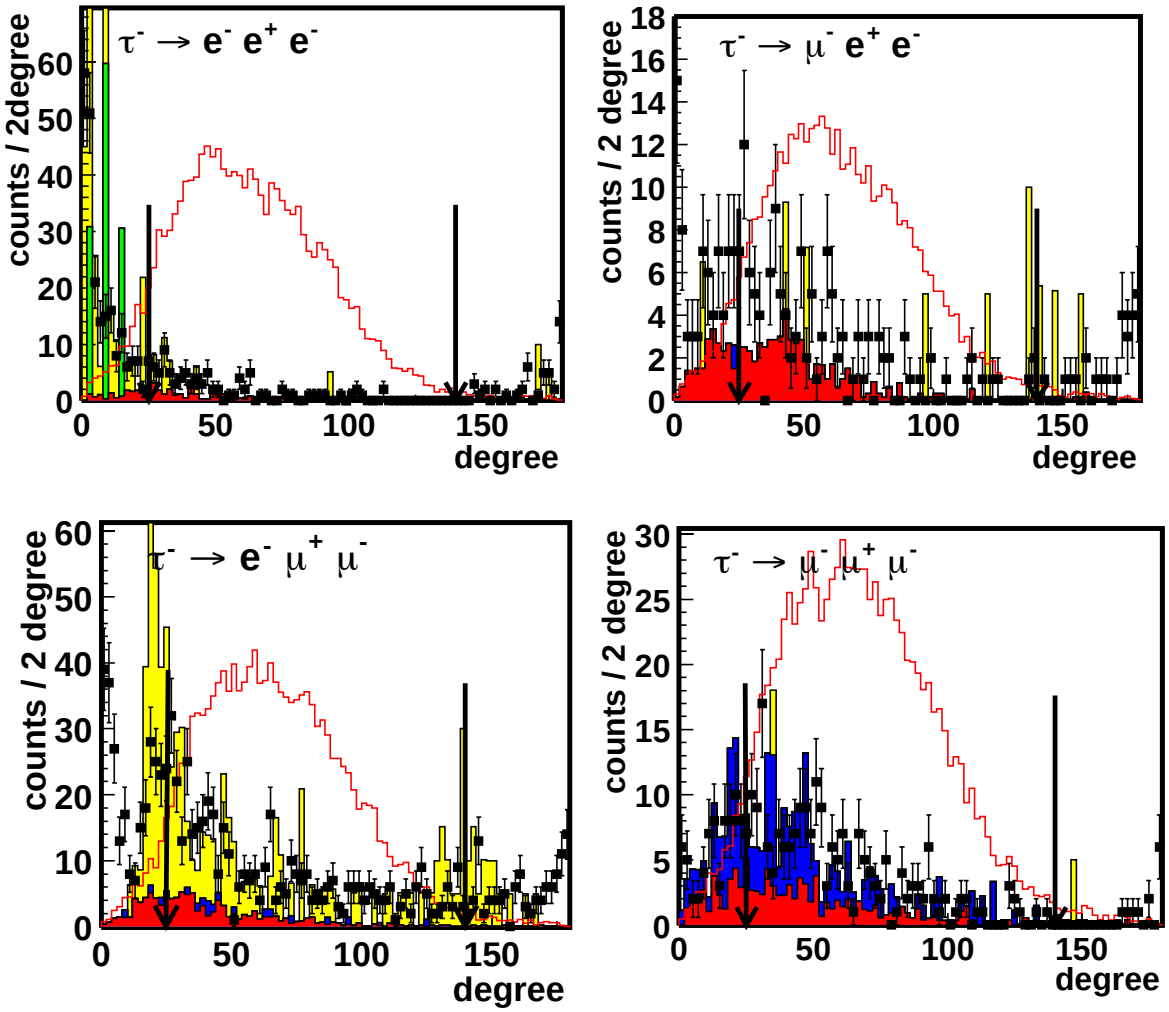

Figure 4.34: $\theta_{\rm miss}$ distributions for $\tau^- \to e^-e^+e^-$ (top left), $\tau^- \to e^-e^+\mu^-$ (top right) $\tau^- \to e^-\mu^+\mu^-$ (bottom left) and $\tau^- \to \mu^-\mu^+\mu^-$ (bottom right) after lepton identification for 100k signal MC (open histogram), experimental data (dots) and MC (filled histogram), respectively. The color of MC histogram represent for its kind of the events: red is hadronic, blue is τ-pair, green is Bhabha and yellow is two-photon events and the number of each of MC is normalized with integrated luminosity of experimental data.

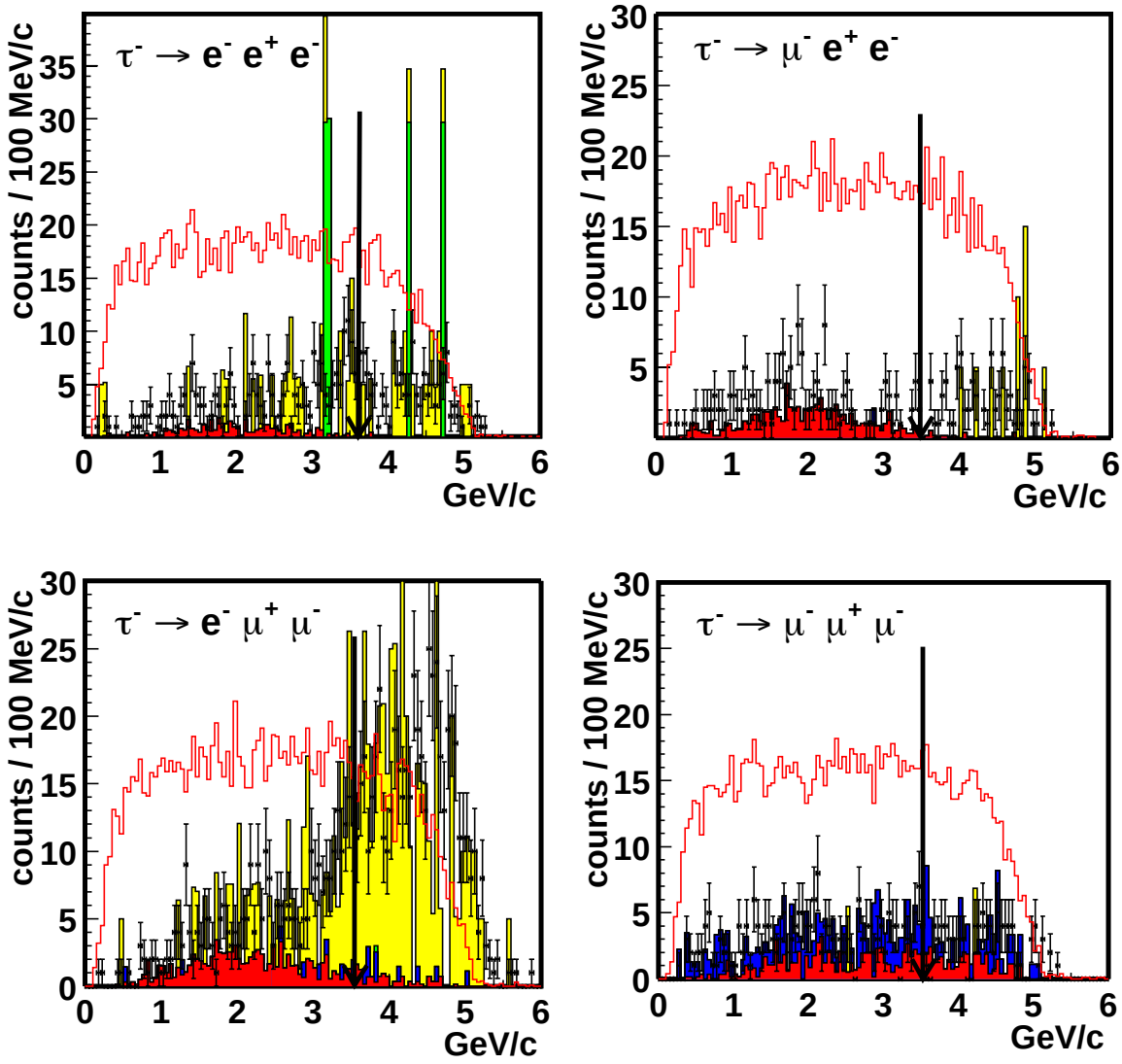

Figure 4.35: $p^*_{\rm lp}$ distributions for $\tau^- \to e^-e^+e^-$ (top left), $\tau^- \to e^-e^+\mu^-$ (top right) $\tau^- \to e^-\mu^+\mu^-$ (bottom left) and $\tau^- \to \mu^-\mu^+\mu^-$ (bottom right) after lepton identification for 100k signal MC (open histogram), experimental data (dots) and MC (filled histogram), respectively. The color of MC histogram represent for its kind of the events: red is hadronic, blue is τ-pair, green is Bhabha and yellow is two-photon events and the number of each of MC is normalized with integrated luminosity of experimental data.

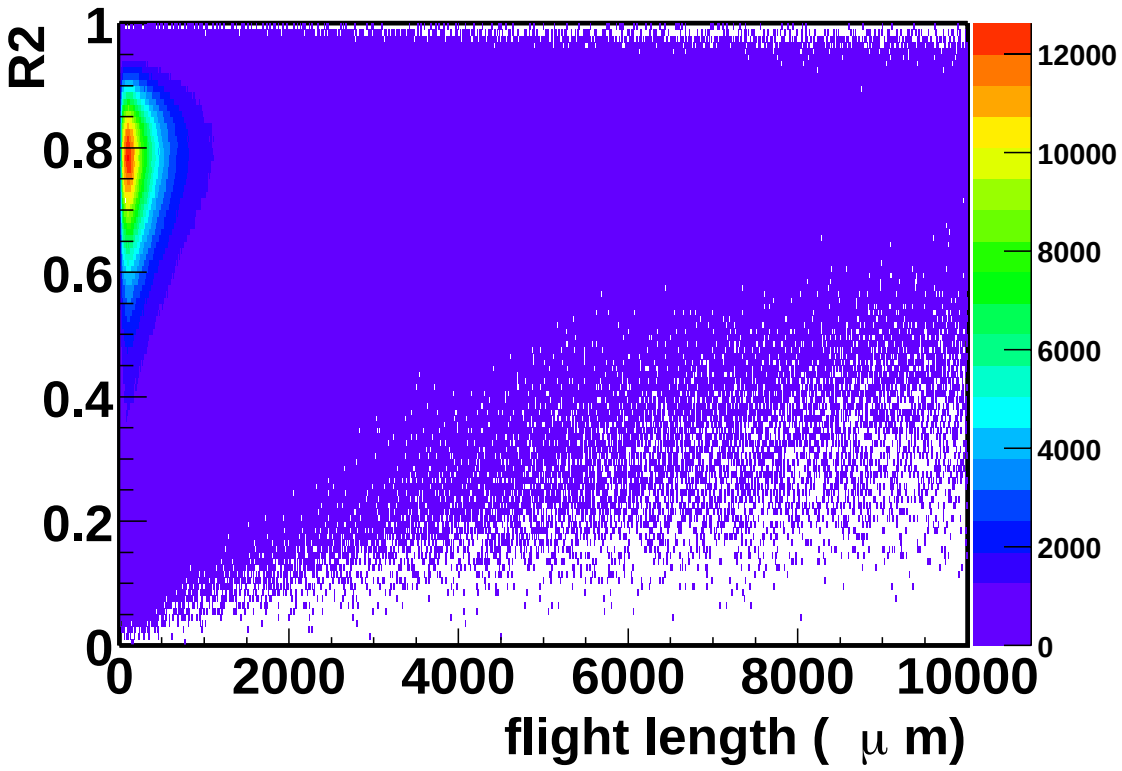

Figure 4.36: Flight length vs. $R2$ distribution for τ-pair MC events.

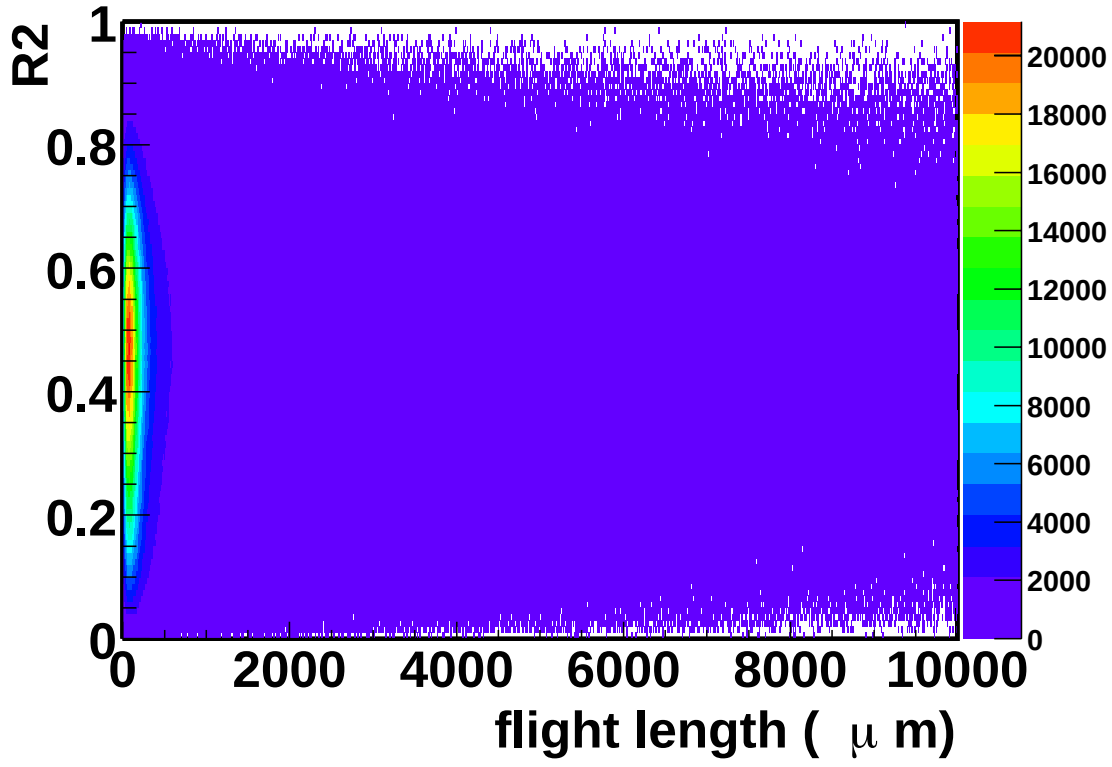

Figure 4.37: Flight length vs. $R2$ distribution for *uds* continuum MC events.

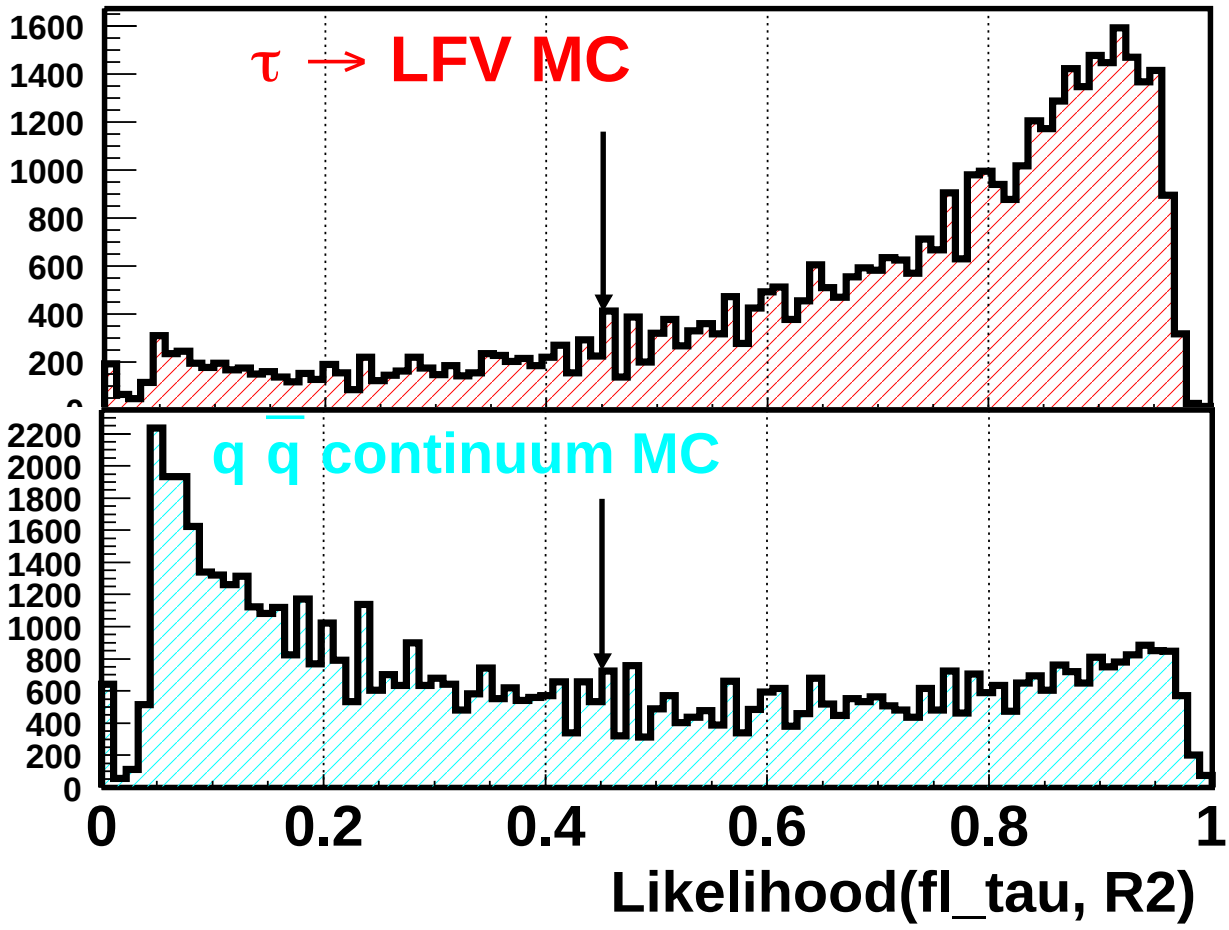

Figure 4.38: The likelihood for continuum veto distribution for LFV τ-pair (top) and *uds* continuum (bottom) MC events, respectively. Arrows indicates selection criteria.

4.5 τ reconstruction

In τ of LFV decay, Mother τ is reconstructed from the three charged tracks in the signal side. The energy E^*_{rec}, momentum $\vec{p^*_{rec}}$ and invariant mass M_{rec} of the reconstructed τ are calculated as

$$\begin{aligned} E^*_{rec} &= \sqrt{M_i^2 + |\vec{p_i}|^2} + \sqrt{M_j^2 + |\vec{p_j}|^2} + \sqrt{M_k^2 + |\vec{p_k}|^2}, \\ \vec{p^*_{rec}} &= \vec{p_i} + \vec{p_j} + \vec{p_k}, \\ M_{rec} &= \sqrt{E^{*2}_{rec} - |\vec{p^*_{rec}}|^2}, \end{aligned} \tag{4.6}$$

where $\vec{p_i}$, $\vec{p_j}$ and $\vec{p_k}$ are measured 3-momentum vectors for 3-prong side particle i, j and k, respectively. M_i, M_j and M_k are given invariant mass of 3-prong side particle from PDG [18] assuming the particle species from the results of particle identification. All quantities are calculated in e^+e^- CMS. From these, we compute following quantities:

$$\begin{aligned} \Delta E^* &\equiv E^*_{rec} - E^*_{\rm beam}, \\ \Delta M &\equiv M_{rec} - M_\tau, \end{aligned} \tag{4.7}$$

where $E^*_{\rm beam}$ is the CMS beam energy and M_τ is the τ mass. In the ΔE^*-ΔM plane, the neutrinoless τ decay events are expected to be distributed close to the origin. The ΔE^* and ΔM expectations based on signal MC for each decay mode are shown in Figure 4.39−4.46. It is seen that each peak in signal MC distribution has a tail on the lower side. Main reasons for the tail is an initial state radiation and bremsstrahlung of a charged particle interacting with the detector material. Because photon radiation probability of electron is much larger than muon, the shape of the peak depends on decay mode. The signal region for each decay mode is given in Table 4.4, and is illustrated as the region between two dashed lines in Figure 4.39−4.46. Signal regions for ΔE^* and ΔM are defined to contain 90% of the signal MC events as plotted in the figures.

4.6 Signal detection efficiency

Efficiencies ϵ for $\tau \to$ LFV decays with a uniform τ decay angle distribution are varied from signal MC after applying all selections as same as experimental data analysis. They are from 9.2% to 9.5% for $\tau \to \ell\ell\ell$ modes and from 6.9% to 3.7% for $\tau \to \ell hh$ modes. They are listed in the second column of Table 4.9.

We test the track finding efficiency using the method called "partial reconstruction technique" which extracts the track finding efficiency using partially reconstructed decays. The efficiency is identified with the finding rate of the track which is not used for reconstruction. In our case, track finding efficiency is measured using partial decays of the D^* meson: $D^* \to \pi D^0, D^0 \to \pi^+\pi^- K^0_S$ and $K^0_S \to \pi^+\pi^-$. For reconstruction of D^*, one of the pion from the K^0_S is not used. The long lifetime of the K^0_S allows to determine its direction of flight using the decay vertex points of K^0_S and

Table 4.4: Definition of the signal regions for each decay mode.

Mode	ΔE^* (GeV)	ΔM (GeV/c^2)
$\tau^- \to e^-e^+e^-$	$-0.36 < \Delta E^* < 0.04$	$-0.032 < \Delta M < 0.010$
$\tau^- \to e^-\mu^+\mu^-$	$-0.32 < \Delta E^* < 0.03$	$-0.017 < \Delta M < 0.010$
$\tau^- \to e^+\mu^-\mu^-$	$-0.32 < \Delta E^* < 0.03$	$-0.017 < \Delta M < 0.010$
$\tau^- \to \mu^-e^-e^+$	$-0.33 < \Delta E^* < 0.04$	$-0.025 < \Delta M < 0.010$
$\tau^- \to \mu^+e^-e^-$	$-0.33 < \Delta E^* < 0.04$	$-0.025 < \Delta M < 0.010$
$\tau^- \to \mu^-\mu^+\mu^-$	$-0.28 < \Delta E^* < 0.03$	$-0.010 < \Delta M < 0.010$
$\tau^- \to e^-\pi^+\pi^-$	$-0.33 < \Delta E^* < 0.04$	$-0.023 < \Delta M < 0.012$
$\tau^- \to e^+\pi^-\pi^-$	$-0.31 < \Delta E^* < 0.04$	$-0.018 < \Delta M < 0.012$
$\tau^- \to \mu^-\pi^+\pi^-$	$-0.31 < \Delta E^* < 0.03$	$-0.012 < \Delta M < 0.011$
$\tau^- \to \mu^+\pi^-\pi^-$	$-0.29 < \Delta E^* < 0.04$	$-0.012 < \Delta M < 0.011$
$\tau^- \to e^-\pi^+K^-$	$-0.35 < \Delta E^* < 0.04$	$-0.018 < \Delta M < 0.010$
$\tau^- \to e^-\pi^-K^+$	$-0.33 < \Delta E^* < 0.04$	$-0.017 < \Delta M < 0.011$
$\tau^- \to e^+\pi^-K^-$	$-0.33 < \Delta E^* < 0.04$	$-0.016 < \Delta M < 0.011$
$\tau^- \to e^-K^+K^-$	$-0.36 < \Delta E^* < 0.04$	$-0.014 < \Delta M < 0.009$
$\tau^- \to e^+K^-K^-$	$-0.35 < \Delta E^* < 0.04$	$-0.014 < \Delta M < 0.009$
$\tau^- \to \mu^-\pi^+K^-$	$-0.33 < \Delta E^* < 0.03$	$-0.010 < \Delta M < 0.009$
$\tau^- \to \mu^-\pi^-K^+$	$-0.32 < \Delta E^* < 0.03$	$-0.011 < \Delta M < 0.010$
$\tau^- \to \mu^+\pi^-K^-$	$-0.32 < \Delta E^* < 0.04$	$-0.010 < \Delta M < 0.010$
$\tau^- \to \mu^-K^+K^-$	$-0.34 < \Delta E^* < 0.03$	$-0.008 < \Delta M < 0.008$
$\tau^- \to \mu^+K^+K^-$	$-0.34 < \Delta E^* < 0.03$	$-0.008 < \Delta M < 0.008$

Table 4.5: Number of total event of $\tau \to \ell\ell\ell$ modes after each selection step for experimental data and background MC listed in Table 4.1.

	$B\bar{B}$	uds	$c\bar{c}$	generic $\tau^+\tau-$	Exp. data
Lepton identification	4336	790	650	23975	162834
$M(e^+e^-) < 0.2$ GeV/c	4060	343	414	2583	13447
N_γ	2973	194	244	2480	12249
$p^*_T > 2.0$ GeV/c	2363	172	196	2172	9977
$p^*_{1p} > 3.0$ GeV/c	2363	144	190	1720	4969
$25^\circ < \theta_{miss} < 140^\circ$	1996	99	137	1436	3496
$\vartheta^*_{1p-\mathrm{miss}} < 90^\circ$	1373	75	77	1237	2594
ΔE^*	5	10	0	71	114
ΔM	0	0	0	0	1

	Bhabha	mu-pair	$eeee$	$ee\mu\mu$	$eeuu$	$eess$	$eecc$
Lepton identification	537	3398	224	395	23	3	9
$M(e^+e^-) < 0.2$ GeV/c	2	1	50	303	4	0	4
N_γ	2	1	50	303	4	0	3
$p^*_T > 2.0$ GeV/c	1	1	17	271	2	0	2
$p^*_{1p} < 3.0$ GeV/c	0	0	5	107	0	0	0
$25^\circ < \theta_{miss} < 140^\circ$	0	0	1	66	0	0	0
$\vartheta^*_{1p-\mathrm{miss}} < 90^\circ$	0	0	1	56	0	0	0
ΔE^*	0	0	0	1	0	0	0
ΔM	0	0	0	0	0	0	0

Table 4.6: Number of event after each selection step for $\tau \to \ell\ell\ell$ mode for 100000 signal MC.

Mode	$e^-e^+e^-$	$e^-e^+\mu^-$	$e^-e^-\mu^+$	$e^-\mu^+\mu^-$	$e^+\mu^-\mu^-$	$\mu^-\mu^+\mu^-$
Lepton identification	14983	14618	14712	13652	13750	12961
$M(e^+e^-) < 0.2$ GeV/c	14211	13893	14051	13069	13116	12365
N_γ	14183	13881	14025	13065	13111	12365
$p^*_T > 2.0$ GeV/c	13770	13506	13646	12765	12794	12084
$p^*_{1p} < 3.0$ GeV/c	11489	11338	11430	10731	10758	10088
$25^\circ < \theta_{miss} < 140^\circ$	11067	10949	11019	10406	10404	9764
$\vartheta^*_{1p-\mathrm{miss}} < 90^\circ$	10937	10767	10861	10226	10264	9650
ΔE^*	8954	9132	9125	8760	8764	8469
ΔM	7970	8189	8178	7976	8009	7751

Table 4.7: Number of total event of $\tau \to \ell hh$ modes after each selection step for experimental data and background MC listed in Table 4.1.

	BB	uds	$c\bar{c}$	generic $\tau^+\tau-$	Exp. data
Particle identification	735971	543790	336279	515464	4053370
$M(e^+e^-) < 0.2$ GeV/c	689540	479862	298720	424528	3437120
N_γ	5084	75675	15394	157937	283347
$q\bar{q}$ continuum veto	35	2224	217	84049	90944
ΔE^*	5	839	44	23418	25086
ΔM	0	11	0	29	93

	Bhabha	mu-pair	$eeee$	$ee\mu\mu$	$eeuu$	$eess$	$eecc$
Particle identification	83	56	24	5	1314	135	441
$M(e^+e^-) < 0.2$ GeV/c	0	0	5	3	1162	111	385
N_γ	0	0	5	3	906	90	232
$q\bar{q}$ continuum veto	0	0	4	3	219	48	19
ΔE^*	0	0	0	0	23	4	0
ΔM	0	0	0	0	0	0	0

Table 4.8: Number of event after each selection step for $\tau \to \ell hh$ mode for 100000 signal MC.

Mode	$e^-\pi^+\pi^-$	$e^+\pi^-\pi^-$	$\mu^-\pi^+\pi^-$	$\mu^+\pi^-\pi^-$
Particle identification	16334	16431	14064	13669
$M(e^+e^-) < 0.2$ GeV/c	15564	15567	13399	13069
N_γ	15200	15193	13144	12817
$q\bar{q}$ continuum veto	7525	7631	6540	6436
ΔE^*	6410	6548	5664	5626
ΔM	5830	5913	5146	5070

Mode	$e^-\pi^+K^-$	$e^-\pi^-K^+$	$e^+\pi^-K^-$	$\mu^-\pi^+K^-$	$\mu^-\pi^-K^-$	$\mu^+\pi^-K^-$
Particle identification	12634	12766	12730	10421	10751	11083
$M(e^+e^-) < 0.2$ GeV/c	11735	11873	11792	9676	10028	10300
N_γ	11462	11639	11516	9474	9856	10100
$q\bar{q}$ continuum veto	5964	6094	5938	5026	5125	5236
ΔE^*	5015	5173	4987	4309	4375	4525
ΔM	4558	4690	4530	3891	3998	4127

Mode	$e^-K^+K^-$	$e^+K^-K^-$	$\mu^-K^+K^-$	$\mu^+K^-K^-$
Particle identification	10269	10338	8654	8768
$M(e^+e^-) < 0.2$ GeV/c	9106	9155	7638	7811
N_γ	8918	8952	7506	7684
$q\bar{q}$ continuum veto	4739	4729	4043	4128
ΔE^*	3944	3976	3438	3496
ΔM	3581	3606	3155	3198

Table 4.9: Signal detection efficiency for each decay mode.

Mode	signal detection efficiency ϵ
$\tau^- \to e^- e^+ e^-$	9.2
$\tau^- \to e^- \mu^+ \mu^-$	9.2
$\tau^- \to e^+ \mu^- \mu^-$	9.2
$\tau^- \to \mu^- e^- e^+$	9.4
$\tau^- \to \mu^+ e^- e^-$	9.5
$\tau^- \to \mu^- \mu^+ \mu^-$	9.0
$\tau^- \to e^- \pi^+ \pi^-$	6.8
$\tau^- \to e^+ \pi^- \pi^-$	6.9
$\tau^- \to \mu^- \pi^+ \pi^-$	5.3
$\tau^- \to \mu^+ \pi^- \pi^-$	5.5
$\tau^- \to e^- \pi^+ K^-$	5.3
$\tau^- \to e^- \pi^- K^+$	4.2
$\tau^- \to e^+ \pi^- K^-$	4.2
$\tau^- \to e^- K^+ K^-$	6.0
$\tau^- \to e^+ K^- K^-$	5.9
$\tau^- \to \mu^- \pi^+ K^-$	4.6
$\tau^- \to \mu^- \pi^- K^+$	4.7
$\tau^- \to \mu^+ \pi^- K^-$	4.8
$\tau^- \to \mu^- K^+ K^-$	3.7
$\tau^- \to \mu^+ K^+ K^-$	3.7

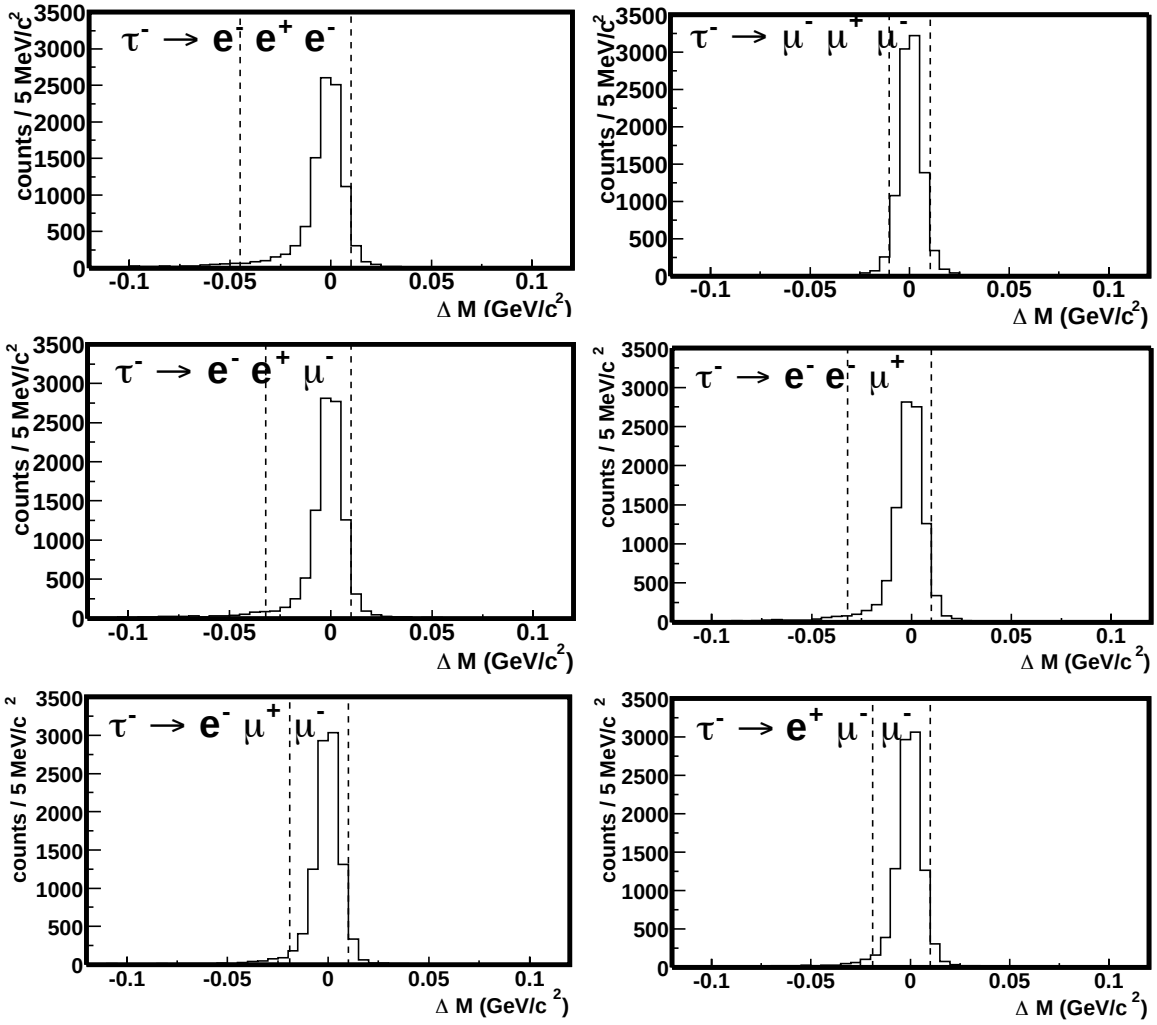

Figure 4.39: ΔE^* distributions after all selection criteria described until Section 4.4 for 100000 $\tau \to \ell\ell\ell$ signal MC sample. Dashed lines shows the boundary of signal region.

D^0. Practically, we use this direction, the D^0 and the K^0_S masses to determine the momentum of the K^0_S daughter pion which is not used for reconstruction. Thus we can reconstruct the momentum of the pion track $p_{\rm recovered}$ and D^* mass distribution and extract the signal yield from fit for the signal and background function for the distribution. We also try to find the pion track which is the companion of daughter pion of K^0_S from the charged track table requiring correct charge and to be closest in momentum space to $p_{\rm recovered}$. K^0_S vertex and all masses are calculated again using the momentum of found track. If the masses are in the correct region, we consider that the track is found. The track finding efficiency $\eta_{\rm found}$ is the ratio between the yield of the signal event which we can find the companion pion track and the total number of signal yield. The efficiency $\eta_{\rm found}$ should be called "total pion finding

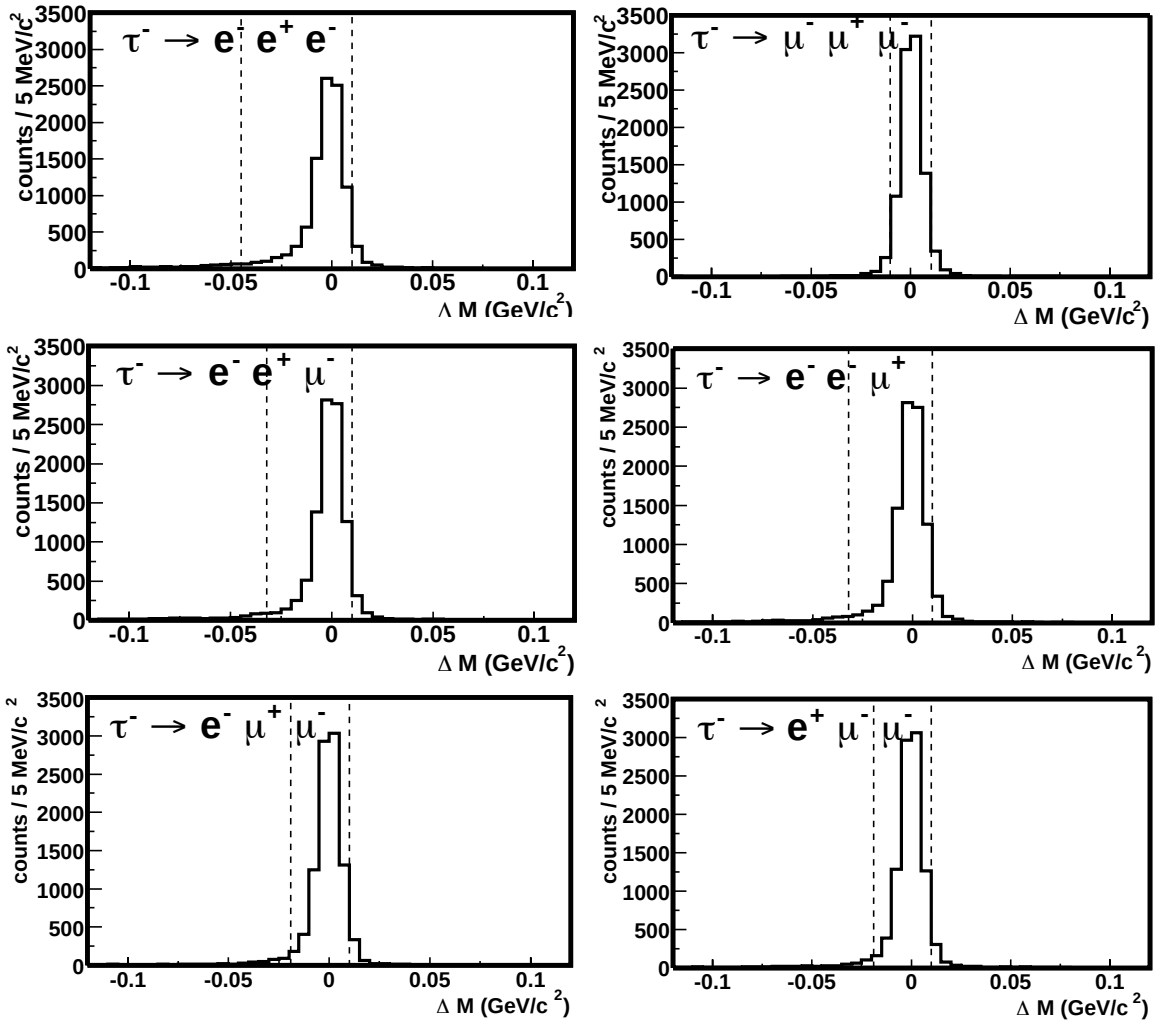

Figure 4.40: ΔM distributions after all selection criteria described until Section 4.4 for 100000 $\tau \to \ell\ell\ell$ signal MC sample. Dashed lines shows the boundary of signal region.

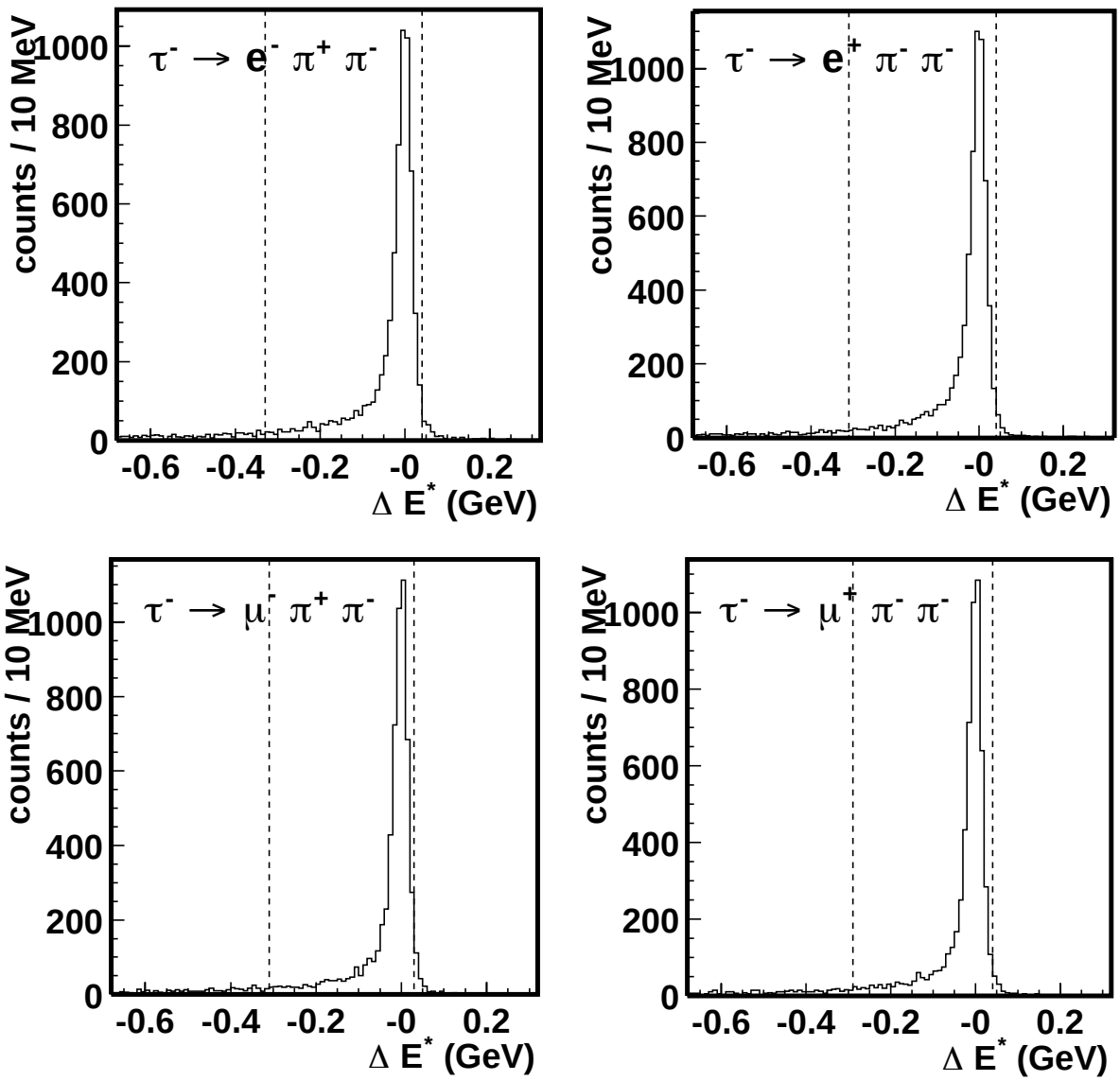

Figure 4.41: ΔE^* distributions after all selection criteria described until Section 4.4 for 100000 $\tau \to \ell\pi\pi$ signal MC sample. Dashed lines shows the boundary of signal region.

efficiency". It is the product of the track finding efficiency $\eta_{\rm track}$ and the efficiency of the selection criteria for masses which is calculated from the momentum of found track $\eta_{\rm sel}$. The $\eta_{\rm sel}$ is due to the width of the mass distribution and thus related the tracking resolution and estimated to be 94% in signal MC events which all tracks are reconstructed. The difference between the track finding efficiency in data and MC full simulation is calculated:

$$r_{\rm tracking} = \frac{\eta_{\rm track}^{\rm Data}}{\eta_{\rm track}^{\rm MC}} - 1 = \frac{\eta_{\rm found}^{\rm Data}}{\eta_{\rm found}^{\rm MC}} / \frac{\eta_{\rm sel}^{\rm Data}}{\eta_{\rm sel}^{\rm MC}} - 1. \tag{4.8}$$

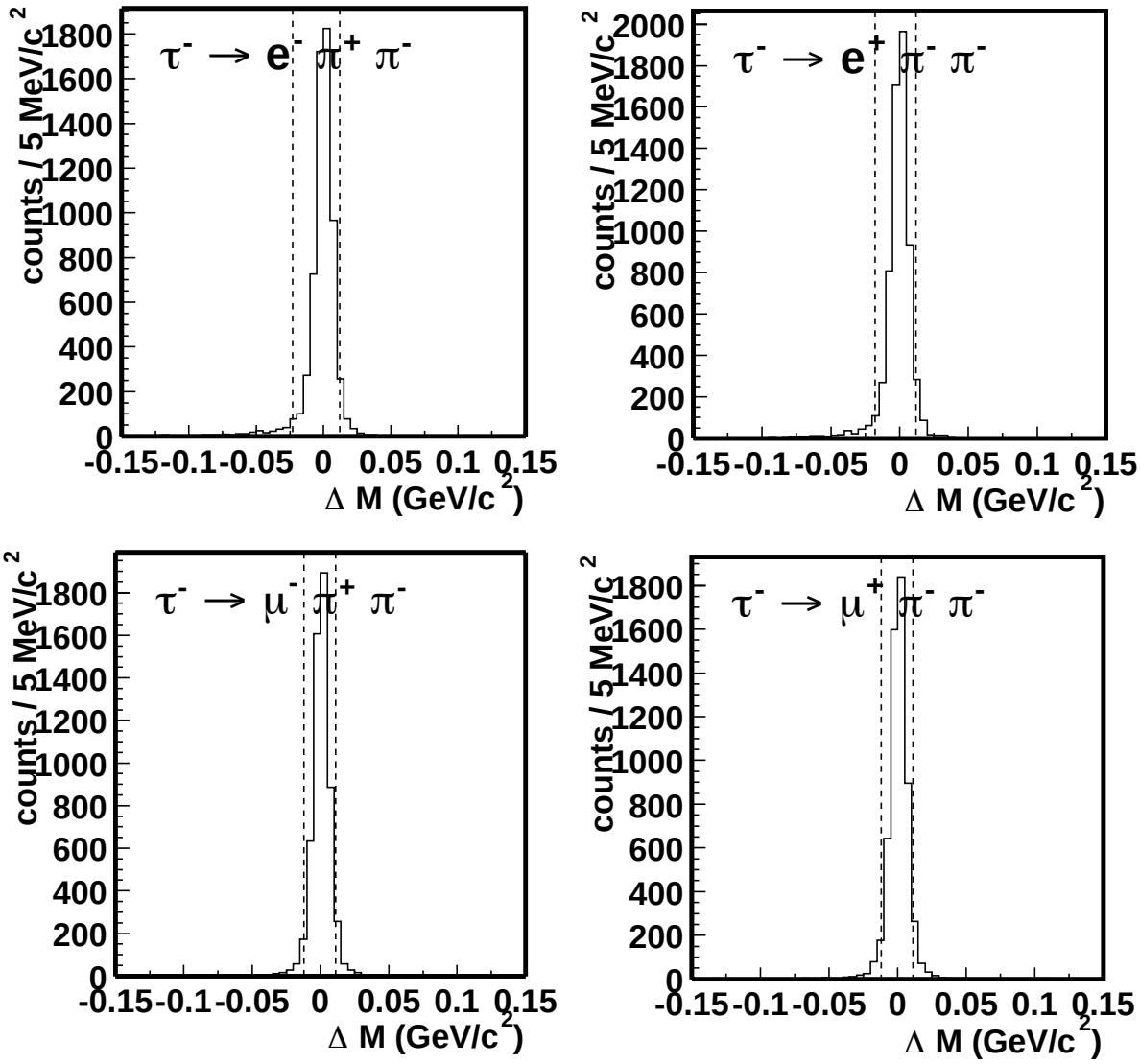

Figure 4.42: ΔM distributions after all selection criteria described until Section 4.4 for 100000 $\tau \to \ell\pi\pi$ signal MC sample. Dashed lines shows the boundary of signal region.

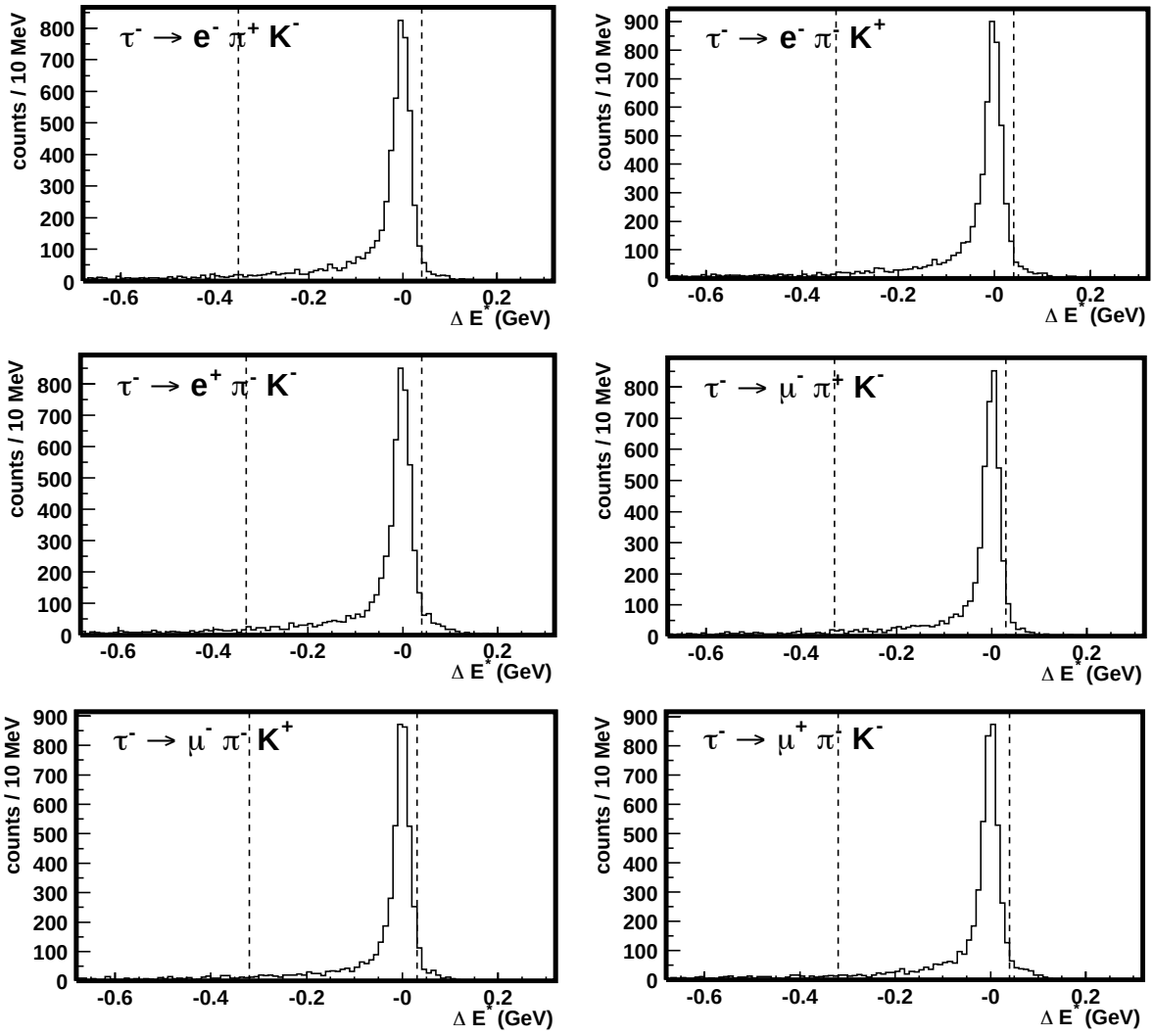

Figure 4.43: ΔE^* distributions after all selection criteria described until Section 4.4 for 100000 $\tau \to \ell\pi K$ signal MC sample. Dashed lines shows the boundary of signal region.

As we have no direct way of measuring the $\eta_{\rm sel}^{\rm Data}$, we assume that it is equal to $\eta_{\rm sel}^{\rm MC}$ and compute a systematic error on $r_{\rm tracking}$ from this assumption. For pion tracks which has a momentum above 250 MeV/c, $r_{\rm track} - 1 = (-0.27 \pm 0.95 \pm 0.20)\%$ which is clearly compatible with 0. Therefore, the signal detection efficiency for $\tau \to$ LFV decay ϵ needs no correction from effect of tracking and assign a systematic error of 1% for each track taking a quadratic sum of a statistical error and systematic error on $r_{\rm tracking}$.

The uncertainty for particle identifications are also non-negligible components on the systematic error. For lepton identifications, systematic errors are obtained from the comparison between the efficiency for embedded MC lepton tracks in experimental data and lepton tracks in two-photon event data. Because the efficiency and

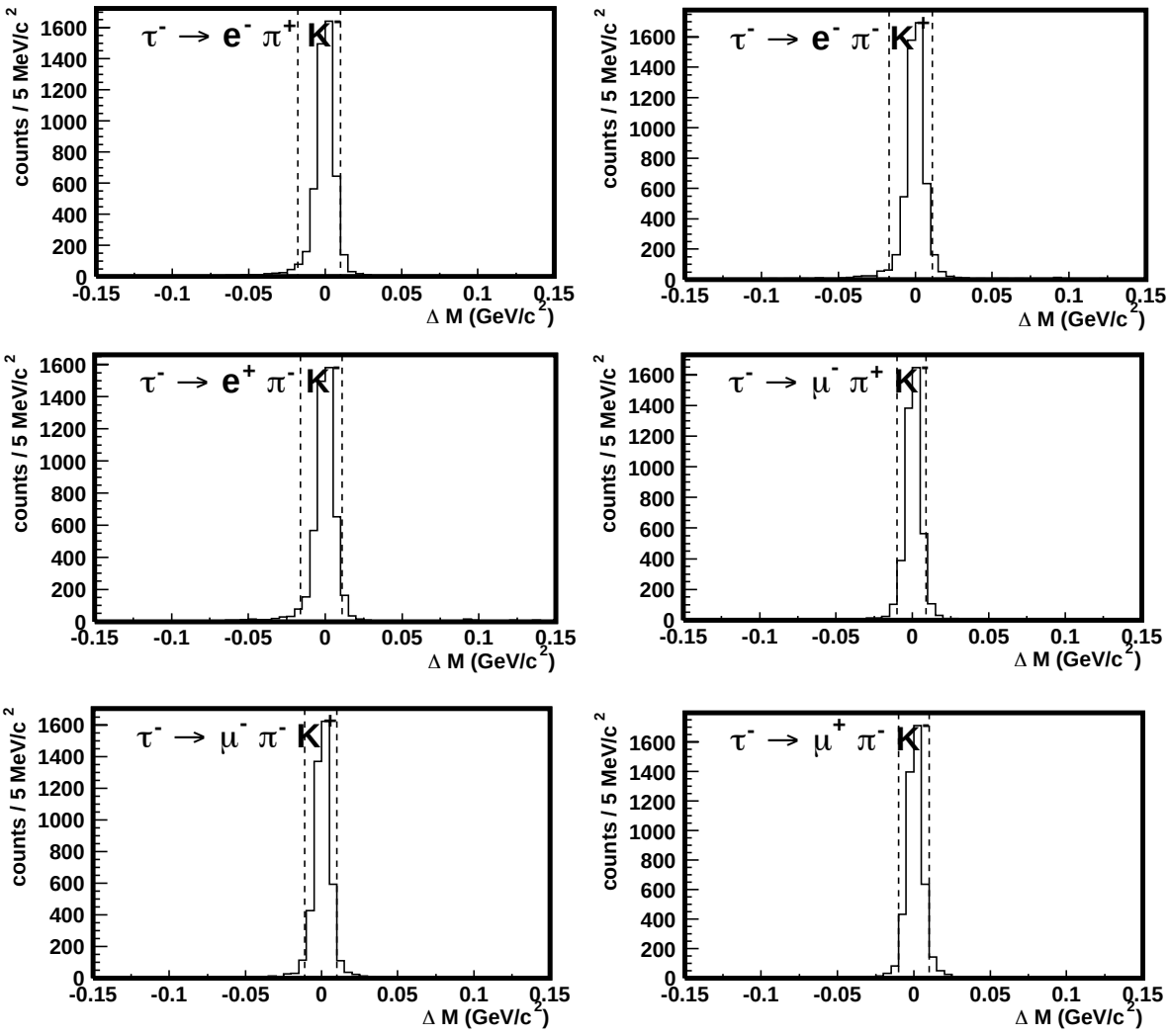

Figure 4.44: ΔM distributions after all selection criteria described until Section 4.4 for 100000 $\tau \to \ell\pi K$ signal MC sample. Dashed lines shows the boundary of signal region.

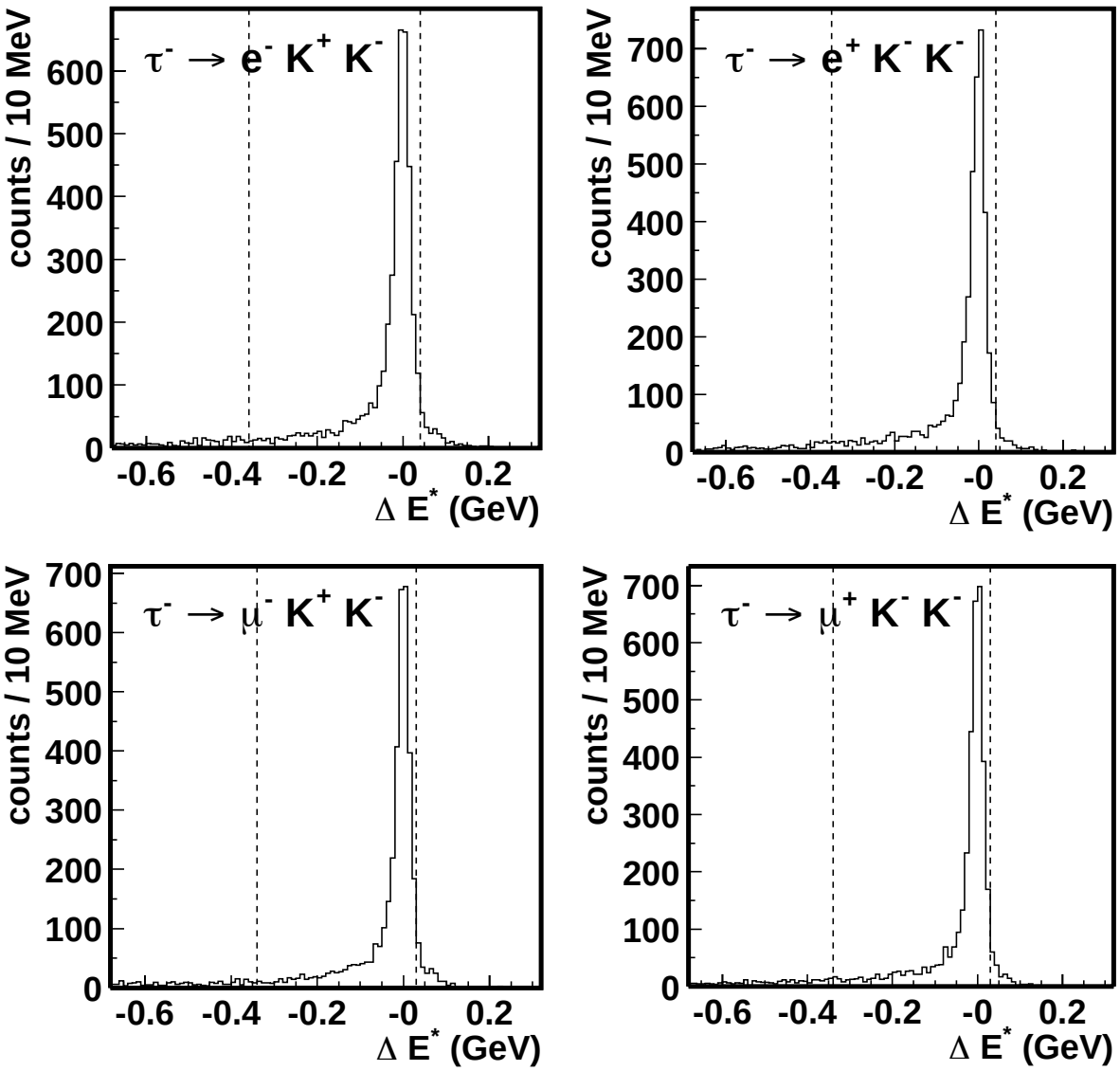

Figure 4.45: ΔE^* distributions after all selection criteria described until Section 4.4 for 100000 $\tau \to \ell KK$ signal MC sample. Dashed lines shows the boundary of signal region.

its error is mainly related to the track momentum and the structure of the detector, the systematic error depends on the polar angle of the track. We calculate the systematic error in each polar angle region as shown in Table 4.10. Using these tables and polar angle distribution of tracks which are identified as leptons after applying the all selection in $\tau \to$ LFV MC, we compute the systematic error on ϵ from lepton identification as 1.1% for an electron and 5.4% for a muon.

The K/π separation efficiency is evaluated from decay of charged D^* meson: $D^{*+} \to D^0\pi^+, D^0 \to K^-\pi^+$. High momentum D^{*+} mesons can be reconstructed with a good signal-to-background ratio even if we require no particle identification

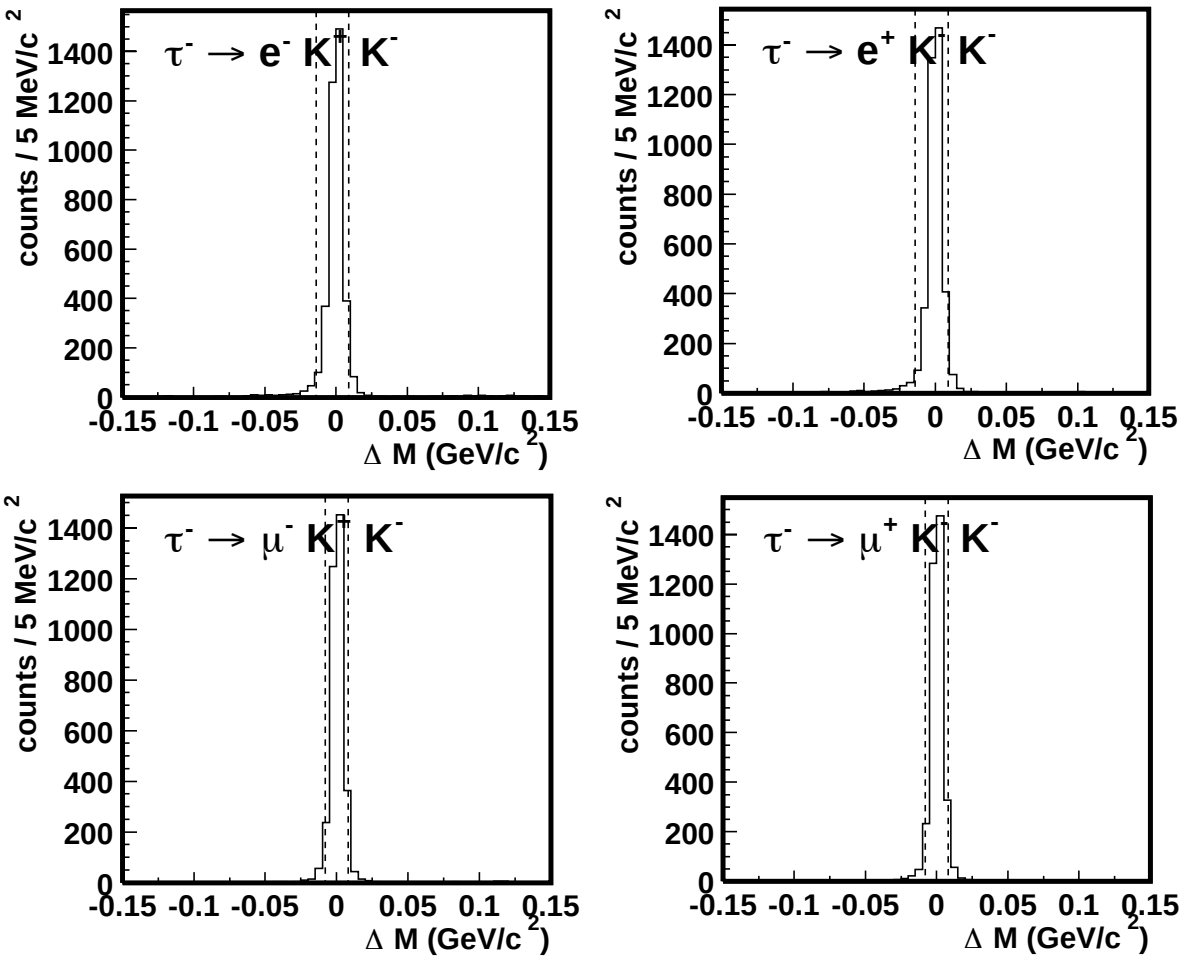

Figure 4.46: ΔM distributions after all selection criteria described until Section 4.4 for 100000 $\tau \to \ell KK$ signal MC sample. Dashed lines shows the boundary of signal region.

Table 4.10: Systematic error of lepton identification in each range of track polar angle.

polar angle region (degree)	systematic error of electron identification (%)
18-25	3.2
25-35	2.7
35-40	1.4
40-60	1.4
60-125	0.7
125-132	4.8
132-151	6.4

polar angle region (degree)	systematic error of muon identification (%)
25-37	11.9
37-51	8.4
51-117	3.9
117-130	7.9
130-150	13.1

because of the slow pion tag and the invariant mass requirements for D^* and D^0. Thus negative charged particle in final state of the decay is easily tagged as kaon in case that we reconstruct the D^{*+} using the kinematics selection criteria. Comparing the kaon finding efficiency between the data and MC, We make table of systematics error on 2-dimensional plane of polar angle and momentum of track in laboratory frame. The systematic error on ϵ from K/π separation is evaluated to be 1.0% for each kaon track from the systematic error table and polar angle and momentum distribution of tracks which is identified as kaon in LFV decay MC.
For multi-tracks events, the systematic errors on the tracking and particle identifications are combined linearly. Th tracking systematic error of 4-charged track event is 4% and the total systematic error for particle identification of each decay mode ($\Delta\epsilon_{\rm PID}/\epsilon_{\rm PID}$) is summarized in second column of table 4.11.
Requirements on the number of CDC tracks and the energy of ECL clusters constitute part of the trigger logic. The impact of the trigger on the efficiency is investigated with application of a simulated trigger system to the signal MC. The number of event after all selection criteria decrease relatively 1.6% after applying trigger condition because the selection criteria used in this analysis are much more restrictive than the trigger conditions. The systematic error for trigger condition is also estimated to be 1.4%.
As mentioned, we use the signal MC which is generated with phase space decay. The actual decay angular distribution, however will depend on the physics model of LFV interaction and spin correlations between the tag side and signal side τ. In order to evaluate the effect of such correlations, we examine $V-A$ and $V+A$ interactions using the formulae given in [62] and efficiency distribution as a function of helicity angle, $\theta_{\rm hel}$, that is defined as the opening angle between the flight direction of τ in CMS and flight direction of daughter particle which has a charge opposite to the mother τ in the system of τ at rest. Figure 4.47 (a) shows the efficiency distribution as the function of $\cos\theta_{\rm hel}$ calculated from generator information for $\tau \to e^-\pi^+\pi^-$ signal MC generated with a phase space. The efficiency is distributed flat because the daughter particles from LFV τ decay is generated to be flat in the MC. Using the same MC samples, we plot the efficiency distribution as the function of $\cos\theta_{\rm hel}$ calculated from the information after detector simulation and selection as shown in figure 4.47 (b). In this plot, the efficiency drops in both end regions of the distribution due to the detector acceptance and bias of selection criteria. We correct this distribution applying assumed another non-flat function in efficiency vs. $\cos\theta_{\rm hel}$ plane instead of analyzing the another MC which has different decay angular distribution of τ decay. Figure 4.47 (c) shows one example of function: $1-\cos\theta_{\rm hel}$, and corrected efficiency distribution is shown in figure 4.47 (d). In [62], the differential cross section for decay angles is given in following formula.

$$
\begin{aligned}
&d\sigma(e^+e^- \to \mu^-\mu^+\mu^+ + \pi^-\nu) = \\
&\quad \sigma(e^+e^- \to \tau^-\tau^+)B(\tau^- \to \pi^-\nu)\left(\frac{m_\tau^5 G_F^2}{128\pi^4}/\Gamma\right)\frac{d\cos\theta_\pi}{2}dx_1dx_2d\cos\phi \\
&\qquad \times\left[X - \frac{s-2m_\tau^2}{s+2m_\tau^2}(Y\cos\theta + Z\sin\theta\cos\phi)\cos\theta_\pi\right] \qquad (4.9)
\end{aligned}
$$

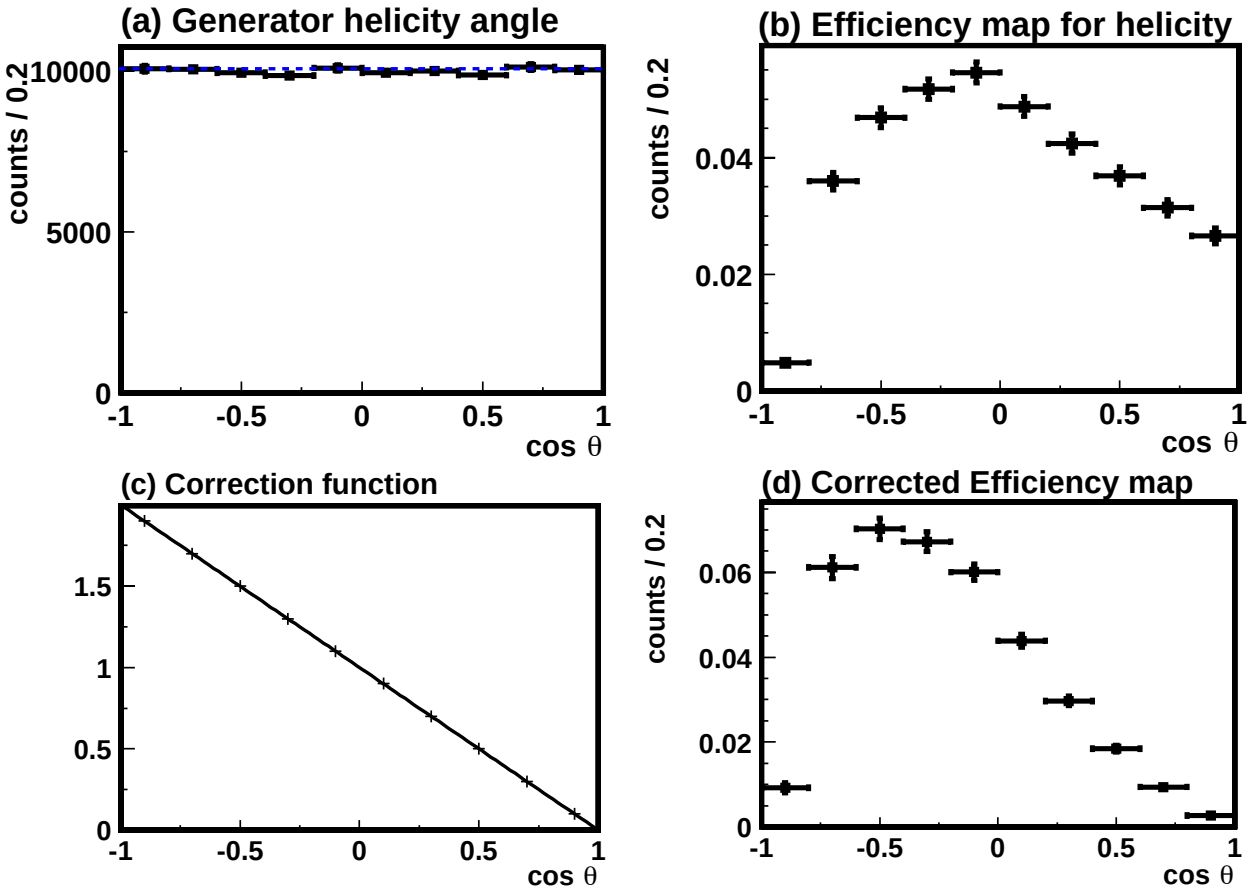

Figure 4.47: Efficiency vs. $\theta_{\rm hel}$ distributions: (a) from generator information (b) from information of simulated detector after reconstruction (c) assumed function shape, $1 - \cos\theta$ (d) corrected distribution obtained from multiplying (b) by (c).

where θ is same definition of $\theta_{\rm hel}$is same angle, ϕ is azimuth angle in τ at rest frame for τ flight direction in e^+e^- CMS, θ_π is the direction of tag side 1-prong track in CMS frame. In this case, tag side decay is considered as $\tau^- \to \pi^-\bar{\nu_\tau}$. m_τ and Γ are mass and width of the τ, G_F and s are the Fermi coupling constant and the e^+e^- CMS energy, respectively. X, Y, Z and W are the function which consist of decay coordinates of τ LFV process, operator with coupling constant, positron charge and components of momentum vector of daughter particle from LFV decay. Detail of the function is described in formula (56)−(59) in [62]. Integrating this formula, last two terms which contains $\sin\theta$ is canceled and the cross section $\sigma(e^+e^- \to \mu^-\mu^+\mu^+ + \pi^-\nu)$ is proportional to $(1-\alpha\cos\theta)$, where α is a constant which has a value between 0 and 1. To evaluate the maximum uncertainty from decay angular distribution considering this model, we use $(1-\cos\theta_{\rm hel})$ as an assumed non-flat function in efficiency vs. $\cos\theta_{\rm hel}$ plane. The differences between efficiencies which we calculate above and in case of a uniform decay angular distribution $\Delta\epsilon_{\rm angle}/\epsilon_{\rm angle}$ are summarized in the third column of Table 4.11 for each decay mode. These errors are different mode-by-mode because efficiency vs. $\cos\theta_{\rm hel}$ distributions ((b) in Figure 4.47) are different between modes due to the bias of particle identifications and track momentum threshold. Component of the systematic error is summarized in Table 4.12 and total systematic error for signal detection efficiency is listed in last column of Table 4.11.

4.7 Experimental data Analysis

Figure 4.48−4.51 show ΔE^* vs. ΔM distributions after all selection except for the selection criteria for ΔE^* and ΔM. From background MC, we find that the remaining events consist of three components: low-multiplicity hadronic events, τ-pair generic 3-prong decay and events from generic two-photon $e^+e^- \to e^+e^-e^+e^-$, $e^+e^- \to e^+e^-\mu^+\mu^-$ and $e^+e^- \to e^+e^-u\bar{u}$ events. In case hadronic and τ-pair generic 3-prong decay becomes background, particle identification tends to be failed.
We observe only few events in Figure 4.48 plots for $\tau \to \ell\ell\ell$ modes. We also find the ΔM distribution near the signal region is almost flat in ΔE^* signal region. To evaluate the background b in the signal region, we assume a uniform background distribution along the ΔM axis. We estimate the number of background events in the signal region from the number of events observed in the ΔE^* signal region and ΔM sideband regions that is defined as -0.12 GeV/$c^2 < \Delta M < 0.12$ GeV/c^2, excluding the ΔM signal region. We normalize the number of observed events in this region to signal region multiplying the factor which corresponds to the ratio of each area. If there is no event observed in signal region, we set upper limit of event in sideband region as 2.44 at 90% CL using "Feldman and Cousins method" [63] in case of absence of observed event. Table 4.13 shows the number of estimated background events and the errors.

In $\tau \to \ell hh$ modes, there are many event appeared in Figure 4.49−4.51 and they are distributed with some structure. To evaluate the background, we perform the fit to the sideband region of ΔM distribution after requiring all selection criteria and

Table 4.11: The systematic error on the efficiencies.

Mode	$\Delta\epsilon_{\rm PID}/\epsilon_{\rm PID}$ (%)	$\Delta\epsilon_{\rm angle}/\epsilon_{\rm angle}$ (%)	$\Delta\epsilon_{\rm total}/\epsilon_{\rm total}$ (%)
$\tau^- \to e^-e^+e^-$	3.3	3.8	6.5
$\tau^- \to e^-\mu^+\mu^-$	11.9	8.7	15.2
$\tau^- \to e^+\mu^-\mu^-$	11.9	1.1	12.0
$\tau^- \to \mu^-e^-e^+$	7.6	0.8	8.5
$\tau^- \to \mu^+e^-e^-$	7.6	12.6	14.7
$\tau^- \to \mu^-\mu^+\mu^-$	16.2	5.6	17.8
$\tau^- \to e^-\pi^+\pi^-$	3.1	5.3	7.0
$\tau^- \to e^+\pi^-\pi^-$	3.1	2.3	5.2
$\tau^- \to \mu^-\pi^+\pi^-$	7.4	2.1	8.4
$\tau^- \to \mu^+\pi^-\pi^-$	7.4	7.7	11.2
$\tau^- \to e^-\pi^+K^-$	3.1	20.5	21.0
$\tau^- \to e^-\pi^-K^+$	3.1	17.4	18.0
$\tau^- \to e^+\pi^-K^-$	3.1	12.8	13.6
$\tau^- \to e^-K^+K^-$	3.1	17.4	22.4
$\tau^- \to e^+K^-K^-$	3.1	5.4	7.1
$\tau^- \to \mu^-\pi^+K^-$	7.4	15.8	17.8
$\tau^- \to \mu^-\pi^-K^+$	7.4	19.1	20.8
$\tau^- \to \mu^+\pi^-K^-$	7.4	25.4	26.7
$\tau^- \to \mu^-K^+K^-$	7.4	8.7	11.9
$\tau^- \to \mu^+K^+K^-$	7.4	38.2	39.1

Table 4.12: The systematic error components for signal detection efficiency.

source	systematic error (%)
Tracking	1.0 per track
Trigger	1.4
electron identification	1.1 per electron
muon identification	5.4 per muon
K/π separation	1.0 per pion/kaon
Decay angular uncertainty	2.1-38 (mode-by-mode, see table 4.11)
signal MC statistics	1.0

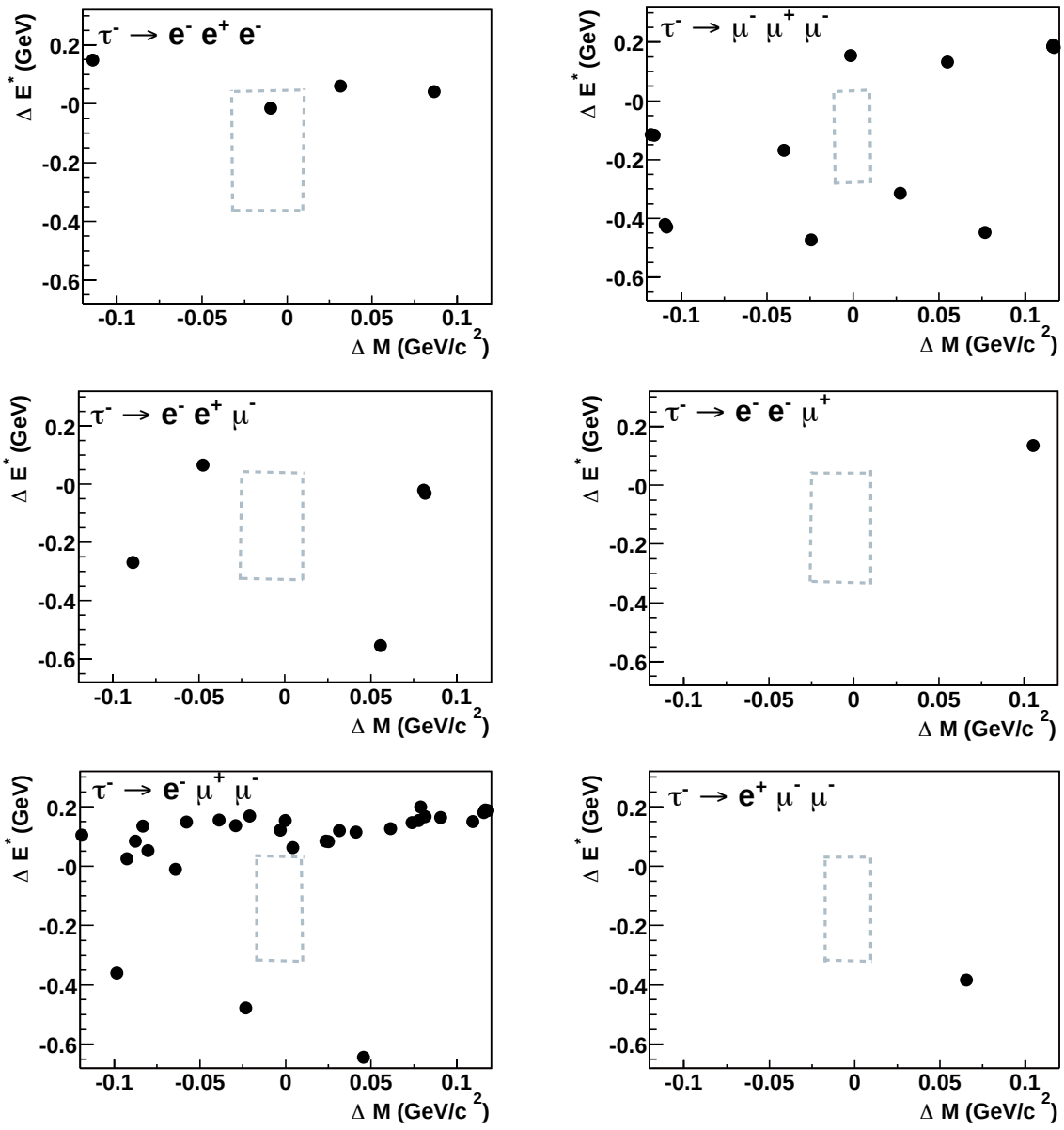

Figure 4.48: ΔE^* vs. ΔM experimental data distributions for $\tau \to \ell\ell\ell$ modes after all selection criteria described until Section 4.4. Dashed box shows the signal area.

extrapolate the fit curve into the signal region. The sideband region which is common to the all $\tau \to \ell hh$ modes is defined as -0.5 GeV/$c^2 < \Delta M < 0.5$ GeV/c^2, blinding the signal region, -96 MeV/$c^2 < \Delta M < 30$ MeV/c^2. uds continuum, τ-pair generic decay processes survive after all selections except for that for ΔM. In addition for $\tau^- \to e^- h^+ h^-$ modes, two-photon background appears in $\Delta M > 0$ region. The background contribution from all other processes is suppressed to be negligible. We decide the shape of background from the MC samples for uds continuum and τ-pair events. For two-photon events, because the statistical error from the fit becomes

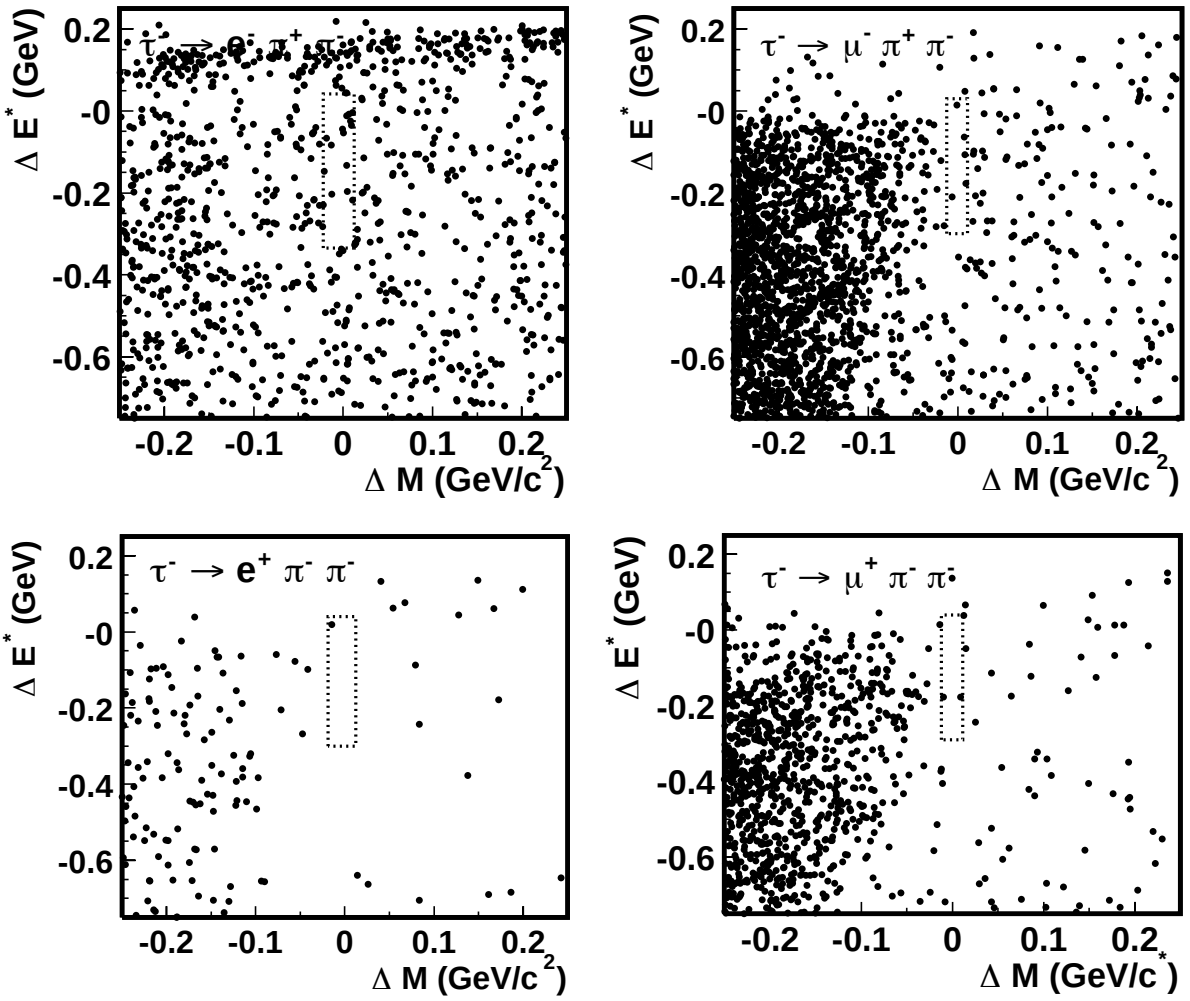

Figure 4.49: ΔE^* vs. ΔM experimental data distributions for $\tau \to \ell\pi\pi$ modes after all selection criteria described until Section 4.4. Dashed box shows the signal area.

very large due to low statistics of two-photon MC sample, the shape used for fitting is determined from experimental data distribution after all selection and additionally requiring the selection criteria for two-photon event collection:

— $p_T^* < 0.4$,

— $\mathcal{L}_{eid} > 0.9$ for tag side track.

To obtain more statistics, we loosen the ΔE^* signal area to -0.75 GeV $< \Delta E^* <$ 0.25 GeV. As shown in Figure 4.52 these parameters do not correlate with ΔM in its sideband region. The fit result distributions are shown in $4.57 - 4.59$ with experimental data distributions and numerical results are summarized in table 4.14. In the signal regions for the twenty decay modes considered, events are appeared in signal region for some modes.

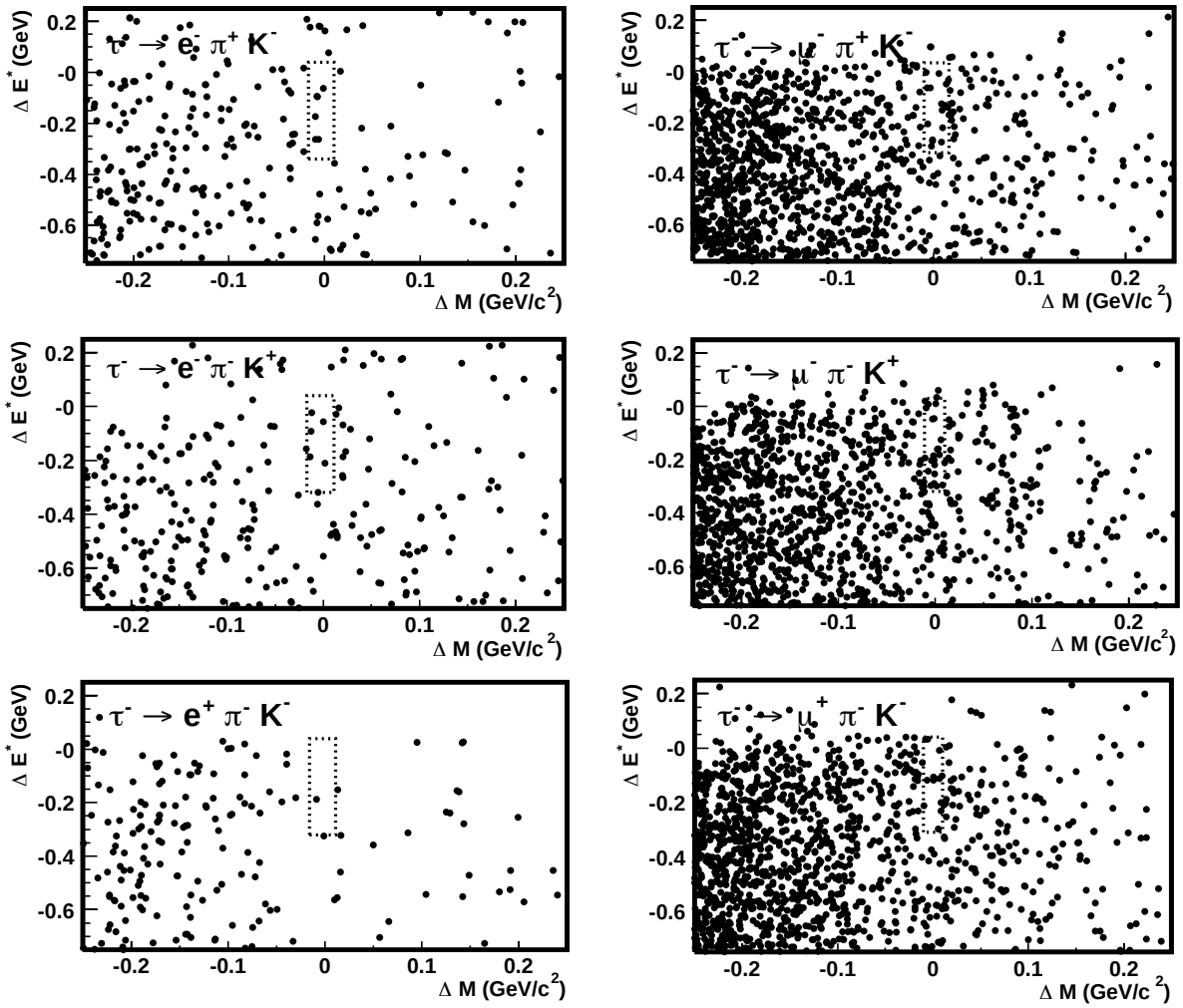

Figure 4.50: ΔE^* vs. ΔM experimental data distributions for $\tau \to \ell\pi K$ modes after all selection criteria described until Section 4.4. Dashed box shows the signal area.

Table 4.13: Number of expected background for $\tau \to \ell\ell\ell$ modes.

	Expected	Data
$\tau^- \to e^-e^+e^-$	< 0.2	1
$\tau^- \to e^-\mu^+\mu^-$	0.1 ± 0.1	0
$\tau^- \to e^+\mu^-\mu^-$	< 0.3	0
$\tau^- \to \mu^-e^+e^-$	0.1 ± 0.1	0
$\tau^- \to \mu^+e^-e^-$	< 0.2	0
$\tau^- \to \mu^-\mu^+\mu^-$	0.1 ± 0.1	0

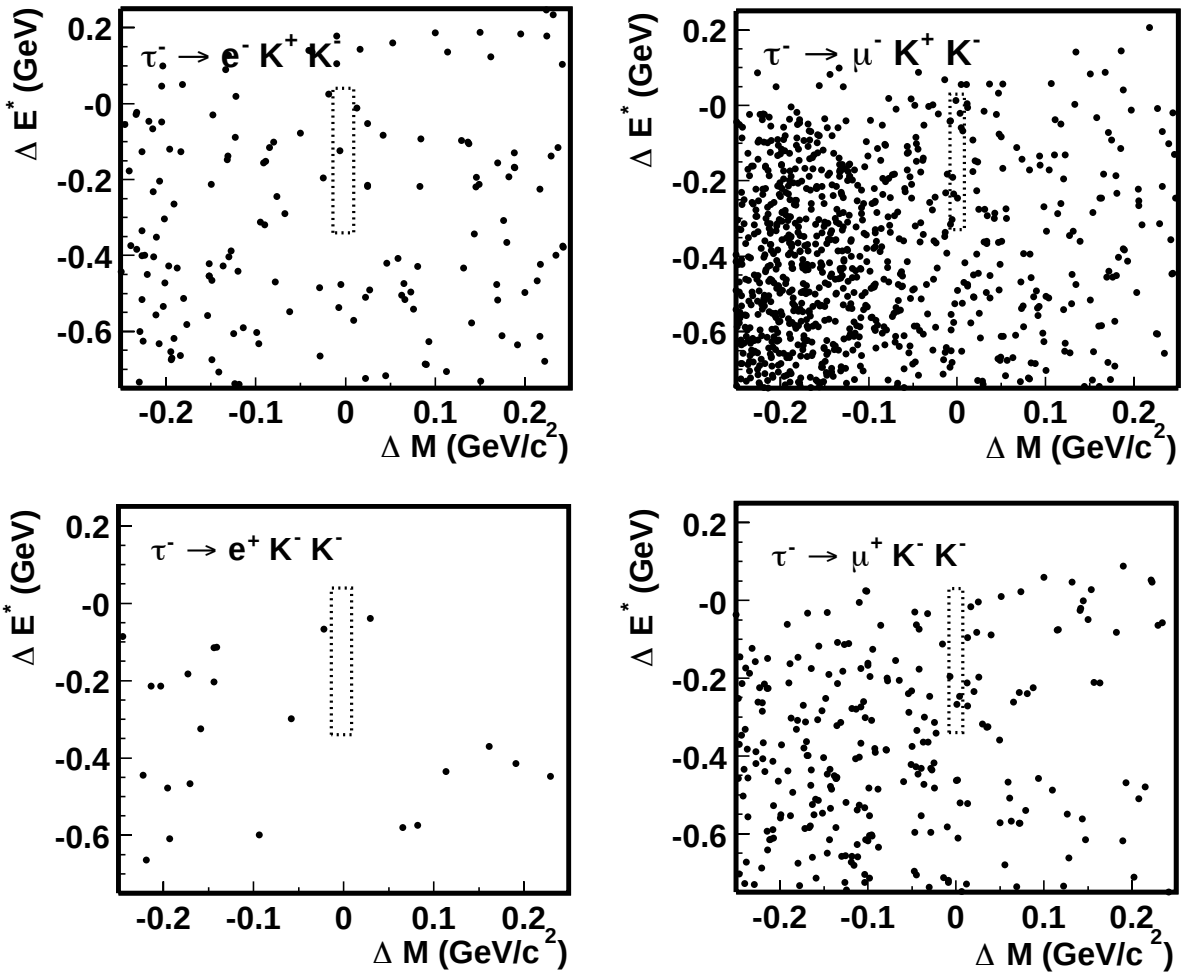

Figure 4.51: ΔE^* vs. ΔM experimental data distributions for $\tau \to \ell KK$ modes after all selection criteria described until Section 4.4. Dashed box shows the signal area.

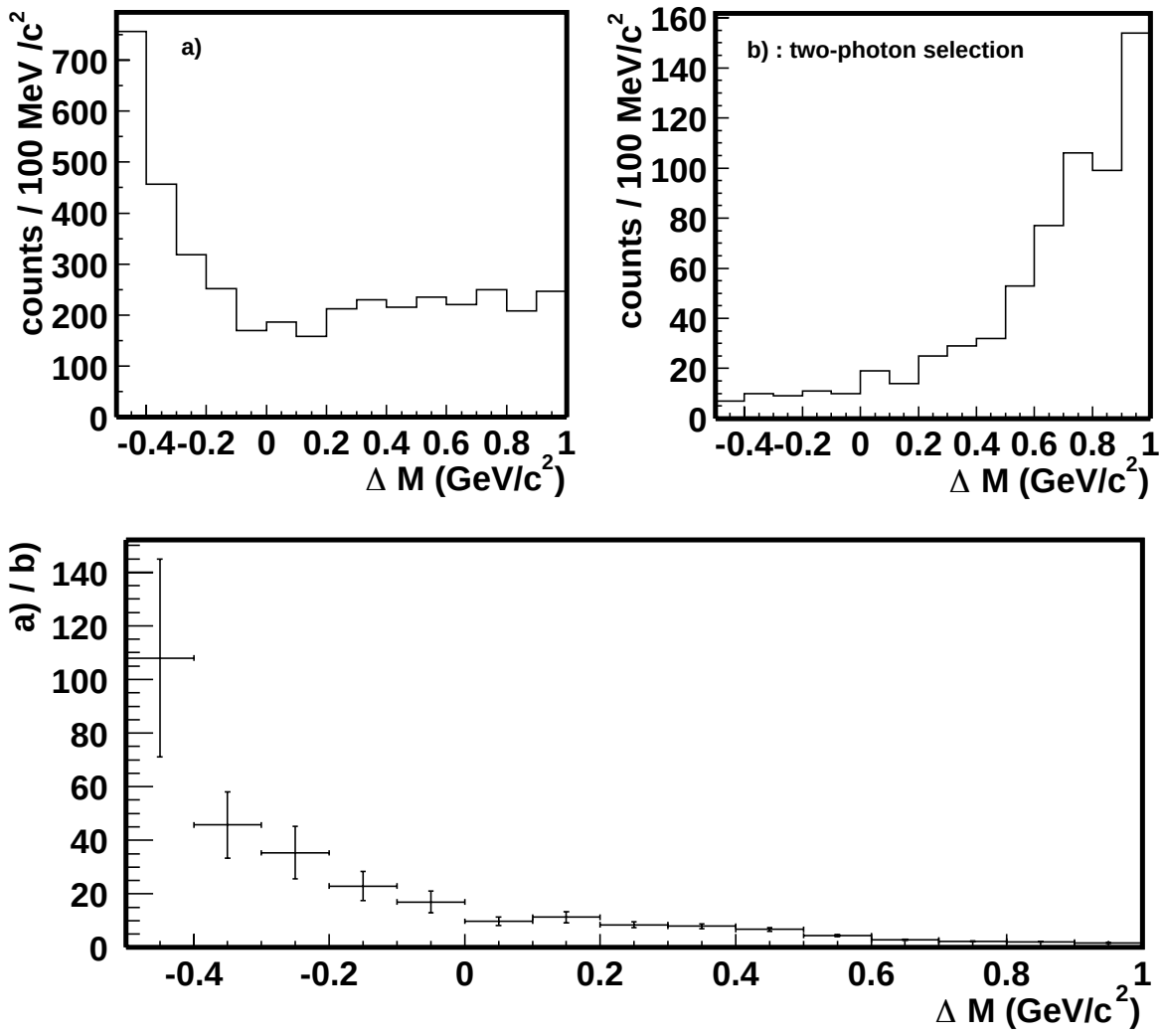

Figure 4.52: Correlation check between ΔM and two-photon selection parameters. Upper two figures show ΔM distributions a): after all selections except for that of ΔM, b): after two-photon selections and all selections except for that of ΔM. Lower plot shows ratio of a) / b), flat distribution can be seen in 0 GeV/c^2 $< \Delta M <$ -0.5 GeV/c^2.

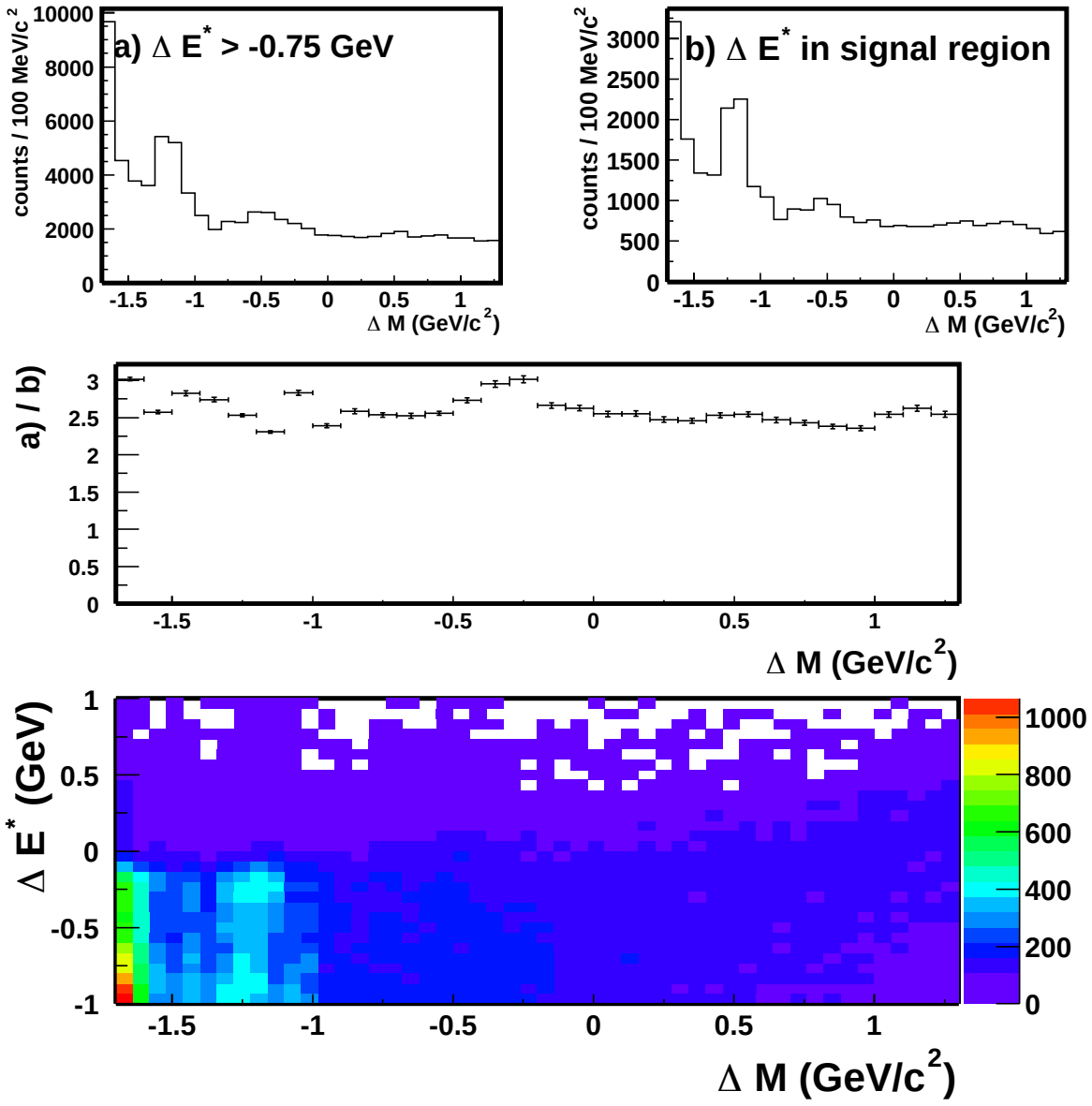

Figure 4.53: Correlation check between ΔM and two-photon selection parameters. Upper two figures show ΔM distributions a): after all selections except for that of ΔM, b): after two-photon selections and all selections except for that of ΔM. Middle plot shows ratio of a) / b), flat distribution is observed in 0 GeV/c^2 $< \Delta M <$ -0.5 GeV/c^2. Lower plot shows the ΔE^* vs. ΔM distribution.

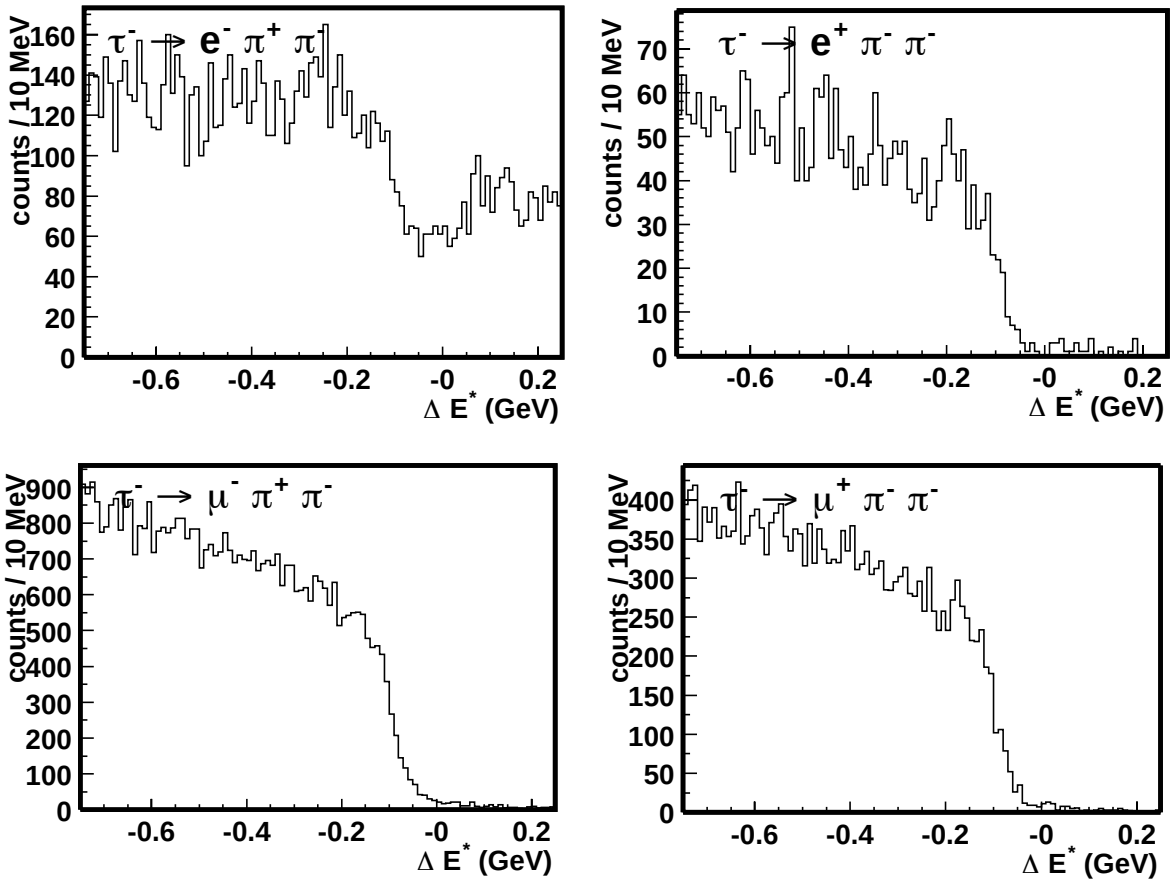

Figure 4.54: ΔE^* experimental data distributions for $\tau \to \ell\pi\pi$ modes after all selection criteria described until Section 4.4.

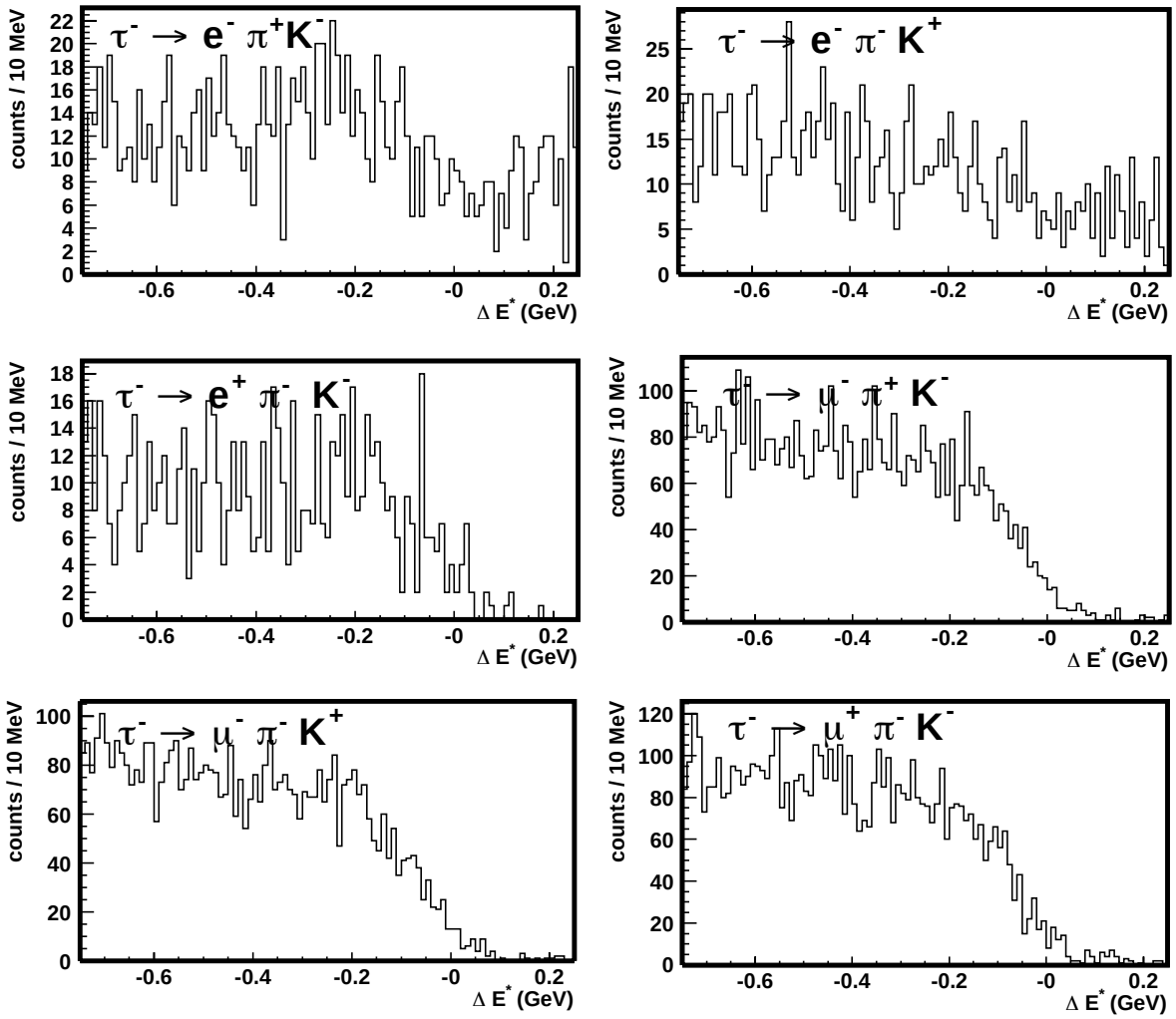

Figure 4.55: ΔE^* experimental data distributions for $\tau \to \ell\pi K$ modes after all selection criteria described until Section 4.4.

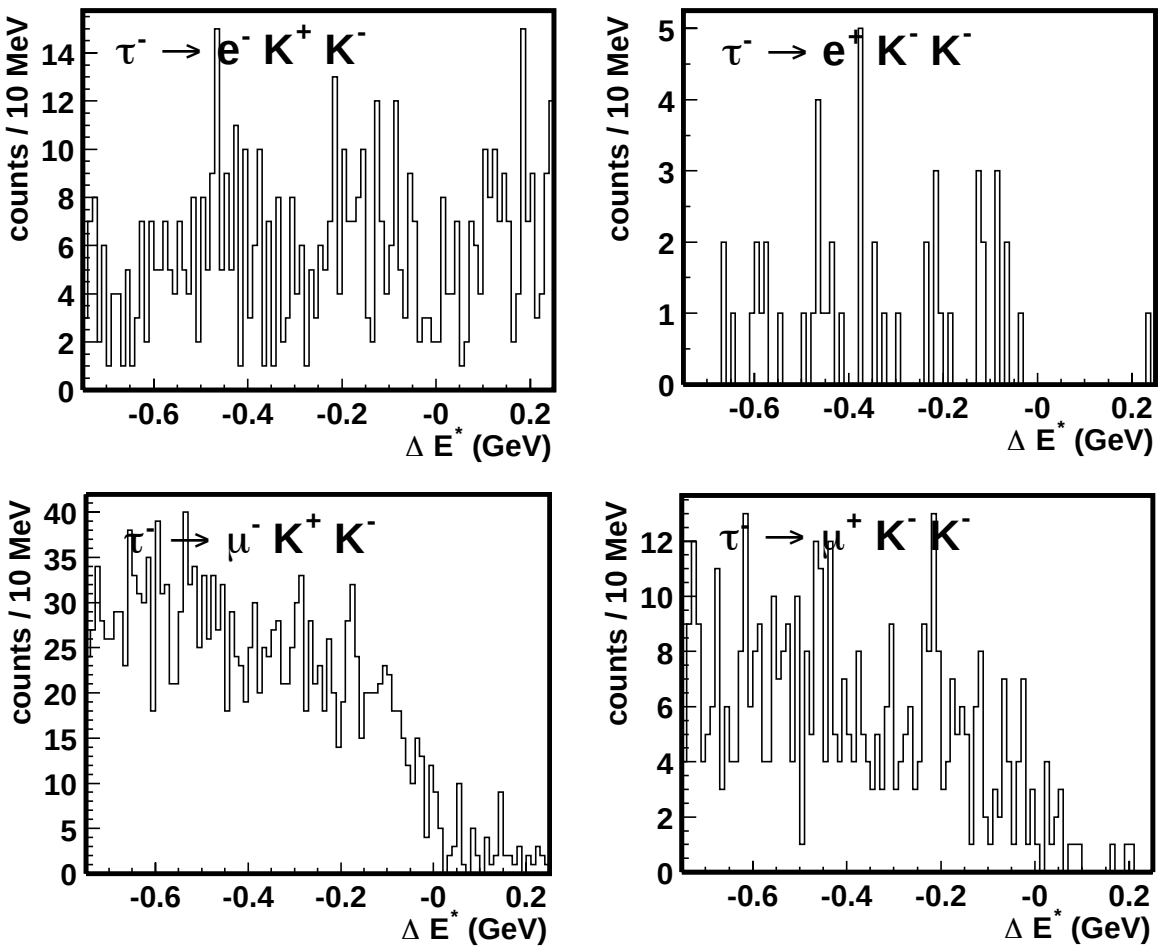

Figure 4.56: ΔE^* experimental data distributions for $\tau \to \ell KK$ modes after all selection criteria described until Section 4.4.

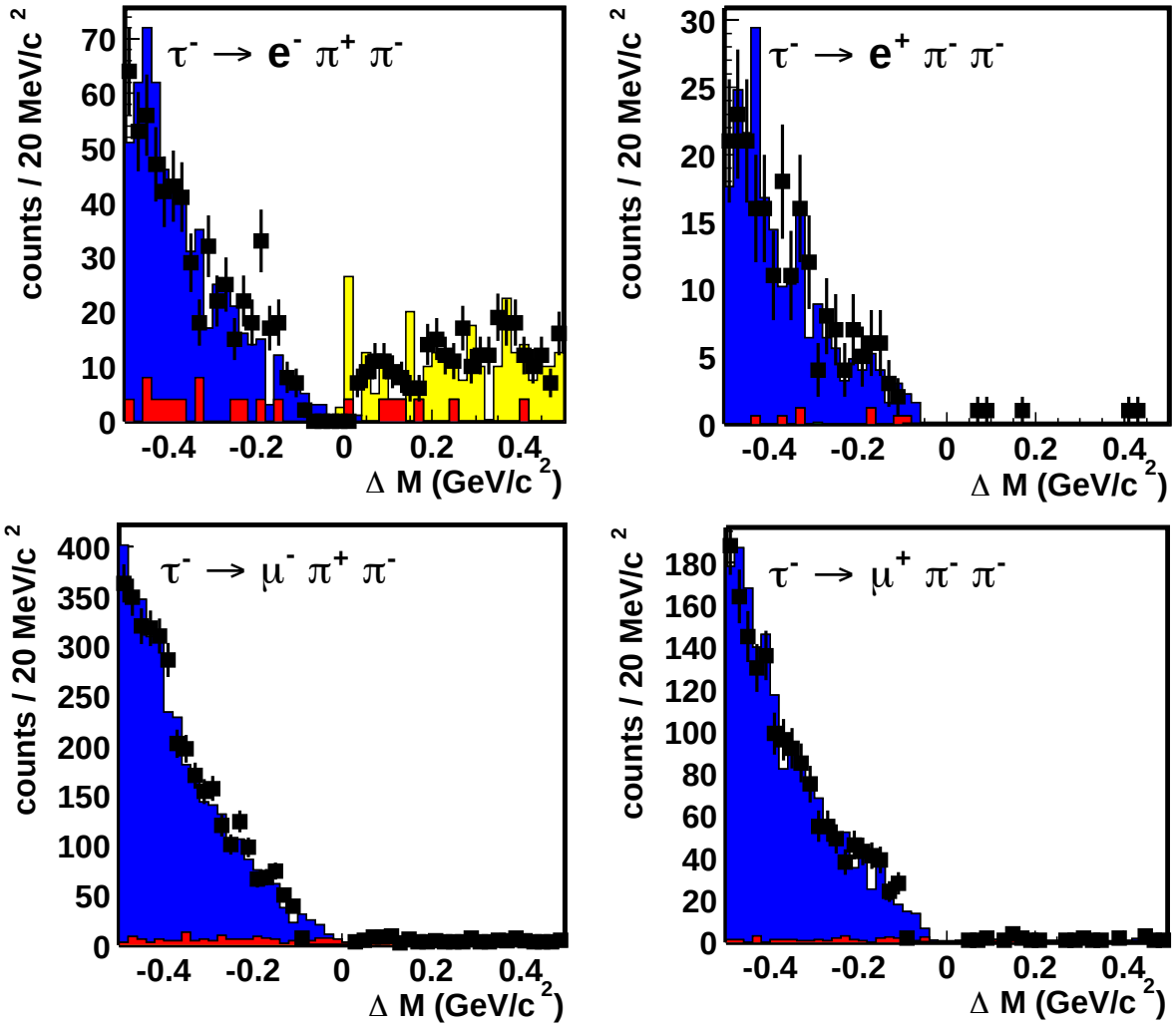

Figure 4.57: ΔM distributions for $\tau \to \ell\pi\pi$ modes after all selection criteria except for selection for ΔM. Dots shows the experimental data and histograms show the MC fit result distributions. Each color of histogram represent for MC component: red for *uds* continuum, blue for τ-pair event and yellow for two-photon event.

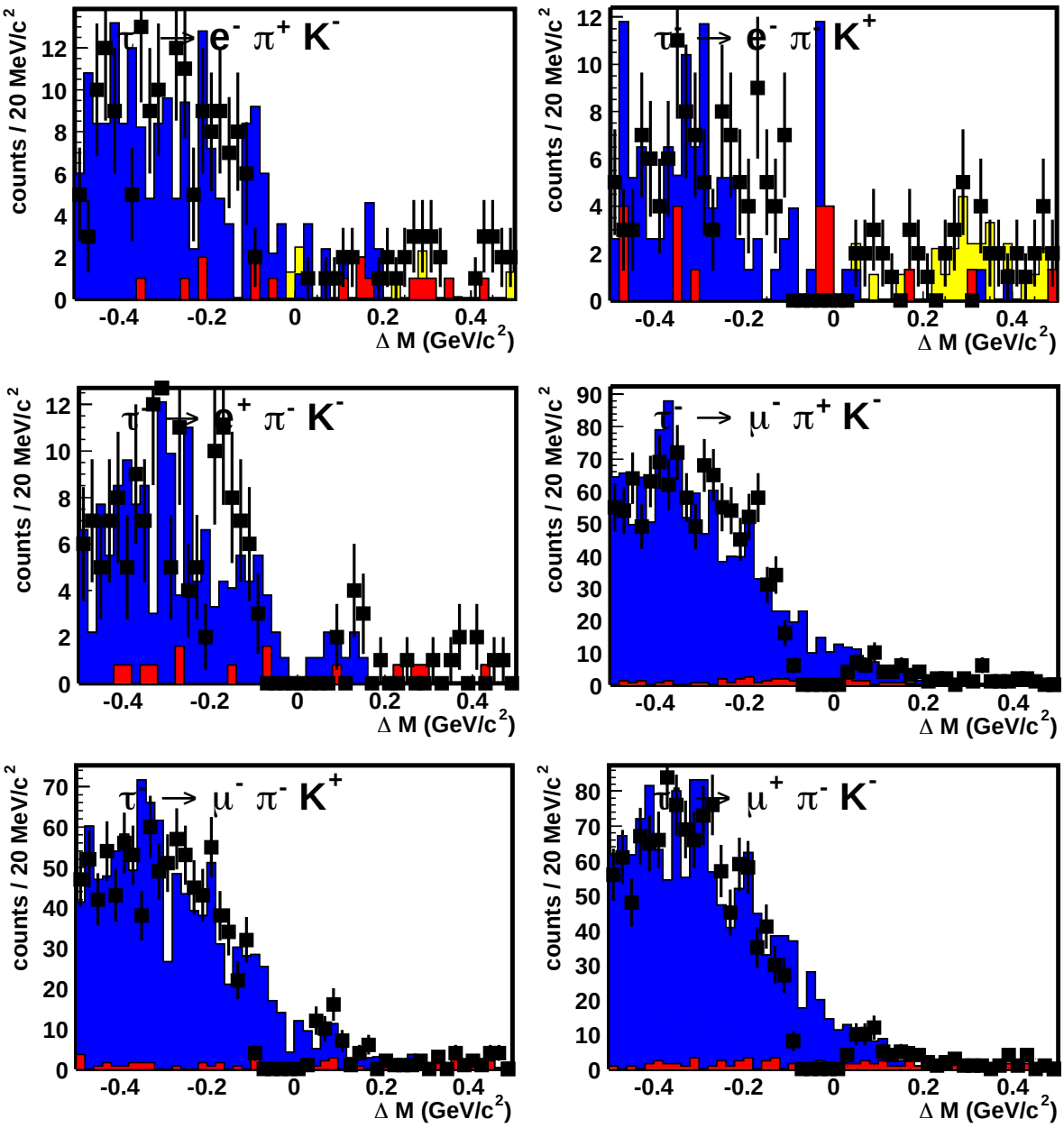

Figure 4.58: ΔM distributions for $\tau \to \ell\pi K$ modes after all selection criteria except for selection for ΔM. Dots shows the experimental data and histograms show the MC fit result distributions. Each color of histogram represent for MC component: red for *uds* continuum, blue for τ-pair event and yellow for two-photon event.

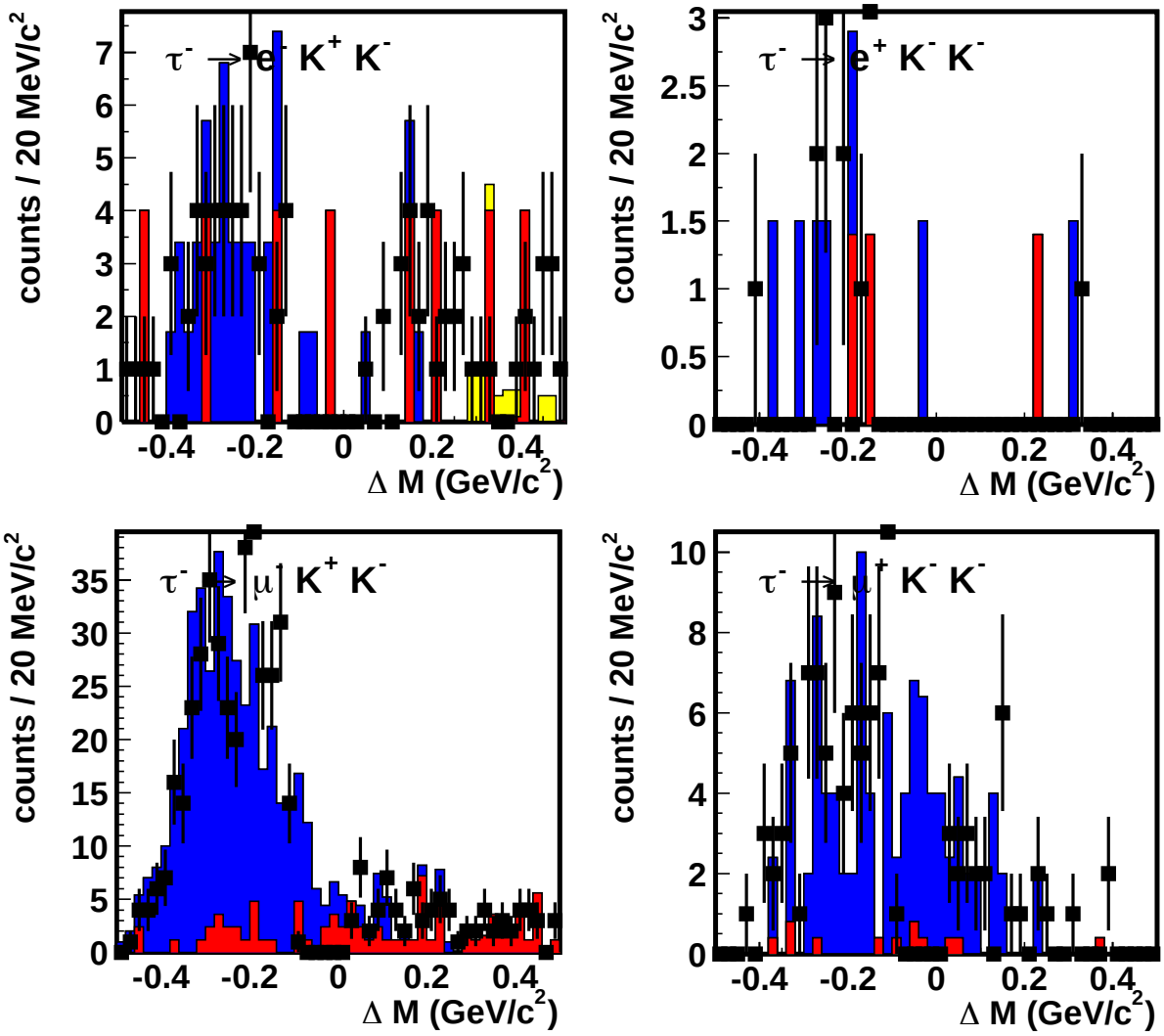

Figure 4.59: ΔM distributions for $\tau \to \ell KK$ modes after all selection criteria except for selection for ΔM. Dots shows the experimental data and histograms show the MC fit result distributions. Each color of histogram represent for MC component: red for *uds* continuum, blue for τ-pair event and yellow for two-photon event.

Table 4.14: Number of expected background with fit in signal region and sideband region. (†: we set upper limit taking the three times of error because expected background is smaller than 0.1.)

Mode	signal region		-0.5 < ΔM < +0.5 GeV/c^2	
	Expected	Data	Expected	Data
$\tau^- \to e^-\pi^+\pi^-$	20.7±6.4	13	815.6±39.6	878
$\tau^- \to e^+\pi^-\pi^-$	$0.2^{+0.3}_{-0.2}$	1	198.2±12.6	222
$\tau^- \to \mu^-\pi^+\pi^-$	11.4±3.4	5	3646.1±58.2	3675
$\tau^- \to \mu^+\pi^-\pi^-$	1.4±1.0	3	1668.7±40.7	1655
$\tau^- \to e^-\pi^+K^-$	4.0±1.9	6	176.4±14.8	217
$\tau^- \to e^-\pi^-K^+$	5.4±1.8	6	132.3±13.9	161
$\tau^- \to e^+\pi^-K^-$	1.1±1.0	2	147.0±12.6	172
$\tau^- \to e^-K^-K^+$	1.3±0.5	1	79.9±9.0	85
$\tau^- \to e^+K^-K^-$	<0.6†	0	10.3±3.8	14
$\tau^- \to \mu^-\pi^+K^-$	14.5±4.2	10	1105.9±39.1	1149
$\tau^- \to \mu^-\pi^-K^+$	13.8±3.9	22	977.0±36.7	1011
$\tau^- \to \mu^+\pi^-K^-$	19.8±5.4	12	1273.0±44.6	1247
$\tau^- \to \mu^-K^-K^+$	5.3±2.2	10	467.6±21.8	466
$\tau^- \to \mu^+K^-K^-$	4.8±2.5	2	78.5±12.2	109

4.8 Upper limit calculation

As listed in Table 4.13 and 4.14, the number of observed events in the signal box is consistent with expected background in its error for all of decay modes. We set the upper limit s_0 on the number of signal events at 90% CL using Baysian approach. To include the uncertainty in the detection efficiency ϵ and expected background b in this limit, we increase s_0 following the prescription of Cousins and Highland [64]. The detail of the statistic computing is described in appendix. Upper limits for branching fractions $\mathcal{B}$ are calculated for each decay mode as follows:

$$\mathcal{B}(\tau^- \to \mathrm{LFV}) < \frac{s_0}{2N_{\tau\tau} \times \epsilon \times \mathcal{B}_{1-\mathrm{prong}}} \tag{4.10}$$

where $N_{\tau\tau}$ is the total number of the τ-pairs produced, and $\mathcal{B}_{1-\mathrm{prong}}$ is the inclusive 1-prong branching fraction of the τ. $N_{\tau\tau} = \sigma_\tau \times \int \mathcal{L}dt$ where the σ_τ is cross section of τ-pair creation from e^+e^- at the CMS energy of 10.6 GeV, and $\mathcal{L}$ is the luminosity. We analyze $\int \mathcal{L}dt$ = 87.1 fb^{-1} and 158 fb^{-1} of the data for $\tau \to \ell\ell\ell$ and $\tau \to \ell hh$ modes, respectively. These corresponds to $N_{\tau\tau}$ = 78 million and 144 million τ-pair events, respectively. The values of s_0 used and the resulting upper limits for the branching fractions are summarized in Table 4.15.

Table 4.15: Upper limits of signal events s_0 and branching ratios 90% confidence level.

Mode	U.L. of signal event (s_0)	U.L. of branching ratio
$\tau^- \to e^-e^+e^-$	4.4	3.5×10^{-7}
$\tau^- \to e^-\mu^+\mu^-$	2.5	2.0×10^{-7}
$\tau^- \to e^+\mu^-\mu^-$	2.6	2.0×10^{-7}
$\tau^- \to \mu^-e^+e^-$	2.5	1.9×10^{-7}
$\tau^- \to \mu^+e^-e^-$	2.6	2.0×10^{-7}
$\tau^- \to \mu^-\mu^+\mu^-$	2.5	2.0×10^{-7}
$\tau^- \to e^-\pi^+\pi^-$	6.8	3.4×10^{-7}
$\tau^- \to e^+\pi^-\pi^-$	4.1	2.0×10^{-7}
$\tau^- \to \mu^-\pi^+\pi^-$	3.4	1.9×10^{-7}
$\tau^- \to \mu^+\pi^-\pi^-$	6.3	3.7×10^{-7}
$\tau^- \to e^-\pi^+K^-$	9.1	5.9×10^{-7}
$\tau^- \to e^-\pi^-K^+$	7.4	4.6×10^{-7}
$\tau^- \to e^+\pi^-K^-$	5.0	3.2×10^{-7}
$\tau^- \to e^-K^-K^+$	3.4	2.8×10^{-7}
$\tau^- \to e^+K^-K^-$	2.5	2.0×10^{-7}
$\tau^- \to \mu^-\pi^+K^-$	6.8	5.1×10^{-7}
$\tau^- \to \mu^-\pi^-K^+$	22.5	16.6×10^{-7}
$\tau^- \to \mu^+\pi^-K^-$	7.5	5.4×10^{-7}
$\tau^- \to \mu^-K^-K^+$	12.4	11.6×10^{-7}
$\tau^- \to \mu^+K^-K^-$	3.8	3.5×10^{-7}

Chapter 5

Conclusion and Future Prospects

We have searched for LFV $\tau \to \ell\ell\ell$ and $\tau \to \ell hh$ decays using an 87.1 fb^{-1} and 158 fb^{-1} data sample, respectively. No evidence for any of these decay mode is observed and upper limits for the branching fractions are obtained in the range $(1.9 - 3.5) \times 10^{-7}$ for $\tau^- \to \ell^-\ell^+\ell^-$ modes and $(1.9 - 16.6) \times 10^{-7}$ for $\tau^- \to \ell hh$ modes; these are approximately of order one magnitude more restrictive than the limits previously obtained in CLEO [39] and comparable to the recent results from BABAR experiment [40].
Comparing the obtained upper limits and the number in Table 2.1, we set upper limits on the combination of parameters $y^2_{\tau e}$ and $y^2_{\tau\mu}$ in the seesaw model which is introduced in chapter 2.1,

$$\begin{aligned} y^2_{\tau e} &< 0.13 \\ y^2_{\tau\mu} &< 0.36. \end{aligned} \tag{5.1}$$

The most restrictive upper limits on $y^2_{\tau e}$ and $y^2_{\tau\mu}$ is set from the upper limit of the branching fractions of $\tau^- \to e^-\pi^+\pi^-$ and $\tau^- \to \mu^-\pi^+\pi^-$, respectively.
In the Higgs-mediated supersymmetric seesaw model that is demonstrated in Section 2.2, we extract the implication of the upper limits using the Eq. (2.74) and obtain the relational expression between $\tan\beta$ and m_A,

$$2 \cdot \left(\frac{m_A}{100\ \mathrm{GeV}/c^2}\right)^4 > \left(\frac{\tan\beta}{60}\right)^6. \tag{5.2}$$

This exclude region in ($\tan\beta$, m_A) is similar to that excluded with the result of direct search for neutral supersymmetric Higgs bosons at CDF experiment [65].
From Eq. (2.81), we also derive the physics meaning from the obtained upper limits in case of the models with contribution of non-universal gauge boson Z':

$$M_Z > \sqrt[4]{\frac{3.52 \times 10^{10}}{k_1}}\ (\mathrm{GeV}/c^2) \tag{5.3}$$

As numerical estimation, M_Z and k_1 are taken as free parameters in this equation. From the vacuum tilting and the constraints from Z-pole physics and $U(1)$ triviality,

Table 5.1: Designed parameters of SuperKEKB

Parameters	LER	HER	Units
Luminosity (L)	100×10^{33}		$\mathrm{cm}^{-2}\mathrm{s}^{-1}$
Crossing angle (θ_x)	+15		mrad
Beta function at IP (β_x^*/β_y^*)	0.15/0.003		m
Beam current (I)	9.4	4.1	A
Natural bunch length (σ_z)	0.3		cm
Bunch spacing (s_B)	0.6		m
Emittance (ϵ_x/ϵ_y)	3.3×10^{-8}/ 2.1×10^{-9}		m
Betatron tune (ν_x/ν_y)	45.515/43.57	44.515/41.57	
Energy loss/turn (U_0)	1.23	3.48	MeV

$k_1 \leq 1$ is required [35]. The limits on the masses of Z' is obtained via studying the effect on various experimental observables [66]. The most constrained one is from the electroweak measurement data fit, the Z' mass should be larger than 1 TeV/c^2 [67]. Although we take low k_1 such as 0.1, the lower limit of M_Z is 770 GeV/c^2 from the result of this analysis. This bound is larger than that is set with the direct search of Z' using the decay of Z' into dileptons [68], however does not reach the limit with electroweak data fit above.

The KEKB and Belle detector is working at the moment and accumulate τ-pair event sample. With the current accelerator, we collect approximately 200 fb^{-1} integrated luminosity of data in one year. The advanced B-factory experiment called "Super B-factory" is planned which achieve a peak luminosity of over ten times larger than current one. The designed machine parameters of the upgraded KEKB accelerator, "SuperKEKB", is listed in the Table 5.1. With SuperKEKB and upgraded Belle detector, we expect to accumulate a few ab^{-1} of data per year. There are several new physics prospect with such an enormous number of data [69]. We expect that the upper limits on the branching fraction for $\tau \to \ell\ell\ell$ modes go down in inverse proportion to the quantity of obtained experimental data because the background approximately near the signal region is very small as shown in Figure 4.48. We plot the boundary of Eq. (2.74) in case of current upper limit and some typical case with SuperKEKB in Figre 5.1. For calculation of the expected line, we assume that the number of background will be kept small although the number of data sample increase. We conclude that the more data sample is obtained, the large $\tan\beta$ region is excluded in case of Higgs mediated supersymmetric model. In Figure 5.2 with a calculated branching fraction as a function of M_Z, we illustrate horizontal line that corresponds to $\mathcal{B}(\tau \to \ell\ell\ell)$ with integrated luminosity of current and expected in the future. We will exceed the lower bound that is set from electroweak data fit when we use a few ab^{-1} of data. We will be able to investigate the existence of non-universal Z' boson whose mass is a few TeV/c^2 indirectly with SuperKEKB.

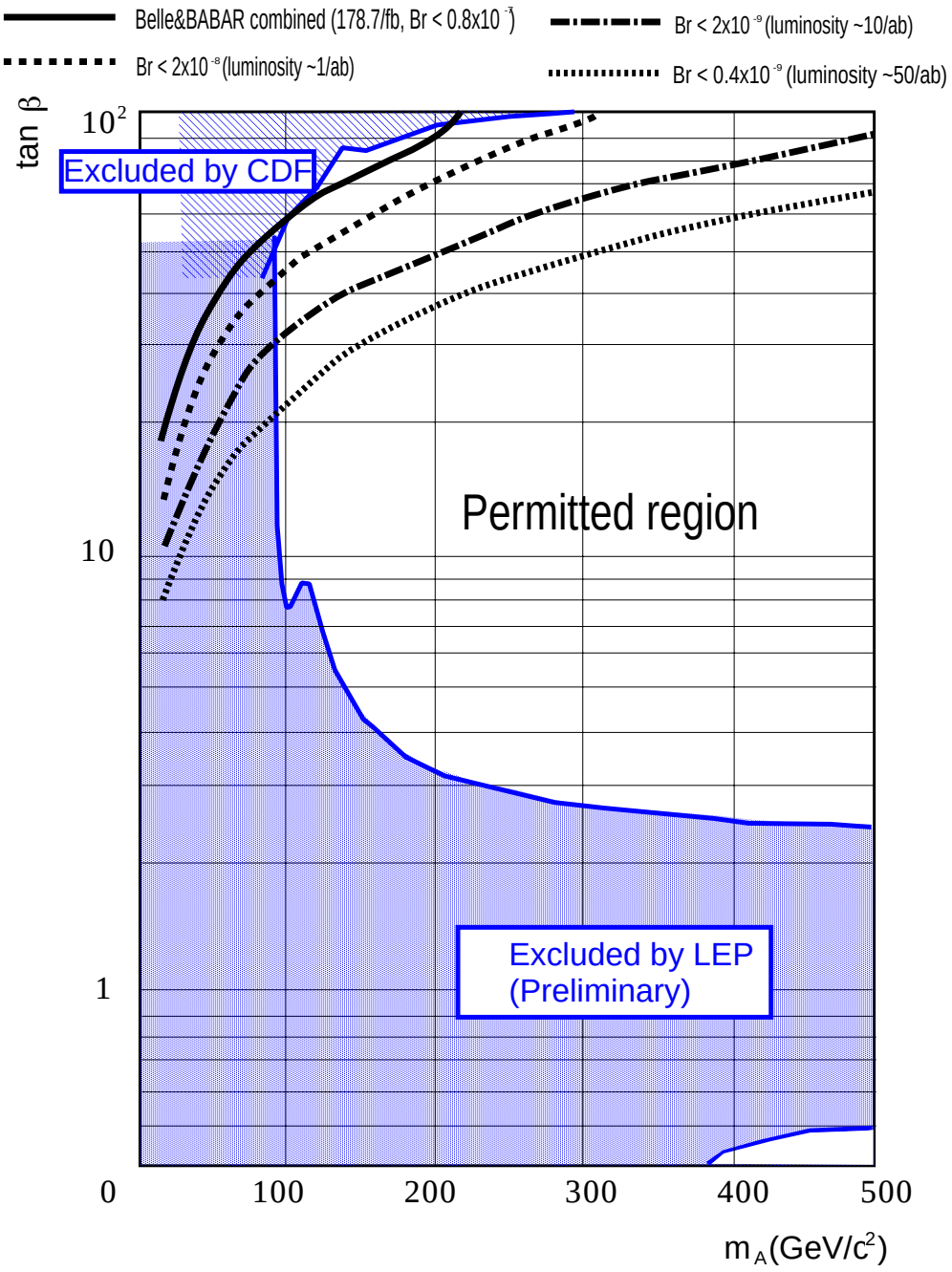

Figure 5.1: The bounds from Eq. (2.74) in case of upper limit from combined result of current Belle and BABAR (solid line) and some typical case with SuperKEKB, branching fraction below 2×10^{-8} (broken line), 2×10^{-9} (dashed line) and 0.4×10^{-9} (dotted line). The 95% CL limits from CDF [65] and LEP [70] are also indicated.

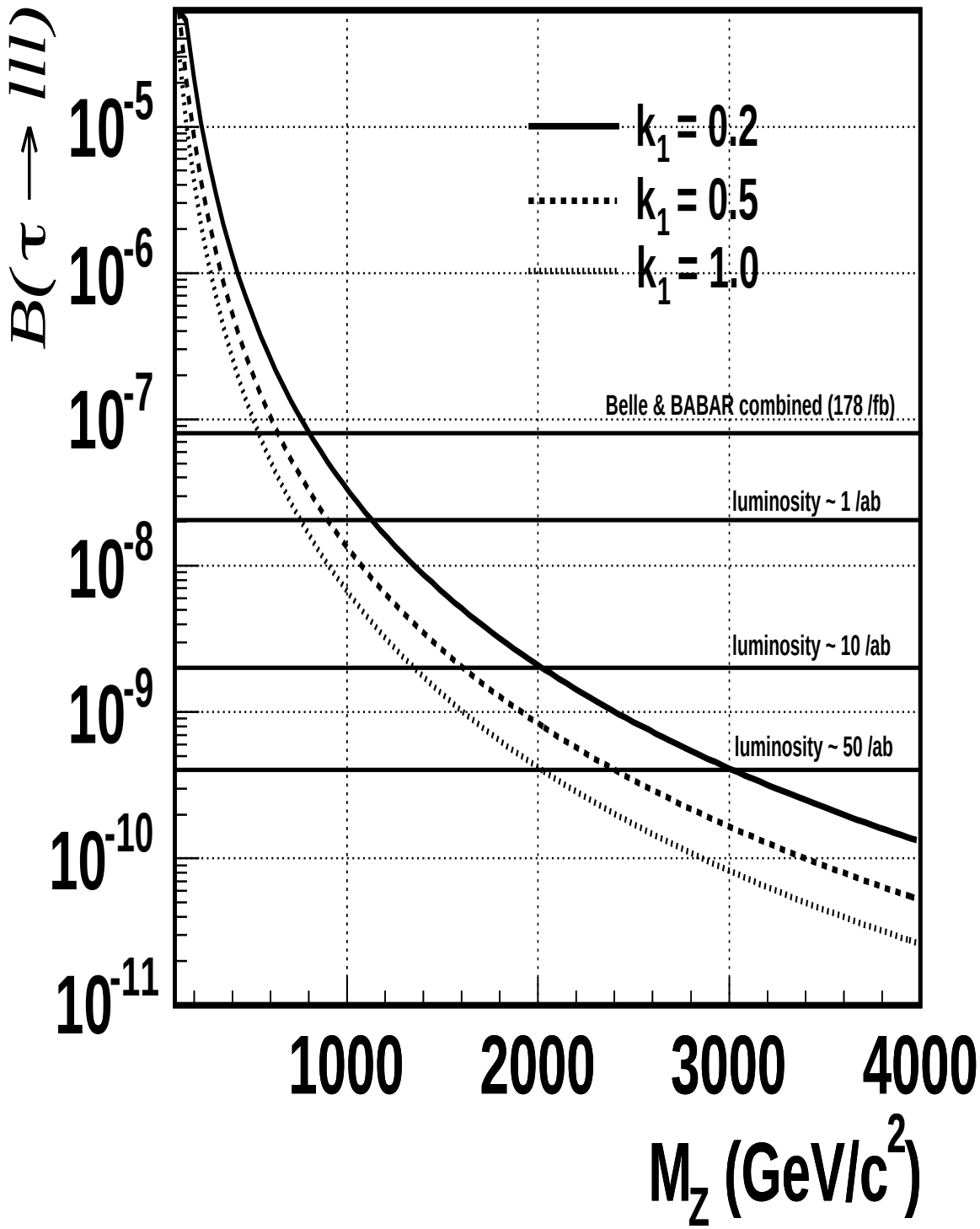

Figure 5.2: $\mathcal{B}(\tau \to \ell\ell\ell)$ as a function of M_Z for $k_1 = 0.2$ (solid line), 0.5 (dashed line) and 1.0 (dotted line). Horizontal lines which correspond current $\mathcal{B}(\tau \to \ell\ell\ell)$ upper limit and future prospects are shown.

Appendix A

Confidence intervals and limits

We describe the technique of the Bayesian approach to determine the limits on physics parameter from outcome of the experiment n in this chapter. The confidence intervals refers frequentest intervals obtained with a procedure proposed by Neyman [71]. We consider a Poisson probability density function (PDF), $p(n, s+b)$, for a signal s which is fixed but unknown in the presence of a known background with mean b. Using this PDF, we can find for a confidence level $(1-\alpha)$ for every value s a set of values n_1 and n_2 so that

$$P(n_1 < n < n_2, s+b) = 1-\alpha = \sum_{n'=n_1}^{n_2} p(n', s+b). \tag{A.1}$$

Because we assume a Poisson distribution for PDF, the equality of the formula will generally not be fulfilled exactly. A set of intervals between n_1 and n_2 which are the function of $s+b$ and α is called confidence belt. Upon the measurement, n_o, the confidence interval $[n_1,\ n_2]$ is determined with the intersection of the vertical line drawn from the measured value n_o and the boundary of the confidence belt in graphic. The probability that the confidence interval will contains the true value s is $(1-\alpha)$, since this is true for all s for each construction. However, the choice of n_1 and n_2 is not unique to define the confidence belt. An additional criterion is applied to obtain certain value of "upper (lower) limit" of confidence belt, n_1 (n_2). We use likelihood ratio based on ordering scheme of the elements in the sum in A.1, called "Feldman and Cousins method" [63]. The following algorithm is applied in solving equation A.1. For each n, the $s_{\rm best}$ is found which maximizes the likelihood $\mathcal{L}(n, s+b)$. In case of a simple Poisson distribution with known background, $s_{\rm best}$ is given in $max(0, n-b)$. For a fixed s the ratio $R(s,n)_{\mathcal{L}}$ is thus computed for each n.

$$R(s,n)_{\mathcal{L}} = \frac{\mathcal{L}_{s+b}(n)}{\mathcal{L}_{s_{\rm best}+b}(n)} \tag{A.2}$$

All n's are consequently ranked corresponding to the value of this ratio. The values of n are included in the confidence belt starting with the n with the highest rank and deceasing rank until the equation A.1 is satisfied. After the confidence belt has been constructed in this way, the confidence interval is found as described above.

Until here, calculation is done in case of no uncertainty for expected background. In case of the presence of uncertainty of background assuming a Gaussian shape, the PDF is modified like following.

$$q(n, s+b) = \frac{1}{\sqrt{2\pi}\sigma_b} \int_0^\infty p(n, s+b') e^{-\frac{(b-b')^2}{2\sigma_b}} db' \tag{A.3}$$

where σ_b is the uncertainty in the expected background. In addition to the uncertainty for background, we should consider to include the uncertainty in the signal detection efficiency ϵ (also assuming the shape is a Gaussian distribution) the PDF is extended to

$$q(n, s+b) = \frac{1}{2\pi\sigma_\epsilon\sigma_b} \int_0^\infty \int_0^\infty p(n, \epsilon' s + b') e^{-\frac{(\epsilon-\epsilon')^2}{2\sigma_\epsilon}} e^{-\frac{(b-b')^2}{2\sigma_b}} d\epsilon' db' \tag{A.4}$$

where σ_ϵ is the uncertainty in the signal detection efficiency. In actual computing the upper confidence intervals, we use the FORTRAN based program called "POLE program" [72].

Bibliography

[1] W.J. Marciano and A.I. Sanda, Phys. Lett. B 67 (1977) 303; B.W. Lee and R.E. Shrock, Phys. Rev. D 16 (1977) 1444; T.P. Cheng and L.F. Li, Phys. Rev. D 16 (1977) 1425.

[2] J.R. Ellis *et al.*, Phys. Rev. D 66 (2002) 115013.

[3] F. Borzumati and A. Masiero, Phys. Rev. Lett. 57 (1986) 961; J. Hisano, T. Moroi, K. Tobe, M. Yamaguchi and T. Yanagida, Phys. Lett. B 357 (1995) 579; J. Hisano, T. Moroi, K. Tobe, and M. Yamaguchi, Phys. Rev. D 53 (1996) 2442; J. Hisano and D. Nomura, Phys. Rev. D 59 (1999) 116005.

[4] K.S. Babu and C. Kolda, Phys. Rev. Lett. 89 (2002) 241802; A. Dedes, J. Ellis and M. Raidal, Phys. Lett. B 549 (2002) 159.

[5] E. Ma, Phys. Rev. D 64 (2001) 097302; E. Ma, M. Raidal and U. Sarkar, Phys. Rev. Lett. 85 (2000) 3769; E. Ma, Phys. Rev. D 66 (2002) 037301.

[6] C. Yue, Y. Zhang and L. Liu, Phys. Lett. B 547 (2002) 252.

[7] J.E. Kim, P. Ko and D. Lee, Phys. Rev. D 56 (1997) 100.

[8] A. Abashian *et al.* (Belle Collaboration), Nucl. Instr. and Meth. A 479 (2002) 117.

[9] S. Kurokawa and E. Kikutani, Nucl. Instr. and Meth. A 499 (2003) 1, and other papers included in this Volume.

[10] S. Nishida *et al.* (Belle Collaboration), Phys. Rev. Lett. 93 (2004) 0318038.

[11] J. Kaneko *et al.* (Belle Collaboration), Phys. Rev. Lett. 90 (2003) 021801.

[12] Y. Fukuda *et al.* (Super-Kamiokande Collaboration) Phys. Rev. Lett. 81 (1998) 1562.

[13] M.H. Ahn *et al.* (K2K Collaboration) Phys. Rev. Lett. 93 (2004) 051801.

[14] T. Araki *et al.* (KamLAND Collaboration), hep-ex/0406035.

[15] B. Aharmim *et al.* (SNO Collaboration), hep-ex/0407029.

[16] S. Weinberg, Phys. Rev. Lett. 19, 1264 (1967); A. Salam, p. 367 of *Elementary Particle Theory*, ed. N. Svartholm (Almquist and Wiksells, Stockholm, 1969); S.L. Glashow, J. Iliopoulos, and L. Maiani, Phys. Rev. D 2 1285 (1970).

[17] M. Kobayashi and T. Maskawa, Prog. Theor. Phys. **49** (1973) 652; N. Cabibbo, Phys. Rev. Lett. 10 (1963) 531 ;

[18] S. Eidelman, et. al. (Particle Data Group), Phys. Lett. B 592 (2004)1

[19] S. K. Kang and C. S. Kim, Phys. Rev. D 63 (2001) 113010; K. Kang, S. K. Kang, C. S. Kim and S. M. Kim, Mod. Phys. Lett. A 16 (2001) 2169.

[20] F. Simkovic *et al.*, Phys. Rev. C 64 (2001) 035501.

[21] P. Langacker and D. London, Phys. Rev. D 38 (1998) 886.

[22] E. Nardi, E. Roulet and D. Tommasini, Phys. Lett. B 327 (1994) 319; *ibid.* 334 (1995) 225; D. Tommasini, G. Barenboim, J. Bernabeu and C. Jarlskog, Nucl. Phys. B 444 (1995) 451.

[23] M. S. Chanowitz, M. A. Furman and I. Hinchliffe, Nucl. Phys. B 153 (1979) 402; L. Durand, J. M. Johnson and J. L. Lopez, Phys. Rev. D 45 (1992) 3112

[24] A. Pilaftsis, Z. Phys. C 55 (1992) 275.

[25] S. Fajfer and A. Ilakovac, Phys. Rev. D 57 (1998) 4219.

[26] J. Bernabeu and P. Pascual, Nucl. Phys. B 228 (1983) 21; J. A. Aguilar-Saavedra, Int. J. Mod. Phys. C 8 (1997) 147.

[27] A. Ilakovac, Phys. Rev. D62 (2000) 036010.

[28] L. J. Hall, R. Rattazzi and U. Sarid, Phys. Rev. D 50 (1994) 7048.

[29] K. S. Babu and C. Kolda, Phys. Rev. Lett 84 (2000) 228.

[30] K. S. Babu and C. Kolda, J. March-Russell and F. Wilczek, D. 59 (1999) 016004.

[31] K. S. Babu and C. Kolda, Phys. Rev. Lett. 84 (2000) 228.

[32] K. Abe *et al.* (Belle Collaboration), Phys. Rev. Lett. 92 (2004) 171802.

[33] J. Hisano, T. Moroi, K.Tobe, M. Yamaguchi and T. Yanagida, phys. Lett. B 357 (1995) 579; J. Hisano, T. Moroi, K. Tobe, and M. Yamaguchi, Phys. Rev. D 53 (1996) 2442.

[34] C. T. Hill, Phys. Lett B 345 (1995) 483; K. Lane and E. Eichten, Phys. Lett. B 352 (1995) 383; K. Lane, Phys. Lett. B 433 (1998) 96; G. Cvetic, Rev. Mod. Phys. 71 (1999) 513.

[35] M. B. Popovic and E. H. Simmons, Phys. Rev. D 58 (1998) 095007; G. Burdman and N. Evans, Phys. Rev. D 59 (1999) 115005.

[36] L. Wolfenstein, Phys. Rev. Lett. 51 (1983) 1945.

[37] S. Nussinov, P. D. Peccei and X. M. Zhang, Phys. Rev. D 63 (2000) 016003.

[38] K.G. Hayes *et al.*, Phys. Rev. D 25 (1982) 1982.

[39] D.W. Bliss *et al.* (CLEO Collaboration), Phys. Rev. D 57 (1998) 5903.

[40] B. Aubert *et al.* (BABAR Collaboration), Phys. Rev. Lett. B 92 (2004) 121801.

[41] B. Aubert *et al.* (BABAR Collaboration), hep-ex/0409036.

[42] G. Alimonti *et al.*, Nucl. Instrum. Methods **A 453**, 71 (2000). Belle SVD Group, "Technical Design Report of Belle SVD" (1998).

[43] H. Hirano *et al.*, Nucl. Instrum. Methods **A 455**, 294 (2000); M. Akatsu *et al.*, Nucl. Instrum. Methods **A 454**, 322 (2000).

[44] T. Iijima *et al.*, Nucl. Instrum. Methods **A 453**, 321 (2000).

[45] TH. Kichimi *et al.*, Nucl. Instrum. Methods **A 453**, 315 (2000).

[46] H. Ikeda *et al.*, Nucl. Instrum. Methods **A 441**, 401 (2000).

[47] A. Abashian *et al.*, Nucl. Instrum. Methods **A 449**, 112 (2000).

[48] Belle Collaboration, "Belle progress report 1995 April - 1996 March", KEK Progress Report 96-1 (1996).

[49] R. E. Kalman, Trans. ASME, J. Bas. Eng. **82D**, 25 (1960); R. E. Kalman and R. S. Bucy, Trans. ASME, J. Bas. Eng. **83D**, 95 (1961).

[50] R. Santonico *et al.*, "RPC: Status and Perspectives.", International Workshop on the RPCs and related detectors, 1993.

[51] R. Itoh, Belle note #161 (1996), unpublished.

[52] R. Brun and D. Lienart, CERN-Y250.

[53] KORALB(v2.4)/TAUOLA(v2.6); S. Jadach and Z. Wąs, Comp. Phys. Commun. 85 (1995) 453; *ibid*, 64 (1991) 267; S. Jadach, Z.Wąs, R. Decker and J.H.Kühn, Comp. Phys. Commun. 76 (1993) 361; *ibid*, 70 (1992) 69; *ibid*, 64 (1991) 275.

[54] Events are generated with KKMC generator: S. Jadach, B.F.L. Ward, Z. Wąs, Comp. Phys. Commun. 130 (2000) 260

[55] CLEO software document homepage:
<http://www.lns.cornell.edu/public/CLEO/soft/QQ/index.html> (1998)

[56] Belle aafhb document homepage:
<http://belle.kek.jp/secured/tautp/aafhb_readme.html> (1999)

[57] F. A. Berends, P. H,, Daverveldt and R. Kleiss, Comp. Phys. Common **40** 285 (1986)

[58] R. Brun *et al.*, GEANT 3.21, CERN Report No. DD/EE/84-1 (1984).

[59] K. Hanagaki *et al.*, Nucl. Instr. and Meth. A 485 (2002) 490.

[60] A. Abashian *et al.*, Nucl. Instr. and Meth. A 491 (2002) 69.

[61] G. C. Fox and S. Wolfram, Phys. Rev. Lett. 41 (1978) 1581.

[62] R. Kitano and Y. Okada, Phys. Rev. D 63 (2001) 113003.

[63] G.J. Feldman and R.D. Cousins, Phys. Rev. D 57 (1998) 3873.

[64] R.D. Cousins and V.L Highland, Nucl. Instr. and Meth. A 320 (1992) 331.

[65] The CDF Collaboration, Phys. Rev. Lett. 86 (2001) 4472.

[66] G. Buchahalla, G. Burdman, C. T. Hill, D. Kominis, Phys. Rev. D 53 (1996) 5185; C. T. Hill and H. Simmons, Phys. Rept. 381 (2003) 235-402; Erratum-ibid. 390 (2004) 553-554.

[67] R. S. Chivukula, E. H. Simmons, Phys.Rev. D66 (2002) 015006.

[68] The CDF Collaboration, Phys. Rev. Lett. 79 (1997) 2192.

[69] A. G. Akeroyd *et al.* (The SuperKEKB Physics Working Group), hep-ex/0406071.

[70] LHWG Note 2001-04.

[71] J. Neyman, Phil. Trans. Royal Soc. London, Series A **236**, 333 (1937), reprinted in *A Selection of Early Statistical Papers on J. Neyman* (University of California Press, Berkeley 1967).

[72] J. Conrad, O. Botner, A. Hallgren and Carlos P. de los Heros, Phys. Rev. D 67 (2003) 012002.